Molten Salt Reactor Chemistry

Structure and Equilibria

Ocadiz flores, J.A.

DOI
10.4233/uuid:a2658b9e-c380-4a36-8049-a0af26fe3e54

Publication date
2021

Document Version
Final published version

Citation (APA)
Ocadiz flores, J. A. (2021). *Molten Salt Reactor Chemistry: Structure and Equilibria*.
https://doi.org/10.4233/uuid:a2658b9e-c380-4a36-8049-a0af26fe3e54

MOLTEN SALT REACTOR CHEMISTRY

STRUCTURE AND EQUILIBRIA

MOLTEN SALT REACTOR CHEMISTRY

STRUCTURE AND EQUILIBRIA

Proefschrift

ter verkrijging van de graad van doctor
aan de Technische Universiteit Delft,
op gezag van de Rector Magnificus prof.dr. ir. T.H.J.J. van der Hagen,
voorzitter van het College voor Promoties,
in het openbaar te verdedigen op vrijdag 12 november 2021 om 12.30 uur

door

Jaén Alonso OCÁDIZ FLORES

Master of Science in Chemical Engineering
Delft University of Technology, Delft, The Netherlands,
geboren te Mexico-Stad, Mexico.

Dit proefschrift is goedgekeurd door de

promotor: prof. dr. R.J.M. Konings
copromotor: dr. A.L. Smith

Samenstelling promotiecommissie:

Rector Magnificus,	voorzitter
Prof. dr. R.J.M. Konings,	Technische Universiteit Delft
Dr. A.L. Smith,	Technische Universiteit Delft
Onafhankelijke leden:	
Prof. dr. ir. J. Sietsma,	Technische Universiteit Delft
Prof. dr. M. Salanne,	Sorbonne Universités, UPMC Univ. Paris 06
Prof. dr. ir. D. Semidubský,	Institute of Chemical Technology, Prague
Dr. C. Guéneau,	Commissariat a l'energie atomique et aux énergies alternatives
Prof. dr. ir. J.L. Kloosterman,	Technische Universiteit Delft, reserve lid
Overige leden:	
Dr. ir. O. Beneš,	Joint Research Centre, Karlsruhe
Dr. A.E. Gheribi,	École Polytechnique, Montreal

Keywords: Molten Salt Reactor, molten salts, actinide fluorides, actinide chlorides, CALPHAD, Differential Scanning Calorimetry (DSC), X-ray diffraction (XRD), Extended X-Ray Absorption Fine Structure (EXAFS), Polarizable Ion Model (PIM), Molecular Dynamics (MD)

ISBN 978-94-6384-270-9

An electronic version of this dissertation is available at
`http://repository.tudelft.nl/`.

He threw his cigar away and looked up at the outstretched Galaxy.
"Back to oil and coal, are they?", he murmured
–and what the rest of his thoughts were he kept to himself.

Isaac Asimov, *Foundation*

CONTENTS

Summary xi

Samenvatting xv

1 Introduction 1
- 1.1 Molten Salt Reactors . . . 2
- 1.2 Applications of MSRs . . . 3
- 1.3 Concerns facing MSRs . . . 4
  - 1.3.1 Impurity driven corrosion . . . 5
  - 1.3.2 Intrinsic corrosion . . . 6
  - 1.3.3 Thermal gradient-driven corrosion . . . 8
  - 1.3.4 Stress corrosion cracking. . . . 8
- 1.4 This dissertation in the context of Molten Salt Reactors . . . 8
- 1.5 Content . . . 9

2 Thermodynamic assessment of the KF-ThF_4, LiF-KF-ThF_4 and NaF-KF-ThF_4 systems 15
- 2.1 Introduction . . . 16
- 2.2 Experimental methods . . . 16
  - 2.2.1 Sample preparation for DSC measurements . . . 16
  - 2.2.2 Synthesis. . . . 17
  - 2.2.3 Powder X-ray diffraction . . . 17
  - 2.2.4 Differential Scanning Calorimetry . . . 18
  - 2.2.5 Enthalpy of mixing measurements . . . 18
  - 2.2.6 Low temperature heat capacity . . . 19
- 2.3 Thermodynamic modelling . . . 20
  - 2.3.1 Pure compounds. . . . 20
  - 2.3.2 Solid solution . . . 21
  - 2.3.3 Liquid solution. . . . 23
  - 2.3.4 Higher order systems . . . 24
- 2.4 Previous evaluations of the KF-ThF_4 system . . . 25
- 2.5 Results and discussion . . . 25
  - 2.5.1 Phase diagram studies in the KF-ThF_4 system . . . 25
  - 2.5.2 Solid solution . . . 30
  - 2.5.3 Low temperature heat capacity of α-K_2ThF_6 . . . 30
  - 2.5.4 Mixing properties of the $(K_xTh_{1-x})F_{4-3x}$ liquid solution . . . 33
  - 2.5.5 CALPHAD assessment of the KF-ThF_4 system . . . 36
  - 2.5.6 CALPHAD assessment of the LiF-KF-ThF_4 system . . . 38
  - 2.5.7 CALPHAD assessment of the NaF-KF-ThF_4 system . . . 41

2.6 Conclusions . . . 49
2.7 CRediT author statement . . . 49
2.8 Acknowledgements . . . 49
A.1 Previous phase diagrams of KF-ThF_4 reported in the literature . . . 50
A.2 Thermodynamic data for $KNaThF_6$ . . . 51
A.3 Lattice parameters of Rietveld and LeBail refinements . . . 52
A.4 Experimental heat capacity data and standard thermodynamic functions for K_2ThF_6 . . . 54
A.5 Representative DSC curves . . . 57
A.6 Excess Gibbs energy parameters of the consitutent binary liquid solutions . 60

3 Thermodynamic description of the ACl-$ThCl_4$ (A= Li, Na, K) systems 67
3.1 Introduction . . . 68
3.2 Thermodynamic modelling . . . 69
3.2.1 Pure compounds . . . 69
3.2.2 Liquid solution . . . 70
3.3 Results and Discussion . . . 72
3.3.1 Phase Diagrams . . . 72
3.3.2 Enthalpy of mixing . . . 73
3.4 Conclusions . . . 78
3.5 Author Contributions . . . 79
3.6 Acknowledgments . . . 79
A.1 Erratum to: Thermodynamic description of the ACl-$ThCl_4$ (A = Li, Na, K) systems . . . 79

4 Examination of the short-range structure of molten salts: ThF_4, UF_4, and related alkali actinide fluoride systems 91
4.1 Introduction . . . 92
4.2 Experimental method . . . 92
4.3 Molecular Dynamics simulations . . . 94
4.4 Results and discussion . . . 95
4.4.1 Local structure of uranium and thorium tetrafluoride . . . 95
4.4.2 Local structure of the AF-UF_4 and AF-ThF_4 melts . . . 101
4.4.3 Main structural features of the liquid mixtures . . . 107
4.4.4 Implications for the transport properties: viscosity and electrical conductivity . . . 112
4.5 Conclusion . . . 113
4.6 CRediT author statement . . . 115
4.7 Supporting Information for: Examination of the short-range structure of molten salts: ThF_4, UF_4, and related alkali actinide fluoride systems . . . 115
4.7.1 Coordination environment of the actinide cations . . . 115
4.7.2 Radial distribution functions of the liquid mixtures . . . 115
4.7.3 XANES data . . . 123

5 New insights and coupled modelling of the structural and thermodynamic properties of the LiF-UF_4 system 129
5.1 Introduction . . . 131
5.2 Experimental methods . . . 132
5.2.1 Reagent preparation and handling . . . 132
5.2.2 Synthesis . . . 132
5.2.3 Powder X-ray diffraction . . . 132
5.2.4 Differential Scanning Calorimetry . . . 133
5.2.5 High-temperature EXAFS measurements . . . 133
5.3 Molecular Dynamics simulations . . . 134
5.4 Thermodynamic modelling . . . 136
5.4.1 Pure compounds . . . 136
5.4.2 Liquid solution . . . 137
5.5 Brief review of literature data on the LiF-UF_4 system . . . 141
5.6 Results and discussion . . . 143
5.6.1 Phase diagram studies in the LiF-UF_4 system . . . 143
5.6.2 Local structure of the (Li,U)F_x melt . . . 147
5.6.3 Excess properties of the (Li,U)F_x liquid solution . . . 155
5.6.4 CALPHAD assessment of the LiF-UF_4 system . . . 160
5.7 Conclusions . . . 161
5.8 CRediT author statement . . . 162
5.9 Acknowledgements . . . 162
5.10 Supplementary Information for: New insights and coupled modelling of the structural and thermodynamic properties of the LiF-UF_4 system . . . 163
5.10.1 Lattice parameters of Rietveld and LeBail refinements . . . 163
5.10.2 Thermal expansion . . . 163
5.10.3 Molar enthalpy . . . 165
5.10.4 Mixing Gibbs energies and entropies of mixing . . . 166

6 Experimental and Computational Exploration of the NaF-ThF_4 Fuel System: Structure and Thermochemistry 175
6.1 Introduction . . . 177
6.2 Methods . . . 178
6.2.1 Computational methods . . . 178
6.2.2 Experimental Methods . . . 178
6.2.3 CALPHAD modelling . . . 181
6.2.4 Structural investigations of the (Na,Th)F_x melt via Molecular Dynamics . . . 183
6.2.5 Thermodynamic studies . . . 186
6.2.6 Coupled structural-thermodynamic model of the NaF-ThF_4 system . 196
6.3 Conclusions . . . 197
6.4 CRediT author statement . . . 199
6.5 Supplementary Information: Experimental and Computational Exploration of the NaF-ThF_4 Fuel System: Structure and Thermochemistry . . . 199
6.5.1 Molecular Dynamics calculations . . . 199
6.5.2 DFT and TSC . . . 202

6.5.3 CALPHAD modelling. 203
6.5.4 Calphad modelling. 203
6.5.5 Phase equilibria and enthalpy of mixing measurements by DSC . . . 207
6.5.6 Density and thermal expansion 207
6.5.7 Density 207
6.5.8 Thermal expansion 208
6.5.9 Medium-range order in the (Na,Th)F_x liquid solution 208

7 Beyond the Phase Diagram: Density and Viscosity Models for Molten Salt Fuel Systems 219
7.1 Introduction 220
7.2 Thermodynamic modelling 221
7.2.1 Phase diagrams 221
7.2.2 Density model 225
7.2.3 Viscosity model 226
7.3 Results and Discussion 227
7.3.1 Thermodynamic assessments 227
7.3.2 Density and viscosity models for the pure liquid components 230
7.3.3 Density and viscosity models for the binary systems 233
7.3.4 Density and viscosity models of the LiF-ThF_4-UF_4 ternary system . . 237
7.4 Conclusions. 238
7.5 Acknowledgements 240

8 Conclusions and Recommendations 247
8.1 General trends in structural and thermochemical properties of molten salts 247
8.2 Detailed outcomes of this dissertation 249
8.2.1 Structure. 249
8.2.2 Phase equilibria 249
8.2.3 Thermophysical properties 250
8.2.4 Structure-property relationship 250
8.3 Recommendations for Future Work 250

Acknowledgements 255

List of Publications 257

About the Author 259

SUMMARY

Molten salts are a class of ionic liquids which have in recent years been the focus of extensive fundamental research given that they are a versatile class of reaction media with a variety of appealing thermophysical and thermochemical properties (e.g. melting points, heat capacities, vapor pressures, densities, thermal conductivities, etc..) suited for a variety of industrial applications, in particular at high temperature. The most well-known is perhaps the production of materials as important as aluminum and sulfuric acid, yet thermal energy storage is also a notable application. One of the most noteworthy application of molten salts, is as fuel and coolant for a type of nuclear fission reactor known as the Molten Salt Reactor (MSR). In its most general sense, a MSR is a class of nuclear reactor in which fissile (^{235}U, ^{233}U, ^{239}Pu) and/or fertile isotopes (e.g. ^{232}Th, ^{238}U) are dissolved in a carrier salt. The resulting mixture acts both as fuel and coolant. The two prototypes which have been built in the past used a fluoride fuel, so historically most work has concentrated on fluoride salt mixtures. However, modern day reactor developers are also interested in chloride fuels, so both molten salt fuel families are relevant at present.

Due to the nature of the fission reaction, MSR fuel is a mixture with considerable chemical complexity, comprising a multi-component salt solution, noble gases, and noble metal precipitates. A thermodynamic description of this complex system must be the foundation of any systematic attempt to select its original composition, predict its behavior in the reactor core during normal operation and accidental conditions, (in particular predict liquidus temperature, precipitation of a given component, stability of structural materials against the fuel), and guide reprocessing schemes after burn-up. In practice, this must be done by dividing the whole system into smaller building blocks for which a very accurate analysis can be provided: first unitary systems, then binary, ternary, and so on. The Gibbs energy is the thermodynamic potential which indicates which phase or combination thereof will be stable at a given composition and isothermal-isobaric state: that which minimizes the total Gibbs energy of the system. Thus every level of description should minimally contain the set of phases involved (end-members, stoichiometric intermediate compounds, solid and liquid solutions) and the Gibbs energy associated with each one.

Solution phases will have a Gibbs energy corresponding to the weighted sum of the Gibbs energies plus a mixing contribution. The mixing contribution in turn will consist of an ideal term arising from the configurational entropy, and an excess term which will be zero if the solution is ideal and non-zero otherwise. In general this excess term is unknown and needs to be optimized, along with any other Gibbs energy functions which may be unknown, so as to reproduce known thermodynamic data. This optimization is at the core of thermodynamic modelling. Closely related to the excess Gibbs energy of the liquid solution is the local structure, which for molten salts may be ionic, molecular, or polymeric, and which will also be manifest in excess contributions to the mixing en-

thalpies and entropies, heat capacities, activities, and other thermophysical properties. As density and viscosity are state functions, they may in principle also be linked to the Gibbs energy of the system and to the local structure.
This dissertation is an effort in the direction of making an explicit link between the structure, thermodynamics, and state properties (density, viscosity) for a set of salts comprised of alkali actinide halides related to MSR technology: ACl-$ThCl_4$ (A = Li, Na, K), LiF-AnF_4 (An = Th, U), NaF-ThF_4, KF-ThF_4, NaCl-UCl_3, and the ternaries LiF-ThF_4-UF_4, LiF-KF-ThF_4, and NaF-KF-ThF_4. Several experimental and computational techniques were used throughout this work to achieve said goal: differential scanning calorimetry (DSC), X-ray diffraction (XRD), thermal relaxation calorimetry, X-ray absorption spectroscopy (XAS), molecular dynamics (MD), and density functional theory (DFT). The collected data were modelled simultaneously with computational thermodynamics, using the so-called CALPHAD method (Calculation of Phase Diagrams).

A thermodynamic assessment of the KF-ThF_4 binary system using the CALPHAD method is reported initially, in which the liquid solution is described by the modified quasi-chemical formalism in the quadruplet approximation. The optimization of the phase diagram is based on experimental data reported in the literature and newly measured XRD and DSC data, which allowed to solve discrepancies between past assessments. The low temperature heat capacity of α-K_2ThF_6 was also measured, using thermal relaxation calorimetry; from these data the heat capacity and standard entropy values were derived at 298.15 K and implemented in the model. Taking existing assessments of the relevant binaries, the new optimization was moreover used to assess the ternary systems LiF-KF-ThF_4 and NaF-KF-ThF_4, for which novel DSC data were also collected. The standard enthalpy of formation and standard entropy of $KNaThF_6$ were re-calculated from published e.m.f data, and included in the assessment of the ternary system.

Since chloride salts are also candidates for MSR fuels, a thermodynamic investigation of the ACl-$ThCl_4$ (A = Li, Na, K) binary systems was furthermore carried out. The excess Gibbs energy of the liquid solutions was also described using the quasi-chemical formalism in the quadruplet approximation. The phase diagram optimizations in this case were based solely on the experimental data available in the literature. The thermodynamic stability of the liquid solutions increases in the order Li $<$ Na $<$ K, in agreement with simplified interactions and structural models.

To develop realistic structural models, the short-range structures of AF-AnF_4 (A = Li, Na, K, Cs; An = Th, U) systems were then probed using *in situ* high temperature Extended X-ray Absorption Fine Structure (EXAFS) spectroscopy. Notably, the EXAFS spectra of pure molten ThF_4 and UF_4 were measured for the first time. The data were interpreted with the aid of MD simulations and standard fitting of the EXAFS equation. As in related studies, a speciation distribution dominated by $[AnF_x]^{4-x}$ (x = 7, 8, 9) coordination complexes was observed. The average coordination number was found to decrease with the increasing size of the alkali cation, and increase with AnF_4 content. An average coordination number close to 6, which had not been detected before in melts of alkali actinide fluorides, was seen when CsF was used as solvent.

Using MD, the structures of the melts were further characterized for composition and temperature domains extended beyond what was possible with the EXAFS technique, for the systems LiF-UF_4 and NaF-ThF_4, which were taken as case studies for the implementation of an advanced quasi-chemical formalism. For both binary systems the phase diagram equilibria were explored with XRD and DSC. The densities, excess molar volumes, thermal expansion, heat capacities, and enthalpies of mixing were moreover extracted from the MD simulations across a range of temperatures and compositions. The distributions of heteropolyanions in the liquid solution were also calculated, and modelled using the quasi-chemical formalism in the quadruplet approximation, thereby explicitly linking the structural and thermodynamic properties to result in a rigorous physical description of the melts. The existence of 7- and 8-coordinated single-shell complexes and of the dimeric species $[U_2F_{14}]^{6-}$ (in the case of LiF-UF_4) and $[Th_2F_{13}]^{5-}$ (in the case of NaF-ThF_4) were taken into account. Subjecting the optimization of the excess Gibbs energy parameters of the liquid solution to the constraints of the phase diagram data and local structure of the melt as derived from the EXAFS and coupled MD simulations, a CALPHAD-type assessment was proposed, linking structural and thermodynamic properties, with a rigorous physical description of the melt. For NaF-ThF_4, the description was made even more rigorous by experimentally deriving the standard entropies from low-temperature heat capacity measurements of two phases appearing in the system, with formula Na_2ThF_6 and $NaTh_2F_9$. Furthermore, the low and high-temperature heat capacities of these phases were successfully bridged with a methodology combining DFT and the Quasi-Harmonic Approximation (QHA).

Finally, an effort was made to compute the density and viscosity functions, in a way consistent with the thermodynamic assessments. Models for four systems were optimized: NaCl-UCl_3, LiF-ThF_4, LiF-UF_4, and LiF-ThF_4-UF_4. Assessment of all four systems, using the modified quasichemical formalism in the quadruplet approximation for the description of the liquid solutions, were carried out. In the case of NaCl-UCl_3, phase diagram and mixing enthalpy data available in the literature were incorporated. For the fluoride systems, recently published data on some solid phases were taken into account, while retaining the most recently published descriptions of the liquid solutions. The densities of the liquid solutions, when not ideal, were modelled using pressure-dependent terms of the excess Gibbs energy, while the viscosities were modelled using an Eyring equation.

Overall, the thesis improves the state of knowledge on the topology of the phase diagrams studied. Throughout the work, structural motifs of actinide-bearing molten salts are discussed, with a view to aid in the prediction of the characteristics of systems which are to this date unexplored. The quasi-chemical formalism has become well-established in the computational thermodynamics of MSR chemistry, and the number of systems assessed is already substantial. This work is a template showing how databases of molten salt fuels may be extended to reflect more largely structure, density, and viscosity in combination with the thermodynamic properties.

SAMENVATTING

Gesmolten zouten vormen een groep van ionaire vloeistoffen die onderwerp van uitgebreid fundamenteel onderzoek zijn geweest in de afgelopen jaren. Dit is te danken aan het feit dat het een veelzijdige reactiemedia betreft, met een verscheidenheid aan aantrekkelijke thermofysische eigenschappen (zoals het smeltpunt, soortelijke warmte, dampspanning, dichtheid, warmtegeleiding, etc...), geschikt voor een veelvoud van industriële toepassingen – in het bijzonder bij hoge temperaturen. Het meest bekend is wellicht de productie van belangrijke materialen zoals aluminium en zwavelzuur, maar daarnaast is ook de mogelijkheid warmte op te slaan noemenswaardig. Een van de meest opmerkelijke toepassingen van gesmolten zouten is als splijtstof en koelvloeistof voor een bepaald type kernreactor, te weten de gesmoltenzoutreactor (MSR). Een MSR is een type kernreactor waarin splijtbare isotopen (^{235}U, ^{233}U, ^{239}Pu) en/of isotopen waaruit splijtbaar materiaal kan worden gekweekt (bijv. ^{232}Th, ^{238}U), zijn opgelost in een zout. Dit mengsel is zowel splijtstof als koelmiddel. De twee prototypes die in het verleden zijn gebouwd, maakten beide gebruik van een fluoride splijtstof, wat ertoe heeft geleid dat historisch het meeste onderzoek zich richtte op fluoride-zoutmengsels. Desalniettemin zijn hedendaagse reactorontwikkelaars ook geïnteresseerd in chloride splijtstoffen, dus beide families van gesmoltenzoutsplijtstoffen zijn momenteel relevant.

Als gevolg van de kernsplijting is MSR-splijtstof een mengsel met een grote chemische complexiteit, en bestaat uit een vloeibare oplossing van meerdere componenten, edelgassen en neergeslagen deeltjes van edelmetalen. Een thermodynamische beschrijving van dit complexe systeem moet ten grondslag liggen aan iedere systematische poging om de initiële zoutsamenstelling te bepalen, het gedrag in de kern van de reactor – zowel tijdens normaal bedrijf als ongevalssituaties – te voorspellen (in het bijzonder de liquidustemperatuur, neerslag van componenten, stabiliteit van structurele materialen ten opzichte van de splijtstof), en verwerkingsschema's voor de opgebrande splijtstof te ontwerpen. In de praktijk wordt dit bewerkstelligd door het opdelen van het complexe systeem in kleinere stukken, waarvan een zeer accurate beschrijving verkregen kan worden: eerst de unaire systemen, daarna de binaire, de ternaire, etc. De Gibbs vrije energie correspondeert met de thermodynamische potentiaal die aangeeft welke fase, of combinatie daarvan, stabiel zal zijn voor een gegeven samenstelling en isothermische-isobare toestand: die waarvoor de totale Gibbs vrije energie van het systeem het laagst is. Op elk niveau zal de beschrijving dus minstens alle betreffende fases moeten omvatten (eindleden, stoichiometrische intermediaire verbindingen, vaste en vloeibare oplossingen), evenals de Gibbs vrije energie van de fases.

Mengfasen hebben een Gibbs vrije energie die overeenkomt met de gewogen som van de Gibbs vrije energieën en een mengbijdrage. De mengbijdrage zal op zijn beurt bestaan uit een ideale waarde overeenkomend met de configurationele entropie, en een

exces bijdrage die nul zal zijn indien de oplossing ideaal is en niet-nul zal zijn in de andere gevallen. Over het algemeen is deze exces waarde onbekend en optimalisatie ervan is nodig, wat ook geldt voor iedere andere Gibbs-energiefunctie die mogelijk onbekend is, teneinde de bekende thermodynamische gegevens te kunnen reproduceren. Deze optimalisatie vormt de kern van thermodynamisch modelleren. De atomaire structuur is nauw verbonden met de exces Gibbs vrije energie van de vloeibare oplossing, welke voor gesmolten zouten ionair, moleculair of polymerisch kan zijn, en tevens tot uiting zal komen in de vorm van exces bijdragen aan mengenthalpie en -entropie, warmtecapaciteit, chemische activiteit, en andere thermofysische eigenschappen. Aangezien dichtheid en viscositeit toestandsfuncties zijn, kunnen zij in beginsel gerelateerd worden aan de Gibbs vrije energie van het systeem, en met de atomaire structuur.

Dit proefschrift wordt de expliciete link onderzocht tussen de structuur, thermodynamica en toestandseigenschappen (dichtheid, viscositeit) voor een groep zouten die zijn samengesteld uit alkali-actinide-halogeniden, relevant voor MSR-technologie: ACl-$ThCl_4$ (A = Li, Na, K), LiF-AnF_4 (An = Th, U), NaF-ThF_4, KF-ThF_4, NaCl-UCl_3, en de ternaire systemen LiF-ThF_4-UF_4, LiF-KF-ThF_4, en NaF-KF-ThF_4. Om bovengenoemd doel te bereiken is gebruik gemaakt van diverse experimentele en computationele technieken: differentiële scanning calorimetrie (DSC), röntgendiffractie (XRD), lage-temperatuurcalorimetrie, röntgenabsorptie-spectroscopie (XAS), moleculaire dynamica (MD), en Dichtheidsfunctionaaltheorie (DFT). Met behulp computationele thermodynamica, gebruikmakend van de zogeheten CALPHAD-methode (berekening van fasediagrammen, Calculation of Phase Diagrams), zijn verzamelde data in modellen verwerkt.

Dit proefschrift beschrijft eerst een thermodynamische evaluatie van het binaire KF-ThF_4-systeem aan de hand van de CALPHAD-methode. De vloeibare oplossing is hier beschreven met het verbeterde quasi-chemische formalisme in de quadruplet benadering . De optimalisatie van het fasediagram is gebaseerd op experimentele data uit de literatuur en nieuwe metingen met behulp van XRD- en DSC, waarmee de discrepanties tussen eerdere metingen konden worden opgelost. Met behulp van lage-temperatuurcalorimetrie is tevens de warmtecapaciteit van α-K_2ThF_6 gemeten, waaruit de warmtecapaciteit- en standaard entropie bij 298.15 K zijn afgeleid en geïmplementeerd in het model. Gebruikmakend van bestaande evaluaties van relevante binaire systemen, zijn voorts de ternaire systemen LiF-KF-ThF_4 en NaF-KF-ThF_4 geëvalueerd, waarvoor ook nieuwe DSC-gegevens werden verzameld. De vormingsenthalpie (onder standaardomstandigheden) en de standaardentropie van $KNaThF_6$ zijn herberekend uit gepubliceerde gegevens van elektromotorische-krachtmetingen, en meegenomen in de evaluatie van het ternaire systeem.

Aangezien chloride-zouten tevens van belang zijn als MSR-splijtstof, is er verder een thermodynamisch onderzoek uitgevoerd naar de binaire systemen ACl-$ThCl_4$ (A = Li, Na, K). De exces Gibbs vrije energie van de vloeibare oplossingen is eveneens beschreven aan de hand van het quasi-chemische formalisme in de quadruplet benadering. De optimalisaties van het fasediagram zijn in dit geval uitsluitend gebaseerd op de beschikbare experimentele gegevens uit de literatuur. De thermodynamische stabiliteit van de

vloeibare oplossingen neemt toe in de volgorde Li < Na < K, in overeenstemming met de vereenvoudigde interacties en structurele modellen.

Teneinde realistische structuurmodellen te ontwikkelen, werden de atomaire structuren van de AF-AnF_4 (A = Li, Na, K, Cs; An = Th, U)-systemen in situ onderzocht met hoge-temperatuur-EXAFS-spectroscopie (Extended X-ray Absorption Fine Structure). Vermeldenswaardig is daarbij dat het EXAFS-spectrum van puur gesmolten ThF_4 en UF_4 voor de eerste keer werd gemeten. De gegevens zijn verder geïnterpreteerd met behulp van MD-simulaties en standaardregressie analyse met de EXAFS-vergelijking. Zoals in vergelijkbare studies werd de verdeling van de moleculaire anionen in de vloeistof overheerst door de coördinatie $[AnF_x]^{4-x}$ (x = 7, 8, 9). Het bleek dat het gemiddelde coördinatiegetal afneemt naarmate het alkali-kation groter wordt, en de concentratie AnF_4 toeneemt. Een gemiddeld coördinatiegetal dat dicht bij 6 ligt - iets dat niet eerder werd geconstateerd in gesmolten alkali-actinide-fluoriden - werd waargenomen wanneer CsF als oplosmiddel werd gebruikt.

Met de toepassing van MD voor de systemen LiF-UF_4 en NaF-ThF_4 werden de structuren van de vloeistiffen verder gekarakteriseerd voor een reeks van composities en temperaturen, in een groter bereik dan mogelijk was met de EXAFS-techniek. Deze systemen werden als case studies genomen voor de implementatie van het verbeterde quasi-chemisch formalisme. Voor beide binaire systemen is het fasediagram onderzocht met XRD en DSC. De dichtheid, exces molaire volume, thermische expansie, warmtecapaciteit en enthalpie van mengsels werden bovendien verkregen met behulp van de MD-simulaties voor een reeks temperaturen en composities. De distributie van heteropolyanionen in de vloeistof fase werden eveneens berekend, en gemodelleerd aan de hand van het quasi-chemische formalisme in de quadruplet benadering. Daarbij werden expliciet de structurele en thermodynamische eigenschappen gekoppeld, met een gedegen fysische beschrijving van de vloeistof fase als resultaat. Er is rekening gehouden met het bestaan van 7- en 8-gecoördineerde enkelvoudige complexen en het dimeer $[U2F_{14}]^{6-}$ in het geval van LiF-UF_4 en $[Th2F_{13}]^{5-}$ in het geval van NaF-ThF_4. In de CALPHAD optimalisatie van de parameters voor de exces Gibbs vrije energie van de vloeibare fase zijn de fasediagramgegevens en de atomaire structuur van de vloeistof, zoals afgeleid uit de EXAFS- en gekoppelde MD-simulaties, als invoer gebruikt, en zijn structuur en thermodynamische eigenschappen gekoppeld in een robuuste fysische beschrijving van de vloeistoffase. In het geval van NaF-ThF_4 was de beschrijving zelfs nog grondiger dankzij gebruik van de standaardentropieën van de twee fases die voorkomen in het systeem, Na_2ThF_6 en $NaTh_2F_9$, verkregen uit metingen van de warmtecapaciteit bij lage temperaturen . Daarnaast is de warmtecapaciteit bij hoge en lage temperaturen van deze fases succesvol verbonden door middel van een combinatie van DFT en de Quasi-Harmonische Benadering (Quasi harmonic approximation, QHA).

Tenslotte zijn berekeningen van dichtheid en viscositeit uitgevoerd met een aanpak die overkomt met de thermodynamische evaluaties. Modellen voor de volgende vier systemen zijn geoptimaliseerd: NaCl-UCl_3, LiF-ThF_4, LiF-UF_4, en LiF-ThF_4-UF_4. Er zijn evaluaties van alle vier de systemen uitgevoerd, waarbij voor de beschrijving van

de vloeibare mengfases gebruik gemaakt werd van het verbeterde quasi-chemische formalisme in de quadruplet benadering. In het geval van NaCl-UCl_3 zijn in de literatuur beschikbare gegevens uit fasediagrammen en mengenthalpiemetingen meegenomen. Voor de fluoridesystemen werden onlangs gepubliceerde gegevens voor enkele vaste fases meegenomen, terwijl de onlangs gepubliceerde beschrijvingingen van de vloeibare oplossingen werden overgenomen. De dichtheid van de vloeibare oplossingen werd, indien niet ideaal, gemodelleerd met drukafhankelijke variabelen voor de exces Gibbs vrije energie, terwijl voor het model van de viscositeit gebruik werd gemaakt van een Eyring-vergelijking.

Samenvattend kan worden gesteld dat dit proefschrift de kennis van de topologie van de bestudeerde fasediagrammen verder heeft gebracht. Dwars door het werk zijn de structuur kenmerken van actinide-houdende gesmolten zouten besproken, met als doel het voorspellen van de eigenschappen van systemen die tot op heden nog niet zijn verkend. Het quasi-chemische formalisme is onderhand gemeengoed geworden in de computationele thermodynamische beschrijving van het chemie van de MSR, en het aantal geëvalueerde systemen is inmiddels aanzienlijk. Dit werk dient als voorbeeld hoe databases van gesmolten-zoutsplijtstoffen kunnen worden uitgebreid om dichtheid en viscositeit in combinatie met de thermodynamische eigenschappen te beschrijven.[1]

[1] Dutch translation provided by Stefanie Klaassen with corrections by Rudy Konings.

1

INTRODUCTION

'You've got to come back with me!'
'Where?'

Back to the Future

1

1.1. MOLTEN SALT REACTORS

The Molten Salt Reactor (MSR, Fig. 1.1) is one of the six nuclear reactor designs retained by the Generation IV International Forum as a promising concept for the next generation of reactors. In its most general sense, a molten salt reactor is a class of nuclear reactor in which fissile (^{235}U, ^{233}U, ^{239}Pu) and/or fertile isotopes (e.g. ^{232}Th, ^{238}U) are dissolved in a carrier salt. The resulting mixture acts both as fuel and coolant. By far most of the work to this date has concentrated on fluoride salts as these have shown advantageous physico-chemical properties and compatibility with corrosion-resistant alloys [23]. What sets it apart from current water-cooled reactors (Pressurized Water Reactor, Boiling Water Reactor, etc.) is that the fuel is in the liquid as opposed to the solid state. The advantages arising from the fluid character of the fuel can be can be grouped into two categories: safety and operational aspects.

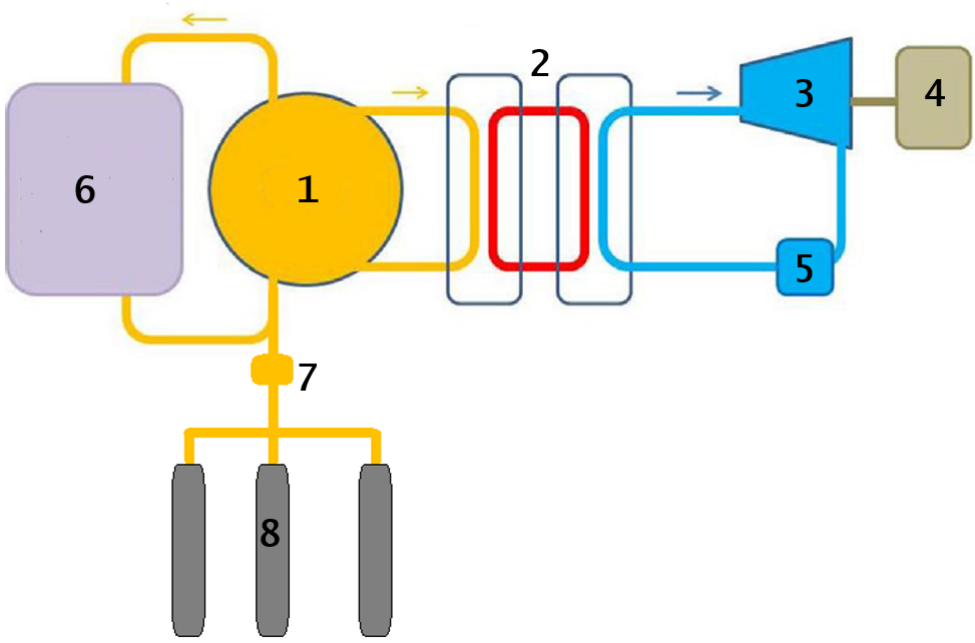

Figure 1.1: Diagram of major MSR components: (1) reactor core, (2) heat exchangers, (3) turbine, (4) generator, (5) heat sink, (6) fuel processing plant, (7) freeze plugs, (8) drain tanks. Figure adapted from [13].

On the one hand, molten salts, and in particular molten fluorides, have low vapor pressures; thus, even in the event of a serious accident -a vessel rupture, for example- there would be no driving force to expel radioactive material from the reactor complex [3]. Moreover, with a melting point of hundreds of Kelvin (strongly dependent on composition), leaking salt would quickly solidify when encountering room temperature. That is, it would be contained on site. Another key feature of molten salt fuels is their inherent negative temperature feedback coefficient: an increase in temperature results

in the expansion of the fuel salt, which would force some of it out of the reactor core and result in decreased reactivity [3]. In the event of an accident, passive safety features requiring no operator intervention can be designed making use of the liquid nature of the fuel. The best known example is a freeze plug. During a prolonged power failure similar to the one in Fukushima, such a plug, actively cooled by a fan under normal operation, would melt and drain the salt from the reactor core into tanks with a subcritical configuration (Fig. 1.1). On the other hand, notable operational advantages of molten fluorides include high solubility for U and Th, high volumetric heat capacity, and relatively good chemical stability towards a few metals commonly used in structural alloys. In addition, the salts do not undergo radiolytic decomposition [24]. Swelling, cracking, and other solid fuel-related mechanical phenomena become irrelevant [3]. Furthermore, the MSR may be single or double-fluid, it may or may not have a moderator, and consequently it may work on a large range of neutron spectra [23]. Also of great importance is the fact that the salt chemistry can be carefully controlled by either batch-wise or online processing: neutron poisons can be removed, and the redox potential and fuel composition can be adjusted while the reactor is operational. Removal of neutron poisons leads to an advantageous neutron economy which can be used to breed fuel from fertile elements. In particular, using a Th-232 (fertile) blanket, a fissile U-233 isotope may be obtained through the following reaction [7]:

$$^{232}_{90}Th + n \xrightarrow{\beta^-} {}^{233}_{90}Th \xrightarrow{\beta^-} {}^{233}_{91}Pa \xrightarrow{\beta^-} {}^{233}_{92}U \tag{1.1}$$

In the same manner, the reactor could be loaded with the fertile U-238 to produce the fissile Pu-239:

$$^{238}_{92}U + n \xrightarrow{\beta^-} {}^{239}_{92}U \xrightarrow{\beta^-} {}^{239}_{93}Np \xrightarrow{\beta^-} {}^{239}_{94}Pu \tag{1.2}$$

1.2. APPLICATIONS OF MSRS

The most obvious application for the MSR is electricity production. Beside its safety characteristics, the MSR has the potential to be remarkably efficient as a power supply. Recall that the theoretical maximum efficiency of a heat engine is given by the Carnot efficiency:

$$\nu_c = 1 - \frac{T_c}{T_h} \tag{1.3}$$

where T_c and T_h are the temperatures of the cold temperature heat sink and the heat source, respectively. Eq. (1.3) tells us that making T_c lower or T_h higher will increase the performance. In the case of MSRs, T_h would be a few hundred degrees higher as compared to conventional nuclear plants, driving the efficiency of the coupled heat engine upwards. Nowadays, Rankine cycles with an operational temperature T_h lower than the temperature that could be achieved by the MSR have an efficiency in the range of 40-49%, and a comparable efficiency could be obtained with a helium-cooled Brayton cycle, while a supercritical CO_2 Brayton cycle could achieve efficiencies of over 50% [11].

Apart from a grid power supply, MSRs could become key decentralized infrastructures, driving industrial clusters with a varied set of activities with high energy input

requirements [4]:

- **Water desalination**
  150 countries depend on desalinated water to some extent [12], with several meeting more than 50% of their freshwater needs with desalination [22]. In all probability, this figure will dramatically increase in the future, given climate change and a rising world population.

- **Ammonia production**
  Ammonia is an important chemical feedstock for many products, most notably fertilizers. The overall process is endothermic and requires high temperatures.

- **Hydrogen production**
  Hydrogen is extensively used already in the petrochemical industry, but could be required in even larger amounts if it becomes an energy carrier in a hypothetical 'hydrogen economy' [6]. MSRs could be apt power sources for two practically feasible routes: electrolysis and the iodine-sulfur cycle.

- **Radionuclide production**
  Valuable medical radioisotopes, notably Mo^{99} used for cancer diagnostic, could be extracted from a MSR while it produces electricity and/or heat for another application.

- **Catalytic cracking**
  Another activity that requires high temperatures for the manufacture of feedstock chemicals.

1.3. CONCERNS FACING MSRS

MSRs are not without their challenges, including:

- **Public acceptance**
  This is not unique to MSRs, but applicable to the nuclear power technology as a whole. Nuclear accidents such as Three Mile Island (1979), Chernobyl (1986), and Fukushima (2011), have decreased the level of trust among members of the public [20]. Consequently, even countries with nuclear experience and sophisticated industrial bases like Germany and Japan have been prompted to phase out their nuclear infrastructure [25]. France, the classical example of a predominantly nuclear-powered country, has been required by law to reduce the share of nuclear in its energy mix from 75 to 50% by 2025 [26].

- **Economics and finance**
  Evaluating the monetary cost of nuclear plants is highly nontrivial, let alone those which only exist on paper. Historically, nuclear power plants (NPPs) have tended to increase in size in order to gain in economies of scale, albeit at huge overhead costs [28]. The modern paradigm shift is to design reactors to be small and modular, so as to be produced in an assembly line and gain in economies of multiples,

thereby reducing the demand-side expenses. Such a shift to small and modular reactors is not unique to MSRs, however, so even within that mode of production MSRs will have to be competitive against other advanced nuclear technologies, not to mention other baseload sources. At present, the only MSR financing claims come from would-be vendors themselves, without assessments from independent experts [28].

- **Proliferation concerns**
  Aside from the concerns normally associated with plutonium reprocessing, introducing the thorium fuel cycle has its own proliferation concerns. As pointed out by Ashley et al. [2], there are well-established pathways to separate protactinium from thorium. This implies that, having irradiated ^{232}Th and separated ^{233}Pa from it, simply letting the latter isotope decay would lead to very pure ^{233}U (see Eq. 1.1).

- **Modelling and simulation**
  These are key aspects while designing and licencing NPPs. MSRs are arguably the most difficult reactors to model and simulate [33] –robust nuclear codes handling circulating as opposed to static fuel are still in the making.

- **Materials**
  High radiation and temperatures, and corrosive salts are punishing environments for structural materials. While thermodynamic considerations allow choosing fresh fuel salts such that the structural materials are stable towards oxidation from the salt, during operation there arise five main mechanisms of corrosion [10, 16, 32]: 1) impurity driven corrosion, 2) intrinsic corrosion, 3) thermal gradient-driven corrosion, 4) dissimilar material corrosion, 5) stress corrosion cracking. Although this dissertation is not directly related to corrosion mechanisms, these should also be studied through the lens of thermodynamic modelling (see Section 8.3), and it is worth discussing them in some more detail.

1.3.1. IMPURITY DRIVEN CORROSION

Although salts and alloys should be thoroughly purified, any impurities that do arise during preparation and handling will dominate corrosion in the first stages of operation, and once depleted, other mechanisms will be more significant [32]. The main impurities are H_2O, HX (X= F, Cl), and oxides and fluorides, either in the salt itself or in the structural alloys [10, 16].

H_2O

Water will react with the salts to form strongly corrosive hydrogen halides via hydrolysis reactions [8, 29, 18]:

$$MF_x + \frac{x}{2} H_2O = MO_{x/2} + xHF(g) \tag{1.4}$$

$$MF_x + zH_2O = MO_zF_{(x-2z)} + 2zHF(g) \tag{1.5}$$

$$MF + H_2O = MOH + HF(g) \tag{1.6}$$

$$MCl_3 + H_2O = MOCl + 2HCl(g) \tag{1.7}$$

$$H_2O(g) + 2F^- = O^{2-} + 2HF(g) \tag{1.8}$$

Water may be evaporated from fluoride salts under Ar flux beyond 573 K [10], yet it has been reported to be more difficult to do so in chlorides [16].

HX (X = F, CL)
HF(g) and HCl(g) will attack metals [16, 18]:

$$M + zHX = MX_z + \frac{z}{2}H_2 \quad X = F, Cl \tag{1.9}$$

and species such as $FeCl_2$ may become further chlorinated [18]:

$$FeCl_2(l) + 2HCl(g) = Fe_2Cl_6(g) + H_2(g) \tag{1.10}$$

Aside from reactions 1.4-1.8, HF and HCl may be left as residues from the halogenation process. To prevent this HF/H_2 mixtures may be used instead of pure HF [10], and excess HCl may be flushed with a further drying cycle under Ar atmosphere [32], or its use can be avoided by using CCl_4 as a chlorinating agent [1].

OXIDES
Oxide impurities in the fuel salt may result in the precipitation of stable oxides such as UO_2 [10]. Oxides on alloy surfaces can result in corrosion by species in the salt, e.g.:

$$2NiO + ZrF_4 = ZrO_2 + 2NiF_2 \tag{1.11}$$

NiF_2 and other transition metal fluorides can then react with Cr, the metal which is most susceptible to fluorination [35, 5]:

$$2NiF_2 + Cr = CrF_2 + Ni \tag{1.12}$$

CrF_2 will moreover be soluble in the salt matrix, with no passivation to prevent it from being extracted from the alloy.

1.3.2. INTRINSIC CORROSION

This mechanism is related to the properties of the fuel salt itself. Even assuming that the specified fresh fuel is not corrosive towards a given structural alloy, this may change as the redox potential changes due to fission and transmutation products. It is linked to the presence of species which can have more than one valence state, such as uranium. In a fluoride-based MSR, uranium can exist as either a trifluoride or a tetrafluoride. The

redox potential of the salt, determined by the UF_4:UF_3 ratio, is given by the Nernst equation [8]:

$$E_{fuelsalt} = E^{\circ'}_{UF4/UF3} + \frac{2.3RT}{F} log \frac{x(UF_4)}{x(UF_3)} \tag{1.13}$$

where R is the ideal gas constant ($J{\cdot}K^{-1}mol^{-1}$), T is the temperature (K), F is the Faraday constant (C) and $E^{\circ'}_{UF4/UF3}$ is the apparent potential of the UF_4/UF_3 couple, a combination of the standard potential of the couple and the activities of both species. The potential thus increases as the UF_4/UF_3 ratio increases. Most of the fission products will have a lower valence state than U(IV), and moreover every fission event produces two fission products. As a result the salt will lose some of its capacity to hold fluoride ions, which will evolve into fluorine gas which can react with UF_3, increasing the potential, schematized by Delpech et al. [9] as follows:

$$UF_3 + n \longrightarrow LnF_3 + M \tag{1.14}$$

$$UF_4 + n \longrightarrow LnF_3 + M + 1/2F_{2(g)} \tag{1.15}$$

$$UF_3 + 1/2F_{2(g)} \longrightarrow UF_4 \tag{1.16}$$

Here M denotes a noble metal, Ln a lanthanide element, and n denotes a neutron. Since a greater redox potential will increase the corrosion rate of the structural material, it is important to keep it within the right margins during the lifetime of the reactor. Upon formation of UF_4 (Eq. 1.16), Cr can be attacked [5] as in Eq. 1.17:

$$2UF_4 + Cr = CrF_2 + 2UF_3 \tag{1.17}$$

For values x(U(IV))/x(U(III)) > 100, reaction 1.17 is strongly driven to the right, while below x(U(IV))/x(U(III))=10, UF_3 disproportionates to UF_4 and U [5]:

$$4UF_3 \longrightarrow 3UF_4(salt) + U(s) \tag{1.18}$$

Since UCl_3 is less susceptible to disproportionation than UF_3, it is expected that ratios of 0.003 < x(U(IV))/x(U(III)) < 0.05 could suffice to control the redox potential in chloride fuels [16].
In the Molten Salt Reactor Experiment (MSRE) [17], metallic Be was used as a reducing agent to keep the U(IV)/U(III) ratio in the right redox window [34]:

$$2UF_4 + Be(s) \longrightarrow 2UF_3 + BeF_2 \tag{1.19}$$

while for the Molten Salt Fast Reactor (MSFR), the European concept currently being developed, $Th(s)$ is proposed instead [9], because the fuel salt is LiF-ThF_4 and contains no Be. In chloride-fueled reactors, the developer Moltex Energy has proposed containing the fuel salt in metallic zirconium cladding as a sacrificial anode, maintaining the salt in a sufficiently reducing state [15].

1.3.3. THERMAL GRADIENT-DRIVEN CORROSION

Since solubility is a function of temperature, solutes in hot sections of the reactor may precipitate out of solution in colder sections like heat exchangers. Reaction 1.17 is responsible for most of the experimentally observed mass transfer going from hot sections to cold sections of convection loops [21]. Its equilibrium constant K_N is given by:

$$K_N = \frac{a(CrF_2)a(UF_3)^2}{a(Cr)a(UF_4)^2} \approx \frac{x(CrF_2)x(UF_3)^2}{x(Cr)x(UF_4)^2} \tag{1.20}$$

where a denotes the activity of a species, and x its concentration. Again, the $x(U(IV))/x(U(III))$ ratio is critical to avoid Cr dissolution.

DISSIMILAR MATERIAL CORROSION

Dissimilar materials close to each other in solution can be a cause for corrosion, driven by gradients in activity or electrode potentials (galvanic corrosion) [16, 32]. For example, corrosion tests on samples of Incoloy 800H in FLiNaK media using graphite crucibles revealed the formation of Cr_7Cr_3 on the crucible, as the high activity of CrF_2 (see Eq. 1.12, 1.17) allowed the migration of Cr to the graphite surface [29, 32].

1.3.4. STRESS CORROSION CRACKING

Stress corrosion cracking is the propagation of cracks in a material exposed to a reactive environment and non-cyclic tensile stresses [31]. During the MSRE, it was found that S, Se, and Te attack structural elements in this mode [10]. Te is especially problematic, as it can attack the structural metals even in the metallic state at low concentrations, through the formation of intermetallics at the grain boundaries, leading to severe embrittlement of the alloys [8]:

$$xTe + yM \longrightarrow M_yTe_x \ (M = Ni, Cr) \tag{1.21}$$

Moreover, Te is produced in appreciable amounts, in the order of 200 moles/year in both fluoride and chloride salts [27]. However, experimental work at Oak Ridge National Laboratory (ORNL), showed that maintaining the salt in a reducing state, with a U(IV)/U(III) ratio below 60, significantly reduces tellurium attack towards Hastelloy-N, the Ni-based structural alloy used to build the MSRE [19].

1.4. THIS DISSERTATION IN THE CONTEXT OF MOLTEN SALT REACTORS

Despite the giant leaps MSR technology has seen since its conception, there remain many technical issues for the technology to reach commercial maturity. As highlighted by the preceding discussion on corrosion, the chemical complexity of the fuel salt belongs to one of these key technical issues. Assuming a well-defined, simple system with two or three end-members as a fuel system and extensively studying its thermodynamic and transport properties is practically feasible. Adding more components in order to obtain operational advantages complicates matters, but is still possible. Once fission occurs, however, the initial solvent becomes a multi-component system. Since the parameters needed to describe it scale combinatorially, and there are deviations from ideality, characterization becomes much more difficult. There is therefore a need to develop

models and simulation tools able to predict the fuel's physico-chemical properties over a wide range of temperatures, compositions and redox potential.
A fundamental understanding of the relationship between the local structure of the molten salt and its physico-chemical and thermodynamic properties is needed to develop such models and gain greater predictive capability over this dynamic, non-ideal salt. It is known that depending on conditions of composition and temperature, the local structure can vary widely with cases where the ions in the melt are completely dissociated, form molecular species, or even exhibit some degree of polymerization [30], [14]. What kind of regime would we expect at the outlet of, say, a Molten Salt Fast Reactor? Would the lanthanide fission products co-polymerize with the actinides in long chains, increasing the viscosity with respect to the fresh fuel? Would the multi-component melt indeed have a low vapor pressure? What would be the solubility of the corrosion products from the structural materials? How much heat could be carried off by this outgoing flow?
These are all necessary design questions which could be answered by experimentation. But all ranges of conditions (temperature, composition, redox potential) of interest cannot be investigated experimentally. To build a comprehensive model for the safety assessment of the reactor requires to perform measurements of simpler systems, for which we can make models that can be extrapolated and benchmarked. In order to gain in accuracy, we also need the models to take into account as much physical information as possible. The approach in this dissertation is therefore multi-disciplinary and includes several techniques: X-ray absorption spectroscopy (XAS), X-ray diffraction (XRD), differential scanning calorimetry (DSC), low-temperature heat capacity measurements (using the Physical Property Measurement System, PPMS, designed by Quantum Design), molecular dynamics (MD) simulations, density functional theory (DFT) and thermodynamic modelling and state function assessments (density, viscosity) using the CALPHAD method (CALculation of PHase Diagrams). Each technique is discussed in more detail as it is mentioned in each chapter.
The salt systems under consideration were those which are germane to MSR development either because they would be part of the fresh fluoride or chloride fuel formulation or, in the case of CsF, because cesium is a fission product that is generated with a high yield. The focus is on binary systems of actinide halides (ThF_4, UF_4, $ThCl_4$, UCl_3) and alkali halides (LiF, NaF, KF, CsF, LiCl, NaCl, KCl). When studying these ionic systems, the thermodynamic properties can reveal trends linked to their most fundamental properties: ionic radius, electronegativity, charge, coordination chemistry, and formation of complex ions. State functions such as the density and the viscosity may be in turn related to such structural information, and may be modelled even making strong simplifications about the structural features of the salts, as will be seen. Hence, at the heart of the work is the structure-property relationship in the salt systems under study.

1.5. CONTENT

The thesis is made up of six chapters apart from the introduction and conclusion, titled:

1. Thermodynamic assessment of the KF-ThF_4, LiF-KF-ThF_4 and NaF-KF-ThF_4 systems

2. Thermodynamic description of the ACl-$ThCl_4$ (A= Li, Na, K) systems

3. Examination of the short-range structure of molten salts: ThF_4, UF_4, and related alkali actinide fluoride systems

4. New insights and coupled modelling of the structural and thermodynamic properties of the LiF-UF_4 system

5. Experimental and Computational Exploration of the NaF-ThF_4 Fuel System: Structure and Thermochemistry

6. Beyond the Phase Diagram: Density and Viscosity Models for Molten Salt Fuel Systems

The first chapter features a study of the KF-ThF_4, LiF-KF-ThF_4 and NaF-KF-ThF_4 systems with extensive use of DSC and XRD. The CALPHAD method used to calculate their phase diagrams is introduced, as is a key player within this methodology: the quasi-chemical formalism, used to describe the excess Gibbs energy parameters of the liquid solutions. The second chapter is similar from a modelling viewpoint, but for three alkali actinide chloride systems. In this chapter only data available in the literature are used: limitations and suggestions for future measurements are put forth. Simple conceptual models of potential and structure are discussed to relate the calculated excess properties of the solutions to the structural changes in the liquids upon mixing, a recurrent theme throughout the thesis. Chapter 3 moves from simplified structural models to experimental observations of the actual coordination environments around the cations, now with fluoride salts, using X-ray Absorption Spectroscopy (XAS) and interpreting the data relying on MD simulations. In Chapters 4 and 5, the quasi-chemical formalism is adapted to reflect the structural motifs identified in the molten fluorides, while reproducing or incorporating experimental data, e.g., phase transitions, heat capacities, and mixing enthalpies. In Chapter 6, the focus is extended beyond phase diagrams to the computation of state functions –density and viscosity– of three binary and one ternary keystone systems belonging to both halide fuel families: LiF-ThF_4, LiF-UF_4, LiF-ThF_4-UF_4, and NaCl-UCl_3. Following these six chapters, concluding remarks summarize the main outcomes. The technical implications of the dissertation at large, outlook, and suggestions for future research are also discussed.

BIBLIOGRAPHY

[1] J.W. Ambrosek. "Molten chloride salts for heat transfer in nuclear systems". PhD thesis. 2011.

[2] S.F. Ashley et al. "Thorium fuel has risks". In: *Nature* 492.7427 (2012), pp. 31–33.

[3] O. Beneš and R. J. M. Konings. *Comprehensive Nuclear Materials, Chapter 3.13: Molten salt reactor fuel and coolant*. Ed. by R.J.M. Konings. 1st. Vol. 3. Elsevier Inc., 2012.

[4] S. Boyd and C. Taylor. "Chemical fundamentals and applications of molten salts". In: *Molten Salt Reactors and Thorium Energy*. Elsevier, 2017, pp. 29–91.

[5] W.H. Cook. "MSRE Program Semiannual Progress Report, July 31, 1964". In: *ORNL* 3708 (1964), pp. 373–389.

[6] G.W. Crabtree, M.S. Dresselhaus, and M.V. Buchanan. "The hydrogen economy". In: *Physics Today* 57.12 (2004), pp. 39–44.

[7] S. David, E. Huffer, and H. Nifenecker. "Revisiting the thorium-uranium nuclear fuel cycle". In: *Europhysics news* 38.2 (2007), pp. 24–27.

[8] S. Delpech et al. "Molten fluorides for nuclear applications". In: *Materials Today* 13.12 (2010), pp. 34–41.

[9] S. Delpech et al. "MSFR: Material issues and the effect of chemistry control". In: *Paris, France 9-10 September 2009* (2009), p. 201.

[10] S. Delpech et al. "Reactor physic and reprocessing scheme for innovative molten salt reactor system". In: *Journal of Fluorine Chemistry* 130.1 (2009). Fluorine Nuclear Energy, pp. 11–17. ISSN: 0022-1139.

[11] L. Dempsey, C. Forsberg, and T.J. Dolan. "Electricity production". In: *Molten Salt Reactors and Thorium Energy*. Elsevier, 2017, pp. 13–28.

[12] *Desalination by the Numbers*. `http://idadesal.org/desalination-101/desalination-by-the-numbers/`. Accessed: 2018-10-06.

[13] T.J. Dolan. "Introduction". In: *Molten Salt Reactors and Thorium Energy*. Elsevier, 2017, pp. 1–12.

[14] V. Dracopoulos, B. Gilbert, and G.N. Papatheodorou. "Vibrational modes and structure of lanthanide fluoride–potassium fluoride binary melts LnF_3–KF (Ln= La, Ce, Nd, Sm, Dy, Yb)". In: *Journal of the Chemical Society, Faraday Transactions* 94.17 (1998), pp. 2601–2604.

[15] Moltex Energy. *An Introduction to the Moltex Energy Technology Portfolio*. 2018.

[16] G.L. Fredrickson et al. *Molten Salt Reactor Salt Processing–Technology Status*. Tech. rep. Idaho National Lab.(INL), Idaho Falls, ID (United States), 2018.

[17] P.N. Haubenreich and J.R. Engel. “Experience with the molten-salt reactor experiment”. In: *Nuclear Technology* 8.2 (1970), pp. 118–136.

[18] Y. Hosoya et al. “Compatibility of structural materials with molten chloride mixture at high temperature”. In: *Journal of nuclear materials* 248 (1997), pp. 348–353.

[19] J.R. Keiser. *Status of tellurium–hastelloy N studies in molten fluoride salts*. Tech. rep. Oak Ridge National Lab., Tenn.(USA), 1977.

[20] Y. Kim, W. Kim, and M. Kim. “An international comparative analysis of public acceptance of nuclear energy”. In: *Energy Policy* 66 (2014), pp. 475–483.

[21] J.W. Koger. *Effect of FeF_2 addition on mass transfer in a Hastelloy N: LiF–BeF_2–UF_4 thermal convection loop system*. Tech. rep. Oak Ridge National Lab., 1972.

[22] S. Lattemann and T. Höpner. “Environmental impact and impact assessment of seawater desalination”. In: *Desalination* 220.1-3 (2008), pp. 1–15.

[23] D. LeBlanc. “Molten salt reactors: A new beginning for an old idea”. In: *Nuclear Engineering and Design* 240.6 (2010), pp. 1644–1656. ISSN: 0029-5493.

[24] L. Luzzi, V. Di Marcello, and A. Cammi. *Multi-physics Approach to the Modelling and Analysis of Molten Salt Reactors*. Nova Science Publishers, 2012.

[25] R. Malischek and J. Trüby. “The future of nuclear power in France: an analysis of the costs of phasing-out”. In: *Energy* 116 (2016), pp. 908–921.

[26] R. Mauger. “Forced nuclear energy reactors shutdown in France: the Energy Transition Act’s mechanisms”. In: *The Journal of World Energy Law & Business* 11.3 (2018), pp. 270–281.

[27] E. Merle-Lucotte et al. “Preliminary design assessment of the molten salt fast reactor”. In: *Proceedings of the ENC2012-Advanced Reactors* (2012), pp. 17–26.

[28] B. Mignacca and G. Locatelli. “Economics and finance of Molten Salt Reactors”. In: *Progress in Nuclear Energy* 129 (2020), p. 103503. ISSN: 0149-1970.

[29] L.C. Olson. “Materials Corrosion in Molten LiF-NaF-KF Eutectic Salt, Nuclear Engineering”. PhD thesis. University of Wisconsin-Madison, 2009.

[30] M. Salanne et al. “Heat-transport properties of molten fluorides: Determination from first-principles”. In: *Journal of Fluorine Chemistry* 130.1 (2009), pp. 38–44.

[31] K. Sieradzki and R.C. Newman. “Stress-corrosion cracking”. In: *Journal of physics and chemistry of solids* 48.11 (1987), pp. 1101–1113.

[32] K. Sridharan and T.R. Allen. “Corrosion in molten salts”. In: *Molten salts chemistry*. Elsevier, 2013, pp. 241–267.

[33] M. Tiberga. “Development of a high-fidelity multi-physics simulation tool for liquid-fuel fast nuclear reactors”. PhD thesis. Delft University of Technology, 2020.

[34] L.M. Toth et al. “Review of ORNL’s MSR Technology and Status”. In: *Oak Ridge National Lab., TN, United States, Funding organisation: USDOE, Washington, DC (United States)* (1996).

[35] D.F. Williams, L.M. Toth, K.T. Clarno, et al. *Assessment of Candidate Molten Salt Coolants for the Advanced High Temperature Reactor (AHTR)*. United States. Department of Energy, 2006.

2

THERMODYNAMIC ASSESSMENT OF THE KF-ThF_4, LiF-KF-ThF_4 AND NaF-KF-ThF_4 SYSTEMS

A thermodynamic assessment of the KF-ThF_4 binary system using the CALPHAD method is presented, where the liquid solution is described by the modified quasichemical formalism in the quadruplet approximation. The optimization of the phase diagram is based on experimental data reported in the literature and newly measured X-ray diffraction and differential scanning calorimetry data, which have allowed to solve discrepancies between past assessments. The low temperature heat capacity of α-K_2ThF_6 has also been measured using thermal relaxation calorimetry; from these data the heat capacity and standard entropy values have been derived at 298.15 K: $C^{o}_{p,m}(K_2ThF_6, cr, 298.15K) = (193.2 \pm 3.9)$ $J{\cdot}K^{-1}{\cdot}mol^{-1}$ and $S^{o}_{m}(K_2ThF_6, cr, 298.15K) = (256.9 \pm 4.8)$ $J{\cdot}K^{-1}{\cdot}mol^{-1}$. Taking existing assessments of the relevant binaries, the new optimization is extrapolated to the ternary systems LiF-KF-ThF_4 and NaF-KF-ThF_4 using an asymmetric Kohler/Toop formalism. The standard enthalpy of formation and standard entropy of $KNaThF_6$ are re-calculated from published e.m.f data, and included in the assessment of the ternary system. A calculated projection of the NaF-KF-ThF_4 system at 300 K and the optimized liquidus projections of both systems are compared to published phase equilibrium data at room temperature and along the LiF-$LiThF_5$ and NaF-$KThF_5$ pseudobinaries, with good agreement.

Jaén A. OCÁDIZ FLORES, Etienne CARRÉ, Jean-Christophe GRIVEAU, Eric COLINEAU, Elisa CAPELLI, Ondrej BENEŠ, Rudy J.M. KONINGS, Anna Louise SMITH

This chapter has been published in its entirety in *Journal of Chemical Thermodynamics* 145 (2020), 106069 [31].

2.1. INTRODUCTION

The Generation IV International Forum, a group of fourteen member countries pursuing research and development for the next generation of nuclear reactors, has selected six nuclear energy systems [19, 20]. Among these, the Molten Salt Reactor (MSR) is, in terms of safety and performance, one of the most promising nuclear reactor designs presently being studied. Its central characteristic is that the nuclear fuel is made of a molten fluoride (or chloride) salt instead of being a solid oxide or a metal. This liquid serves both as the fuel and coolant for the reactor. Two experimental MSRs have been built in the past: the Aircraft Reactor Experiment (ARE) [9] in 1954, and the Molten Salt Reactor Experiment (MSRE), which operated successfully between 1965-1969 [23]. A comprehensive knowledge of the physico-chemical properties of the salt is needed for the safety assessment and design of modern reactors, as the irradiated salt constitutes a complex and multi-component system.

The ^{7}LiF-NaF-KF-ThF_4-UF_4-AnF_3 (An= actinide) system has been proposed for the fuel of an actinide burner design [37], and still needs a full thermodynamic characterization. In particular, studies on many of the KF-containing systems are either absent in the literature or need to be revisited, namely KF-UF_3 (some intermediate compounds have been synthesized [46]), KF-UF_4 (phase diagram information exists [47], but a CALPHAD model is missing), KF-PuF_3 (there is no phase diagram information available), and KF-ThF_4. Two sets of authors, Emelyanov and Evstyukhin [16] and Asker et al. [2] have studied the potassium fluoride-thorium fluoride binary system, with fair agreement in some regions of the system. However, they have reported conflicting interpretations in other regions, which need to be resolved. To this end, we present a re-evaluation of the KF-ThF_4 binary system, using X-ray diffraction (XRD), Differential Scanning Calorimetry (DSC), and low temperature heat capacity measurements. A thermodynamic assessment using the CALPHAD method is moreover reported for the first time, where the Gibbs energy of the liquid solution is described using the quasi-chemical model in the quadruplet approximation. The assessment of the binary system is subsequently used to extrapolate to the ternary LiF-KF-ThF_4 and NaF-KF-ThF_4 systems.

2.2. EXPERIMENTAL METHODS

2.2.1. SAMPLE PREPARATION FOR DSC MEASUREMENTS

The purity of the four constituent salts, LiF (ultra-dry), NaF, KF, (all from Alfa Aesar, 0.9999 ± 0.0001[1] mass fraction purity) and ThF_4 was confirmed using X-ray diffraction (XRD) and Differential Scanning Calorimetry (DSC). NaF and KF had to be dried further, for 4 h at 673 K in an open nickel boat under Ar flow, in order to reach the adequate purity for thermodynamic measurements. ThF_4 was synthesized in JRC-Karlsruhe as described in [44]. All salts were of white color, and were handled in either powder or pressed pellet form. The experimental compositions reported hereafter were prepared by mixing either powder or pellet fragments of the pure salts in the corresponding stoichiometric ratios. As fluoride salts are highly sensitive to water and oxygen, handling and preparation of samples took place inside the dry atmosphere of an argon-filled glove box, where H_2O and O_2 content were kept below 1 ppm.

[1] The reported uncertainty corresponds to the standard uncertainty.

Table 2.1: Provenance and purity of the samples used in this study.

Formula	Source	**State**	**Color**	**Mass fraction purity***	**Purity analysis method**
LiF	Alfa Aesar	Powder	White	0.9999 ± 0.0001	Provided by supplier
KF	Alfa Aesar	Powder	White	0.9999 ± 0.0001	Provided by supplier
NaF	Alfa Aesar	Powder	White	0.9999 ± 0.0001	Provided by supplier
ThF_4	JRC-Karlsruhe	Powder	White	0.995 ± 0.005	ICP-MS, XRD, DSC
K_2ThF_6	Solid-state synthesis	Powder	White	0.99 ± 0.01	XRD, DSC

*The quoted uncertainties correspond to standard uncertainties.

[a]The secondary phase was K_2ThF_6.

2.2.2. SYNTHESIS

The samples whose X-ray diffraction patterns are shown in this work were made by two methods. The first consisted in grinding powder mixtures and heating them inside a closed stainless steel crucible with a Ni liner in a tubular furnace under Ar flow. The second method consisted in heating powder mixtures in a DSC crucible above melting. The conditions are given below in Table 1.

Table 2.2: Synthesis conditions

Composition	Starting reagents[a]	High-temperature instrument[b]	Conditions[c]
$K_5ThF_9 + K_2ThF_6$	$(KF:ThF_4) = (0.833:0.167)$	Furnace	923 Kfor 12 h
$K_5ThF_9 + K_2ThF_6$	$(KF:ThF_4) = (0.750:0.250)$	Furnace	1073 K for 12 h
K_2ThF_6	$(KF:ThF_4) = (0.667:0.333)$	Furnace	873 K for 12 h
$K_2ThF_6 + K_7Th_6F_{31}$	$(KF:ThF_4) = (0.582:0.418)$	DSC	Max T = 1373 K, cooling 2 K/min
$KTh_2F_9 + KTh_6F_{25}$	$(KF:ThF_4) = (0.250:0.750)$	DSC	Max T = 1373 K, cooling 2 K/min
$KTh_2F_9 + KTh_6F_{25}$	$(KF:ThF_4) = (0.143:0.857)$	Furnace	1073 K for 12 h

[a] Standard uncertainty on the composition of the starting reagents was $u(X(ThF_4)) = 0.005$.

[b] The DSC measurements were performed at a pressure P = (0.10 ± 0.01) MPa.
The syntheses in the furnace were carried out at a pressure P = (0.10 ± 0.04) MPa in the furnace.
The quoted uncertainties correspond to the standard uncertainties.

[c] Standard uncertainties u are u(T) = 15 K for the furnace and u(T) = 10 K for the DSC temperature.

2.2.3. POWDER X-RAY DIFFRACTION

X-ray powder diffraction (XRD) data were collected at room temperature (T = 293 ± 5 K[2]) using a PANalytical X'Pert PRO X-ray diffractometer and a Cu anode (0.4 mm x 12 mm line focus, 45 kV, 40 mA) by step scanning at a rate of 0.0104 $^o \cdot s^{-1}$ in the range $10^o<2\theta<120^o$ in a Bragg-Brentano configuration. The X-ray scattered intensities were

[2]The reported uncertainty corresponds to the standard uncertainty.

measured with a real time multi strip (RTMS) detector (X'Celerator). Structural analysis was performed with the Rietveld and LeBail methods using the FullProf suite [38].

2.2.4. DIFFERENTIAL SCANNING CALORIMETRY

3D-heat flow DSC measurements were performed using a Setaram Multi-Detector HTC module of the 96 Line calorimeter under argon flow at a pressure of (0.10 ± 0.01 MPa[3]). All samples were placed inside a nickel liner and encapsulated for the calorimetric measurements inside a stainless steel crucible closed with a screwed bolt as described in [7] to avoid vaporization at high temperatures. Two kinds of information were sought using the DSC technique: phase diagram equilibria points and mixing enthalpies. In all cases the measurement program began with one heating cycle reaching 1483 K and was maintained at that temperature for at least 300 s to ensure complete mixing and melting of the end-members. In general, this first cycle was followed by three successive heating cycles with a heating rate ranging between 4 to 10 K·min^{-1}, and 20-15-10-5 K·min^{-1} cooling rates. The procedure followed for the mixing enthalpy measurements is described in detail in section 2.2.5.

Temperatures were monitored throughout the experiments by a series of interconnected S-types thermocouples. The temperature on the heating ramp was calibrated by measuring the melting points of standard high purity metals (In, Sn, Pb, Al, Ag, Au). The temperature on the cooling ramp was obtained by extrapolation to 0 K·min^{-1} cooling rate. The melting temperatures of pure compounds and transition temperatures of mixtures were derived on the heating ramp as the onset temperature using tangential analysis of the recorded heat flow, while the liquidus temperatures of mixtures were taken as the minimum of the last thermal event as recommended in [10]. The data measured on the cooling ramp were not retained for the phase diagram optimization due to the occurrence of supercooling effects. The uncertainty on the measured temperatures is estimated to be $\pm$ 5 K for the pure compounds and $\pm$ 10 K for mixtures[4].

The DSC measurements support the purity indicated by the suppliers and XRD data, as the heat flow signal for each of the four salts (LiF, NaF, KF, ThF_4) showed only one peak corresponding to the melting event, and no peaks that could be assigned to impurities. The measured onset temperatures are in good agreement with the literature: (1118 ± 5 K), (1268 ± 5 K), (1129 ± 5 K), and (1381 ± 5 K[5]), respectively, vs. 1121.3 K (LiF, [14]), 1269.0 K (NaF, [14]), 1131.0 K (KF, [14]), and 1383.0 K (ThF_4, [25]).

2.2.5. ENTHALPY OF MIXING MEASUREMENTS

Enthalpies of mixing measurements were made in the same DSC calorimeter as the aforementioned equilibrium data, using a technique described in detail in [12]. The starting end-members KF and ThF_4 materials were pressed into pellets. The KF pellet (compound with the lowest melting point) was placed under the ThF_4 pellet, with a Ni liner separating them to avoid eutectic melting upon heating. Upon melting of KF, the Ni

[3] The reported uncertainty corresponds to the standard uncertainty.
[4] The reported uncertainty corresponds to the standard uncertainty.
[5] The reported uncertainties for LiF, NaF, KF, and ThF_4 correspond to the standard uncertainty.

liner sank to the bottom and solid ThF_4 came into contact with molten KF, and melted too. The enthalpy of mixing is then calculated as the difference between the measured heat and the melting enthalpies of the end-members:

$$\Delta_{mix}H^o(T_{fus,KF}) = \Delta_{meas}H^o(T_{fus,KF}) - x_{(1-ThF_4)}\Delta_{fus}H^o(KF,T_{fus,KF}) - x_{ThF_4}\Delta_{fus}H^o(ThF_4,T_{fus,KF}) \quad (2.1)$$

The values used for the enthalpies of fusion of KF and ThF_4 were taken from the SGTE database [1] and the work by Capelli et al. [12], respectively: Δ_{fus}H(KF) = 27.2 kJ·mol^{-1} and Δ_{fus}H(ThF_4) = (41.9 $\pm$ 2.0) kJ·mol^{-1}. As in the work by Capelli et al., the main assumption used in this method for ThF_4 is that the enthalpy of fusion is invariant with temperature, at least down to the melting point of the lower-melting salt, KF (T_{fus} = 1131 K). This assumption is supported by the fact that supercooling of ThF_4 is observed until 1081 K during cooling at 10 K/min, while the area of the peak is almost as large as for the 10 K/min heating curve which resulted in a melting event at the expected temperature of fusion (1381 $\pm$ 5) K[6].

The sensitivity of the calorimeter, from which the measured enthalpies are calculated, was determined on each individual run by using a silver standard in the reference crucible, as described in [12]. The sensitivity coefficient used to determine the mixing enthalpies was validated by testing on the end-members. The enthalpy of fusion of ThF_4 was measured to be: (38.7 $\pm$ 3.2)[7] kJ·mol^{-1}, while that of KF was measured as (27.8 $\pm$ 2.3)[8] kJ·mol^{-1}. Thus both measurements were within the stated uncertainties in agreement with the published values. Moreover, enthalpy of fusion measurements for LiF and NaF also gave values in agreement with the literature. The results are listed in Table 2.3 along with those of KF and ThF_4. These results give us good confidence in the chosen calibration factor. The errors reported in Table 2.7 are based on the propagation of the standard uncertainty of the sensitivity coefficient obtained from the calibration process.

2.2.6. LOW TEMPERATURE HEAT CAPACITY

Low temperature heat capacity measurements were performed on m=7.29 mg[9] of K_2ThF_6 in the temperature range T = (1.8-298.5) K using a PPMS (Physical Property Measurement System, Quantum Design) instrument with no applied magnetic field. A critical assessment of this thermal relaxation calorimetry method can be found in [26]. The contributions of the sample platform, wires, and grease were taken into account by a separate measurement of an addenda curve. From previous studies with standard materials and other compounds [24, 42], the relative standard uncertainty was estimated at about 2 % above 270 K, 1% from 100 to 270 K, and reaching about 3 % at the lowest temperatures [26, 24].

[6] The quoted uncertainty corresponds to the standard uncertainty.
[7] The quoted uncertainty corresponds to the standard uncertainty.
[8] The quoted uncertainty corresponds to the standard uncertainty.
[9] Standard uncertainties u are $u(m)$=0.05 mg.

Table 2.3: Comparison between measured and available data for enthalpies of fusion of different salts at their respective fusion temperatures and $(0.10 \pm 0.01)^a$ MPa.

Salt	Measured[a] $\Delta_{fus}H(T_{fus,salt})$ kJ·mol^{-1}	Reference[b] $\Delta_{fus}H(T_{fus,salt})$ kJ·mol^{-1}
LiF	25.9 ± 2.1	27.087 [1]
NaF	33.9 ± 2.8	33.3 [1]
KF	27.8 ± 2.3	27.2 [1]
ThF_4	38.7 ± 3.2	41.9 ± 2.0 [12]

[a] The quoted uncertainty corresponds to the standard uncertainty.
[b] Standard uncertainty not reported when not found in the reference.

2.3. THERMODYNAMIC MODELLING

Optimizations of the phase diagrams were carried out by the CALPHAD (CALculation of PHase Diagram) method [28] using the Factsage software [3]. To carry out such an optimization, the identity of the phases present in the system of interest must be known, as well as their respective Gibbs energy functions.

2.3.1. PURE COMPOUNDS

The Gibbs energy function of a pure compound is given by:

$$G(T) = \Delta_f H^{\circ}_{\mathrm{m}}(298) - S^{\circ}_{\mathrm{m}}(298)T + \int_{298}^{T} C_{\mathrm{p,m}}(T)dT - T\int_{298}^{T} \frac{C_{\mathrm{p,m}}(T)}{T}dT \tag{2.2}$$

where $\Delta_f H^{\circ}_{\mathrm{m}}(298)$ is the standard enthalpy of formation, $S^{\circ}_{\mathrm{m}}(298)$ is the standard absolute entropy, both evaluated at a reference temperature, in this case 298.15 K (throughout this work 298 will be understood to mean 298.15 K for simplicity), and $C_{\mathrm{p,m}}$ is the isobaric heat capacity expressed as a polynomial:

$$C_{\mathrm{p,m}}(T) = a + bT + cT^2 + dT^{-2} + eT^3 \tag{2.3}$$

with more terms added if necessary.

In this work, the Neumann-Kopp rule [27] applied to KF and ThF_4 was used to estimate the heat capacities of intermediate compounds in the absence of experimental data. The only exceptions were α-K_2ThF_6(cr) and β-K_2ThF_6(cr), for which a fit was made. The fit included the low temperature heat capacity points measured herein in the 250-300 K range as well as high temperature points given by the Neumann-Kopp rule in the 500-1500 K range. Moreover, the temperature-independent term of the heat capacity, a, was optimized such that C_p(K_2ThF_6,(cr),298.15 K) = 193.2 J·K^{-1}·mol^{-1}, the same value found by fitting of the low temperature heat capacity data of α-K_2ThF_6(cr) (see Section 2.5.3).

The thermodynamic data for all compounds in this study are listed in Table 1. The convention used throughout this paper is that the lower temperature phases are denoted with α; the opposite convention is used by [2] and [16] (respectively: Figs. A.1 and A.2). The data for both solid and liquid alkali fluorides (LiF, NaF, KF) and ThF_4 were taken from [14] and [13], respectively. All thermodynamic functions of the intermediate compounds in the LiF-ThF_4 and NaF-ThF_4 systems were derived by optimization in [13], while those for intermediate compounds in the KF-ThF_4 system were obtained in this work by optimization using phase equilibrium and mixing enthalpy data.
The transition temperature and enthalpy of transition of K_5ThF_9 ($\Delta_{tr}H^o_m = (9.3 \pm 0.8)$ kJ·mol^{-1}, T_{tr}=926 $\pm$ 5) K, K_2ThF_6 ($\Delta_{tr}H^o_m = (22.0 \pm 2.0)$ kJ·mol^{-1}, T_{tr}=952 $\pm$ 5) K, and $KNaThF_6$ ($\Delta_{tr}H^o_m = (15.3 \pm 0.6)$ kJ·mol^{-1}, T_{tr}=825 $\pm$ 5) K were measured in this work by DSC using a similar procedure to the mixing enthalpies with a silver standard in the reference crucible. The experimentally determined values were implemented in the model without further optimization.
No quaternary fluorides have been reported in the LiF-KF-ThF_4 system, while $KNaThF_6$ (which displays a phase transition) is the only quaternary fluoride reported in the NaF-KF-ThF_4 system [16], and its thermodynamic properties were studied by Mukherjee and Dash by means of DSC and solid electrolyte galvanic cell [30]. Based on the former technique, the authors derived the heat capacity in the temperature range 300-870 K, while with the latter, they obtained the Gibbs energy of formation in the temperature range 773-849 K from which they derived standard enthalpy of formation and standard entropy values at 298 K. The heat capacity reported by them results in an extremely stable phase, such that unreasonably high excess parameters would have to be applied to the liquid NaF-KF-ThF_4 solution in order to stabilize it even at high temperatures. For this reason, this work approximated the heat capacity function of $KNaThF_6$ using the Neumann-Kopp rule applied to NaF, KF, and ThF_4. In addition, we have reassessed the enthalpy of formation and entropy at 298 K based on the experimental data of [30] and carefully selected auxiliary data (see Appendix for details). The final optimized standard enthalpy of formation and standard entropy yield a Gibbs energy which is only $\sim$1 % larger than the experimental value.

2.3.2. SOLID SOLUTION

The total Gibbs energy function of the two-component solid solutions in the present system is given by:

$$G(T) = X_1 G^{\circ}_{\mathrm{m},1}(T) + X_2 G^{\circ}_{\mathrm{m},1}(T) + X_1 RTlnX_1 + X_2 RTlnX_2 + G^{xs}_m \tag{2.4}$$

where X_i are the molar fractions and $G^{\circ}_{\mathrm{m,i}}$(T) are the standard molar Gibbs energies of the pure end members. The excess Gibbs energy parameter is described using the polynomial formalism:

$$G^{xs}_m = \sum_{i,j} X_1^i \cdot X_2^j \cdot L_{i,j} \tag{2.5}$$

where $L_{i,j}$ is a coefficient which may depend on temperature in the form of the general equation

Table 2.4: Thermodynamic data for end-members and intermediate compounds used in this work for the phase diagram assessment: $\Delta_f H^o_m$(298 K)/(kJ·mol^{-1}), S^o_m(298 K)/(J·K^{-1}·mol^{-1}), and heat capacity coefficients $C_{p,m}$(T/K)/(J·K^{-1}·mol^{-1}), where $C_{p,m}(T/K) = a + b{\cdot}T + c{\cdot}T^2 + d{\cdot}T^{-2} + e{\cdot}T^3$. Optimized data are shown in **bold**.

Compound	$\Delta_f H^o_m$(298 K)/ (kJ·mol^{-1})	S^o_m(298 K)/ (J·K^{-1}·mol^{-1})	$C_{p,m}$(T/K)/(J·K^{-1}·mol^{-1})= a + b·T + c·T^2 + d·T^{-2} + e·T^3 a	b	c	d	e	Reference
LiF(cr)	-616.931	35.66	43.309	0.016312	$5.0470\cdot10^{-7}$	$-5.691\cdot10^{5}$		[14]
LiF(l)	-598.654	42.962	64.183					[14]
NaF(cr)	-576.650	51.21	47.63	0.01479		-464300		[14]
NaF(l)	-557.730	52.755	72.989					[14]
KF(cr)	-568.606	66.547	68.757414	$-5.775688\cdot10^{-2}$	$7.540486\cdot10^{-5}$	-766718.34	$-2.38856\cdot10^{-8}$	[14]
KF(l)	-554.374	67.769	71.965					[14]
ThF_4(cr)	-2097.900	142.05	122.173	0.00837		$-1.255\cdot10^{6}$		[25]
ThF_4(l)	-2103.654	101.237	170					[25],[12]
Li_3ThF_7(cr)	-3960.259	236.1	282.100	0.05730	$1.514\cdot10^{-6}$	$-2.962\cdot10^{6}$		[13]
$LiThF_5$(cr)	-2719.490	181.89	165.482	0.02468	$5.047\cdot10^{-7}$	$-1.824\cdot10^{6}$		[13]
$LiTh_2F_9$(cr)	-4822.329	324.29	287.655	0.03305	$5.047\cdot10^{-7}$	$-3.079\cdot10^{6}$		[13]
$LiTh_4F_{17}$(cr)	-9021.140	609.0	532.001	0.04979	$5.047\cdot10^{-7}$	$-5.589\cdot10^{6}$		[13]
Na_4ThF_8(cr)	-4355.195	450.4	312.693	0.067530		$-3.11220\cdot10^{6}$		[5]
$Na_7Th_2F_{15}$(cr)	-8285.600	677.6	577.756	0.12027		$-5.76010\cdot10^{6}$		[5]
Na_2ThF_6(cr)	-3282.870	255.9	217.433	0.037950		$-2.18360\cdot10^{6}$		[5]
$Na_3Th_2F_{11}$(cr)	-5910.275	526.4	387.236	0.061110		-3902900		[5]
$Na_7Th_6F_{31}$(cr)	-16653.219	1364.0	1066.448	0.15375		$-1.07801\cdot10^{7}$		[5]
$NaThF_5$(cr)	-2693.871	199.2	169.803	0.023160		$-1.71930\cdot10^{6}$		[5]
$NaTh_2F_9$(cr)	-4791.776	348.3	291.976	0.031530		$-2.97430\cdot10^{6}$		[5]
K_5ThF_9-α(cr)	**-5048.000**	**473.0**	465.960	-0.28041	$3.77024\cdot10^{-4}$	$-5.088592\cdot10^{6}$	$-1.19428\cdot10^{-7}$	This work
K_5ThF_9-β(cr)	-5038.700	483.0	465.960	-0.28041	$3.77024\cdot10^{-4}$	$-5.088592\cdot10^{6}$	$-1.19428\cdot10^{-7}$	This work
K_2ThF_6-α(cr)	**-3340.000**	256.9	**208.616**	**0.03925**	$\mathbf{3.04459\cdot10^{-6}}$	$\mathbf{-2.434407\cdot10^{6}}$		This work
K_2ThF_6-β(cr)	-3318.000	280.0	**208.616**	**0.03925**	$\mathbf{3.04459\cdot10^{-6}}$	$\mathbf{-2.434407\cdot10^{6}}$		This work
K_3ThF_7(cr)	**-3837.250**	**411.5**	328.445	-0.16490	$2.26214\cdot10^{-4}$	$-3.555155\cdot10^{6}$	$-7.16569\cdot10^{-8}$	This work
$K_7Th_6F_{31}$(cr)	**-16938.800**	**1327.0**	1214.340	-0.35408	$5.27834\cdot10^{-4}$	$-1.2897028\cdot10^{7}$	$-1.67199\cdot10^{-7}$	This work
KTh_2F_9(cr)	**-4830.425**	**346.0**	313.103	-0.04102	$7.54049\cdot10^{-5}$	$-3.276718\cdot10^{6}$	$-2.38856\cdot10^{-8}$	This work
KTh_6F_{25}(cr)	**-13223.100**	**913.9**	801.795	$-7.53688\cdot10^{-3}$	$7.54049\cdot10^{-5}$	$-8.296718\cdot10^{6}$	$-2.38856\cdot10^{-8}$	This work
$KNaThF_6$-α(cr)	**-3322.100**	**252.2**	238.560	-0.03460	$7.54049\cdot10^{-5}$	$-2.486018\cdot10^{6}$	$-2.38857\cdot10^{-8}$	This work, [30]
$KNaThF_6$-β(cr)	-3306.800	270.7	238.560	-0.03460	$7.54049\cdot10^{-5}$	$-2.486018\cdot10^{6}$	$-2.38857\cdot10^{-8}$	This work, [30]

$$L_{i,j} = A + BT + CTlnT + DT^2 \tag{2.6}$$

Solid solutions are formed in the NaF-KF and NaF-ThF_4 binary systems, with optimizations taken from the literature, shown in Eq. (2.7) [6] and (2.8) [5]:

$$G^{xs}_{(Na,K)F} = X_{NaF}X_{KF} \cdot 26750 + X^3_{NaF}X_{KF} \cdot 20000\ J \cdot mol^{-1} \tag{2.7}$$

$$G^{xs}_{(Na_x,Th_{1-x})F_{4-3x}} = X_{NaF}X^2_{ThF_4} \cdot (-15500) + X^3_{NaF}X_{ThF_4} \cdot 40000\ J \cdot mol^{-1} \tag{2.8}$$

2.3.3. LIQUID SOLUTION

All excess Gibbs energy terms of liquid solutions presented here have been modelled using the modified quasi-chemical model proposed by Pelton et al. [33], in the quadruplet approximation. The quasi-chemical model is particularly well adapted to describe ionic liquids such as in the present system, as it allows to select the composition of maximum short-range ordering (SRO) by varying the ratio between the cation-cation coordination numbers $Z^A_{AB/FF}$ and $Z^B_{AB/FF}$ (the fluorine is in this case the only anion present). The quadruplet approximation assumes a quadruplet, composed of two anions and two cations, to be the basic unit in liquid solution, and the excess parameters to be optimized are those related to the following second-nearest neighbor (SNN) exchange reaction:

$$(A-F-A) + (B-F-B) \longrightarrow 2(A-F-B)\ \ \Delta g_{AB/F} \tag{2.9}$$

where the fluoride anions are represented by F, and A and B denote the cations. $\Delta g_{AB/F}$ is the Gibbs energy change associated with the SNN exchange reaction, and has the following form:

$$\Delta g_{AB/F} = \Delta g^o_{AB/F} + \sum_{i \geqslant 1} g^{i0}_{AB/F}\chi^i_{AB/F} + \sum_{j \geqslant 1} g^{0j}_{AB/F}\chi^j_{BA/F} \tag{2.10}$$

where $\Delta g^o_{AB/F}$ and $g^{ij}_{AB/F}$ are coefficients which may or may not be temperature-dependent, but which are independent of composition.

The dependence on composition is given by the $\chi_{AB/F}$ terms defined as:

$$\chi_{AB/F} = \frac{X_{AB}}{X_{AA} + X_{AB} + X_{BB}} \tag{2.11}$$

where X_{AA}, X_{BB} and X_{AB} represent cation-cation pair mole fractions.

The anion coordination number is finally fixed by conservation of charge in the quadruplet:

$$\frac{q_A}{Z^A_{AB/FF}} + \frac{q_B}{Z^B_{AB/FF}} = \frac{2q_F}{Z^F_{AB/FF}} \tag{2.12}$$

where q_i are the charges of the different ions, and $Z^F_{AB/FF}$ is the anion-anion coordination number, in this case fluorine-fluorine.

The cation-cation coordination numbers used in this work are listed in Table 3. These were chosen to represent the composition of maximum short-range ordering, where the Gibbs energy tends to have its minimum. In the case of KF-ThF_4, the point of maximum SRO can be reasonably expected to lie near X(ThF_4) = 0.33, i.e. where the liquid solution seems to be especially stable as indicated by the low liquidus in the vicinity of that composition. Hence, the cation-cation coordination numbers were chosen to fix maximum SRO around X(Th_4) = 0.33. Similarly, the cation-cation coordination numbers in the LiF-ThF_4 and NaF-ThF_4 systems were chosen to fix maximum SRO around X(Th_4) = 0.25, because the liquidus those phase diagrams is lowest in the vicinity of that composition.

Table 2.5: Cation-cation coordination numbers of the liquid solution.

A	B	$Z^A_{AB/FF}$	$Z^B_{AB/FF}$
Li^+	Li^+	6	6
Na^+	Na^+	6	6
K^+	K^+	6	6
Th^{4+}	Th^{4+}	6	6
Li^+	K^+	6	6
Na^+	K^+	6	6
Li^+	Th^{4+}	2	6
Na^+	Th^{4+}	2	6
K^+	Th^{4+}	3	6

The optimized excess Gibbs energy parameters of the binary liquid solution in the KF-ThF_4 system are shown in Eq. 2.13. The parameters were optimized based on the enthalpy of mixing data and on the phase diagram equilibria points of the liquidus. The excess Gibbs energy parameters of the other binary liquid solutions needed to calculate the ternary systems are given in Appendix A.6.

$$\Delta g_{KTh/FF} = -35472 + (-14644 + 8.35 \cdot T)\chi_{KTh/FF} + (-8786 + 9 \cdot T)\chi_{ThK/FF}\ J \cdot mol^{-1} \tag{2.13}$$

2.3.4. HIGHER ORDER SYSTEMS

The ternary diagrams LiF-KF-ThF_4 and NaF-KF-ThF_4 have each been extrapolated from the constituting binary sub-systems using the asymmetric Toop formalism [34]. The salts belong to two groups of symmetry based on their tendency to remain as dissociated ionic liquids (LiF, NaF, KF) or to form molecular species in the melt (ThF_4). The optimized excess ternary parameters are:

$$\Delta g_{ThLi(K)/FF} = 3000\ J \cdot mol^{-1} \tag{2.14}$$

$$\Delta g_{KTh(Li)/FF} = 1000\ J \cdot mol^{-1} \tag{2.15}$$

$$\Delta g_{LiK(Th)/FF} = 3000\ J \cdot mol^{-1} \tag{2.16}$$

$$\Delta g_{KTh(Na)/FF} = -5000\ J \cdot mol^{-1} \tag{2.17}$$

2.4. PREVIOUS EVALUATIONS OF THE KF-ThF_4 SYSTEM

Phase diagram studies of this system have been reported by Bergman and Dergunov [15], Asker et al. [2] (Fig. A.1), and Emelyanov and Evstyukhin [16] (Fig. A.2). Bergman and Dergunov report a phase diagram which is certainly too simple, with four eutectics and three congruent melting points corresponding to the compounds K_3ThF_7, $KThF_5$, and KTh_3F_{13}; these results markedly differ from those of the other two authors. Emelyanov and Evstyukhin [16] and Asker et al. [2] agree on the existence of K_5ThF_9, K_3ThF_7, $KThF_5$, and K_2ThF_9, and the melting points they report for these compounds are similar. However, they report different ternary compounds for close compositions: KTh_3F_{13} (X(ThF_4) = 0.75, [2]) vs. KTh_6F_{25} (X(ThF_4) = 0.85, [16]); K_2ThF_6 (X(ThF_4) = 0.33, [2]) vs. $K_3Th_2F_{11}$ (X(ThF_4) = 0.4 [16]). Unlike the former pair, for which similar melting points were reported, K_2ThF_6 and $K_3Th_2F_{11}$ are reported to have dissimilar behavior: the former with a peritectic decomposition at 1023 K, and the latter with a congruent melting at 1160 K. In addition, these authors find different allotropic transformations: Asker et al. report two phases for K_5ThF_9 and K_2ThF_6, while Emelyanov and Evstyukhi report two phases only for KTh_2F_9. Finally, Asker et al. suggest the existence of a solid solution close to pure ThF_4, yet Emelyanov and Evstyukhin do not. Our studies focused on exploring the differences found between the two sets of authors.

2.5. RESULTS AND DISCUSSION

2.5.1. PHASE DIAGRAM STUDIES IN THE KF-ThF_4 SYSTEM

K_5ThF_9

Attempts to synthesize K_5ThF_9 did not yield pure K_5ThF_9, but a mixture with K_2ThF_6 (diffractogram shown in Fig. 2.1). K_5ThF_9 has orthorhombic symmetry space group $Cmc2_1$ [39]), with a diffractogram with many small reflections, while K_2ThF_6 is hexagonal (space group $P\bar{6}2m$ [51]). The structure could be refined with the model proposed by Ryan and Penneman [39], with distorted anti-prism for K and Th, and pentagonal bipyramid for the polyhedra of K. The refined cell parameters and table of atomic positions are reported in Appendix 5.10.1.

Our DSC data from a sample made with a stoichiometric mixture of KF and ThF_4 powders suggest a first transition taking place at (926 $\pm$ 10) K, which is higher than the transition temperature recorded by Asker et al. (908 K), but similar to the temperature that Evstyukhin and Emelyanov attribute to the first eutectic of the system (935 K). We assign the event to an allotropic transition as the thermogram at this composition shows three other thermal events which are coherent with the existence of a high temperature K_5ThF_9 phase: eutectic (968 $\pm$ 10 K), peritectic decomposition (982 $\pm$ 10 K), and liquidus (1013 $\pm$ 10 K). With a measurement in the DSC using a silver reference method,

the enthalpy of transition for K_5ThF_9 was found to be $\Delta_{tr}H^o_m = (9.3 \pm 0.8)$ kJ·mol^{-1}.

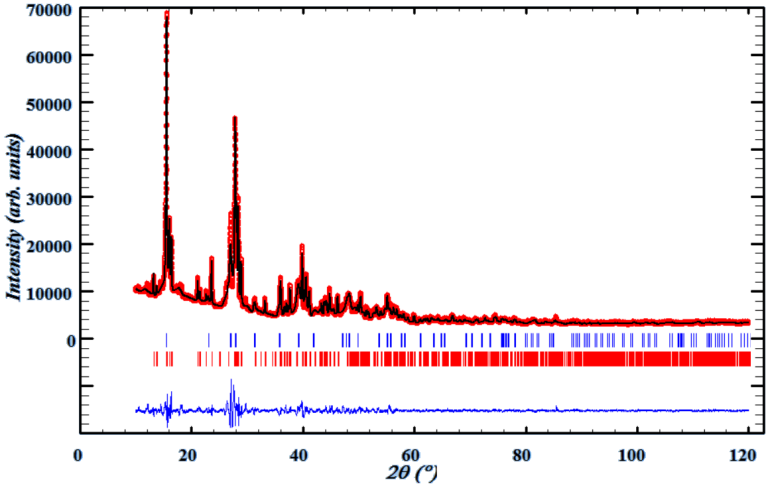

Figure 2.1: Diffractogram of the K_5ThF_9-K_2ThF_6 mixture X(ThF_4) = 0.17. Comparison between the observed (Y_{obs}, in red) and calculated (Y_{calc}, in black) X-ray diffraction patterns. Y_{obs} - Y_{calc}, in blue, is the difference between the experimental and calculated intensities. The Bragg's reflection angular positions are marked in blue (K_2ThF_6), and red (K_5ThF_9).

K_3ThF_7

K_3ThF_7 is not stable at room temperature according to Asker et al. [2] (Fig. A.2). The main goal of the present investigation at this composition was to confirm its eutectoid decomposition into K_2ThF_6 and K_5ThF_9 around 840 K as reported by [2]. The XRD pattern indeed revealed a mixture of K_2ThF_6 and K_5ThF_9, as illustrated in Figures 2.2a and 2.2b. Although a satisfactory Rietveld refinement of the XRD pattern of the sample could not be obtained because of the poor crystallinity of the K_5ThF_9 phase in the mixture, the main Bragg reflections of both phases could clearly be identified, such that we were able to confirm that K_3ThF_7 is not stable at room temperature.

K_2ThF_6

K_2ThF_6 was successfully synthesized in pure form (hexagonal in space group $P\bar{6}2m$ [51], Fig. 2.3). A Rietveld refinement of the XRD data showed the sample was the low temperature hexagonal phase. In another attempt (Fig. 2.4), the synthesized sample was a mixture of the two phases reported in the literature, the high temperature phase being cubic and belonging to the space group $Pm\bar{3}m$ [51]. After a second annealing of this mixture at 873 K, below the transition temperature (918 K [2]), the diffractogram (Fig. 2.4) no longer showed any Bragg reflections attributable to the cubic phase, indicating the complete transformation of the cubic phase to the hexagonal form (Fig. 2.3). The DSC measurement of pure α-K_2ThF_6 shows an event at (952 $\pm$ 10) K which is higher than the temperature assigned by Asker et al. to the allotropic transformation (918 K). Using a silver reference the enthalpy of transition was measured to be $\Delta_{tr}H^o_m = (22.0 \pm 2.0)$ kJ·mol^{-1}.

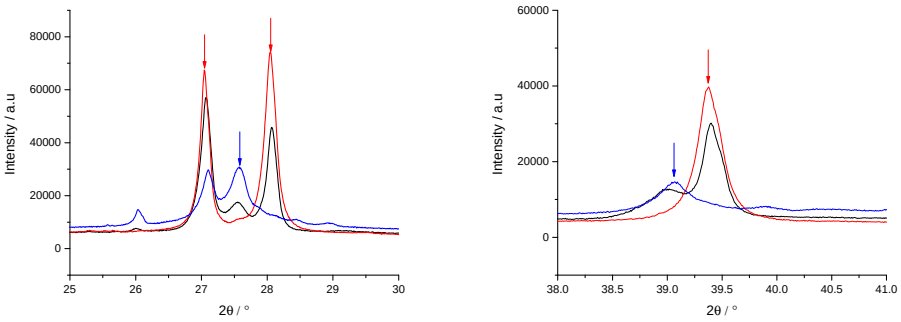

(a) (b)

Figure 2.2: Insets of the diffractogram of the sample of composition X(ThF_4) = 0.25, revealing Bragg reflections corresponding to the "K_3ThF_7" composition (black), compared to K_2ThF_6 (red) and K_5ThF_9 (blue).

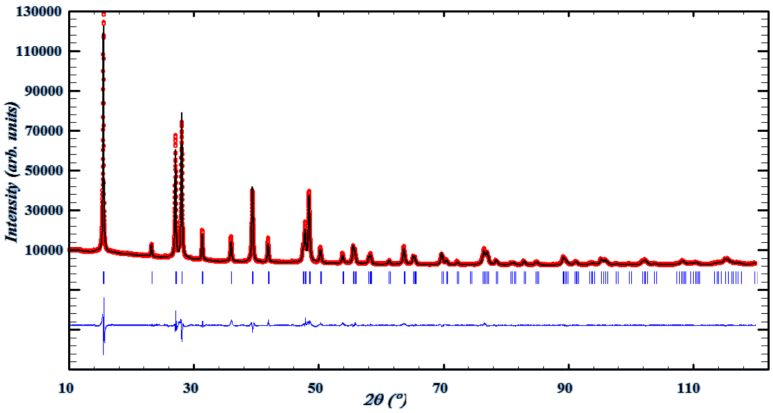

Figure 2.3: XRD pattern of the pure hexagonal K_2ThF_6, X(ThF_4 = 0.33). Comparison between the observed (Y_{obs}, in red) and calculated (Y_{calc}, in black) X-ray diffraction patterns. Y_{obs} - Y_{calc}, in blue, is the difference between the experimental and calculated intensities. The Bragg's reflection angular positions are marked in blue.

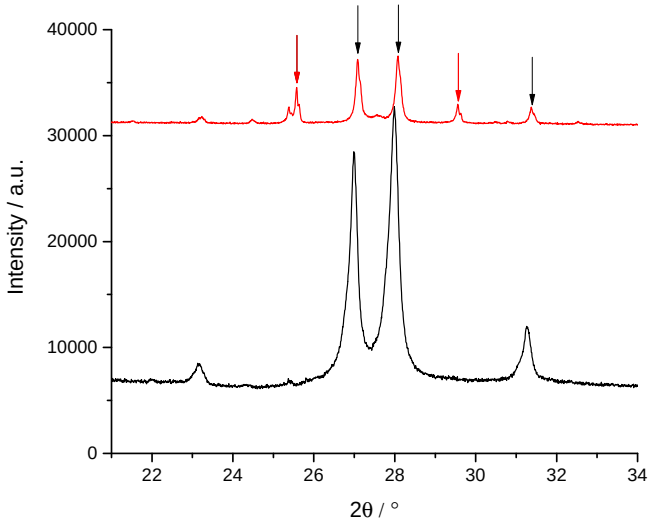

Figure 2.4: Detail of the diffractogram of sample at composition X(ThF_4) = 0.33 after the first heating treatment at 973 K (red) and after a second annealing treatment at 873 K (black). The red arrows indicate Bragg reflections corresponding to the cubic phase, while the black arrows indicate those of the hexagonal phase. It is observed that the high temperature cubic phase disappears after the second annealing treatment, revealing a reversible phase transition.

$K_7Th_6F_{31}$

Both previously reported phase diagrams and a study by Zachariasen during the Manhattan project agree on the existence of $KThF_5$ (rhombohedral in space group $R\bar{3}$, [51]). A compound with this composition has not been described in later structural works, however. Rather, later studies identify $K_7Th_6F_{31}$ as the line compound in the neighborhood of $X(ThF_4)$ = 0.5. This was first reported at Oak Ridge National Laboratory [45], where having studied other $(AF:ThF_4)$=(7:6) compounds in alkali fluoride-thorium tetrafluoride systems, the authors predicted the existence of such a compound in the KF-ThF_4 system and confirmed its existence with thermal analysis of slowly cooled melts. Indeed, a melt of composition $X(ThF_4)$ = 0.462 displayed a single event upon slow cooling and a single phase according to post-characterization by XRD. By comparing the XRD data of this phase with the spacings for $Na_7U_6F_{31}$ and $K_7U_6F_{31}$, the authors were able to classify it as having rhombohedral symmetry. Moreover, the melting temperature, (1172 $\pm$ 2) K, was very close to that reported for $KThF_5$: 1178 K [2] and 1166 K [16]. Brunton [11] and more recently Grzechnik et al. [22] were able to fully solve the crystal structure of $K_7Th_6F_{31}$ ($R\bar{3}$), both using single-crystal X-ray diffraction data. A sample of composition $X(ThF_4)$= 0.418 (after having been subjected to a DSC measurement) was found in this work to be a mixture of K_2ThF_6 and $K_7Th_6F_{31}$ according to the Rietveld refinement (Fig. 2.5) of the XRD data. Supporting this result is a sample of mole fraction $X(ThF_4)$= 0.494 (between KF:ThF_4 = 7:6 and 1:1 compositions) measured in the DSC which did not show thermal events close to 950 or 1000 K (corresponding to the equilibria of K_2ThF_6); these equilibria would be visible between K_2ThF_6 and the putative compound $KThF_5$ if $K_7Th_6F_{31}$ were not a stable phase (see Fig. 2.11). Finally, due to the lack of convincing experimental evidence for the existence of $KThF_5$, in particular the absence of reported Wyckoff positions, we discarded it from the phase diagram.

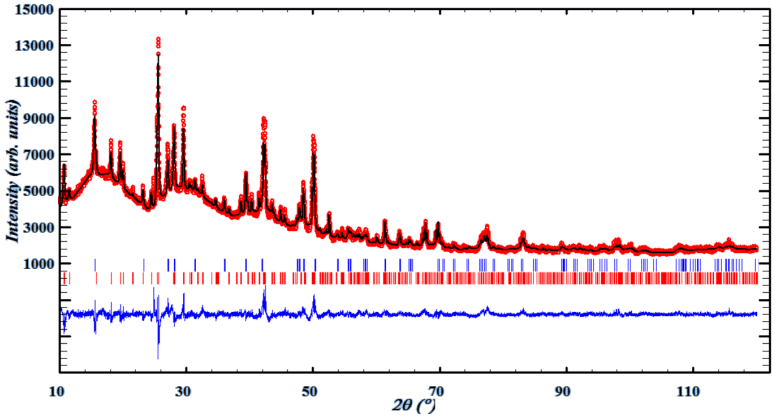

Figure 2.5: XRD pattern of a sample with composition $X(ThF_4)$ = 0.418 after DSC measurements. Comparison between the observed (Y_{obs}, in red) and calculated (Y_{calc}, in black) X-ray diffraction patterns. Y_{obs} - Y_{calc}, in blue, is the difference between the experimental and calculated intensities. The Bragg's reflection angular positions are marked in blue (K_2ThF_6), and red ($K_7Th_6F_{31}$).

KTh_6F_{25}

To discern whether the phase with the highest thorium content was KTh_3F_{13} or KTh_6F_{25}, we attempted a synthesis of both compounds (see Table 1). The XRD pattern of the sample with composition X(ThF_4) = 0.857 was found to be a mixture of KTh_2F_9 (space group $Pnma$) and KTh_6F_{25} (space group $P6_3mmc$) from a LeBail refinement (Fig. 2.6). Unreacted excess KF was possibly not detected by XRD. In the same manner, the sample with composition X(ThF_4) = 0.75 revealed reflections corresponding to KTh_2F_9 and KTh_6F_{25}. Furthermore, KTh_3F_{13} is not mentioned in the literature outside the work of Asker et al., which brings further doubt on its existence. The phase was hence not retained in the present thermodynamic assessment.

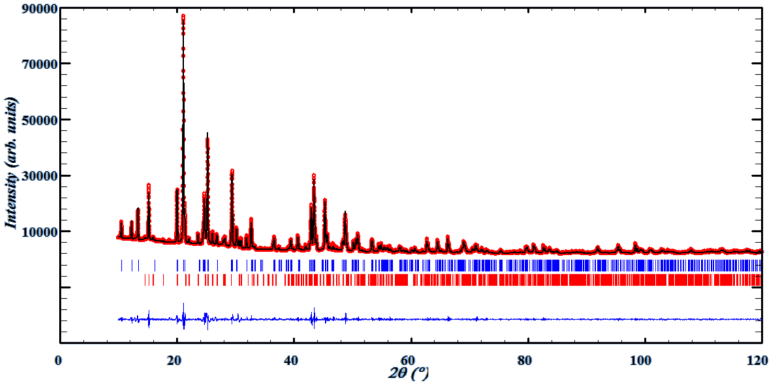

Figure 2.6: XRD pattern of a sample with composition at X(ThF_4)= 0.857. Comparison between the observed (Y_{obs}, in red) and calculated (Y_{calc}, in black) X-ray diffraction patterns. Y_{obs} - Y_{calc}, in blue, is the difference between the experimental and calculated intensities. The Bragg's reflection angular positions are marked in blue (KTh_6F_{25}), and red (KTh_2F_9).

2.5.2. SOLID SOLUTION

Asker et al. [2] report the existence of a solid solution between KTh_3F_{13} and ThF_4 extending up to about 16 % KF in ThF_4. No evidence for such solid solution was found in the present DSC measurements, however, for three compositions between KTh_6F_{25} and ThF_4: X(ThF_4)= 0.902, 0.942, 0.979. These measurements only showed two thermal events (Fig. 2.7) which we assign to the peritectic decomposition of KTh_6F_{25} and liquidus.

2.5.3. LOW TEMPERATURE HEAT CAPACITY OF α-K_2ThF_6

The low temperature heat capacity data of α-K_2ThF_6 measured in the temperature range T=(1.8-298.5) K are shown in Figure 2.8a and listed in Table A.3. The heat capacity reaches values that are about 40 J·K^{-1}·mol^{-1} below the classical Dulong-Petit limit ($C_{lat} = 3nR \sim 224$ J·K^{-1}·mol^{-1} for the nine atoms in the formula unit) as the temperature approaches 298.15 K. The collected data exhibit an anomaly in the neighborhood of the 65-120 K range, evident in the plot of C_p/T (Fig. 2.8b). Repeated operation of the instrument with diverse reference samples has shown that this is a systematic error at-

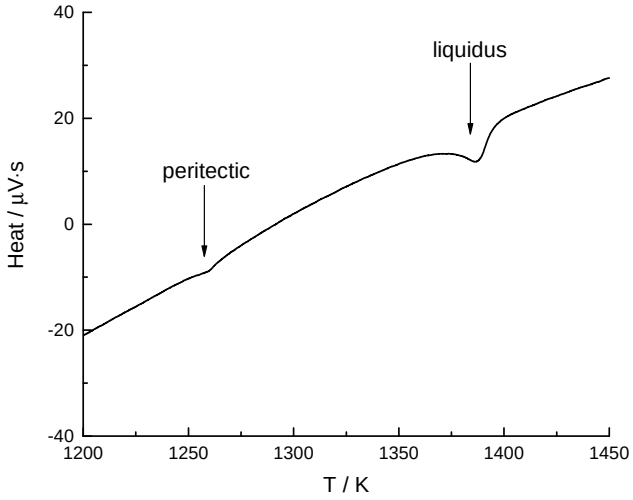

Figure 2.7: Representative DSC signal of a sample with high ThF_4 content: X(ThF_4) = 0.979. There are two events which we assigned to a peritectic decomposition and liquidus.

tributable to the specific measuring puck upon which the sample is placed, and not an intrinsic feature of the measured material. This error is corrected by the fitted curve.

The thermodynamic functions of α-K_2ThF_6 were derived at 298.15 K by fitting the experimental data using the OriginPro 2015 software to theoretical functions below T = 10.0 K [29], and a combination of Debye and Einstein heat capacity functions [50, 49, 43] from T = (10.0 to 297.0) K. The fitting was done with the Levenbergh Marquardt iteration algorithm, using Origin C type fitting function above T = 10.0 K, and a simple harmonic lattice-type function below T = 10.0 K. The fitted data are shown with solid lines in Figures 2.8a and 2.8b.

In the low temperature limit (T < 10.0 K), the phonon contribution can be adequately approximated by the harmonic lattice model [29], the form of which is given in Eq. 2.18:

$$C_{latt} = \sum B_n T^n, \quad where\ n = 3,5,7,9... \tag{2.18}$$

Three terms, with coefficients listed in Table 2.6, were used over the temperature range T = (1.9 to 10.0) K. The electronic contribution of the conduction electrons at the Fermi surface are represented with a linear term γT [21]. In this case, K_2ThF_6 being a poor conductor, the electronic specific heat is nearly zero.

In the region 10.0 < T < 297.0 K the main contribution comes from the lattice term, modelled here with a combination of Debye and Einstein functions, denoted by $D(\theta_D)$ and $E(\theta_E)$, respectively, shown in Eq. 2.19:

$$C_{\mathrm{p,m}} = n_D D(\theta_D) + n_{E1} E(\theta_{E1}) + n_{E2} E(\theta_{E2}) \tag{2.19}$$

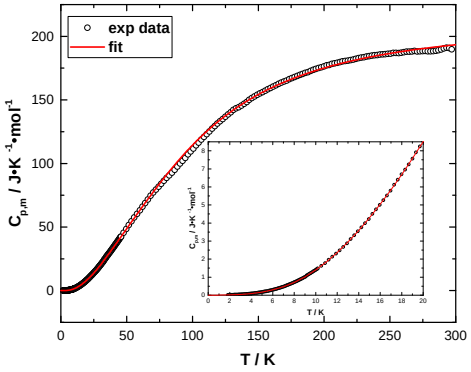

(a) C$_{p,m}$

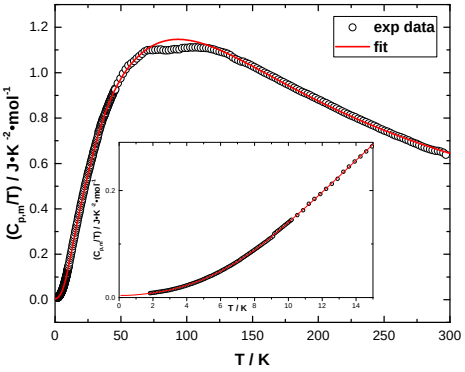

(b) C$_{p,m}$/T

Figure 2.8: Heat capacity of K_2ThF_6 (◯) measured in zero magnetic field and fit to the data (red line): (a) C$_{p,m}$ and (b) C$_{p,m}$/T.

Table 2.6: Summary of fitting parameters of the heat capacity of K_2ThF_6 within the temperature range T = (1.8 to 10.0) K and T = (10.0 to 297.0) K.

Harmonic lattice-model		**Debye and Einstein fit**	
Temp. range/K	1.8-10.0	**Temp. range/K**	10.0-298.5
γ**/mJ·mol^{-1}·K^{-2}**	0.00389	n_D**/mol**	1.1135
B_3**/mJ·mol^{-1}·K^{-4}**	0.00111	θ_D**/K**	115.24
B_5**/mJ·mol^{-1}·K^{-6}**	$4.79569\cdot10^{-6}$	n_{E1}**/mol**	2.8066
B_7**/mJ·mol^{-1}·K^{-8}**	$-2.23822\cdot10^{-8}$	θ_{E1}**/K**	187.12
		n_{E2}**/mol**	4.5253
		θ_{E2}**/K**	392.70
		$n_D + n_{E1} + n_{E2}$**/mol**	8.4

Two Einstein functions were needed in order to achieve an adequate fit of the data, which was carried out excluding the problematic 65-120 K region. The fitted coefficients are listed in Table 2.6. The sum over n atoms is equal to 8.4, quite close to 9 as should be expected. The Debye and Einstein functions have the following forms:

$$D(\theta_D) = 9R(\frac{1}{x})^3 \int_0^x \frac{exp(x)x^4}{[exp(x)-1]^2} \cdot dx, \quad x = \frac{\theta_D}{T} \tag{2.20}$$

$$E(\theta_E) = 3Rx^2 \frac{exp(x)}{[exp(x)-1]^2}, \quad x = \frac{\theta_E}{T} \tag{2.21}$$

where the universal gas constant is denoted by R and is equal to 8.3144598 J·K^{-1}·mol^{-1}.

The heat capacity value at 298.15 K obtained by interpolation is $C^{o}_{p,m}(K_2ThF_6, cr, 298.15\ \text{K}) = (193.2 \pm 3.9)$ J·K^{-1}·mol^{-1}. The experimental standard entropy at 298.15 K determined by numerical integration of $(C_{p,m}/T) = f(T)$ using the aforementioned fitted functions, is $S^{o}_{m}(K_2ThF_6, cr, 298.15\ \text{K}) = (256.9 \pm 4.8)$[10] J· K^{-1}·mol^{-1}. The heat capacity and entropy functions were calculated at selected temperatures between T = (0 and 300) K and are listed in Table A.5.

2.5.4. MIXING PROPERTIES OF THE $(K_xTh_{1-x})F_{4-3x}$ LIQUID SOLUTION

The determination of the mixing enthalpy of the liquid solution is very useful in the assessment of a complex system such as KF-ThF_4 as it provides another dataset, besides the phase diagram points, to optimize the excess Gibbs energy terms of the liquid phase. Table 2.7 reports the values for the mixing enthalpies of the $(K_xTh_{1-x})F_{4-3x}$ liquid solution as determined in this work at the melting temperature of KF, i.e., (1131 $\pm$ 10) K. The range of investigated compositions is limited by the large difference in molar masses between the two salts: at high X(ThF_4) mole fraction, the mass of ThF_4 is much larger compared to the mass of the solvent KF, with lower melting temperature, such that complete mixing of liquid KF with ThF_4, is difficult to obtain. However, complete mixing of the liquid solution compositions reported in Table 2.7 was ensured by the presence of one single event which corresponded to the combination of KF melting, ThF_4 melting, and mixing event, and the absence of other events such as the melting of residual ThF_4, invariant equilibrium reactions, or the liquidus at the given composition. An example of a successful measurement is shown in Figure A.5.

The experimental data obtained in this work and the curve predicted by our model are plotted for comparison (green) in Fig. 2.9a against the mixing enthalpies of the LiF-ThF_4 (red), NaF-ThF_4 (blue) and CsF-ThF_4 (black) systems as calculated respectively from the thermodynamic assessments of Capelli et al. [13], Beneš et al. [5] and Vozárová et al. [48]. The present experimental data and modelled mixing enthalpies are more negative than for the LiF-ThF_4 and NaF-ThF_4 systems, which is consistent with the increase in the alkali cation ionic radius. Depending on composition and temperature, liquid fluoride salts can form dissociated ions, molecular species, or even a polymeric network. The larger K^+ ion offers a larger steric hindrance than Li^+ and Na^+, isolating the coordination complexes ThF_n^{4-n} from each other, and therefore stabilizing the coordination shell around Th^{4+}. Evidence of this stability was provided by Pauvert et al. in the analogous AF-ZrF_4 systems [32]. The authors calculated the lifetimes of the Zr^{4+} first solvation shells in LiF-ZrF_4, NaF-ZrF_4, and KF-ZrF_4 melts at X(ZrF_4)= 0.35 using molecular dynamics. As in [40],[41], they defined the lifetime τ to be the time at which the cage-out correlation function [35] decays to a value of $1/e$. Pauvert et al. found the lifetimes to increase with the ionic radius of the alkali metal (calculated as 3.1, 15.7, and 76.4 ps, respectively). Similarly to the behavior in AF-MCl_2 melts [17], (A = alkali metal, M = transition metal), a coordination complex around Th^{4+} in the (K,Th)F_x liquid solution is also likely to be further stabilized compared to its analogue in (Li,Th)F_x or (Na,Th)F_x liquid solutions due to polarization effects: lighter alkali ions are more polarizing than

[10] The quoted uncertainty corresponds to the standard uncertainty.

Table 2.7: Mixing enthalpy of the $(1-x)$KF(l) + $x$$ThF_4$(l*) system determined in this work at T = 1131 ± 10 K and (0.10 ± 0.01)[d] MPa. KF melts at the measurement temperature, while ThF_4 is solid, although the initial state is taken to be a hypothetical liquid. The final state was an undercooled liquid mixture. The scanning temperature range was from (303 ± 10) K to (1373 ± 10) K.

X(ThF_4)[a]	$\Delta_{mix}H_m^{o}$ [b] / kJ·mol^{-1}	m(KF) / mg[c]	m(ThF_4) / mg[c]
0.109	-15.0 ± 1.4	29.2	18.9
0.200	-29.5 ± 1.8	23.6	31.3
0.305	-30.3 ± 0.2	21.9	50.9
0.338	-30.8 ± 1.0	14.9	40.4
0.401	-31.7 ± 0.7	57.9	16.3
0.504	-32.9 ± 3.0	39.3	7.3

[a] Standard uncertainties u are u(X(ThF_4)) = 0.005.

[b] The error is based on the standard uncertainty determined during calibration.

[c] Standard uncertainties u are u(m) = 0.1 mg.

[d] The quoted uncertainty corresponds to the standard uncertainty.

* Indicates a hypothetical liquid state.

K^+ and thus are able to attract F^- more strongly, leading to longer Th^{4+}-F^- distances and weaker complexes. The most negative mixing enthalpy curve, corresponding to the largest cation Cs^+, fits this trend.
Gibbs energies of mixing (Fig. 2.10a) also reflect this trend in stability, with the composition of maximum stability indicated by the minimum in the curve. This composition is related to the choice of cation-cation coordination numbers (Table 3), as is the maximum of the M-Th-F-F pair fractions (Fig. 2.10b), which is around X(ThF_4) = 0.25 for Li, Na systems and X(ThF_4) = 0.33 for K, Cs systems. The basicity of the systems can be qualitatively gauged from the shape and value of the M-Th-F-F maximum: a strongly basic system would lead to complete dissociation of the cation-cation pairs to result in perfect SNN ordering, i.e., a bond fraction of unity at the composition of maximum short-range ordering. In this case, the systems can be qualified as moderately to reasonably basic with a round shape for the M-Th-F-F fraction and maximum value between 0.55 and 0.79. Moreover the degree of basicity is closely linked with the stability trend just discussed: the maximum fraction of the Li-Th-F-F distributions is the lowest, those of K-Th-F-F and Cs-Th-F-F are the highest. It is interesting to note that not even CsF-ThF_4 is basic enough for Cs-Th-F-F to reach unity; it can be expected that FrF-ThF_4 would come closest.

The entropies of mixing are plotted in Fig. 2.9b. Capelli et al. [12] related the maximum for mixing entropy in LiF-ThF_4 at X(ThF4) ≈ 0.25 to a higher content of free F^-, observed in NMR studies by Bessada et al. [8]. The computed curves suggest that there would be less free F^-, at least in the KF and CsF-based systems. Structural studies such as NMR or EXAFS on these systems at high ThF_4 compositions could help understand if this trend is correct.

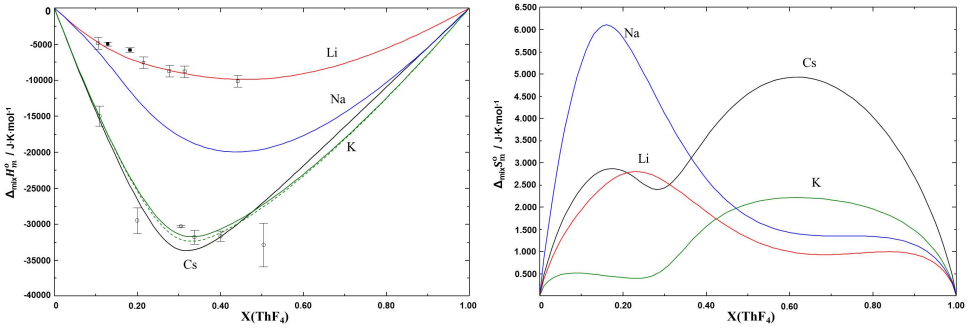

(a) Mixing enthalpies (b) Mixing entropies

Figure 2.9: (a) Mixing enthalpies and (b) mixing entropies of the LiF-ThF_4 (red) [12], NaF-ThF_4 (blue) [13], KF-ThF_4 (green, this work) and CsF-ThF_4 (black) [48]. The calculations were done at T = 1400 K considering KF(l) and ThF_4(l) as initial states and the liquid solution as the final state.

Circles: experimentally measured enthalpies of KF(l)-ThF_4(s) mixing at 1131 K (see Table 2.7); squares: experimentally measured points by [12] at 1121 K (LiF(l)-ThF_4(s), white) and 1383 K (LiF(l)-ThF_4(l), black).The dashed green line corresponds to KF-ThF_4 at T = 1131 K. Initial states were KF(l) and (hypothetical) ThF_4(l) , the final state was the liquid solution (hypothetical for most of the composition range).

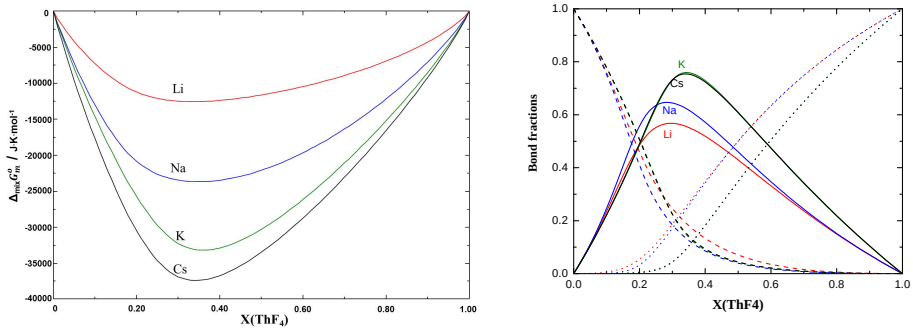

(a) Gibbs energy of mixing (b) Pair fractions

Figure 2.10: (a) Gibbs energy of mixing at T = 1400 K. Red: LiF-ThF_4, blue: NaF-ThF_4, green: KF-ThF_4, black: CsF-ThF_4. Initial states were the liquid end-members, the final state was the liquid solution. (b) Bond fractions of the LiF-ThF_4 (red) [12], NaF-ThF_4 (blue) [13], KF-ThF_4 (green, this work) and CsF-ThF_4 (black) [48] systems calculated at T = 1400 K. Dashed lines: M-M-F-F, solid lines: M-Th-FF, dotted lines: Th-Th-F-F pair fractions.

2.5.5. CALPHAD ASSESSMENT OF THE KF-ThF_4 SYSTEM

The KF-ThF_4 system (Fig. 2.11) was finally optimized based on our measured DSC equilibrium and mixing enthalpy data, all of which are presented in Table 2.8.There are 6 intermediate compounds: K_5UF_9 (α and β phases), K_3ThF_7, K_2ThF_6 (α and β phases), $K_7Th_6F_{31}$, KTh_2F_9, and KTh_6F_{25}.The phase diagram is further characterized by four eutectics (X(ThF_4) = 0.152, 0.298, 0.511, 0.681), three peritectics (X(ThF_4) = 0.165, 0.333, 0.743), three congruent melting points (X(ThF_4) = 0.25, 0.462, 0.667), and two limits of stability (X(ThF_4) = 0.25, 0.333); the temperatures and compositions of these equilibria are listed in Table 2.9. It can be seen that the liquidus temperatures measured in this work are sometimes slightly higher than those reported by the previous studies. This is most likely because the authors [2] and [16] used onset temperatures rather than minimum temperatures on the heat flow events for liquidus determination (see Fig. A.3 for an explanation of how these are determined in this work in a typical DSC measurement). In fact, the agreement with the previous studies [16], [2] becomes much better if the onset temperatures of the liquidus equilibria as measured in this work (▽, red) are selected (see Fig. 2.11).

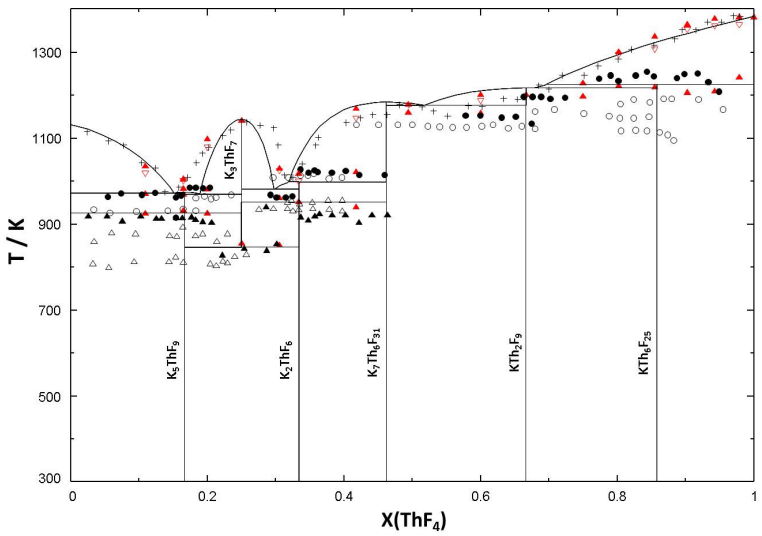

Figure 2.11: Optimized KF-ThF_4 phase diagram superimposed against experimental points by Asker et al. (▲,+,●) [2], Emelyanov and Evstyukhin (△, ○) [16], and this study (▲, liquidus onset ▽, red).

Table 2.8: Equilibrium data in the KF-ThF_4 system as measured in this work by DSC.

$X(ThF_4)$[a]	T/K[b]	Equilibrium	Equilibrium reaction
0.000	1129	KF congruent melting	KF = L
0.109	926	Polymorphic transition	K_5ThF_9-α = K_5ThF_9-β
0.109	971	Eutectic	KF + K_5ThF_9-β = L
0.109	1036	Liquidus	KF + L' = L
0.165	931	Polymorphic transition	K_5ThF_9-α = K_5ThF_9-β
0.165	968	Eutectic	KF + K_5ThF_9-β = L
0.165	982	Peritectic	K_5ThF_9-β = K_3ThF_7 + L
0.165	1005	Liquidus	K_3ThF_7 + L = L'
0.167	919	Polymorphic transition	K_5ThF_9-α = K_5ThF_9-β
0.167	966	Eutectic	KF + K_5ThF_9-β = L
0.167	1057	Liquidus	K_3ThF_7 + L = L'
0.200	925	Polymorphic transition	K_5ThF_9-α = K_5ThF_9-β
0.200	982	Peritectic	K_5ThF_9-β = K_3ThF_7 + L
0.200	1098	Liquidus	K_3ThF_7 + L' = L
0.25	856	Eutectoid	K_3ThF_7 = K_5ThF_9-α + K_2ThF_6-α
0.25	1141	Congruent melting	K_3ThF_7 = L
0.305	851	Eutectoid	K_3ThF_7 = K_5ThF_9-α + K_2ThF_6-α
0.305	961	Eutectic	K_3ThF_7 + K_2ThF_6-β = L
0.305	1029	Liquidus	K_3ThF_7 + L' = L
0.333	952	Polymorphic transition	K_2ThF_6-α = K_2ThF_6-β
0.333	1000	Peritectic	K_2ThF_6-β = $K_7Th_6F_{31}$ + L
0.418	940	Polymorphic transition	K_2ThF_6-α = K_2ThF_6-β
0.418	1021	Peritectic	K_2ThF_6-β = $K_7Th_6F_{31}$ + L
0.418	1169	Liquidus	$K_7Th_6F_{31}$ + L' = L
0.494	1159	Eutectic	$K_7Th_6F_{31}$ + K_2ThF_9 = L
0.494	1178	Liquidus	$K_7Th_6F_{31}$ + L' = L
0.600	1157	Eutectic	$K_7Th_6F_{31}$ + K_2ThF_9 = L
0.600	1201	Liquidus	K_2ThF_9 + L' = L
0.666	1202	Congruent Melting	K_2ThF_9 = + L
0.749	1197	Eutectic	K_2ThF_9 + KTh_6F_{25} = L
0.749	1218	Peritectic	KTh_6F_{25} = L + ThF_4
0.802	1221	Peritectic	KTh_6F_{25} = L + ThF_4
0.802	1300	Liquidus	ThF_4 + L' = L
0.855	1218	Peritectic	KTh_6F_{25} = L + ThF_4
0.855	1336	Liquidus	ThF_4 + L' = L
0.902	1206	Peritectic	KTh_6F_{25} = L + ThF_4
0.902	1365	Liquidus	ThF_4 + L' = L
0.942	1209	Peritectic	KTh_6F_{25} = L + ThF_4
0.942	1379	Liquidus	ThF_4 + L' = L
0.979	1241	Peritectic	KTh_6F_{25} = L + ThF_4
0.979	1383	Liquidus	ThF_4 + L' = L
1.000	1381	Congruent melting	ThF_4 = L

[a] Standard uncertainties u are $u(X(ThF_4))$= 0.005.

[b] Standard uncertainties u are u(T)= 5 K for the pure end-members, u(T)= 10 K for mixtures.

The pressure was (0.10 $\pm$ 0.01) MPa.

2

2.5.6. CALPHAD ASSESSMENT OF THE LiF-KF-ThF_4 SYSTEM

LiF-$KThF_5$ PSEUDOBINARY SECTION

Some equilibrium data were collected along the LiF-$KThF_5$ pseudobinary section in order to optimize the liquidus surface of the LiF-KF-ThF_4 ternary system. The section is relatively simple, as shown in Fig. 2.12. LiF is the first compound to crystallize below ~ 25 mol % X($KThF_5$), beyond that the liquid solution is in equilibrium with $K_7Th_6F_{31}$. Below the solidus the calculation shows that there are two ternary phase fields throughout the composition range: {LiF + Li_3ThF_7 + $K_7Th_6F_{31}$} and {Li_3ThF_7 + KTh_2F_9 + $K_7Th_6F_{31}$}. Below ~662 K the equilibrium is between LiF, KTh_2F_9, and $K_7Th_6F_{31}$. The experimental points, however, suggest that the temperature range in which {LiF + Li_3ThF_7 + $K_7Th_6F_{31}$} and {Li_3ThF_7 + KTh_2F_9 + $K_7Th_6F_{31}$} exist is much more narrow. The phase equilibria of the experimental points are given in Table 2.12.

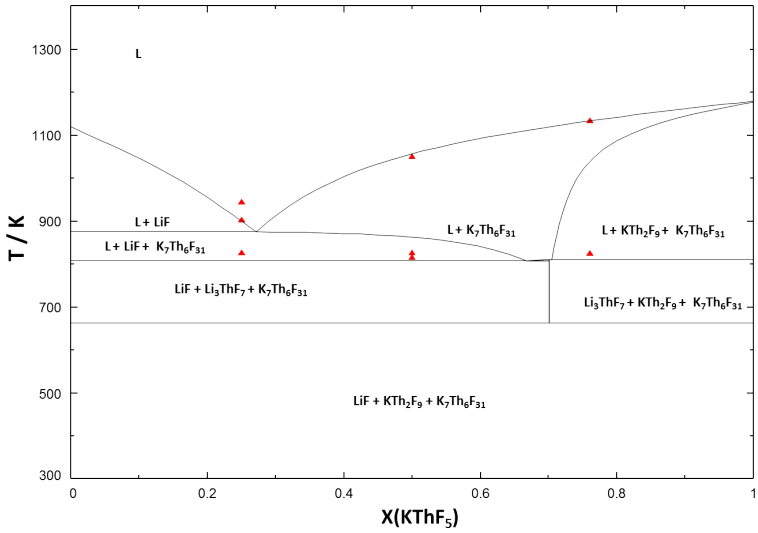

Figure 2.12: Phase diagram of the LiF-$KThF_5$ pseudobinary section as calculated in this study superimposed against experimental points measured in this work (▲, red, listed in Table 2.12).

LiF-KF-ThF_4 LIQUIDUS PROJECTION

The LiF-KF-ThF_4 system (Fig. 2.13) as calculated in this study is characterized by fifteen primary fields of crystallization and nineteen invariant points: nine quasi-peritectics, four saddle points, two peritectics, and four eutectics, the lowest of which is calculated at T = 755 K, very close to the LiF-KF eutectic: (X(ThF_4), X(LiF), X(KF)) = (0.023, 0.461, 0.516). DSC analysis of an experimental point in the neighborhood of this ternary eutectic (X(ThF_4), X(LiF), X(KF)) = (0.037, 0.463, 0.500) showed only one event at T = (753 $\pm$ 10 K), which can be assigned to the invariant reaction LiF(cr) + KF(cr) + K_5ThF_9(cr) = L. Hence, the point is a ternary eutectic. The agreement between the measured and calculated liquidus points is reported in Table 2.10. The solid phases in equilibrium with the liquid, compositions, and temperatures of all calculated invariant equilibria are listed in

Table 2.9: Invariant equilibrium data in the KF-ThF_4 system.

Equilibrium	Invariant reaction	This study (calc.)		DSC equilib. global average		Emelyanov and Evstyukhin[c] [16]		Asker et al. [2]	
		X(ThF_4)	T / K	X(ThF_4)[a]	T / K[b]	X(ThF_4)	T / K	X(ThF_4)[d]	T / K[e]
Eutectic	KF + K_5ThF_9-β = L	0.152	971.8	-	968[k]	-	935	0.14	967
Peritectic	K_5ThF_9-β = K_3ThF_7 + L	0.167	973.5[f]	0.167	977[k]	0.167	966	0.14	967
α-β transition	K_5ThF_9-α = K_5ThF_9-β	0.167	926	0.167	926[h]	0.167	874[g]	0.167	908
Eutectoid	K_3ThF_7 = K_5ThF_9-α + K_2ThF_6-α	0.25	844.9	0.25	854[k]	-	-	0.25	843
Congruent melting	K_3ThF_7 = L	0.25	1142.8	0.25	1141	0.25	1129	0.25	1138
Eutectic	K_3ThF_7 + K_2ThF_6-β = L	0.299	980.3	-	961	0.34	1014	0.31	964
α-β transition	K_2ThF_6-α = K_2ThF_6-β	0.333	952	0.333	952	-	936[h]	0.333	918
Peritectic	K_2ThF_6-β = L + $K_7Th_6F_{31}$	0.333	997.2	0.333	1000	-	-	0.333	1020
Congruent melting	$K_7Th_6F_{31}$ = L	0.462	1183.4	-	-	0.5	1166	0.5	1178
Eutectic	$K_7Th_6F_{31}$ + K_2ThF_9 = L	0.511	1174.9	-	1158[k]	0.54	1133	0.56	1148
Congruent melting	K_2ThF_9 = L	0.667	1217.2	0.666	1202	0.666	1173	0.66	1203
Peritectic	KTh_6F_{25} = ThF_4 + L	0.857	1224	0.857	1220[k]	0.857	1203	0.78	1253[i]

[a] Standard uncertainties u are u(X(ThF_4))) = 0.05.
[b] Standard uncertainties u are u(T) = 5 K for pure end-members, 10 K for mixtures.
[c] No uncertainties reported for composition or temperature.
[d] ThF_4 reagent is estimated to be 99 % pure, no other composition errors are reported.
[e] Reported standard uncertainties u are u(T) = 5 K for phase transitions and incongruent melting points, no uncertainties reported for liquidus points.
[f] Calculated as congruent melting.
[g] Attributed to be a lower limit of stability.
[h] The authors did not attribute it to any equilibrium.
[i] Interpreted by the authors to be a congruent melting point.
[j] Interpreted by the authors to be a eutectic.
[k] Global average of the experimental runs appearing in Table 2.8.
Measurements done at (0.10 $\pm$ 0.01) MPa.

Table 2.10. The rest of the equilibria measured by DSC are listed in Table 2.11. There are no ternary stoichiometric compounds or solid solutions in the ternary system reported in the literature.

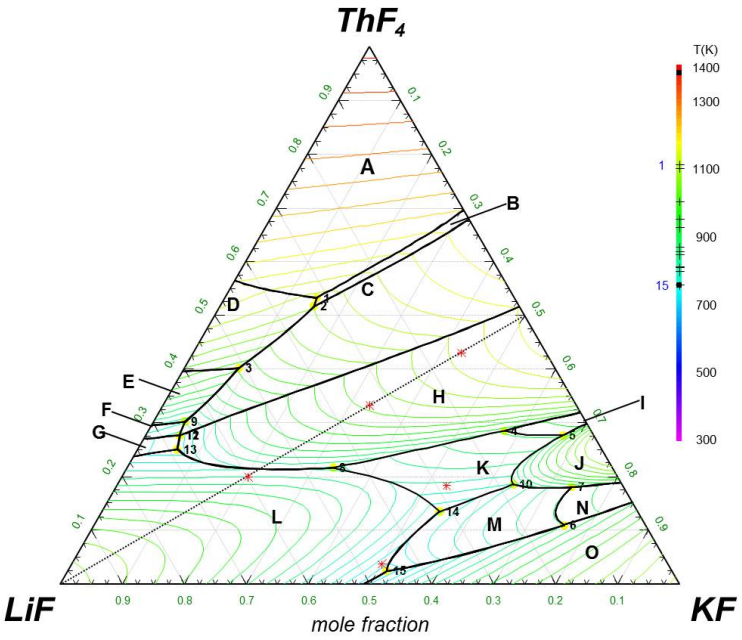

Figure 2.13: Liquidus projection and primary crystallization fields in the LiF-KF-ThF_4 system as calculated in this study. The spacing between the isotherms is 25 K. The dashed line represents the LiF-$KThF_5$ pseudobinary section shown in Figure 2.12. Experimental points: (*). Primary crystallization phase fields: (A) ThF_4(s); (B) KTh_6F_{25}; (C) KTh_2F_9; (D) $LiTh_4F_{17}$; (E) $LiTh_2F_9$; (F) $LiThF_5$; (G) Li_3ThF_7; (H) $K_7Th_6F_{31}$; (I) β-K_2ThF_6; (J) K_3ThF_7; (K) α-K_2ThF_6; (L) LiF; (M) α-K_5ThF_9; (N) β-K_5ThF_9; (O) KF

.

Table 2.10: Calculated vs. experimental liquidus temperatures in the LiF-KF-ThF_4 system.

X(ThF_4)[a]	X(LiF)[a]	X(KF)[a]	Equilibrium reaction	T_{calc} / K	T^b_{exp} / K
0.037	0.463	0.500	LiF + KF + α-K_5ThF_9 = L	783[c]	753[d]
0.183	0.285	0.532	K_2ThF_6-α + L' = L	866	839
0.430	0.138	0.432	$K_7Th_6F_{31}$ + L' = L	1133	1133
0.200	0.597	0.203	LiF + L' = L	901	943
0.333	0.334	0.333	$K_7Th_6F_{31}$ + L' = L	1056	1050

[a] Standard composition error is $u(||(X(ThF_4), X(LiF), X(KF))||) = 0.006$.

[b] Standard uncertainties u are $u(T)$=10 K.

[c] Calculated as LiF + L' = L at the experimental composition, since the eutectic does not exactly match the experimental one.

[d] Eutectic temperature calculated as 755 K in the vicinity of the experimental composition, see Table 2.11.

Measurements done at (0.10 $\pm$ 0.01) MPa.

Table 2.11: Invariant equilibrium data and saddle points calculated in the LiF-KF-ThF_4 system.

X(ThF_4)	X(LiF)	X(KF)	T_{calc} / K	Equilibrium	Solid phases present
0.533	0.319	0.148	1113.5	Quasi-peritectic	KTh_6F_{25} + $LiTh_4F_{17}$ + ThF_4
0.517	0.331	0.152	1101.4	Quasi-peritectic	KTh_2F_9 + KTh_6F_{25} + $LiTh_4F_{17}$
0.402	0.510	0.088	1003.2	Quasi-peritectic	KTh_2F_9 + $LiTh_2F_9$ + $LiTh_4F_{17}$
0.285	0.140	0.575	952.0	Peritectic	α-K_2ThF_6 + β-K_2ThF_6 + $K_7Th_6F_{31}$
0.276	0.049	0.674	952.0	Quasi-peritectic	α-K_2ThF_6 + β-K_2ThF_6 + K_3ThF_7
0.109	0.131	0.760	926.0	Peritectic	KF + α-K_5ThF_9 + β-K_5ThF_9
0.165	0.103	0.732	926.1	Saddle point	α-K_5ThF_9 + β-K_5ThF_9
0.180	0.084	0.736	926.0	Quasi-peritectic	α-K_5ThF_9 + β-K_5ThF_9 + K_3ThF_7
0.214	0.827	0.286	879.5	Saddle point	$K_7Th_6F_{31}$ + LiF
0.194	0.390	0.416	877.6	Saddle point	$K_7Th_6F_{31}$ + LiF
0.215	0.451	0.334	869.0	Eutectic	α-K_2ThF_6 + $K_7Th_6F_{31}$ + LiF
0.302	0.647	0.051	852.9	Quasi-peritectic	KTh_2F_9 + $LiTh_2F_9$ + $LiThF_5$
0.185	0.176	0.639	846.4	Quasi-peritectic	α-K_2ThF_6 + K_3ThF_7 + α-K_5ThF_9
0.276	0.669	0.054	810.2	Quasi-peritectic	KTh_2F_9 + Li_3ThF_7 + $LiThF_5$
0.275	0.669	0.054	809.9	Quasi-peritectic	$K_7Th_6F_{31}$ + KTh_2F_9 + Li_3ThF_7
0.251	0.685	0.064	807.7	Eutectic	$K_7Th_6F_{31}$ + Li_3ThF_7 + LiF
0.107	0.355	0.538	803.7	Saddle point	LiF + α-K_5ThF_9
0.135	0.319	0.546	797.7	Eutectic	α-K_2ThF_6 + α-K_5ThF_9 + LiF
0.023	0.461	0.516	754.8	Eutectic	α-K_5ThF_9 + KF + LiF

Table 2.12: Phase diagram equilibria of the LiF-KF-ThF_4 system as measured in this study by DSC.

X(ThF_4)[a]	X(LiF)[a]	X(KF)[a]	T_{exp} / K[b]	Equilibrium	Equilibrium Reaction
0.037	0.463	0.500	753	Eutectic	LiF + KF + α-K_5ThF_9 = L
0.183	0.285	0.532	816	Eutectic	LiF + α-K_5ThF_9 + α-K_2ThF_6 = L
			839	Liquidus	α-K_2ThF_6 + L'= L
0.430	0.138	0.432	825	Eutectic	Li_3ThF_7 + $K_7Th_6F_{31}$ + KTh_2F_9 = L
			1133	Liquidus	$K_7Th_6F_{31}$ + L' = L
0.200	0.597	0.203	826	Eutectic	LiF + Li_3ThF_7 + $K_7Th_6F_{31}$ = L
			902	Quasi-peritectic	L' + LiF + $K_7Th_6F_{31}$ = L + LiF
			943	Liquidus	LiF + L' = L
0.333	0.334	0.333	815	Eutectoid	Li_3ThF_7 + $K_7Th_6F_{31}$ = LiF + KTh_2F_9
			825	Eutectic	Li_3ThF_7 + $K_7Th_6F_{31}$ + LiF = L
			1050	Liquidus	$K_7Th_6F_{31}$ + L' = L

[a] Standard composition error is $u(||(X(ThF_4), X(LiF), X(KF))||) = 0.006$.

[b] Standard uncertainties u are $u(T)$=10 K.

The pressure was (0.10 $\pm$ 0.01) MPa.

2.5.7. CALPHAD ASSESSMENT OF THE NAF-KF-ThF_4 SYSTEM

2

NaF-$KThF_5$ PSEUDOBINARY SECTION

The NaF-$KThF_5$ pseudobinary section, studied by Emelyanov and Evstyukhin, is the only set of data reported in the literature related to the liquidus surface of the NaF-KF-ThF_4 ternary system. As measured by the authors, the pseudo-binary section shows only one intermediate compound: the quaternary fluoride $KNaThF_6$, displaying a phase transition at 813 K [16], and incongruent melting at 938 K. In this work the α-β transition of $KNaThF_6$ was observed at (825 $\pm$ 10) K. The enthalpy of transition was measured to be $\Delta_{tr}H^o_m = (15.3 \pm 0.6)$ kJ·mol^{-1}. The melting event was observed at (940 $\pm$ 10) K. The authors reported a peritectic decomposition, which agrees with the phase transition predicted by our calculation, namely

$$\beta - KNaThF_6 \longrightarrow K_7Th_6F_{31} + L \tag{2.22}$$

In our calorimetric measurement we were not able to detect a third event which would correspond to the liquidus, and neither did [16] (Fig. 2.14). This might be due to a very close proximity of the incongruent melting event to the liquidus surface, making it hard to detect.

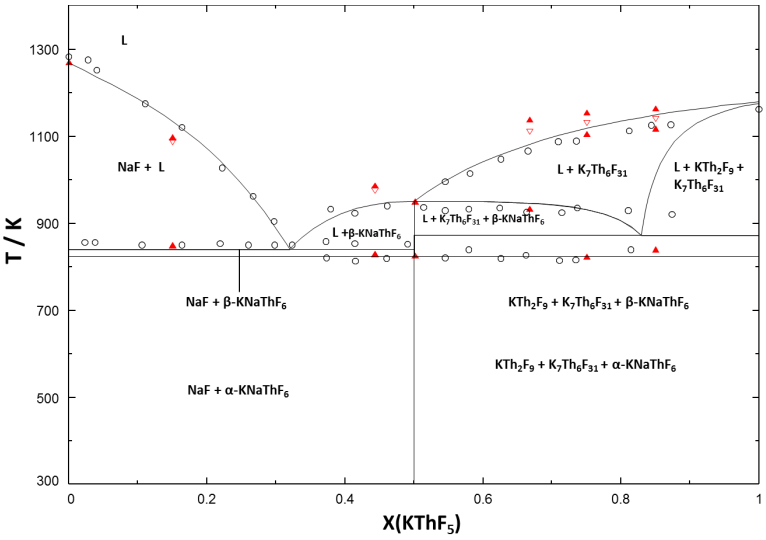

Figure 2.14: Phase diagram of the NaF-$KThF_5$ pseudobinary section as calculated in this study superimposed against experimental points by Emelyanov and Evstyukhin [16], (○, black) and experimental points measured in this work (▲, liquidus onset ▽, red, included in Table 2.16).

PHASE EQUILIBRIA AT 300 K

In addition to the section of the liquidus surface which can be observed along the NaF-$KThF_5$ pseudobinary section, Emelyanov and Evstyukhin [16] analyzed several melts of the ternary phase diagram at room temperature using XRD to determine their phase composition, reported in Table 2.13. These are compared to the equilibrium phase fields as calculated herein. The authors concluded that within this region of the phase diagram there are six equilibrium ternary phase fields having the following compositions:

1. NaF + K_3ThF_7 + KF
2. NaF + $K_3Th_2F_{11}$ + K_3ThF_7
3. NaF + $KNaThF_6$ + $K_3Th_2F_{11}$
4. NaF + Na_2ThF_6 + $KNaThF_6$
5. Na_2ThF_6 + $KNaThF_6$ + $KThF_5$
6. $KNaThF_6$ + $KThF_5$ + $K_3Th_2F_{11}$

In the present assessment 12 ternary phase fields are calculated (Fig. 2.15):

1. NaF + (Na,K)F + K_5ThF_9
2. NaF + K_2ThF_6 + K_5ThF_9
3. NaF + K_2ThF_6 + $KNaThF_6$
4. NaF + Na_2ThF_6 + $KNaThF_6$
5. K_2ThF_6 + $K_7Th_6F_{31}$ + $KNaThF_6$
6. $NaThF_5$ + Na_2ThF_6 + $KNaThF_6$
7. KTh_2F_9 + $K_7Th_6F_{31}$ + $KNaThF_6$
8. $NaThF_5$ + KTh_2F_9 + $KNaThF_6$
9. $NaThF_5$ + KTh_2F_9 + KTh_2F_9
10. $NaThF_5$ + KTh_2F_9 + KTh_6F_{25}
11. $Na_xTh_{1-x}F_{4-3x}$ + $NaTh_2F_9$ + KTh_6F_{25}
12. $Na_xTh_{1-x}F_{4-3x}$ + KTh_6F_{25}

Among these, (2)-(8) are found within the region studied by the authors. The main differences can be related to those already discussed in the KF-ThF_4 binary phase diagram: [16] observed K_3ThF_7 in fields (a) and (b). We find this compound to decompose around 979 K, however, and so we predict K_5ThF_9 to be the stable phase instead. In experimental points represented by (half-filled square) they reported unidentified lines, which possibly were those of K_5ThF_9. Similarly, they observed phase fields with $K_3Th_2F_{11}$ whereas our model predicts the phase K_2ThF_6. Fields (d) and (4) coincide fully, but again e) disagrees with our calculation having established that $KThF_5$ is not a true stable phase. However, our model does predict that $K_7Th_6F_{31}$ exists in those regions where they reported $KThF_5$ to be present. Finally, phase fields (f) and (5) also coincide fully allowing for the fact that the authors misinterpreted XRD patterns of $KThF_5$ and $K_3Th_2F_{11}$ with those of $K_7Th_6F_{31}$ and K_2ThF_6, respectively. The only compound in the region of interest which was not reported by them but which appears in our projection

is $NaThF_5$, which was possibly observed given that points represented by (half-filled diamond) showed Bragg reflections they could not identify. Overall, the agreement is close enough to consider the description of solid equilibra as satisfactory.

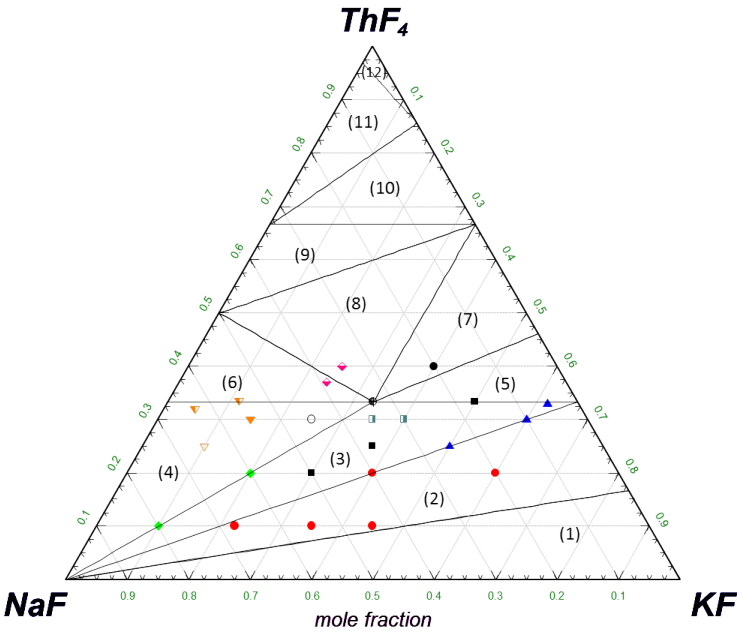

Figure 2.15: Projection of the NaF-KF-ThF_4 ternary system as calculated in this study at 300 K superimposed against experimental compositions analyzed using XRD by [16]: red circles: {NaF + K_3ThF_7 + KF}; blue triangles: {NaF + $K_3Th_2F_{11}$ + K_3ThF_7}; black squares: unidentified patterns; green diamonds: {NaF + $KNaThF_6$}; half-filled squares: phase similar to $KNaThF_6$ and unidentified lines; half-filled circle: {$KNaThF_6$}; black circle: {$KNaThF_6$ + $KThF_5$}; half-filled diamond: {$KThF_5$ + $KNaThF_6$ + unidentified lines}; half-filled orange triangle: {Na_2ThF_6 + unidentified lines}; filled orange triangle:{Na_2ThF_6 + $KNaThF_6$}; empty orange triangle: {Na_2ThF_6 + $KNaThF_6$ + Na_4ThF_8(?)}; white circle: {$KNaThF_6$ + weak lines}. These data are also compared in Table 2.13 for more clarity. Phases in equilibrium in phase fields (1)-(11) are listed in section 2.5.7.

NAF-KF-ThF_4 LIQUIDUS PROJECTION

The NaF-KF-ThF_4 (Fig. 2.16) system is an even more complex system, with one quaternary compound (displaying a phase transition), 19 primary crystallization fields and 31 invariant points (Table 2.14). Of these, nineteen are quasi-peritectic, five are saddle points, four are peritectic, and four are eutectic, with the lowest one occurring at 804 K and X(ThF_4) = (0.219,0.234,0.547). We have found the liquidus temperatures of eight samples (points shown in red) to closely match the calculated ones only in most instances (Table 2.15). All equilibria measured experimentally are given in Table 2.16.

Table 2.13: Projection of the NaF-KF-ThF_4 system at 300 K.

Set of points	Experimentally observed phases by [16]	Calculated phases, this study
red circles	NaF + K_3ThF_7 + KF	NaF + K_5ThF_9 + $KNaThF_6$
blue triangles	NaF + $K_3Th_2F_{11}$ + K_3ThF_7	NaF + K_5ThF_9 + $KNaThF_6$ / K_2ThF_6 + $KNaThF_6$ + K_5ThF_9
black squares	unidentified lines	NaF + K_5ThF_9 + $KNaThF_6$ / $KNaThF_6$ + K_2ThF_6
green diamonds	NaF + $KNaThF_6$	NaF + $KNaThF_6$
half-filled squares	phase similar to $KNaThF_6$ and unidentified lines	NaF + K_5ThF_9 + $KNaThF_6$
half-filled circle	$KNaThF_6$	$KNaThF_6$
black circle	$KNaThF_6$ + $KThF_5$	KTh_2F_9 + $K_7Th_6F_{31}$ + $KNaThF_6$
half-filled diamond	$KThF_5$ + $KNaThF_6$ + unidentified lines	$NaThF_5$ + Na_2ThF_6 + $KNaThF_6$ / $NaThF_5$ + KTh_2F_9 + $KNaThF_6$
half-filled orange triangle	Na_2ThF_6 + unidentified lines	NaF + Na_2ThF_6 + $KNaThF_6$ / Na_2ThF_6 + $KNaThF_6$
filled orange triangle	Na_2ThF_6 + $KNaThF_6$	NaF + Na_2ThF_6 + $KNaThF_6$
empty orange triangle	Na_2ThF_6 + $KNaThF_6$ + Na_4ThF_8(?)	NaF + Na_2ThF_6 + $KNaThF_6$
white circle	$KNaThF_6$ + weak lines	NaF + Na_2ThF_6 + $KNaThF_6$

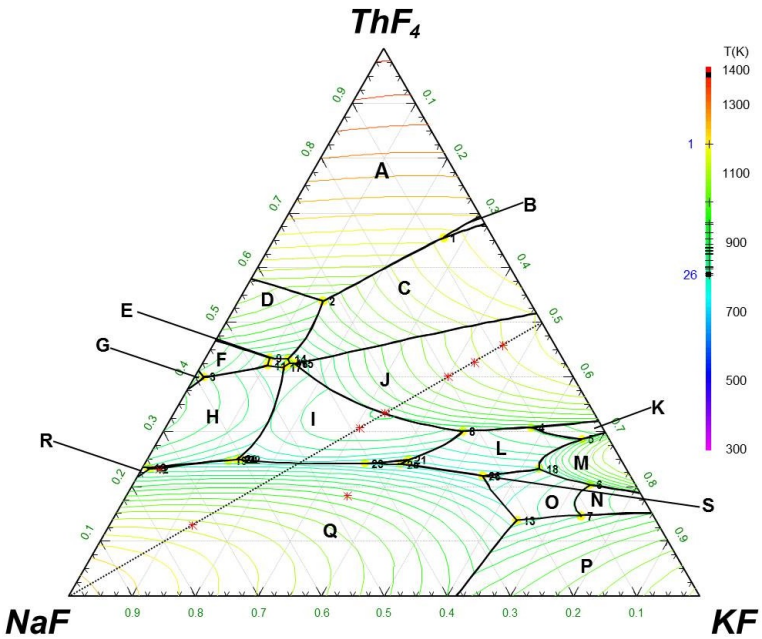

Figure 2.16: Liquidus projection and primary crystallization fields of the NaF-KF-ThF_4 system as calculated in this study. The spacing between the isotherms is 25 K. Experimental points: (*). The dashed line is the pseudobinary section shown in Figure 2.14. Primary crystallization phase fields: (A) $(Na_xTh_{1-x})F_{4-3x}$; (B) KTh_6F_{25}; (C) KTh_2F_9; (D) $NaTh_2F_9$; (E) $NaThF_5$; (F) $Na_7Th_6F_{31}$; (G) $Na_3Th_2F_{11}$; (H) Na_2ThF_6; (I) β-$KNaThF_6$; (J) $K_7Th_6F_{31}$; (K) β-K_2ThF_6; (L) α-K_2ThF_6; (M) K_3ThF_7; (N) β-K_5ThF_9; (O) α-K_5ThF_9; (P) (Na,K)F; (Q) NaF; (R) Na_4ThF_8; (S) α-$KNaThF_6$.

Table 2.14: Invariant equilibrium data calculated in the NaF-KF-ThF_4 system.

X(ThF_4)	X(NaF)	X(KF)	T_{calc} / K	Equilibrium	Solid phases present
0.654	0.078	0.268	1185.3	Quasi-peritectic	KTh_6F_{25} + KTh_2F_9 + $(Na_xTh_{1-x})F_{4-3x}$
0.538	0.327	0.135	1017.7	Quasi-peritectic	KTh_2F_9 + $NaTh_2F_9$ + $(Na_xTh_{1-x})F_{4-3x}$
0.399	0.587	0.014	954.7	Quasi-peritectic	Na_2ThF_6 + $Na_3Th_2F_{11}$ + $Na_7Th_6F_{31}$
0.301	0.100	0.599	952.9	Saddle point	α-K_2ThF_6 + β-K_2ThF_6
0.308	0.112	0.580	952.0	Quasi-peritectic	α-K_2ThF_6 + β-K_2ThF_6 +$K_7Th_6F_{31}$
0.285	0.044	0.671	952.0	Quasi-peritectic	α-K_2ThF_6 + β-K_2ThF_6 +K_3ThF_7
0.187	0.093	0.720	927.9	Saddle point	α-K_5ThF_9 + β-K_5ThF_9
0.204	0.071	0.725	926.0	Peritectic	α-K_5ThF_9 + β-K_5ThF_9 + K_3ThF_7
0.147	0.114	0.739	926.0	Quasi-peritectic	α-K_5ThF_9 + β-K_5ThF_9 + (Na,K)F
0.300	0.225	0.475	909.2	Peritectic	$K_7Th_6F_{31}$ + β-$KNaThF_6$ + α-K_2ThF_6
0.331	0.511	0.158	900.1	Saddle point	Na_2ThF_6 + β-$KNaThF_6$
0.434	0.465	0.101	892.8	Peritectic	$Na_7Th_6F_{31}$ + $NaTh_2F_9$ + $NaThF_5$
0.233	0.759	0.008	884.3	Quasi-peritectic	Na_2ThF_6 + Na_4ThF_8 + $Na_7Th_2F_15$
0.421	0.474	0.105	883.2	Quasi-peritectic	Na_2ThF_6 + $Na_7Th_6F_{31}$ + $NaThF_5$
0.231	0.756	0.013	883.0	Quasi-peritectic	Na_4ThF_8 + $Na_7Th_2F_15$ + NaF
0.138	0.220	0.642	882.5	Quasi-peritectic	NaF + α-K_5ThF_9 + (Na,K)F
0.432	0.436	0.132	873.4	Quasi-peritectic	KTh_2F_9 + $NaTh_2F_9$ + $NaThF_5$
0.242	0.535	0.223	842.0	Saddle point	β-$KNaThF_6$ + NaF
0.424	0.429	0.147	872.9	Quasi-peritectic	KTh_2F_9 +$K_7Th_6F_{31}$ + β-$KNaThF_6$
0.425	0.437	0.138	866.2	Quasi-peritectic	$NaThF_5$ + KTh_2F_9 + β-$KNaThF_6$
0.418	0.450	0.132	865.4	Quasi-peritectic	$NaThF_5$ +Na_2ThF_6 + β-$KNaThF_6$
0.232	0.137	0.631	846.2	Quasi-peritectic	α-K_2ThF_6 + α-K_5ThF_9 + K_3ThF_7
0.231	0.300	0.469	816.3	Saddle point	α-K_2ThF_6 + NaF
0.247	0.624	0.1129	829.2	Quasi-peritectic	Na_2ThF_6 + $Na_7Th_2F_15$ + NaF
0.248	0.337	0.415	825.0	Peritectic	α-$KNaThF_6$ + β-$KNaThF_6$ + α-K_2ThF_6
0.250	0.606	0.144	825.0	Quasi-peritectic	α-$KNaThF_6$ + NaF + β-$KNaThF_6$
0.248	0.601	0.151	825.0	Quasi-peritectic	α-$KNaThF_6$ + NaF + β-$KNaThF_6$
0.241	0.411	0.348	825.0	Eutectic	α-$KNaThF_6$ + β-$KNaThF_6$ + NaF
0.249	0.608	0.143	822.1	Eutectic	α-$KNaThF_6$ + Na_2ThF_6 + NaF
0.241	0.353	0.406	808.1	Quasi-peritectic	α-$KNaThF_6$ + α-K_2ThF_6 + NaF
0.219	0.234	0.547	804.3	Eutectic	α-K_2ThF_6 + α-K_5ThF_9 + NaF

Table 2.15: Calculated vs. experimental liquidus temperatures in the NaF-KF-ThF_4 system.

X(ThF_4)[a]	X(NaF)[a]	X(KF)[a]	Equilibrium Reaction	T_{calc} / K	T^b_{exp} / K
0.307	0.386	0.307	L' + β-$KNaThF_6$ = L	943	986
0.130	0.739	0.131	NaF + L' = L	1133	1096
0.230	0.741	0.029	NaF + L' = L	893	888
0.334	0.332	0.334	L' + $K_7Th_6F_{31}$ = L	950	-
0.183	0.467	0.350	NaF + L' = L	995	977
0.401	0.199	0.400	L' + $K_7Th_6F_{31}$ = L	1082	1136
0.428	0.143	0.430	L' + $K_7Th_6F_{31}$ = L	1117	1153
0.459	0.082	0.459	L' + $K_7Th_6F_{31}$ = L	1148	1163

[a]Standard composition error is $u(||(X(ThF_4), X(NaF), X(KF))||) = 0.006$.

[b]Standard uncertainties u are u(T)=10 K.

The pressure was (0.10 ± 0.01) MPa.

Table 2.16: Phase diagram equilibria of the NaF-KF-ThF_4 system as measured in this study by DSC.

X(ThF_4)[a]	X(NaF)[a]	X(KF)[a]	T_{exp} / K[b]	Equilibrium	Equilibrium Reaction
0.307	0.386	0.307	827	$KNaThF_6$ transition	α-K_2ThF_6 = β-K_2ThF_6
			986	Liquidus	L' + β-$KNaThF_6$ = L
0.130	0.739	0.131	848	Eutectic	NaF + β-$KNaThF_6$ = L
			1096	Liquidus	NaF + L' = L
0.230	0.741	0.029	802	Eutectoid	$Na_7Th_2F_15$ = NaF + Na_2ThF_6
			888	Liquidus	NaF + L' = L
0.334	0.332	0.334	825	$KNaThF_6$ transition	α-K_2ThF_6 = β-K_2ThF_6
			948	Peritectic	β-K_2ThF_6 = L + $K_7Th_6F_{31}$
0.183	0.467	0.350	819	$KNaThF_6$ transition	α-K_2ThF_6 = β-K_2ThF_6
			866	K_2ThF_6 transition	α-K_2ThF_6 = β-K_2ThF_6
			977	Liquidus	NaF + L' = L
0.401	0.199	0.400	931	Peritectic	β-K_2ThF_6 = L + $K_7Th_6F_{31}$
			1136	Liquidus	L' + $K_7Th_6F_{31}$ = L
0.428	0.143	0.430	821	$KNaThF_6$ transition	α-$KNaThF_6$ = β-$KNaThF_6$
			1104	Quasi-peritectic	L' + KTh_2F_9 + $K_7Th_6F_{31}$ = L + $K_7Th_6F_{31}$
			1153	Liquidus	L' + $K_7Th_6F_{31}$ = L
0.459	0.080	0.459	839	$KNaThF_6$ transition	α-K_2ThF_6 = β-K_2ThF_6
			1116	Quasi-peritectic	L' + KTh_2F_9 + $K_7Th_6F_{31}$ = L + $K_7Th_6F_{31}$
			1163	Liquidus	L' + $K_7Th_6F_{31}$ = L

[a]Standard composition error is $u(||(X(ThF_4), X(NaF), X(KF))||) = 0.006$.

[b]Standard uncertainties u are u(T)=10 K.

The pressure was (0.10 ± 0.01) MPa.

2.6. CONCLUSIONS

A thermodynamic assessment for the KF-ThF_4 binary system using the CALPHAD method is reported for the first time in combination with XRD and calorimetric measurements. The main characteristics of the sytem are: i) two allotropes of K_5ThF_9, ii) formation of K_2ThF_6, with both low and high temperature phases, instead of $K_3Th_2F_{11}$ as reported earlier [16], iii) a eutectoid decomposition for K_3ThF_7 at 856 K, iv) existence of the $K_7Th_6F_{31}$ phase instead of $KThF_5$ as previously reported [2, 16], v) congruent melting of KTh_2F_9, vi) existence of KTh_6F_{25} instead of KTh_3F_{13} as reported earlier [2], vii) no formation of solid solution. This new assessment, coupled with existing assessments of the LiF-KF, LiF-ThF_4, NaF-KF, and NaF-ThF_4 systems, was used to extrapolate and optimize the LiF-KF-ThF_4 and NaF-KF-ThF_4 ternary systems. The lowest melting point in the LiF-KF-ThF_4 system is calculated at (X(ThF_4, X(LiF), (X(KF)) = (0.023, 0.461, 0.516), T = 755 K. The lowest eutectic temperature in the NaF-KF-ThF_4 system is predicted to be 804 K, at composition (X(ThF_4, X(NaF), (X(KF)) = (0.219,0.234,0.547).

2.7. CREDIT AUTHOR STATEMENT

J.A. Ocádiz-Flores: Conceptualization, Methodology, Formal analysis, Investigation, Data Curation, Writing - Original Draft preparation, Visualization **E. Carré**: Data Curation, Investigation **J.-C. Griveau**: Investigation **E. Colineau**: Investigation **E. Capelli**: Verification **P. Souček**: Resources **O. Beneš**: Resources, Writing- Review & Editing **R.J.M. Konings**: Writing - Review & Editing **A.L. Smith**: Conceptualization, Resources, Writing - Review & Editing, Supervision, Project Administration, Funding acquisition

2.8. ACKNOWLEDGEMENTS

A.L. Smith acknowledges financial support from the Netherlands Organisation for Scientific Research (NWO) (project 722.016.005).

A.1. PREVIOUS PHASE DIAGRAMS OF KF-ThF_4 REPORTED IN THE LITERATURE

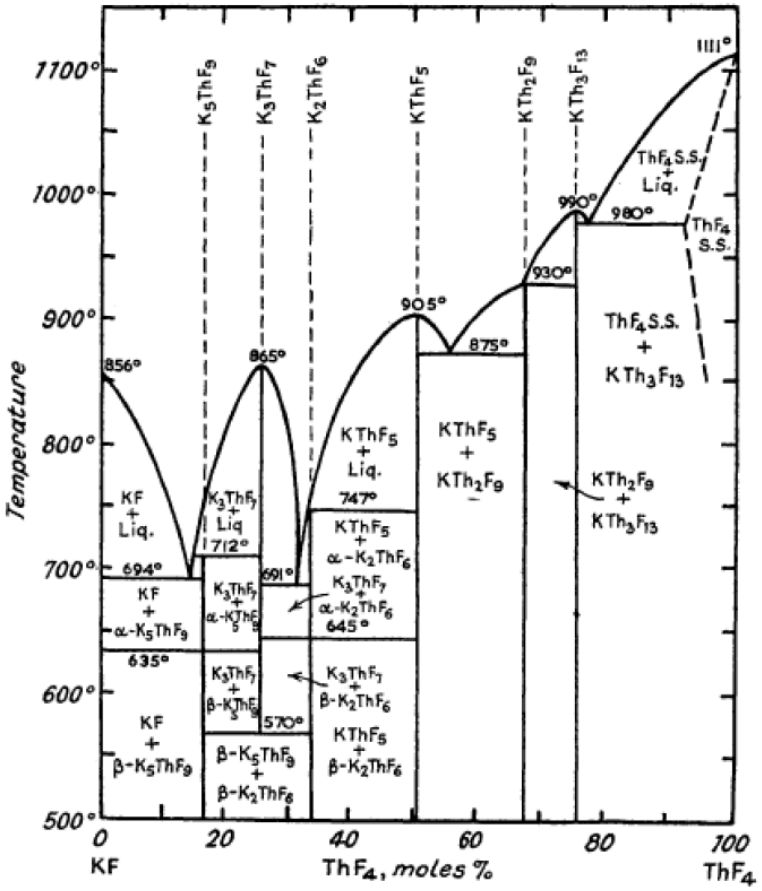

Figure A.1: KF-ThF_4 phase diagram reported by Asker et al. [2], reproduced with permission from the Royal Society of Chemistry.

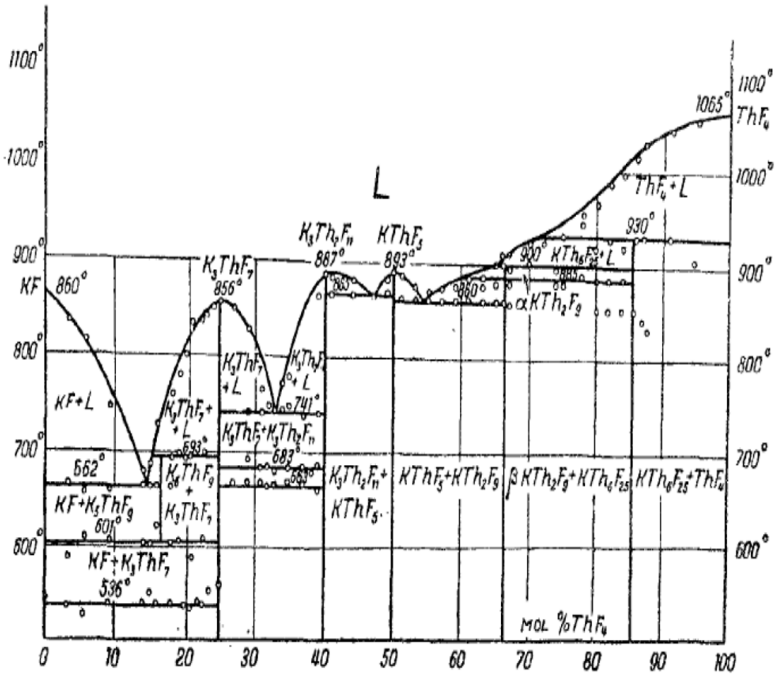

Figure A.2: KF-ThF_4 phase diagram reported by Emelyanov and Evstyukhin [16]. Reproduced with permission from Springer.

A.2. THERMODYNAMIC DATA FOR $KNaThF_6$

As mentioned in Section 7.2, Mukherjee and Dash characterized the properties of $KNaThF_6$ by means of DSC to derive the heat capacity and solid electrolyte galvanic cell to derive the Gibbs energy of formation [30]. Herein we describe our recalculation of the standard enthalpy of formation and standard entropy based on the data published by the authors [30] and carefully selected auxiliary data.

The solid electrolyte galvanic cell used by Mukherjee and Dash can be described by:

$$\begin{aligned}(-)Pt,\{ThOF_2(cr)+KNaThF_6(cr)+NaF(cr)\\ +KF(cr)\}|CaF_2(cr)|\{NiO(cr)+NiF_2(cr)\},Pt(+)\end{aligned} \tag{A.1}$$

The reaction at the cathode is:

$$NiF_2(cr)+\frac{1}{2}O_{2(g)}+2e^- = NiO(cr)+2F^- \tag{A.2}$$

and at the anode:

$$KF(cr)+NaF(cr)+ThOF_2(cr)+2F^- = KNaThF_6(cr)+\frac{1}{2}O_{2(g)}+2e^- \tag{A.3}$$

with the net reaction being:

$$KF(cr)+NaF(cr)+ThOF_2(cr)+NiF_2(cr) = KNaThF_6(cr)+NiO(cr) \tag{A.4}$$

The authors measured the electromotive force (e.m.f) as a function of temperature and found linear relationships with two different slopes, corresponding to the two phases of $KNaThF_6(cr)$ [30]: one in the interval 773-848 K and one in the interval 848-973 K. In the lower temperature range of 773-848 K, the following expression was reported:

$$E(T)/V \pm 0.0014 = 0.2772 - 1.586 \cdot 10^{-5} \cdot (T/K)\ (773-848)\,K \tag{A.5}$$

with the associated Gibbs energy of reaction given by:

$$\Delta_r G^{o}_{m}(T) \pm 0.02\,kJ\,mol^{-1} = -53.5 + 0.031 \cdot (T/K)\ (773-848)\,K \tag{A.6}$$

Using carefully selected data reported in the literature (Table A.1, [14], [18], [36]), the Gibbs energy of formation of $KNaThF_6$ is derived as:

Table A.1: Standard molar Gibbs energies of formation of compounds in Eq. (A.4) expressed as $\Delta_f G^{o}_{m}$(T) (kJ·mol^{-1}) = $A + B \cdot T(K)$

Compound	A / kJ·mol^{-1}	B / kJ·K^{-1}·mol^{-1}
$ThOF_2$	-1654.7	0.232
NaF	-575.7	0.1026
KF	-567.9	0.1012
NiF_2	-655.05	0.155
NiO	-238.33	0.0918

$$\Delta_f G^{o}_{m}(KNaThF_6, cr, T) = -3268.52 + 0.5023\ (773-848)K \tag{A.7}$$

Applying the second law of thermodynamics, the enthalpy of formation and entropy of $KNaThF_6$ are deduced at the average measurement temperature (811 K). Having derived $\Delta_f H^o_m(811K)$ and $\Delta_f S^o_m(811K)$, the values at 298.15 K are estimated from the enthalpy increment $\Delta_f H^o_m(T_{ave})$ - $\Delta_f H^o_m(298K)$ calculated with the heat capacity data as given by the Neumann-Kopp rule. Finally, the auxiliary data of the constituent elements of $KNaThF_6$ in Eq. (A.4) can be used again, to obtain $S^o(KNaThF_6, cr, 298K)$. The values so derived are: $\Delta_f H^{o}_{m}(KNaThF_6, cr, 298K) = -(3282 \pm 30)$ kJ·mol^{-1}, $S^{o}_{m}(KNaThF_6, cr, 298K)$ = (253.5 $\pm$ 4) J·K^{-1}· mol^{-1}.

A.3. LATTICE PARAMETERS OF RIETVELD AND LEBAIL REFINEMENTS

Table A.2 lists the lattice parameters of different intermediate phases as refined in this work, as well as a comparison with the literature values and the corresponding space groups.

Table A.2: Experimental lattice parameters of pure phases and mixtures obtained with Rietveld or LeBail refinements at 0.10 ± 0.005 MPa. RT = (293 ± 5) K.

Phases	Composition[a]	a[b] / nm	b[b] /nm	c[b] /nm	α, β, γ [o]	Space Group	Density[c] / $g \cdot cm^{-3}$	Literature data / $g \cdot cm^{-3}$
K_5ThF_9	$X(ThF_4) = 0.167$	0.7848	1.2840	1.0785	$\alpha = \beta = \gamma = 90$	$Cmc2_1$	3.66 ± 0.01	3.66 [39]
K_5ThF_9	$X(ThF_4) = 0.25$	0.7846	1.2858	1.0780	$\alpha = \beta = \gamma = 90$	$Cmc2_1$	3.66 ± 0.01	3.66 [39]
K_2ThF_6	$X(ThF_4) = 0.25$	0.6596	0.6596	0.3862	$\alpha = \beta = 90, \gamma = 120$	$P\bar{6}2m$	4.84 ± 0.02	4.95 [51]
K_2ThF_6	$X(ThF_4) = 0.33$	0.6579	0.6579	0.3824	$\alpha = \beta = 90, \gamma = 120$	$P\bar{6}2m$	4.92 ± 0.01	
K_2ThF_6	$X(ThF_4) = 0.418$	0.6576	0.6576	0.3825	$\alpha = \beta = 90, \gamma = 120$	$P\bar{6}2m$	4.92 ± 0.01	
$K_7Th_6F_{31}$	$X(ThF_4) = 0.418$	1.5346	1.5346	1.0511	$\alpha = \beta = 90, \gamma = 120$	$R\bar{3}h$	5.24 ± 0.01	5.31 [22]
KTh_2F_9	$X(ThF_4) = 0.857$	0.8843	1.1602	0.7185	$\alpha = \beta = \gamma = 90$	Pnma	6.07 ± 0.3	6.08 [51]
KTh_6F_{25}	$X(ThF_4) = 0.857$	0.8326	0.8326	1.6828	$\alpha = \beta = 90, \gamma = 120$	$P6_3mmc$	6.26 ± 0.01	6.29 [51]

A.4. EXPERIMENTAL HEAT CAPACITY DATA AND STANDARD THERMODYNAMIC FUNCTIONS FOR K_2ThF_6

Table A.3: Experimental heat capacity data[a] for K_2ThF_6 measured at p=1.25 mPa[b] and magnetic field B = 0 T.

T/K	$C_{p,m}(J\cdot K^{-1}\cdot mol^{-1})$	T/K	$C_{p,m}(J\cdot K^{-1}\cdot mol^{-1})$	T/K	$C_{p,m}(J\cdot K^{-1}\cdot mol^{-1})$
297.03	189.74	183.74	170.36	70.25	77.18
295.03	190.82	181.72	169.64	68.21	74.56
293.01	191.01	179.69	168.78	66.18	71.68
290.97	190.53	177.67	168.05	64.15	68.82
288.95	189.59	175.63	167.14	62.11	65.97
286.92	189.03	173.61	166.28	60.08	63.16
284.90	188.68	171.58	165.22	57.90	60.26
282.88	188.35	169.55	164.41	55.74	57.49
280.85	188.25	167.52	163.57	53.74	54.52
278.84	188.17	165.49	162.54	51.71	51.50
276.82	188.45	163.47	161.54	49.68	48.40
274.80	188.42	161.44	160.50	47.66	45.40
272.79	188.14	159.40	159.38	45.63	42.40
270.75	188.11	157.38	158.39	45.72	42.29
268.73	188.43	155.35	157.24	45.37	41.90
266.72	188.03	153.32	156.14	45.06	41.43
264.70	187.97	151.29	155.07	44.70	40.96
262.68	187.89	149.26	153.99	44.37	40.49
260.66	187.52	147.22	152.74	44.03	39.90
258.64	187.11	145.19	151.37	43.72	39.39
256.61	186.78	143.16	150.03	43.35	38.94
254.58	186.90	141.33	148.26	43.02	38.45
252.56	186.88	139.24	146.86	42.69	37.97
250.55	186.43	137.27	145.46	42.35	37.39
248.52	186.30	135.19	144.28	42.01	36.90
246.49	185.92	133.16	143.36	41.67	36.43
244.46	185.84	131.13	142.04	41.34	35.96
242.43	185.62	129.10	140.29	41.00	35.48
240.41	185.24	127.07	138.50	40.66	35.03
238.38	185.11	125.04	136.69	40.33	34.46
236.35	184.82	123.01	134.92	39.99	33.99
234.32	184.36	120.99	133.24	39.66	33.52
232.30	184.07	118.96	131.32	39.32	33.04
230.27	183.51	116.93	129.37	38.98	32.58
228.25	183.28	114.89	127.37	38.65	32.10
226.23	182.86	112.86	125.17	38.33	31.52
224.21	182.30	110.83	122.95	37.99	31.06
222.19	181.75	108.80	120.81	37.64	30.58
220.16	181.32	106.78	118.68	37.30	30.15
218.14	180.88	104.75	116.36	36.96	29.68
216.12	180.59	102.72	114.16	36.53	29.14
214.09	180.23	100.70	111.71	36.22	28.79
212.06	179.77	98.67	109.43	35.87	28.22
210.04	179.20	96.64	107.12	35.61	27.78
208.02	178.71	94.60	104.33	35.18	27.31
206.00	178.30	92.58	102.10	34.85	26.87
203.98	177.51	90.55	99.94	34.54	26.44
201.96	177.17	88.51	97.50	34.28	25.95
199.94	176.33	86.48	95.04	33.83	25.41
197.92	175.67	84.45	92.73	33.59	24.97
195.89	175.08	82.42	90.57	33.14	24.50
193.87	174.41	80.38	88.56	32.93	23.97
191.84	173.67	78.35	86.30	32.58	23.40
189.81	172.75	76.32	83.97	32.21	22.85
187.79	171.86	74.29	81.66	31.89	22.44
185.77	171.21	72.26	79.47	31.55	22.00

[a]The standard uncertainties u on the temperature are:
$u(T)$=0.01 K for 1.9 < T/K < 20, $u(T)$=0.02 K for 20<T/K<100,
$u(T)$=0.05 K for 100 < T/K< 300.
The relative standard uncertainties on the values of the heat capacities are determined to be $u_r(C_{p,m})$=0.03 for T/K < 15, $u_r(C_{p,m})$=0.02 for 15 < T/K < 70, $u_r(C_{p,m})$=0.04 for 70 < T/K < 120, $u_r(C_{p,m})$=0.01 for 120 < T < 270 K, and $u_r(C_{p,m})$=0.02 for T > 270 K.
[b]The standard uncertainty on the pressure is u(p) = 0.01 mPa.

Table A.4: Experimental heat capacity data[a] for K_2ThF_6 measured at p=1.25 mPa[b] and magnetic field B= 0 T (*continued*).

T/K	$C_{p,m}$(J·K^{-1}·mol^{-1})	T/K	$C_{p,m}$(J·K^{-1}·mol^{-1})	T/K	$C_{p,m}$(J·K^{-1}·mol^{-1})
31.21	21.57	12.23	2.482	6.072	0.3053
30.87	21.14	11.89	2.300	5.989	0.2924
30.53	20.61	11.55	2.128	5.904	0.2803
30.20	20.18	11.21	1.961	5.820	0.2681
29.86	19.76	10.87	1.773	5.735	0.2568
29.52	19.35	10.53	1.620	5.651	0.2462
29.18	18.92	10.19	1.478	5.561	0.2339
28.84	18.42	10.18	1.472	5.478	0.2236
28.50	18.00	10.10	1.443	5.393	0.2136
28.17	17.61	10.02	1.408	5.309	0.2044
27.82	17.18	9.936	1.378	5.224	0.1948
27.49	16.77	9.852	1.343	5.139	0.1857
27.15	16.38	9.767	1.312	5.055	0.1773
26.82	15.90	9.683	1.279	4.972	0.1685
26.47	15.51	9.598	1.248	4.887	0.1601
26.14	15.11	9.515	1.215	4.801	0.1523
25.80	14.73	9.431	1.185	4.717	0.1447
25.46	14.36	9.349	1.155	4.632	0.1371
25.12	14.01	9.264	1.124	4.548	0.1303
24.78	13.63	9.179	1.096	4.463	0.1235
24.44	13.17	9.096	1.038	4.379	0.1168
24.10	12.79	9.006	1.008	4.294	0.1104
23.75	12.42	8.924	0.9823	4.209	0.1046
23.42	12.06	8.839	0.9555	4.124	0.0986
23.07	11.72	8.757	0.9300	4.041	0.0928
22.73	11.37	8.672	0.9047	3.957	0.0874
22.39	10.94	8.591	0.8792	3.872	0.0823
22.05	10.58	8.505	0.8532	3.787	0.0773
21.71	10.23	8.422	0.8289	3.702	0.0725
21.37	9.891	8.338	0.8047	3.617	0.0681
21.05	9.566	8.254	0.7814	3.534	0.0641
20.69	9.165	8.170	0.7581	3.450	0.0603
20.37	8.854	8.085	0.7353	3.366	0.0565
20.01	8.534	8.002	0.7129	3.276	0.0529
19.70	8.238	7.918	0.6905	3.190	0.0492
19.34	7.909	7.834	0.6685	3.104	0.0459
19.02	7.563	7.749	0.6464	3.018	0.0429
18.66	7.245	7.666	0.6248	2.933	0.0399
18.33	6.959	7.582	0.6041	2.848	0.0373
18.00	6.696	7.497	0.5835	2.764	0.0348
17.65	6.396	7.413	0.5636	2.679	0.0327
17.31	6.116	7.330	0.5441	2.594	0.0304
16.98	5.786	7.244	0.5247	2.509	0.0282
16.64	5.525	7.161	0.5061	2.423	0.0259
16.29	5.264	7.097	0.4924	2.338	0.0242
15.96	5.007	7.002	0.4725	2.253	0.0225
15.62	4.754	6.917	0.4551	2.167	0.0207
15.28	4.508	6.833	0.4382	2.082	0.0190
14.94	4.219	6.749	0.4215	1.999	0.0175
14.60	3.986	6.666	0.4052	1.915	0.0162
14.26	3.760	6.581	0.3895	1.830	0.0149
13.93	3.537	6.497	0.3753		
13.59	3.323	6.413	0.3614		
13.25	3.113	6.329	0.3469		
12.92	2.867	6.242	0.3317		
12.57	2.671	6.156	0.3183		

[a]The standard uncertainties u on the temperature are:
[a] $u(T)$=0.01 K for 1.9 < T/K < 20, $u(T)$=0.02 K for 20<T/K<100,
[a] $u(T)$=0.05 K for 100 < T/K< 300.
The relative standard uncertainties on the values of the heat capacities are determined to be $u_r(C_{p,m})$=0.03 for T/K < 15, $u_r(C_{p,m})$=0.02 for 15 < T/K < 70, $u_r(C_{p,m})$=0.04 for 70 < T/K < 120, $u_r(C_{p,m})$=0.01 for 120 < T < 270 K, and $u_r(C_{p,m})$=0.02 for T > 270 K.
[b]The standard uncertainty on the pressure is u(p) = 0.01 mPa.

Table A.5: Standard thermodynamic functions for K_2ThF_6 at pressure p = 100 kPa. $\phi^o_m(T)$=$S^o_m(T) - [H^o_m(T) - H^o_m(0)]/T$.[a]

T/K	$C^o_{p,m}(T/K)/$ (J·K^{-1}·mol^{-1})	$S^o_m(T/K)/$ (J·K^{-1}·mol^{-1})	$H^o_m(T/K) - H^o_m(0)/$ (kJ·mol^{-1})	$\phi^o_m(T/K)/$ (J·K^{-1}·mol^{-1})
0	0	0	0	–
0.5	2.0800E-03	1.8000E-03	5.04E-07	7.8911E-04
1	5.0000E-03	4.0700E-03	2.23E-06	1.8400E-03
2	0.01681	0.01077	1.31E-05	4.2100E-03
3	0.04276	0.02210	4.29E-05	7.8000E-03
4	0.09114	0.04062	1.10E-04	0.01315
5	0.17144	0.06916	2.41E-04	0.02093
6	0.29413	0.11081	4.74E-04	0.03182
7	0.47013	0.16890	8.56E-04	0.04661
8	0.70965	0.24684	0.00145	0.06609
9	1.0203	0.34787	0.00231	0.09110
10	1.4047	0.47479	0.00352	0.12245
11	1.8475	0.62900	0.00515	0.16086
12	2.3628	0.81143	0.00725	0.20687
13	2.9447	1.0231	0.00991	0.26095
14	3.5882	1.2645	0.01317	0.32348
15	4.2883	1.5356	0.01711	0.39476
16	5.0402	1.8361	0.02178	0.47500
17	5.8403	2.1654	0.02722	0.56433
18	6.6861	2.5229	0.03348	0.66282
19	7.5759	2.9080	0.04061	0.77049
20	8.5088	3.3200	0.04865	0.88733
25	13.800	5.7679	0.10402	1.6073
30	20.023	8.8216	0.18825	2.5465
35	26.881	12.417	0.30532	3.6933
40	34.064	16.473	0.45761	5.0325
45	41.364	20.906	0.64615	6.5466
50	48.679	25.642	0.87127	8.2168
55	55.963	30.624	1.13289	10.026
60	63.183	35.803	1.43079	11.957
65	70.307	41.142	1.76456	13.995
70	77.295	46.609	2.13363	16.129
75	84.106	52.175	2.53721	18.346
80	90.703	57.815	2.97432	20.636
85	97.054	63.506	3.44382	22.990
90	103.13	69.227	3.9444	25.400
95	108.92	74.959	4.47466	27.858
100	114.42	80.687	5.03313	30.356
110	124.51	92.075	6.22872	35.450
120	133.44	103.30	7.51937	40.638
130	141.30	114.30	8.89389	45.883
140	148.19	125.03	10.34208	51.154
150	154.23	135.46	11.85485	56.429
160	159.53	145.59	13.42423	61.686
170	164.18	155.40	15.04329	66.912
180	168.28	164.90	16.70603	72.093
190	171.89	174.10	18.40726	77.222
200	175.10	183.00	20.14253	82.289
210	177.94	191.61	21.90797	87.291
220	180.47	199.95	23.70024	92.224
230	182.73	208.03	25.51644	97.084
240	184.76	215.85	27.35407	101.87
250	186.58	223.43	29.21093	106.58
260	188.23	230.78	31.0851	111.22
270	189.71	237.91	32.97491	115.78
273.15	190.15	240.11	33.57319	117.20
280	191.06	244.83	34.87887	120.26
290	192.29	251.56	36.79569	124.68
298.15	193.20	256.90	38.3666	128.22
300	193.40	258.10	38.72421	129.02

[a]The relative combined standard uncertainties in the values of the fitted heat capacities are determined from the experimental and fitted uncertainties to be $u_r(C_{p,m})$=0.031 for T/K < 15, $u_r(C_{p,m})$=0.021 for 15 < T/K < 70, $u_r(C_{p,m})$=0.041 for 70 < T/K < 120, $u_r(C_{p,m})$=0.011 for 120 < T < 270 K, and $u_r(C^o_{p,m})$=0.021 for 270 < T/K.

A.5. REPRESENTATIVE DSC CURVES

This section contains representative examples of DSC measurements carried out in this work and how the data were extracted. Figure A.3 is a DSC heating ramp with two event corresponding to eutectic and liquidus temperatures. The intersection between the baseline and the line tangent to the first inflection point of a given event is the onset temperature, T_{onset}, and the temperature assigned to all events except for the liquidus of mixtures. The intersection between the baseline and the line tangent to the second inflection point of a given event is the offset temperature, T_{offset}. In this work, the minimum of the peak, T_min, was chosen as the liquidus temperature except for congruent melting. Nevertheless, onset temperatures are also drawn in Fig. 2.11 as ($\triangledown$, red) for the liquidus events to illustrate this choice as a likely source of disagreement with previous authors.
Figure A.4 overlays the heating curve of ThF_4 when it is being melted for the first time with the curve of the same ThF_4 sample as it undergoes a second heating cycle, showing that the heat capacity remains the same before and after melting.
Finally, Fig. A.5 is a representative example of a measurement of the mixing enthalpy. The gray area is the mixing event. Note that the curve does not have the pseudo-gaussian shape of the other events in Figs. A.3, A.4, or A.5, but a slightly more complex shape which arises from the endothermic contribution of the melting of KF and ThF_4 and the simultaneous exothermic mixing. Still, as the shading indicates, the total area of the mixing event is measured the same way as for all the other events: as the area constrained by the baseline and the curve which departs from it. Since the areas have opposite signs, they partially cancel each other out, and this is taken into account. The second thermal event corresponds to the melting of the silver reference, after the mixing event has concluded, such that they are both well resolved. The fusion of silver is endothermic, yet appears as exothermic because the silver sits in the reference crucible. The superimposed red DSC curve corresponds to a heating ramp of pure ThF_4. Crucially, after the fusion of silver in the mixing enthalpy heating cycle there is no fusion event at the melting temperature of ThF_4; this is an indication of complete mixing. Data from mixing enthalpy measurements were only deduced for those runs which showed complete mixing.
For every run, a sensitivity could be assigned based on the heat measured on the silver reference, as mentioned in Section 2.2.5. The total heat measured during the event at the melting temperature of KF, $\Delta_{meas}H^o(T_{fus,KF})$, is given by:

$$\Delta_{meas}H^o(T_{fus,KF}) = S_{salt/Ag} \cdot \frac{Q_{meas}}{S_{Ag,i}} \tag{A.8}$$

where Q_{meas} is the heat measured per mole of sample during the mixing experiment, i.e. the gray area in Fig. A.5, $S_{salt/Ag}$ is the sensitivity coefficient determined during the calibration process, and $S_{Ag,i}$ is the sensitivity of silver during measurement i. Finally, the molar enthalpy of mixing can be derived based on Eq. 6.1.

Table A.6: Extended mixing enthalpy of the $(1-x)$KF(l) + $x$$ThF_4$(l*) system determined in this work at T = 1131 ± 10 K and (0.10 ± 0.01)[d] MPa. KF melts at the measurement temperature, while ThF_4 is solid, although the initial state is taken to be a hypothetical liquid. The final state was an undercooled liquid mixture. The scanning temperature range was from (303 ± 10) K to (1373 ± 10) K.

X(ThF_4)[a]	$\Delta_{mix}H_m^o$ [b] / kJ·mol^{-1}	m (KF) / mg[c]	m (ThF_4) / mg[c]	mass Ag_{ref} / mg[c]	$\Delta_{meas}H^o(T_{fus,KF})$ [b] / kJ·mol^{-1}
0.109	-15.0 ± 1.4	29.2	18.9	62.0	13.8 ± 1.4
0.200	-29.5 ± 1.8	23.6	31.3	61.9	0.1 ± 1.8
0.305	-30.3 ± 0.2	21.9	50.9	61.80	1.4 ± 0.2
0.338	-30.8 ± 1.0	14.9	40.4	129.0	1.3 ± 1.0
0.401	-31.7 ± 0.7	57.9	16.3	61.8	0.5 ± 0.7
0.504	-32.9 ± 3.0	39.3	7.3	61.7	1.7 ± 3.0

[a] Standard uncertainties u are u(X(ThF_4)) = 0.005.

[b] The error is based on the standard uncertainty determined during calibration.

[c] Standard uncertainties u are u(m) = 0.1 mg.

[d] The quoted uncertainty corresponds to the standard uncertainty.

* Indicates a hypothetical liquid state.

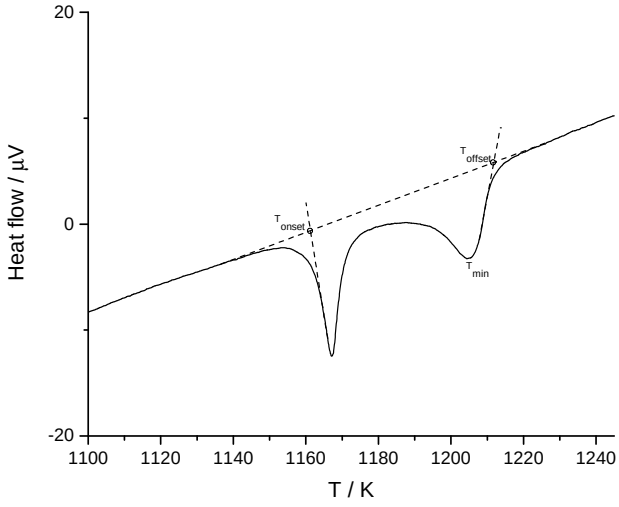

Figure A.3: Representative example of a DSC heating ramp indicating how T_{onset} and T_{offset} were determined. T_{min} was chosen as the liquidus temperature.

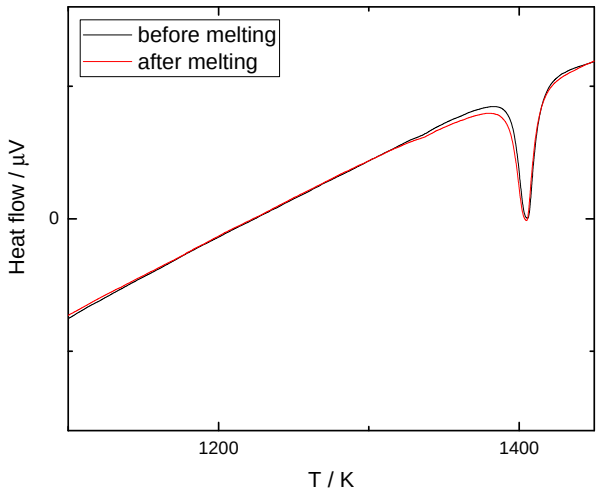

Figure A.4: DSC heating curve of pure ThF_4 the first time being melted (black, first heating cycle) compared to the second time (red, second heating cycle), showing the heat capacity does not change between cycles.

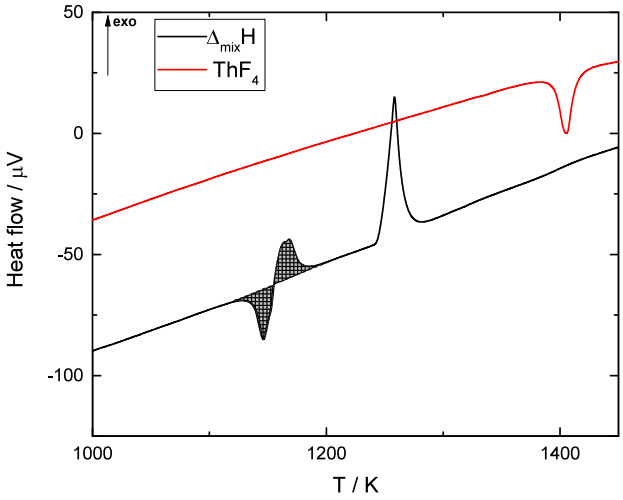

Figure A.5: Representative example of a mixing enthalpy measurement. Shaded area: [Melting of KF + melting of ThF_4 + mixing of KF with ThF_4]. Second event: melting of the silver reference. Red curve: heating cycle of pure ThF_4 compared against the mixing experiment.

A.6. EXCESS GIBBS ENERGY PARAMETERS OF THE CONSITUTENT BINARY LIQUID SOLUTIONS

The excess Gibbs energy parameters of the binary solutions needed to calculate the ternary systems were taken from existing assessments and are listed below for completeness.

$$\Delta g_{LiK/FF} = -7615 + 4.861 \cdot T - 0.001674 \cdot T^2 + (-958 + 1.255 \cdot T)\chi_{LiK/FF} + (-690 + 1.966 \cdot T)\chi_{KLi/FF} \; J \cdot mol^{-1} \quad (9)$$

(JRCSMSD thermodynamic database on halide salts, JRC-Karlsruhe.)

$$\Delta g_{LiTh/FF} = -10878 + (-6694 + 2.929 \cdot T)\chi_{LiTh/FF} + (-20920 + 19.46 \cdot T)\chi_{ThLi/FF} \; J \cdot mol^{-1} \quad (10)$$

(JRCSMSD thermodynamic database on halide salts, JRC-Karlsruhe.)

$$\Delta g_{NaK/FF} = -118 + 0.847 \cdot T \; J \cdot mol^{-1} \quad (11)$$

[4]

$\Delta g_{NaTh/FF} = -26784 + (10046 - 12.56 \cdot T)\chi_{NaTh/FF} + (-30106 + 16.74 \cdot T)\chi_{ThNa/FF}\ J \cdot mol^{-1}$ (12)

[13]

BIBLIOGRAPHY

[1] I. Ansara and B. Sundman. *Scientific Group Thermodata Europe, Computer Handling and Determination of Data*. North Holland, Amsterdam, 1986.

[2] W.J. Asker, E.R. Segnit, and A.W. Wylie. “857. The potassium thorium fluorides”. In: *Journal of the Chemical Society (Resumed)* (1952), pp. 4470–4479.

[3] C.W. Bale et al. “FactSage thermochemical software and databases, 2010–2016”. In: *Calphad* 54 (2016), pp. 35–53.

[4] O. Beneš. “Thermodynamics of molten salts for nuclear applications”. PhD thesis. Institute of Chemical Technology, Prague, 2008.

[5] O. Beneš, M. Beilmann, and R.J.M. Konings. “Thermodynamic assessment of the LiF–NaF–ThF_4–UF_4 system”. In: *Journal of Nuclear materials* 405.2 (2010), pp. 186–198.

[6] O. Beneš and R.J.M. Konings. “Thermodynamic evaluation of the MF–LaF_3 (M=Li, Na, K, Rb, Cs) systems”. In: *Calphad* 32.1 (2008), pp. 121–128.

[7] O. Beneš et al. “A DSC study of the $NaNO_3$–KNO_3 system using an innovative encapsulation technique”. In: *Thermochimica Acta* 509.1-2 (2010), pp. 62–66.

[8] C. Bessada et al. “Lanthanide and actinide speciation in molten fluorides: A structural approach by NMR and EXAFS spectroscopies”. In: *Journal of Nuclear Materials* 360.1 (2007), pp. 43–48.

[9] E. S. Bettis et al. “The aircraft reactor experiment—design and construction”. In: *Nuclear Science and Engineering* 2.6 (1957), pp. 804–825.

[10] W.J. Boettinger et al. “DTA and Heat-flux DSC measurements of alloy melting and freezing”. In: *Methods for Phase Diagram Determination*. Ed. by J.-C. Zhao. Oxford: Elsevier Science Ltd, 2007, pp. 151–221.

[11] G. Brunton. “The crystal structure of $K_7Th_6F_{31}$”. In: *Acta Crystallographica Section B* 27.11 (Nov. 1971), pp. 2290–2292.

[12] E. Capelli et al. “"Thermodynamic investigation of the LiF–ThF_4 system "”. In: *The Journal of Chemical Thermodynamics* 58 (2013), pp. 110–116.

[13] E. Capelli et al. “Thermodynamic assessment of the LiF–NaF–BeF_2–ThF_4–UF_4 system”. In: *Journal of Nuclear Materials* 449.1-3 (2014), pp. 111–121.

[14] M.W. Chase. *NIST-JANAF Thermochemical Tables (Journal of Physical and Chemical Reference Data Monograph No. 9)*. 1998.

[15] E.P. Dergunov and A.G. Bergman. “Complex formation between alkali metal fluorides and fluorides of metals of the fourth group”. In: *Doklady Akademii Nauk SSSR* 60.3 (1948), pp. 391–394.

[16] V.S. Emelyanov and A.I. Evstyukhin. “An investigation of fused-salt systems based on thorium fluoride-II”. In: *Journal of Nuclear Energy (1954)* 5.1 (1957), pp. 108–114.

[17] S.N. Flengas and A.S. Kucharski. “Theory of Enthalpy of Mixing in Reactive Charge Asymmetrical Molten Salt Systems. Part I. Binary Solutions”. In: *Canadian Journal of Chemistry* 49.24 (1971), pp. 3971–3985.

[18] H. Gamsjäger et al. *Chemical thermodynamics of nickel*. OECD Nuclear Energy Agency, Data Bank, Issy-les-Moulineaux (France), 2005.

[19] *GIF, Annual report 2013, Generation IV International Forum, Tech. Rep., www.gen-4.org/gif/upload/docs/application/pdf/2014-06/gif_2013_annual_report-final.pdf*. 2013.

[20] *GIF, Technology Roadmap Update for Generation IV Nuclear Energy Systems, Tech. Rep., www.gen-4.org/gif/upload/docs/application/pdf/2014-03/gif-tru2014.pdf*. 2014.

[21] E.S.R. Gopal. *Specific Heats at Low Temperatures (International Cryogenics Monograph Series)*. 1966.

[22] A. Grzechnik et al. “Crystal structures and stability of K_2ThF_6 and $K_7Th_6F_{31}$ on compression”. In: *Journal of Fluorine Chemistry* 150 (2013), pp. 8–13.

[23] P.N. Haubenreich and J.R. Engel. “Experience with the molten-salt reactor experiment”. In: *Nuclear Technology* 8.2 (1970), pp. 118–136.

[24] P. Javorsk et al. “Low-temperature heat capacity measurements on encapsulated transuranium samples”. In: *Journal of Nuclear Materials* 344.1-3 (2005), pp. 50–55.

[25] R.J.M. Konings, J.P.M. Van der Meer, and E. Walle. “Chemical Aspects of Molten Salt Reactor Fuel”. In: *European Commission Joint Research Centre* (2005).

[26] JC Lashley et al. “Critical examination of heat capacity measurements made on a Quantum Design physical property measurement system”. In: *Cryogenics* 43.6 (2003), pp. 369–378.

[27] J. Leitner et al. “Application of Neumann–Kopp rule for the estimation of heat capacity of mixed oxides”. In: *Thermochimica Acta* 497.1-2 (2010), pp. 7–13.

[28] H.L. Lukas, S.G. Fries, and B. Sundman. *Computational Thermodynamics. The Calphad Method*. Cambridge University Press, 2007.

[29] J. Majzlan et al. “Phonon, spin-wave, and defect contributions to the low-temperature specific heat of α-FeOOH”. In: *Journal of low temperature physics* 130.1-2 (2003), pp. 69–76.

[30] S. Mukherjee and S. Dash. “Thermodynamic properties of complex fluoride in KF–NaF–ThF4 system”. In: *Journal of Radioanalytical and Nuclear Chemistry* 313.3 (Sept. 2017), pp. 481–486.

[31] J.A. Ocádiz-Flores et al. “Thermodynamic assessment of the KF-ThF_4, LiF-KF-ThF_4 and NaF-KF-ThF_4 systems”. In: *The Journal of Chemical Thermodynamics* 145 (2020), p. 106069.

[32] O. Pauvert et al. “Ion Specific Effects on the Structure of Molten AF-ZrF4 Systems (A+ = Li+, Na+, and K+)”. In: *The Journal of Physical Chemistry B* 115.29 (2011). PMID: 21675783, pp. 9160–9167.

[33] A. D. Pelton et al. “"The modified quasichemical model I—Binary solutions"”. In: *Metallurgical and Materials Transactions B* 31.4 (2000), pp. 651–659.

[34] A.D. Pelton. “A general “geometric” thermodynamic model for multicomponent solutions”. In: *Calphad* 25.2 (2001), pp. 319–328.

[35] E. Rabani, J.D. Gezelter, and B.J. Berne. “Calculating the hopping rate for self-diffusion on rough potential energy surfaces: Cage correlations”. In: *The Journal of chemical physics* 107.17 (1997), pp. 6867–6876.

[36] M Rand et al. “Chemical Thermodynamics of Thorium (Chemical Thermodynamics”. In: *Paris: OCDE-NEA* (2008).

[37] C. Renault et al. “The Molten Salt Reactor (MSR) in Generation IV: Overview and Perspectives”. In: *GIF Symposium, Paris(France), 9-10 September 2009*. 2013, pp. 191–200.

[38] J. Rodriguez-Carvajal. “Recent advances in magnetic structure determination by neutron powder diffraction”. In: *Physica B* 192 (1993), pp. 55–69.

[39] R.R. Ryan and R.A. Penneman. “The crystal structure of potassium enneafluorothorate”. In: *Acta Crystallographica Section B* 27.4 (Apr. 1971), pp. 829–833.

[40] M. Salanne et al. “A First-Principles Description of Liquid BeF_2 and Its Mixtures with LiF: 2. Network Formation in LiF- BeF_2”. In: *The Journal of Physical Chemistry B* 110.23 (2006), pp. 11461–11467.

[41] M. Salanne et al. “Conductivity- Viscosity- Structure: Unpicking the Relationship in an Ionic Liquid”. In: *The Journal of Physical Chemistry B* 111.18 (2007), pp. 4678–4684.

[42] A.L. Smith et al. “Thermodynamic study of Cs 3 Na (MoO 4) 2: Determination of the standard enthalpy of formation and standard entropy at 298.15 K”. In: *The Journal of Chemical Thermodynamics* 120 (2018), pp. 205–216.

[43] S.J. Smith et al. “Heat capacities and thermodynamic functions of TiO2 anatase and rutile: Analysis of phase stability”. In: *American Mineralogist* 94.2-3 (2009), pp. 236–243.

[44] P. Souček et al. “Synthesis of UF_4 and ThF_4 by HF gas fluorination and re-determination of the UF4 melting point”. In: *Journal of Fluorine Chemistry* 200 (2017), pp. 33–40.

[45] R.E. Thoma. *Crystal Structures of Some Compounds of UF4 and ThF4 with Alkali Fluorides, ORNL-CF-58-12-40*. Tech. rep. Oak Ridge National Lab., Tenn., 1958.

[46] R.E. Thoma, H.A. Friedman, and R.A. Penneman. “Isomorphous Complex Fluorides of Tri-, Tetra-, and Pentavalent Uranium1”. In: *Journal of the American Chemical Society* 88.9 (1966), pp. 2046–2047.

[47] R.E. Thoma et al. “Phase Equilibria in the Alkali Fluoride-Uranium Tetrafluoride Fused Salt Systems: II, The Systems KF-UF_4 and RbF-UF_4”. In: *Journal of the American Ceramic Society* 41.12 (1958), pp. 538–544.

[48] N. Vozárová et al. “Thermodynamic determination and assessment of the CsF-ThF4 system”. In: *The Journal of Chemical Thermodynamics* 114 (2017), pp. 71–82.

[49] B.F. Woodfield et al. “Molar heat capacity and thermodynamic functions for $CaTiO_3$”. In: *The Journal of Chemical Thermodynamics* 31.12 (1999), pp. 1573–1583.

[50] B.F. Woodfield et al. “Molar heat capacity and thermodynamic functions of zirconolite $CaZrTi_2O_7$”. In: *The Journal of Chemical Thermodynamics* 31.2 (1999), pp. 245–253.

[51] W.H. Zachariasen. “Double fluorides of potassium or sodium with uranium, thorium or Lanthanum”. In: *Journal of the American Chemical Society* 70.6 (1948), pp. 2147–2151.

3

THERMODYNAMIC DESCRIPTION OF THE ACL-THCL$_4$ (A= LI, NA, K) SYSTEMS

The ACl-$ThCl_4$ (A = Li, Na, K) systems could be of relevance to the nuclear industry in the near future. A thermodynamic investigation of the three binary systems is presented herein. The excess Gibbs energy of the liquid solutions is described using the quasi-chemical formalism in the quadruplet approximation. The phase diagram optimizations are based on the experimental data available in the literature. The thermodynamic stability of the liquid solutions increases in the order Li < Na < K, in agreement with idealized interactions and structural models.

Jaén A. OCÁDIZ FLORES, Bas A.S. ROOIJAKKERS, Rudy J.M. KONINGS, Anna Louise SMITH

This chapter has been published in *Thermo*, 2021, **1(2)**, (122-133) [41].

3.1. INTRODUCTION

Glenn Seaborg called the discovery of ^{232}Th being a fertile isotope, yielding fissile ^{233}U after neutron absorption and subsequent decay, 'a fifty quadrillion discovery' [36] [32]. That notwithstanding, industrial use of thorium is still virtually nonexistent in modern-day society. If it is to fulfill its potential as a vastly abundant energy source, reactor and fuel cycle designs are needed that are optimised for the efficient breeding and utilisation of ^{233}U. Studies have shown that thorium can be used in a wide variety of reactors [25]. Therefore it is important to continue characterizing the thermophysical properties of the chemical forms it may take as an advanced nuclear fuel, e.g. metallic, oxide, nitride, or halide. As part of that effort, a thermodynamic description of the binary systems ACl-$ThCl_4$ (A = Li, Na, K) is presented herein, since these are systems from which metallic thorium powder may be produced [4], and because they may be part of a fuel matrix in a Molten Salt Reactor (MSR) [26]. Metal chlorides are receiving increasing attention in the MSR community, as they allow high loading of actinides compared to the more studied fluorides, although they are best suited for fast neutron systems.

Even though it has been the subject of several studies, $ThCl_4$ is not fully characterized. It has been reported to crystallize in two phases. The low-temperature phase is tetragonal in space group $I4S_1/a$, while the high-temperature phase belongs to space group $I4_1/amd$ [50]. The latter phase is metastable below the phase transition temperature, 679 K, and it is the one usually reported by experimentalists [38, 17, 53, 39, 8, 52]. The low-temperature phase has only been isolated by Mason et al. [37], who used a very slow cooling rate. For this reason, the recommended thermodynamic data in the literature is for the high-temperature polymorph. The value of the standard enthalpy of formation recommended by Fuger et al. [50] is an average of values determined via solution calorimetry [19, 21, 56]. The standard entropy was estimated by Konings considering lattice and electronic contributions [29], and the high-temperature heat capacity was estimated by Rand [2]. Intriguingly, there could also be a very low-temperature phase, below 70 K [27].
Some studies for the ACl-$ThCl_4$ (A = Li, Na, K) binary phase diagrams are available in the literature. Despite this and their apparent simplicity compared to their fluoride counterparts, their topology is not well-established to this date, however. In the LiCl-$ThCl_4$ system, Oyamada found no intermediate phase [43], yet Vokhmyakov et al. [61], Tanii [58], and Vdovenko et al.[1] [60] observed an incongruently melting compound of composition Li_4ThCl_8. In the NaCl-$ThCl_4$ system, all available sources agree on the existence of Na_2ThCl_6 and no other compound, but Vdovenko et al. [60] observed $NaThCl_5$ instead. Finally, in the KCl-$ThCl_4$ system, different groups report the existence of K_3ThCl_7, K_2ThCl_6, and $KThCl_5$. The observations are summarized in Table 1.

From these mixed accounts, it can be seen that there is a need for a comprehensive study to establish a coherent description of these phase diagrams. An interpretation of their most likely topology is put forward in this work, and CALPHAD models for their calculation are presented.

[1] Original work not available to us, but described in *The Chemistry of Actinide and Transactinide Elements* [16].

Table 1: Phases occurring in the alkali thorium chloride binary systems according to different sources.

System	Compounds	References
LiCl-$ThCl_4$	Li_4ThCl_8	[61, 58, 60]
	none	[43]
NaCl-$ThCl_4$	Na_2ThCl_6	[61, 58, 43]
	$NaThCl_5$	[60]
KCl-$ThCl_4$	K_3ThCl_7	[43, 22]
	K_2ThCl_6	[58, 22]
	$KThCl_5$	[22, 43]

3.2. THERMODYNAMIC MODELLING

3.2.1. PURE COMPOUNDS

The thermodynamic assessments were performed with the Factsage software [3] (Version 7.2). A thermodynamic assessment consists of optimizing unknown parameters related to the Gibbs energy functions of all the phases occurring in a system, in order to develop a thermodynamic model consistent with experimentally determined information such as phase diagram equilibria, thermodynamic data, enthalpies of fusion, vapor pressures, and activities. The Gibbs energy function of a pure end-member in a system is given by:

$$G^o(T) = \Delta_f H^{\mathrm{o}}_{\mathrm{m}}(298) - S^{\mathrm{o}}_{\mathrm{m}}(298)T + \int_{298}^{T} C^o_{\mathrm{p,m}}(T)dT - T\int_{298}^{T} \frac{C^o_{\mathrm{p,m}}(T)}{T}dT \tag{3.1}$$

where $\Delta_f H^{\mathrm{o}}_{\mathrm{m}}(298)$ is the standard enthalpy of formation, and $S^{\mathrm{o}}_{\mathrm{m}}(298)$ is the standard absolute entropy, both evaluated at a reference temperature, typically taken to be 298.15 K (denoted here as 298 K for simplicity). $C_{\mathrm{p,m}}$ is the isobaric heat capacity expressed as a polynomial:

$$C_{\mathrm{p,m}}(T) = a + bT + cT^2 + dT^{-2} \tag{3.2}$$

Isobaric heat capacity data is only available for the end-members. To estimate the heat capacities and standard entropies of intermediate compounds, the Neumann-Kopp rule [33] was applied.

The thermodynamic functions of LiCl(cr,l) and KCl(cr,l) were taken from SGPS [18]. Those of NaCl(cr,l) were taken from the IVTAN tables by Glushko et al. [23], while the heat capacity of NaCl(l) was recently recommended by van Oudenaren et al. [42]. The authors critically reviewed the four studies available on the determination of the heat capacity of NaCl(l) [48, 49, 40, 14] and found that there was no discrepancy between the data by Dawson et al. [14] and the rest of the authors, in contrast with what Glushko et al. had argued. Considering the average of the four studies, van Oudenaren et al. recommend

(68 $\pm$ 1) kJ·mol^{-1} in the 1074-2500 K range. In the case of $ThCl_4$(cr,l), the data used were recommended by Fuger et al. [50] and Capelli and Konings [10]. As mentioned in the introduction, $ThCl_4$ crystallizes in two phases. Using an adiabatic calorimeter, Chiotti et al. [12] measured an enthalpy of transition equal to (5.0 $\pm$ 1.5) kJ· mol^{-1} at (679 $\pm$ 2) K. Taking the heat capacity of $ThCl_4$-α (the low-temperature phase) to be equal to that recommended for $ThCl_4$-β (the high-temperature phase), the standard enthalpy of formation and standard entropy of $ThCl_4$-α were optimized in this work such that the transition between both phases matched the values reported by Chiotti et al. [12]. The enthalpy of fusion (61.5 $\pm$ 5.0) kJ· mol^{-1}, melting temperature (T = 1042 K), and heat capacity recommended by Capelli and Konings [10] were used to describe $ThCl_4$(l). The thermodynamic functions of the intermediate compounds were optimized in this work to match the experimentally determined phase diagrams as closely as possible. All values are given in Table 1.

3.2.2. LIQUID SOLUTION

The excess Gibbs energy terms of liquid solutions were modelled using the modified quasi-chemical model in the quadruplet approximation proposed by Pelton et al. [46]. This formalism is apt to describe ionic liquids like the melts examined here, as it allows to select the composition of maximum short-range ordering (SRO) by varying the ratio between the cation-cation coordination numbers $Z^A_{AB/Cl}$ and $Z^B_{AB/Cl}$ (see Table 3). It has been used to assess a significant number of molten salt systems for nuclear applications [6, 9], becoming a standard of sorts for the MSR thermochemistry community [1]. Despite its practicality, structural features such as molecular species and network formation, are not accounted for. However, structural features may be imposed on the model, for example by explicitly introducing ions with different coordinations [55, 51]. In this formalism, a set of two anions and two cations makes up a quadruplet, taken to be the basic unit in the liquid solution, and the excess parameters to be optimized are those related to the following second-nearest neighbor (SNN) exchange reaction:

$$(A-Cl-A)+(B-Cl-B) \longrightarrow 2(A-Cl-B) \;\; \Delta g_{AB/Cl} \tag{3.3}$$

where the chloride anions are represented by Cl, and A and B denote the cations. $\Delta g_{AB/Cl}$ denotes the Gibbs energy change associated with the SNN exchange reaction:

$$\Delta g_{AB/Cl} = \Delta g^0_{AB/Cl} + \sum_{i\geqslant 1} g^{i0}_{AB/Cl} \chi^i_{AB/Cl} + \sum_{j\geqslant 1} g^{0j}_{AB/Cl} \chi^j_{BA/Cl} \tag{3.4}$$

$\Delta g^o_{AB/Cl}$ and $g^{ij}_{AB/Cl}$ are coefficients which may have temperature dependence, but which are independent of composition. The composition dependence is specified by the $\chi_{AB/Cl}$:

$$\chi_{AB/Cl} = \frac{X_{AA}}{X_{AA}+X_{AB}+X_{BB}} \tag{3.5}$$

where X_{AA}, X_{BB} and X_{AB} represent cation-cation pair mole fractions. Finally, charge conservation over the quadruplet imposes the anion coordination number:

Table 2: Thermodynamic data for end-members and intermediate compounds used in this work for the phase diagram assessment: $\Delta_f H^o_m$(298 K)/(kJ·mol^{-1}), S^o_m(298 K)/(J·K^{-1}·mol^{-1}), and heat capacity coefficients $C_{p,m}$(T/K)/(J·K^{-1}·mol^{-1}), where $C_{p,m}$(T/K) = a + b·T + c·T^2 + d·T^{-2} + e·T^3. Optimized data are shown in **bold**.

Compound	$\Delta_f H^o_m$(298 K)/ (kJ·mol^{-1})	S^o_m(298 K)/ (J·K^{-1}·mol^{-1})	$C_{p,m}$(T/K)/(J·K^{-1}·mol^{-1})= a + b·T + c·T^2 + d·T^{-2} a	b	c	d	Range	Reference
LiCl(cr)	-408.266	59.3	44.70478	0.01792765	1.863482·10^{-6}	-194457.7	298-883	[18]
			73.30619	-0.009430108		33070.5	883-2000	[18]
LiCl(l)	-388.4342	81.76	44.70478	0.01792765	1.863482·10^{-6}	-194457.7	298-883	[18]
			73.30619	-0.009430108		33070.5	883-2000	[18]
NaCl(cr)	-411.260	72.15	47.72158	0.0057	1.21466·10^{-5}	-882.996	298-1074	[23]
			68.0				1074-2500	[42]
NaCl(l)	-383.060	98.407	47.72158	0.0057	1.21466·10^{-5}	-882.996	298-1074	[23]
			68.0				1074-2500	[42]
KCl(cr)	-436.6841	82.555	50.47661	0.005924377	7.496682·10^{-6}	-144173.9	298-700	[18]
			143.5698	-0.1680399	9.965702·10^{-5}	-8217836	700-1044	[18]
			73.59656			-8217836	1044-2000	[18]
KCl(l)	-410.4002	107.7311	50.47661	0.005924377	7.496682·10^{-6}	-144173.9	298-700	[18]
			143.5698	-0.1680399	9.965702·10^{-5}	-8217836	700-1044	[18]
			73.59656				1044-2000	[18]
α-$ThCl_4$(cr)	**-1191.3012**	**176.135**	120.293	0.0232672		-615050	298-1042	this work, [12]
β-$ThCl_4$(cr)	-1186.300	183.5	120.293	0.0232672		-615050	298-1042	[50],[10]
$ThCl_4$(l)	-1149.740	197.626	167.4				298-1500	[50],[10]
Li_4ThCl_8(cr)	**-2837.9656**	**413.34**	299.11212	0.0949778	7.453928·10^{-6}	-1392880.8	298-883	this work
			413.51776	-0.014453232		-482768	883-1042	
			437.1957	-0.037720432		132282	1042-2000	
Na_2ThCl_6(cr)	**-2066.540**	**327.57**	215.73616	0.0346672	2.42932·10^{-5}	-616815.992	298-1042	this work
			239.41	0.0114	2.42932·10^{-5}	-1765.992	1042-1074	
			279.971					
$KThCl_5$(cr)	**-1693.000**	**258.69**	170.76961	0.029191577	7.496682·10^{-6}	-759223.9	298-700	this work
			263.8628	-0.1447727	9.965702·10^{-5}	-8832886	700-1042	
			287.5408	-0.1680399	9.965702·10^{-5}	-8217836	1042-1044	
			217.568				1044-2000	
K_2ThCl_6(cr)	**-2167.568**	**363.25**	221.24622	0.035115954	1.4993364·10^{-5}	-903397.8	298-700	this work
			407.4326	-0.3128126	1.9931404·10^{-4}	-17050722	700-1042	
			431.1106	-0.3360798	1.9931404·10^{-4}	-16435672	1042-1044	
			291.16408				1042-2000	

$$\frac{q_A}{Z^A_{AB/Cl}} + \frac{q_B}{Z^B_{AB/Cl}} = \frac{2q_{Cl}}{Z^{Cl}_{AB/Cl}} \tag{3.6}$$

where q_i are the charges of the different ions, and $Z^{Cl}_{AB/Cl}$ is the anion-anion coordination number. These were chosen to represent the composition of maximum short-range ordering, where the Gibbs energy tends to have its minimum. Typically, the point of maximum short-range ordering can be expected to lie near the lowest eutectic. The cation-cation coordination numbers are listed in Table 3.

Table 3: Cation-cation coordination numbers of the liquid solution.

A	B	$Z^A_{AB/Cl}$	$Z^B_{AB/Cl}$
Li^+	Li^+	6	6
Na^+	Na^+	6	6
K^+	K^+	6	6
Th^{4+}	Th^{4+}	6	6
Li^+	Th^{4+}	4	6
Na^+	Th^{4+}	3	6
K^+	Th^{4+}	4	6

The optimized excess Gibbs energy parameters of the binary liquid solutions are shown in Eq. 3.7-3.9. The parameters were optimized based on the phase diagram equilibria points of the liquidus.

$$\Delta g_{LiTh/Cl} = -8000 - 4000 \cdot \chi_{LiTh/Cl} - 2700 \cdot \chi_{ThLi/Cl}\, J \cdot mol^{-1} \tag{3.7}$$

$$\Delta g_{NaTh/Cl} = -27700 - 10000\chi^2_{NaTh/Cl} + -20000\chi_{ThNa/Cl}\ J \cdot mol^{-1} \tag{3.8}$$

$$\Delta g_{KTh/Cl} = -28000 + -16000 \cdot \chi^2_{KTh/Cl} + -25000 \cdot \chi_{ThK/Cl}\ J \cdot mol^{-1} \tag{3.9}$$

3.3. RESULTS AND DISCUSSION

3.3.1. PHASE DIAGRAMS

The calculated phase diagrams are shown in Figs. 3.1-3.3, and invariant equilibria are listed in Table 4. For the LiCl-ThCl$_4$ system, the modelling choice to include Li_4ThCl_8 was very clear: three different authors reported they had observed it. Incidentally, in the LiCl-UCl$_4$ phase diagram there is also a ternary chloride, although the formula is Li_2UCl_6 [59]. It has been determined to belong to space group $P6_3/mmc$ [5]. The calculated phase diagram closely reproduces the equilibria found by Tanii [58]. The melting points of the end-members measured by Tanii agree well with the recommended values,

indicating quite pure reagents. Oyamada [43], on the other hand, reports melting points for the end-members which are more than 20 K higher, which could be due to oxygen or water contamination. It can be seen that the $\alpha - \beta$ transition of $ThCl_4$ is very close to the eutectic of the system, which would make both events very difficult to resolve experimentally.

In the NaCl-$ThCl_4$ system, the modelling choice is also clear: three authors agree that Na_2ThCl_6 forms and that is melts congruently, and only Vdovenko et al. [60] report a different stoichiometry ($NaThCl_5$). In the analogous NaCl-UCl_4 system a compound with formula $NaUCl_5$ was not observed, but Na_2UCl_6 was [30, 31, 59]. Furthermore, its crystal structure was studied and it is known to belong to space group *P-3m1* [5]. These observations support the choice to include Na_2ThCl_6. In this phase diagram the $\alpha - \beta$ transition of $ThCl_4$ is again very close to the second eutectic of the system, making it experimentally difficult to observe.

The KCl-$ThCl_4$ system has greatest discrepancies in the 0.25 < $ThCl_4$ < 0.33 region. Gershanovich and Suglobova [22] reported both K_3ThCl_7 and K_2ThCl_6, Oyamada [43] reported only the former, and Tanii [58] and Vokhmyakov [61] reported only the latter (see Table 1). In fact, Gershanovich and Suglobova [22] characterized the crystal structure of K_2ThCl_6, which belongs to space group *Cmcm*, so this phase was retained in the assessment. Including K_3ThCl_7 raises the liquidus around the line compound and can be done without re-optimizing the Gibbs energy terms of the other intermediate phases. However, much larger excess Gibbs energy parameters would need to be imposed on the liquid solution to obtain in this new optimization the solidus temperature close to the experimental points. Relying yet again on what is known on the KCl-UCl_4 system, in which a phase with formula K_2UCl_6 was reported [59, 30], the phase K_3ThCl_7 was discarded. As for $KThCl_5$, Tanii [58] is the only author who did not suggest its existence, although his calorimetric measurements form a concavity with a maximum centered around X($ThCl_4$) = 0.5 (Fig. 3.3, $*$), which can very well be interpreted as the congruent melting of a phase with stoichiometry $KThCl_5$. For that reason, the phase was retained in the assessment.

3.3.2. ENTHALPY OF MIXING

The mixing enthalpies are of great interest since they are linked to the stability of the liquid solutions. They have not been measured for these systems, yet the calculated values, shown in Fig. 3.4a (T = 1100 K), may serve as another data set, apart from the phase diagrams, to gauge the validity of the models optimized here. There are three things to notice. First of all, the mixing enthalpies are negative at all compositions. Second, the depth of the curves increases in magnitude in the order Li < Na < K. Third, the curves are not symmetric, but display minima in the ACl-rich regions (A = Li, Na, K). Although ions do not behave like hard charged spheres [7], it may be a useful exercise to model them with such an idealized potential in order to gain insight into the energetics of mixing in the melt:

$$V_{qq}(r_{ij}) = \sum_{i<j} \frac{q_i q_j}{r_{ij}} \quad r_{ij} > r_{0,ij} \tag{3.10}$$

Table 4: Invariant equilibrium data in the ACl-$ThCl_4$ systems.

System	Equilibrium	Invariant reaction	This study (calc.)		Tanii et al. [58]		Vokhmyakov et al. [61]		Oyamada [43]	
			X($ThCl_4$)	T / K	X($ThCl_4$)	T / K	X($ThCl_4$)	T / K	X($ThCl_4$)	T / K
LiCl-$ThCl_4$	Congruent Melting	LiCl = L	1	883	1	881			1	910
	Peritectic	Li_4ThCl_8 = LiCl + L	0.2	725	0.2	725	0.2	723	-	-
	Eutectic	Li_4ThCl_8 + β-$ThCl_4$ = L	0.347	684	-	690	0.38	681	0.35	703
	α-β transition	α-$ThCl_4$ = β-$ThCl_4$	1	679						
	Congruent Melting	β-$ThCl_4$ = L	1	1042	1	1041			1	1070
NaCl-$ThCl_4$	Congruent melting	NaCl = L	0	1074	0	1074			0	1097
	Eutectic	NaCl + Na_2ThCl_6 = L	0.269	652	-	639	0.255	633	0.26	667
	Congruent Melting	Na_2ThCl_6 = L	1/3	702	1/3	708	1/3	708	1/3	729
	Eutectic	Na_2ThCl_6 + α-$ThCl_4$ = L	0.430	661	-	637	0.45	648	0.49	686
KCl-$ThCl_4$	Congruent melting	KCl = L	0	1044	0	1043			0	1070
	Eutectic	KCl + K_2ThCl_6 = L	0.193	911	-	895	0.25	903	0.15	917
	Congruent melting	K_2ThCl_6 = L	1/3	977	1/3	988	1/3	978	0.25[a]	997
	Eutectic	K_2ThCl_6 + $KThCl_5$ = L	0.449	702	-	705	0.42	668	0.43	681
	Congruent melting	$KThCl_5$ = L	0.5	714			0.5	703	0.5	741
	Eutectic	$KThCl_5$ + β-$ThCl_4$ = L	0.521	714			0.54	693	0.56	706

[a] Interpreted by the author to be the congruent melting of K_3ThCl_7.

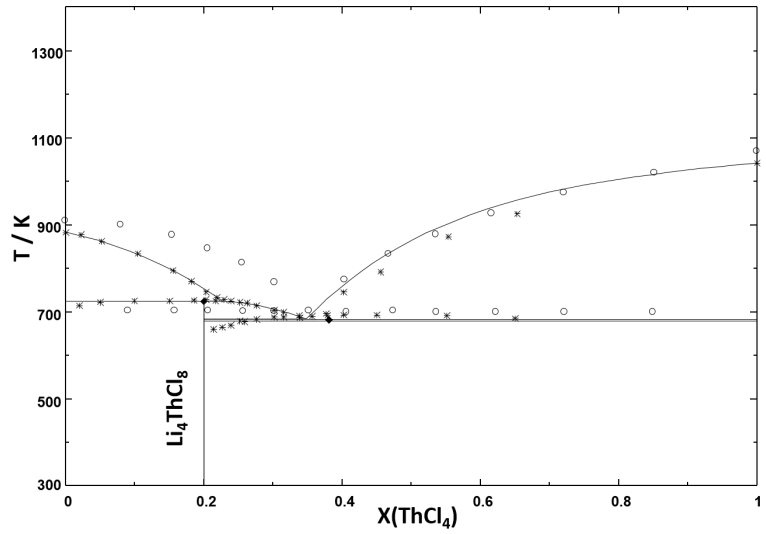

Figure 3.1: The LiCl-$ThCl_4$ phase diagram as calculated in this work. Symbols: phase diagram data reported by Tanii [58] (⋇), Oyamada [43] (○), and Vokhmyakov et al. [61] (⬥).

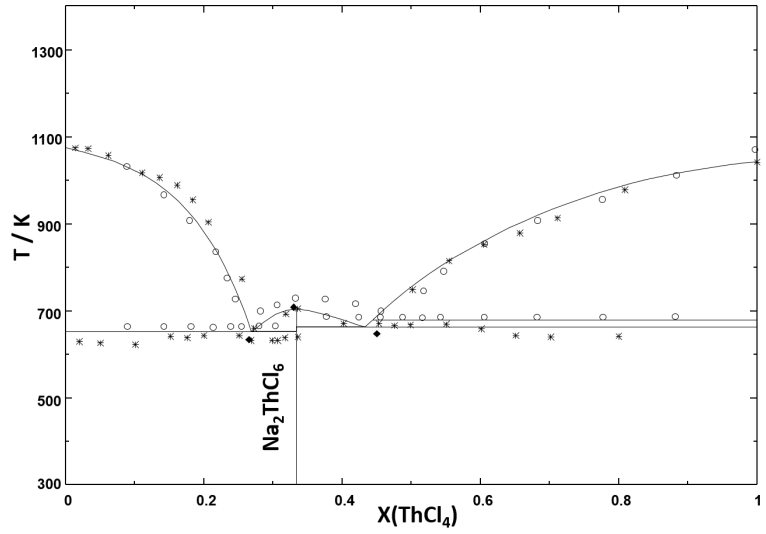

Figure 3.2: The NaCl-$ThCl_4$ phase diagram as calculated in this work. Symbols: phase diagram data reported by Tanii [58] (⋇), Oyamada [43] (○), and Vokhmyakov et al. [61] (⬥).

$$V_{rep}(r_{ij}) = \infty \quad r_{ij} \leqslant r_{0,ij} \tag{3.11}$$

In Eq. (3.10,3.11), q denotes formal charge of ions i and j, r_{ij} is the internuclear distance, and $r_{0,ij}$ is the sum of the radii of ions i and j. Retaining the quadruplets as a crude

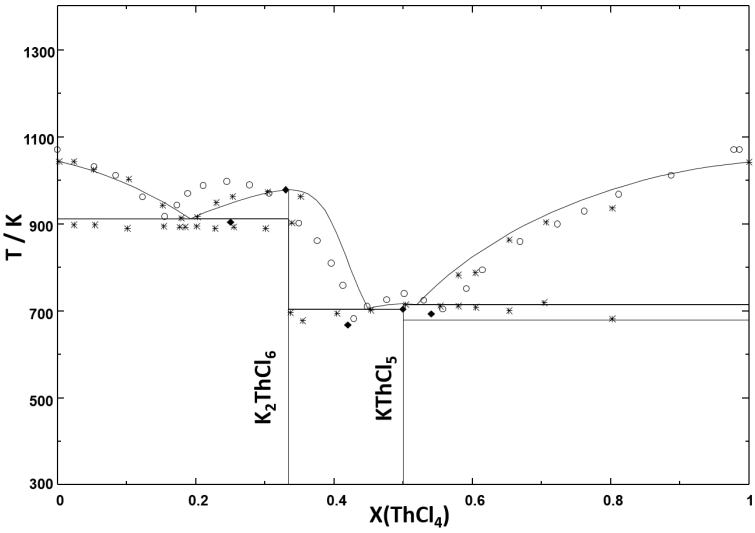

Figure 3.3: The KCl-ThCl$_4$ phase diagram as calculated in this work. Symbols: phase diagram data reported by Tanii [58] (∗), Oyamada [43] (○), and Vokhmyakov et al. [61] (◆).

structural model, the energy change upon SNN exchange (Eq. 7.6) is:

$$\Delta V_{SNNexchange} = 2\frac{q_A q_{Th} + q_{Cl} q_{Cl}}{\sqrt{r_{ThCl}^2 + r_{ACl}^2}} - \frac{q_{Th} q_{Th} + q_{Cl} q_{Cl}}{r_{ThCl}\sqrt{2}} - \frac{q_A q_A + q_{Cl} q_{Cl}}{r_{ACl}\sqrt{2}} \tag{3.12}$$

In rocksalt structures, the cation-anion coordination number is 6, and a coordination number of 6 has been seen to be prevalent about Th^{4+} in LiCl-ThCl$_4$ melts with Molecular Dynamics (MD) simulations [34]. Taking into account the Shannon radii [54] for such coordinations, the values in Table 5 are obtained. Note that they are meant only to illustrate general qualitative trends: a quantitative description requires taking into account physically realistic structural models and multiple interactions over the long range, as in molecular dynamics simulations.

From this simplified picture, the enthalpies of mixing can be expected to be favorable from a Coulombic point of view. Moreover, Table 5 agrees with the trend of progressive stabilization with increasing alkali radius shown by the curves in Fig. 3.4a. This trend is also related to an increased stability of first-nearest neighbor (FNN) shells around Th^{4+} as the polarizing ability of the alkali cation diminishes with increasing size [13]. Furthermore, if the mixing event is considered as an acid-base reaction:

$$nACl + ThCl_4 = [ThCl_{4+n}]^{-n} + nA^+ \tag{3.13}$$

the increasing radius of the alkali cation implies its charge is spread over a larger volume, resulting in a more stable conjugate chloroacid A^+, contributing to the overall stability of the liquid solution. The third effect, the asymmetry, is related to the choice

Table 5: Change in exchange energy due to SNN exchange reactions

Ion	Coordination[a]	Shannon ionic radius r_i(Å) [54]	$\Delta V_{SNNexchange}$ (hartree)
Li^+	VI	0.76	-4.1
Na^+	VI	1.0	-4.2
K^+	VI	1.38	-4.9
Th^{4+}	VI	0.94	
Cl^-	VI	1.81	

[a]Not to be confused with the cation-cation coordination number of Table 3.

of cation-cation coordination numbers (Table 3), chosen to reflect the compositions of the lowest-melting eutectics and maximum short-range ordering. Such an asymmetry would also be expected in experimentally measured curves. For instance, calorimetric studies of the ACl-MCl_2 systems (M=Mn, Fe, Co, Ni, Cd; A= Li, Na, K, Rb, Cs) [45],[44], [28] revealed a minimum for the enthalpy of mixing near X(MCl_2)=0.33, the stoichiometry which favours the formation of tetrahedral MCl_4^{2-} complexes in the melt. Complexes of these kind have been observed spectroscopically in studies in which $NiCl_2$ is dissolved in alkali chlorides [24, 57]. The coordination of $[ThCl_x]^{4-x}$ shells has been studied with Raman spectroscopy by Photiadis and Papatheodorou [47], and they were found to be 6 (octahedral) and 7-coordinated (pentagonal bipyramidal) in melts rich in alkali chloride (A = Li, Na, K, Cs). Beyond $\sim$0.3 $ThCl_4$ content, bridging of these shells was observed via shared chlorides, up to pure $ThCl_4$. The relatively limited stability of $[ThCl_x]^{4-x}$ cages when LiCl is the solvent, compared to the other alkali chlorides would yield the most symmetric curve, as in Fig 3.4a. Calorimetric measurements have shown this to be the case for the (Li,Th)F_x melt [11].

The thermodynamic stability of solutions is also affected by entropy effects. For example, in systems with shallow mixing enthalpies and negative mixing entropies, miscibility gaps may result, although that is more common in metallic systems [35]. In the present systems, the calculated mixing entropies of the (Li,Th)Cl_x and (Na,Th)Cl_x liquid solutions are positive throughout the composition range (Fig. 3.4b), contributing to the stability of the mixtures. In agreement with the structural features just discussed, (Li,Th)Cl_x tends to regular solution behavior, and (Na,Th)Cl_x deviates from regularity, showing a minimum at the point of maximum short-range ordering (SRO). (K,Th)Cl_x displays such strong SRO that the entropy of mixing is negative at its minimum near X($ThCl_4$) = 0.4: the mixing is least favourable from an entropic perspective where it is most favourable from an enthalpic point of view. However, the mixing enthalpies dominate the contribution, and the Gibbs energies of mixing which govern overall liquid phase stability are arranged in the same order (Fig. 3.5). A high stability of the liquids is a desirable property, as it makes it more likely to find alloys which can withstand their corrosive properties, as well as contributing to their stability under irradiation [20].

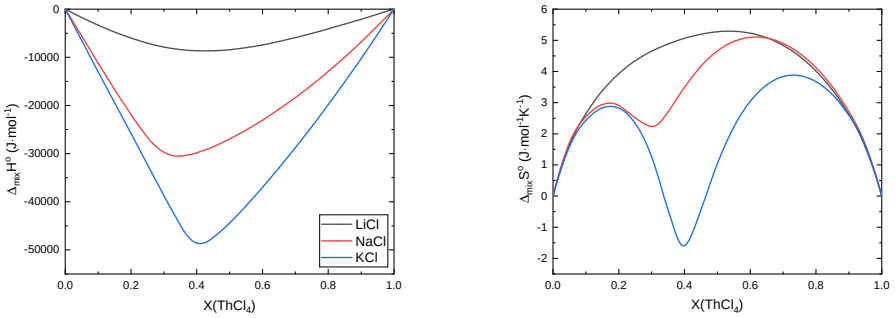

(a) (b)

Figure 3.4: (a) Enthalpies and (b) entropies of mixing of the (A,Th)Cl$_x$ liquid solutions calculated at T = 1100 K.

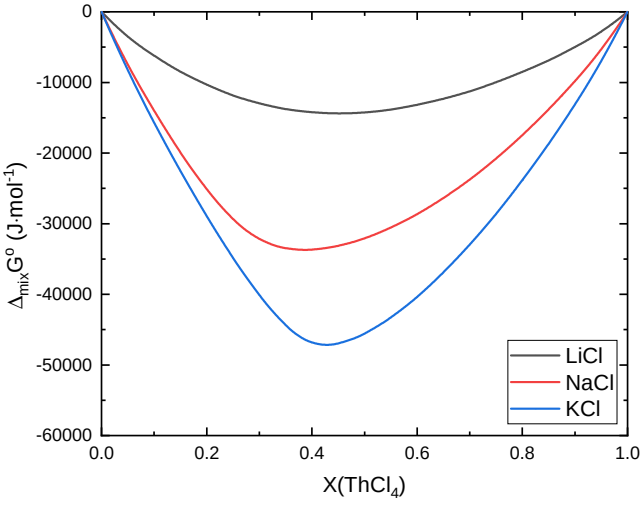

Figure 3.5: Gibbs energies of mixing of the (A,Th)Cl$_x$ liquid solutions calculated at T = 1100 K.

3.4. CONCLUSIONS

The ACl-ThCl$_4$ (A = Li, Na, K) systems are of metallurgical and nuclear importance. CALPHAD models have been parametrized for them, with a view to assess whether further research on these binary systems is required. The models describe the experimental phase diagrams with a good accuracy. The enthalpies of mixing substantially contribute to the thermodynamic stability of the melts, which increases in the order Li $<$ Na $<$ K. Strong short-range order is apparent in the calculated mixing entropy curves, which be-

come less favourable with increasing size of the alkali cation: (K,Th)Cl_x even displays negative entropy of mixing where the enthalpy of mixing is greatest in magnitude. The trends in the mixing properties are consistent with simple Coulombic and structural considerations of these salts in the molten state. Still, novel data on these systems is called for to better ascertain their phase diagrams and thermodynamic data. Relatively easy access to β-$ThCl_4$ from a reaction between widely available ThO_2 and $AlCl_3$, has recently been described by Deubner et al. [15]. This provides an opportunity to, among other things:

- isolate the intermediate phases Li_4ThCl_8, Na_2ThCl_6, and $KThCl_5$ and and elucidate their crystal structures
- derive their standard enthalpies of formation and standard entropies
- obtain novel phase equilibrium data with calorimetry, particularly for the KCl-$ThCl_4$ system
- measure enthalpies of mixing for the liquid solutions

3.5. AUTHOR CONTRIBUTIONS

J.A. Ocádiz Flores: Conceptualization, Methodology, Investigation, Formal analysis, Visualization, Data Curation, Writing - Original Draft preparation **B.A.S. Rooijakkers**: Investigation **R.J.M. Konings**: Supervision, Conceptualization, Writing - Review & Editing **A.L. Smith**: Conceptualization, Methodology, Supervision, Resources, Project Administration, Writing - Review & Editing.

3.6. ACKNOWLEDGMENTS

J.A. Ocádiz Flores gratefully acknowledges CONACYT-SENER for financial support.

A.1. ERRATUM TO: THERMODYNAMIC DESCRIPTION OF THE ACL-$THCL_4$ (A = LI, NA, K) SYSTEMS

The optimized Gibbs energies for the second-nearest neighbor (SNN) exchange reactions of the liquid solutions were incorrectly reported to be polynomial expansions in terms of pair fraction expansions in Eqs.(7)-(9) of our recent work [41]. Rather, they were polynomial expansions in terms of coordination-equivalent fractions Y_A, Y_{Th} (A = Li, Na, K). Given $Z^A_{AB/Cl}$ and $Z^B_{AB/Cl}$, the SNN coordination numbers of ions A and B in a binary chloride melt, their equivalent pair fractions are defined as [46]:

$$Y_A = Z^A_{AB/Cl} \cdot n_A / (Z^A_{AB/Cl} \cdot n_A + Z^B_{AB/Cl} \cdot n_B) \tag{A.1}$$

$$Y_B = 1 - Y_A \tag{A.2}$$

where n_i corresponds to the number of moles of species i. To be consistent with the notation just introduced, the aforementioned Eqs. (7)-(9) in [41] should have been written as:

$$\Delta g_{LiTh/Cl} = -8,000 - 4,000 \cdot Y_{Li} - 2,700 \cdot Y_{Th}\ J \cdot mol^{-1} \tag{A.3}$$

$$\Delta g_{NaTh/Cl} = -27,700 - 10,000 \cdot Y_{Na}^2 - 20,000 \cdot Y_{Th}\ J \cdot mol^{-1} \tag{A.4}$$

$$\Delta g_{KTh/Cl} = -28,000 - 16,000 \cdot Y_K^2 - 25,000 \cdot Y_{Th}\ J \cdot mol^{-1} \tag{A.5}$$

However, in order to be compatible with existing molten salt databases for nuclear applications, the excess Gibbs energies of the liquid solutions should better be expressed as polynomial expansions in the composition term χ:

$$\chi_{AB/Cl} = \frac{X_{AA}}{X_{AA} + X_{AB} + X_{BB}} \tag{A.6}$$

where X_{AA}, X_{BB} and X_{AB} represent cation-cation pair mole fractions. Note that in the case of binary solutions with a common anion, $\chi_{AB/Cl} = X_{AA}$, and $\chi_{BA/Cl} = X_{BB}$. Eqs. A.7-A.9 were found to reproduce the ACl-ThCl$_4$ (A = Li, Na, K) phase diagrams with comparable accuracy to that obtained with expressions A.3-A.5.

$$\Delta g_{LiTh/Cl} = -8,000 - 3,600 \cdot \chi_{LiTh/Cl} - 7,300 \cdot \chi_{ThLi/Cl}\ J \cdot mol^{-1} \tag{A.7}$$

$$\Delta g_{NaTh/Cl} = -27,700 - 7,500 \cdot \chi_{NaTh/Cl} - 14,000 \cdot \chi_{ThNa/Cl}\ J \cdot mol^{-1} \tag{A.8}$$

$$\Delta g_{KTh/Cl} = -40,000 - 10,000 \cdot \chi_{ThK/Cl}\ J \cdot mol^{-1} \tag{A.9}$$

The Gibbs energy terms of the intermediate phases needed some adjustment also, namely the standard enthalpies of formation and in the case of K_2ThCl_6, also the standard entropy. The re-assessed values are given in Table A.1.

The phase diagrams as calculated with this corrected model are shown in Figs. A.1-A.3, and invariant equilibria are listed in Table A.2, while the mixing properties of the liquid solutions are shown in Figs. A.4a-A.5. The latter properties display the same trends (discussed in [41]) as those appearing when polynomials in coordination-equivalent sites were used.

Table A.1: Thermodynamic data for intermediate compounds used in this work for the phase diagram assessment: $\Delta_f H^o_m(298\ K)/(kJ\cdot mol^{-1})$, $S^o_m(298\ K)/(J\cdot K^{-1}\cdot mol^{-1})$, and heat capacity coefficients $C_{p,m}(T/K)/(J\cdot K^{-1}\cdot mol^{-1})$, where $C_{p,m}(T/K) = a + b\cdot T + c\cdot T^2 + d\cdot T^{-2} + e\cdot T^3$. Re-optimized data with respect to [41] are shown in **bold**.

Compound	$\Delta_f H^o_m(298\ K)/(kJ\cdot mol^{-1})$	$S^o_m(298\ K)/(J\cdot K^{-1}\cdot mol^{-1})$	$C_{p,m}(T/K)/(J\cdot K^{-1}\cdot mol^{-1}) = a + b\cdot T + c\cdot T^2 + d\cdot T^{-2}$ a	b	c	d	Range	Reference
LiCl(cr)	-408.266	59.3	44.70478	0.01792765	$1.863482\cdot10^{-6}$	-194457.7	298-883	[18]
			73.30619	-0.009430108		33070.5	883-2000	[18]
LiCl(l)	-388.4342	81.76	44.70478	0.01792765	$1.863482\cdot10^{-6}$	-194457.7	298-883	[18]
			73.30619	-0.009430108		33070.5	883-2000	[18]
NaCl(cr)	-411.260	72.15	47.72158	0.0057	$1.21466\cdot10^{-5}$	-882.996	298-1074	[23]
			68.0				1074-2500	[42]
NaCl(l)	-383.060	98.407	47.72158	0.0057	$1.21466\cdot10^{-5}$	-882.996	298-1074	[23]
			68.0				1074-2500	[42]
KCl(cr)	-436.6841	82.555	50.47661	0.005924377	$7.496682\cdot10^{-6}$	-144173.9	298-700	[18]
			143.5698	-0.1680399	$9.965702\cdot10^{-5}$	-8217836	700-1044	[18]
			73.59656			-8217836	1044-2000	[18]
KCl(l)	-410.4002	107.7311	50.47661	0.005924377	$7.496682\cdot10^{-6}$	-144173.9	298-700	[18]
			143.5698	-0.1680399	$9.965702\cdot10^{-5}$	-8217836	700-1044	[18]
			73.59656				1044-2000	[18]
α-$ThCl_4$(cr)	**-1191.300**	**176.135**	120.293	0.0232672		-615050	298-1042	this work, [12]
β-$ThCl_4$(cr)	-1186.300	183.5	120.293	0.0232672		-615050	298-1042	[50],[10]
$ThCl_4$(l)	-1149.716	197.706	167.4				298-1500	[50],[10]
Li_4ThCl_8(cr)	**-2834.966**	413.34	299.11212	0.0949778	$7.453928\cdot10^{-6}$	-1392880.8	298-883	this work
			413.51776	-0.014453232		-482768	883-1042	
			437.1957	-0.037720432		132282	1042-2000	
Na_2ThCl_6(cr)	**-2051.540**	328.0	215.73616	0.0346672	$2.42932\cdot10^{-5}$	-616815.992	298-1042	this work
			239.41	0.0114	$2.42932\cdot10^{-5}$	-1765.992	1042-1074	
			279.971					
$KThCl_5$(cr)	**-1685.000**	258.69	170.76961	0.029191577	$7.496682\cdot10^{-6}$	-759223.9	298-700	this work
			263.8628	-0.1447727	$9.965702\cdot10^{-5}$	-8832886	700-1042	
			287.5408	-0.1680399	$9.965702\cdot10^{-5}$	-8217836	1042-1044	
			217.568				1044-2000	
K_2ThCl_6(cr)	**-2139.850**	**380.5**	221.24622	0.035115954	$1.4993364\cdot10^{-5}$	-903397.8	298-700	this work
			407.4326	-0.3128126	$1.9931404\cdot10^{-4}$	-17050722	700-1042	
			431.1106	-0.3360798	$1.9931404\cdot10^{-4}$	-16435672	1042-1044	
			291.16408				1042-2000	

Table A.2: Invariant equilibrium data in the ACl-$ThCl_4$ systems.

System	Equilibrium	Invariant reaction	This study (calc.)		Tanii et al. [58]		Vokhmyakov et al. [61]		Oyamada [43]	
			$X(ThCl_4)$	T / K	$X(ThCl_4)$	T / K	$X(ThCl_4)$	T / K	$X(ThCl_4)$	T / K
LiCl-$ThCl_4$	Congruent Melting	LiCl = L	1	883	1	881			1	910
	Peritectic	Li_4ThCl_8 = LiCl + L	0.2	723	0.2	725	0.2	723	-	-
	Eutectic	Li_4ThCl_8 + β-$ThCl_4$ = L	0.343	695	-	690	0.38	681	0.35	703
	α-β transition	α-$ThCl_4$ = β-$ThCl_4$	1	679						
	Congruent Melting	β-$ThCl_4$ = L	1	1042	1	1041			1	1070
NaCl-$ThCl_4$	Congruent melting	NaCl = L	0	1074	0	1074			0	1097
	Eutectic	NaCl + Na_2ThCl_6 = L	0.252	667	-	639	0.255	633	0.26	667
	Congruent Melting	Na_2ThCl_6 = L	1/3	710	1/3	708	1/3	708	1/3	729
	Eutectic	Na_2ThCl_6 + α-$ThCl_4$ = L	0.459	661	-	637	0.45	648	0.49	686
KCl-$ThCl_4$	Congruent melting	KCl = L	0	1044	0	1043			0	1070
	Eutectic	KCl + K_2ThCl_6 = L	0.206	894	-	895	0.25	903	0.15	917
	Congruent melting	K_2ThCl_6 = L	1/3	977	1/3	988	1/3	978	0.25[a]	997
	Eutectic	K_2ThCl_6 + $KThCl_5$ = L	0.467	697	-	705	0.42	668	0.43	681
	Congruent melting	$KThCl_5$ = L	0.5	702			0.5	703	0.5	741
	Eutectic	$KThCl_5$ + β-$ThCl_4$ = L	0.536	699			0.54	693	0.56	706

[a] Interpreted by the author to be the congruent melting of K_3ThCl_7.

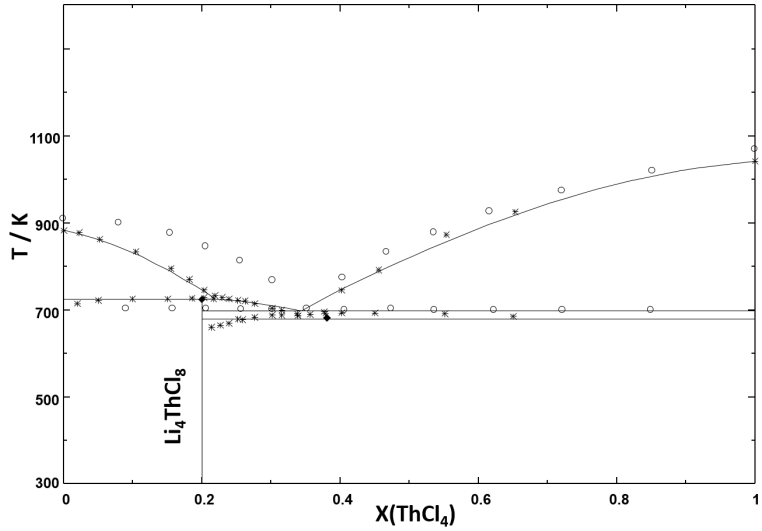

Figure A.1: The LiCl-ThCl$_4$ phase diagram as re-calculated in this work. Symbols: phase diagram data reported by Tanii [58] (⁎), Oyamada [43] (○), and Vokhmyakov et al. [61] (⬥).

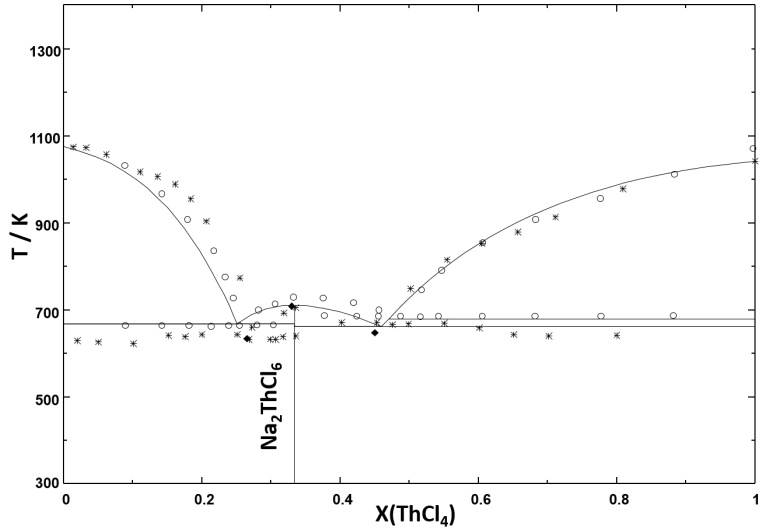

Figure A.2: The NaCl-ThCl$_4$ phase diagram as re-calculated in this work. Symbols: phase diagram data reported by Tanii [58] (⁎), Oyamada [43] (○), and Vokhmyakov et al. [61] (⬥).

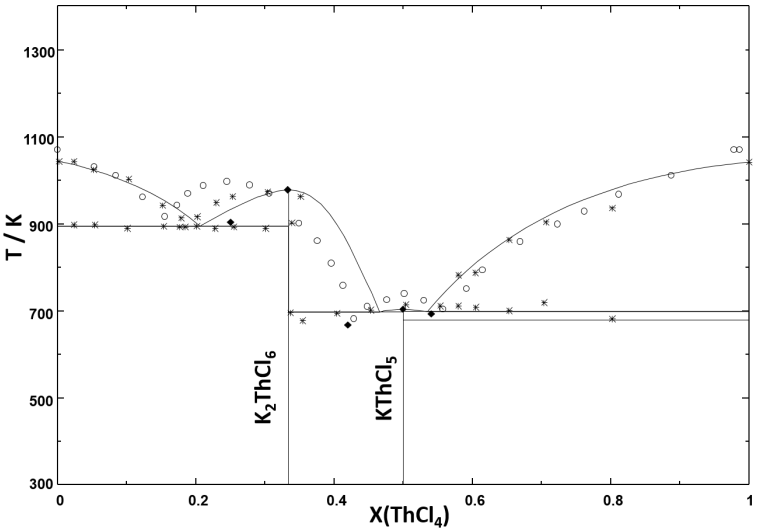

Figure A.3: The KCl-$ThCl_4$ phase diagram as re-calculated in this work. Symbols: phase diagram data reported by Tanii [58] (⁎), Oyamada [43] (○), and Vokhmyakov et al. [61] (◆).

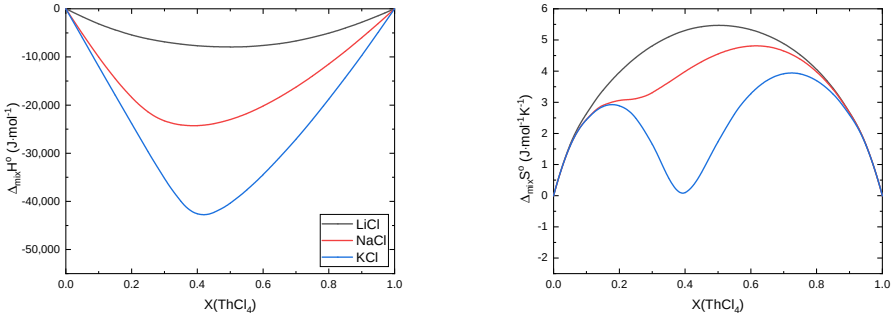

(a) (b)

Figure A.4: (a) Enthalpies and (b) entropies of mixing of the (A,Th)Cl_x liquid solutions calculated at T = 1100 K.

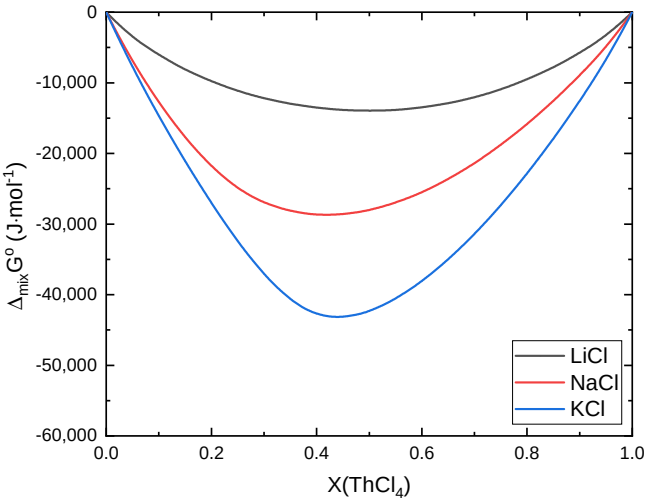

Figure A.5: Gibbs energies of mixing of the (A,Th)Cl$_x$ liquid solutions calculated at T = 1100 K.

BIBLIOGRAPHY

[1] J. Ard et al. *FY20 Status report on the Molten Salt Thermodynamic Database (MSTDB) development*. Tech. rep. Oak Ridge National Lab.(ORNL), Oak Ridge, TN (United States), 2020.

[2] *Atomic Energy Review, Special Issue No. 5 Thorium: Physic-chemical Properties of Its Compounds and Alloys*. Atomic Energy Review. Special issue. Vienna: International Atomic Energy Agency, 1975.

[3] Ch W Bale et al. "FactSage thermochemical software and databases". In: *Calphad* 26.2 (2002), pp. 189–228.

[4] W.W. Beaver and K.G. Wikle. "Powder Metallurgy of Thorium". In: *Powder Metallurgy in Nuclear Engineering: Proceedings of the Conference on Powder Metallury in Atomic Energy*. 1958, p. 82.

[5] P.J. Bendall, A.N. Fitch, and B.E.F. Fender. "The structure of Na_2UCl_6 and Li_2UCl_6 from multiphase powder neutron profile refinement". In: *Journal of Applied Crystallography* 16.2 (Apr. 1983), pp. 164–170.

[6] O. Beneš. "Thermodynamics of molten salts for nuclear applications". PhD thesis. Institute of Chemical Technology, Prague, 2008.

[7] M. Blander. "Thermodynamic properties of molten salt solutions". In: *Molten Salt Chemistry*. Springer, 1987, pp. 17–62.

[8] D. Brown, T.L. Hall, and P.T. Moseley. "Structural parameters and unit cell dimensions for the tetragonal actinide tetrachlorides (Th, Pa, U, and Np) and tetrabromides (Th and Pa)". In: *Journal of the Chemical Society, Dalton Transactions* 6 (1973), pp. 686–691.

[9] E Capelli. "Thermodynamic characterization of salt components for Molten Salt Reactor fuel". PhD thesis. Delft University of Technology, 2016.

[10] E. Capelli and R.J.M. Konings. "Halides of the Actinides and Fission Products Relevant for Molten Salt Reactors". In: *Comprehensive Nuclear Materials*. Elsevier, 2020.

[11] E. Capelli et al. ""Thermodynamic investigation of the LiF–ThF_4 system ""." In: *The Journal of Chemical Thermodynamics* 58 (2013), pp. 110–116.

[12] P. Chiotti et al. "Heats of Fusion and Transformation for Some Metals and Compounds." In: *Journal of Chemical and Engineering Data* 11.4 (1966), pp. 571–574.

[13] V. Danek. *Physico-chemical analysis of molten electrolytes*. Elsevier, 2006.

[14] R. Dawson, E.B. Brackett, and T.E. Brackett. "A high temperature calorimeter; the enthalpies of α-aluminum oxide and sodium chloride". In: *The Journal of Physical Chemistry* 67.8 (1963), pp. 1669–1671.

[15] H.L. Deubner, S.S. Rudel, and F. Kraus. “A simple access to pure thorium (IV) halides ($ThCl_4$, $ThBr_4$, and ThI_4)”. In: *Zeitschrift für anorganische und allgemeine Chemie* 643.23 (2017), pp. 2005–2010.

[16] N. Edelstein et al. *The Chemistry of the Actinide and Transactinide Elements*. 2011.

[17] R. Elson et al. “The tetravalent and pentavalent states of Protactinium”. In: *Journal of the American Chemical Society* 72.12 (1950), pp. 5791–5791.

[18] Scientific Group Thermodata Europe. *SGPS-SGTE Pure substances database (v13.1), 2018. (Accessed via FactSage 7.2)*.

[19] L. Eyring and Edgar F. Westrum Jr. “The Heat of Formation of Thorium Tetrachloride1a”. In: *Journal of the American Chemical Society* 72.12 (1950), pp. 5555–5556.

[20] C.W. Forsberg. “Reactors with molten salts: options and missions”. In: *Frederick Joliot & Otto Hahn Summer School on Nuclear Reactors, Physics and Fuels Systems, Cadarache, France* (2004).

[21] J. Fuger and D. Brown. “Thermodynamics of the actinide elements. Part IV. Heats and free energies of formation of the tetrachlorides, tetrabromides, and tetraiodides of thorium, uranium, and neptunium”. In: *Journal of the Chemical Society, Dalton Transactions* 4 (1973), pp. 428–434.

[22] A.Y. Gershanovich and I.G. Suglobova. “Thermographic and x-ray diffraction studies of binary systems formed by thorium tetrachloride with potassium, rubidium, and cesium chlorides.” In: *Radiokhimiya* 22.2 (1980), pp. 265–270.

[23] V.P. Glushko et al. “The IVTAN Data Bank on the Thermodynamic Properties of Individual Substances”. In: (1978).

[24] D.M. Gruen and R.L. McBeth. “Tetrahedral $NiCl_4$- Ion in Crystals and in Fused Salts. Spectrophotometric Study of Chloro Complexes of Ni (II) in Fused Salts”. In: *The Journal of Physical Chemistry* 63.3 (1959), pp. 393–398.

[25] D. Haas, M. Hugon, and M. Verwerft. “Overview of European Experience with Thorium Fuels”. In: *Nuclear Back-end and Transmutation Technology for Waste Disposal* (2015), p. 197.

[26] B.A. Hombourger. “Thermochemical investigation of molten fluoride salts for Generation IV nuclear applications-an equilibrium exercise”. PhD thesis. EPFL, 2018.

[27] S. Hubert et al. “Observation of a phase transition in $ThBr_4$ and $ThCl_4$ single crystals by far-infrared and Raman spectroscopy study”. In: *Journal of Solid State Chemistry* 36.1 (1981), pp. 36–44.

[28] O.J. Kleppa and G.N. Papatheodorou. “Enthalpies of mixing of binary liquid mixtures of cadmium chloride with cesium and lithium chlorides”. In: *Inorganic Chemistry* 10.4 (1971), pp. 872–873.

[29] R.J.M. Konings. “The heat capacity and entropy of actinide (IV) compounds”. In: *The Journal of Chemical Thermodynamics* 36.2 (2004), pp. 121–126.

[30] C. Kraus. *Phase Diagram of Some Complex Salts of Uranium with Halides of the Alkali and Alkaline Earth Metals*. Tech. rep. Naval Research Laboratory, 1943.

[31] T. Kuroda and T. Suzuki. “The Equilibrium State Diagrams of UCl_4-NaCl, UCl_4-KCl, UCl_4-$CaCl_2$ and UCl_4-$BaCl_2$ Systems”. In: *Journal of The Electrochemical Society of Japan* 26.7-9 (1958), E140–E141.

[32] D. LeBlanc. “Molten salt reactors: A new beginning for an old idea”. In: *Nuclear Engineering and Design* 240.6 (2010), pp. 1644–1656. ISSN: 0029-5493.

[33] J. Leitner et al. “Application of Neumann–Kopp rule for the estimation of heat capacity of mixed oxides”. In: *Thermochimica Acta* 497.1-2 (2010), pp. 7–13.

[34] J.B. Liu et al. “Polarizable force field parameterization and theoretical simulations of $ThCl_4$–LiCl molten salts”. In: *Journal of Computational Chemistry* 39.29 (2018), pp. 2432–2438.

[35] A. Manzoor et al. “Entropy contributions to phase stability in binary random solid solutions”. In: *Computational Materials* 4.1 (2018), pp. 1–10.

[36] Richard Martin. *Superfuel: thorium, the green energy source for the future*. St. Martin’s Press, 2012.

[37] J.T. Mason, M.C. Jha, and P. Chiotti. “Crystal structures of $ThCl_4$ polymorphs”. In: *Journal of the Less Common Metals* 34.1 (1974), pp. 143–151.

[38] R.C.L. Mooney. “"The crystal structure of $ThCl_4$ and UCl_4"”. In: *Acta Crystallographica* 2.3 (1949), pp. 189–191.

[39] K.F. Mucker et al. “Refinement of the crystal structure of $ThCl_4$”. In: *Acta Crystallographica Section B: Structural Crystallography and Crystal Chemistry* 25.11 (1969), pp. 2362–2365.

[40] I.G. Murgulescu et al. “Heat Capacities in Molten Alkaline Halides”. In: *Rev. Roumaine Chim.* 22.5 (1977), pp. 683–689.

[41] J.A. Ocádiz Flores et al. “Thermodynamic Description of the ACl-ThCl4 (A= Li, Na, K) Systems”. In: *Thermo* 1.2 (2021), pp. 122–133.

[42] G.I.L. van Oudenaren, J.A. Ocádiz-Flores, and Smith A.L. “Coupled structural modelling of the molten salt system NaCl-UCl_3”. Submitted. 2021.

[43] R. Oyamada. “Phase Diagrams of $ThCl_4$ Systems Containing NaCl, KCl and LiCl and the Limitation of the Congruently Melting Compounds Formation”. In: *Denki Kagaku Oyobi Kogyo Butsuri Kagaku* 39.1 (1971), pp. 2–5.

[44] G.N. Papatheodorou and O.J. Kleppa. “Enthalpies of mixing in the liquid mixtures of the alkali chlorides with MnCl2, FeCl2 and CoCl2”. In: *Journal of Inorganic and Nuclear Chemistry* 33.5 (1971), pp. 1249–1278.

[45] G.N. Papatheodorou and O.J. Kleppa. “Enthalpies of mixing of liquid nickel (II) chloride-alkali chloride mixtures at 810 C”. In: *Journal of Inorganic and Nuclear Chemistry* 32.3 (1970), pp. 889–900.

[46] A. D. Pelton et al. “"The modified quasichemical model I—Binary solutions"”. In: *Metallurgical and Materials Transactions B* 31.4 (2000), pp. 651–659.

[47] G.M. Photiadis and G.N. Papatheodorou. “Co-ordination of thorium (IV) in molten alkali-metal chlorides and the structure of liquid and glassy thorium (IV) chloride”. In: *Journal of the Chemical Society, Dalton Transactions* 20 (1999), pp. 3541–3548.

[48] W. Plato. “Erstarrungserscheinungen an anorganischen Salzen und Salzgemischen. I.” In: *Zeitschrift für Physikalische Chemie* 55.1 (1906), pp. 721–737.

[49] B.C. Pyashyenko. In: *Metallurgiya* 10.11 (1935), p. 85.

[50] M. Rand et al. *Chemical Thermodynamics of Thorium*. OECD Nuclear Energy Agency, 2008.

[51] C. Robelin and P. Chartrand. “Thermodynamic evaluation and optimization of the (NaF+AlF_3+CaF_2+BeF_2+Al2O_3+BeO) system”. In: *The Journal of Chemical Thermodynamics* 57 (2013), pp. 387–403.

[52] T. Schleid, G. Meyer, and L.R. Morss. “"Facile synthesis of UCl_4 and $ThCl_4$, metallothermic reductions of UCl_4 with alkali metals and crystal structure refinements of UCl3, UCl_4 and Cs_2UCl_6"”. In: *Journal of the Less Common Metals* 132.1 (1987), pp. 69–77.

[53] P.A. Sellers et al. “The Preparation of Some Protactinium Compounds and the Metal1”. In: *Journal of the American Chemical Society* 76.23 (1954), pp. 5935–5938.

[54] R.D. Shannon. “Revised effective ionic radii and systematic studies of interatomic distances in halides and chalcogenides”. In: *Acta Crystallographica A* 32.5 (1976), pp. 751–767.

[55] A.L. Smith et al. “A new approach for coupled modelling of the structural and thermo-physical properties of molten salts. Case of a polymeric liquid LiF-BeF_2”. In: *Journal of Molecular Liquids* 299 (2020), p. 112165.

[56] B.C. Smith, L. Thakur, and M.A. Wassef. *Thermochemical Studies of Thorium (IV) and Uranium (IV) Chlorides*. Tech. rep. London Univ., 1969.

[57] G.P. Smith, C.R. Boston, and J. Brynestad. “Electronic Spectra and Coordination Geometry in Molten Mixtures of CsCl and NiCl2 Containing up to 60 Mole% NiCl2”. In: *The Journal of Chemical Physics* 45.3 (1966), pp. 829–834.

[58] S. Tanii. “Phase Diagrams of the systems Thorium Chloride-Alkali Chlorides and Thorium Chloride-Alkali Chlorides”. In: *Denki Kagaku Oyobi Kogyo Butsuri Kagaku* 32.2 (1964), pp. 167–170.

[59] R.E. Thoma. *Phase diagrams of nuclear reactor materials*. Vol. 2548. Oak Ridge National Laboratory, 1959.

[60] V.M. Vdovenko, A.Y. Gershanovich, and I.G. Suglobova. “Thermal and x-ray diffraction studies of thorium chloride-lithium chloride and thorium chloride-sodium chloride binary systems”. In: *Radiokhimiya* 16.6 (1974), pp. 886–89.

[61] A.N. Vokhmyakov, V.N. Desyatnik, and N.N. Kurbatov. “Interaction of thorium tetrachloride with chlorides of the alkali metals”. In: *Sov. At. Energy (Engl. Transl.), v. 35, no. 6, pp. 1122-1123* (1973).

4

EXAMINATION OF THE SHORT-RANGE STRUCTURE OF MOLTEN SALTS: ThF_4, UF_4, AND RELATED ALKALI ACTINIDE FLUORIDE SYSTEMS

Jaén A. OCÁDIZ FLORES, Aimen E. GHERIBI, John VLIELAND, Dick DE HAAS, Kathy DARDENNE, Jörg ROTHE, Rudy J.M. KONINGS, Anna Louise SMITH

The short-range structures of LiF-ThF_4, NaF-AnF_4, KF-AnF_4, and Cs-AnF_4 (An = Th, U), were probed using in situ high temperature Extended X-ray Absorption Fine Structure (EXAFS) spectroscopy. Signally, the EXAFS spectra of pure molten ThF_4 and UF_4 were measured for the first time. The data were interpreted with the aid of Molecular Dynamics (MD) and standard fitting of the EXAFS equation. As in related studies, a speciation distribution dominated by $[AnF_x]^{4-x}$ (x = 7, 8, 9) coordination complexes was observed. The average coordination number was found to decrease with the increasing size of the alkali cation, and increase with AnF_4 content. An average coordination number close to 6, which had not been detected before in melts of alkali actinide fluorides, was seen when CsF was used as solvent.

This chapter has been published in *Phys. Chem. Chem. Phys.*, 2021, **23**, (11091-11103) [32].

4.1. INTRODUCTION

Molten salts are a class of ionic liquids which have in recent years been the focus of extensive fundamental research. This can be explained by the fact that they are a versatile class of reaction media, e.g. carbonates, nitrates, fluorides, chlorides, with a variety of melting points, heat capacities, vapor pressures, densities, and other thermophysical properties suited for a variety of industrial applications. The most well-known is perhaps the production of materials as important as aluminum and sulfuric acid, yet thermal energy storage is also a notable application. In the future, molten salts may be used for processes as important as the production of hydrogen [22] and ammonia [30], carbon capture and storage [53], nuclear fuel pyroprocessing [26], and as nuclear fuels [6], [39].

Understanding the speciation and structure of the molten salts, which are closely related to their thermodynamic and transport properties, is crucial for the design and operation of any intended application. Salt systems which have been subject of this type of analysis in the literature include AF-ZrF_4 (A = Li, Na, K), [36], KF-ThF_4 [3], LiF-ThF_4 [46] and LiF-ThF_4-UF_4 systems [5]. In these studies, the experimental technique used is in-situ high temperature Extended X-ray Absorption Fine Structure (EXAFS) spectroscopy. This element-specific, non-destructive, oxidation state-sensitive technique requires very small masses of sample, making it very powerful and ideally suited for radioactive, corrosive salts at high temperature. It provides detailed information about the local structure such as interatomic distances among nearest neighbors and second-nearest neighbor elements.
However, EXAFS spectroscopy of liquids is less straightforward than that of solids because the standard EXAFS equation [31] may be inaccurate to describe the measured experimental data since it relies on a Gaussian distribution of interatomic distances, which liquids do not have. Another approach, known as cumulant expansion, is also inadequate because of a strong correlation between the fitting parameters [16],[35],[3]. Hence, this work relied on configurations generated from Molecular Dynamics (MD) simulations as the underlying structural models. MD has demonstrated already in numerous studies to be a strikingly valuable tool in its own right for calculating the thermo-physical and thermo-chemical properties of molten salts [28], [21], [15], [20]. In other works, our group has presented EXAFS data of the LiF-ThF_4 [46], LiF-UF_4 (submitted), and NaF-ThF_4 [46] systems. In order to arrive at a comprehensive picture of the local structure of alkali actinide fluoride binary systems as a function of the alkali and actinide ions, this work extends to NaF-UF_4 and focuses on larger alkali ions: KF-ThF_4, KF-UF_4, CsF-UF_4, and CsF-ThF_4. Notably, EXAFS data for pure molten ThF_4 and UF_4 were collected for the first time.

4.2. EXPERIMENTAL METHOD

EXAFS measurements were performed at the INE beamline [40] of the KARA (Karlsruhe Research Accelerator) synchrotron facility (Karlsruhe, Germany), with 2.5 GeV and 150-170 mA as operating conditions in the storage ring. The beamline uses a Ge(422) double-crystal monochromator (DCM). Rh-coated mirrors before (flat, cylindrically bent) and

after (toroidal) the DCM are used to collimate and focus the synchrotron beam, respectively, producing a spot size of 300 m × 500 m at the sample surface. Transmission and fluorescence geometries could be measured in unison, and samples were probed at the L_3 edges of Th (16.300 keV) and U (17.166 keV), scanning from ∼16.1 to ∼17.05 keV and ∼17.14 to ∼17.77 keV, respectively.

A dedicated experimental set-up, previously described in detail by Smith et al. [46] and built to operate at the INE beamline, was used for the measurements. The set-up consists of a specifically designed furnace inside a custom-made glovebox. The salts themselves were sealed in pre-dried boron nitride containment cells loaded into the furnace chamber, which was evacuated under operation down to $\sim 2 \cdot 10^{-5}$ mbar to avoid reaction of the salts with residual oxygen or water. Once under vacuum, the samples were heated up to (50 ± 10) K above their liquidus temperatures. Quick scans were made during the heating ramp to detect the melting of the material. If the measurement temperature of the sample was less than the melting point of the pure alkali fluoride end-member, the temperature was ramped up to the melting point of the end-member and held for about 15 minutes to ensure complete melting and homogenization. The temperature was subsequently adjusted to a set value (50 ± 20) K above liquidus. In addition, an equilibration time of ∼15-30 min was employed before collecting the X-ray Absorption Spectroscopy (XAS) data to ensure the signal had stabilized. EXAFS data were collected up to ∼12.5 Å, and were Fourier transformed using the Hanning window over the k-range 3-12 $Å^{-1}$ (dk = 2) for solids, and 3-9 $Å^{-1}$ (dk = 2) for liquids. A step size of 0.8 eV was used in the X-ray absorption near edge structure (XANES) region.

The samples (8-25 mg) were prepared by mixing and grinding stoichiometric amounts of metal fluorides in the desired stoichiometric ratio, and then pressed in the form of pellets of thickness less than 100 m by applying a pressure of 10 tons·cm^{-2}. Sodium, potassium, and cesium fluorides were sourced from Alfa Aesar (99.99%, metals basis) and dried at 673 K for 4 h in an open nickel boat under Ar flow. The thorium fluoride was supplied by the Joint Research Center, Karlsruhe, Germany, ((0.995 ± 0.005), synthesized as described in [47]. The UF_4 was obtained from International Bio-Analytical Industries (0.9999 ± 0.0001 metals basis). All the samples in this work were handled in the inert and dry atmosphere of an argon-filled glovebox (H_2O and O_2 contents below 5 ppm), and in a nitrogen atmosphere when handled in the self-designed glovebox containing the furnace set-up at the KARA-INE beamline.

Each liquid-state scan took close to 30 minutes, and three to four scans were accumulated to be averaged. The energy E_0 of the edge absorption threshold position was identified as the first x-intercept of the second derivative of the signal, which also corresponds to the first inflexion point of the signal. Before averaging, the spectra were aligned with the XANES spectrum of an appropriate reference: a ThO_2-BN pellet in the case of AF-ThF_4 (A = Li, Na, K, Cs) and ThF_4, a metallic yttrium (K edge = 17.0384 keV) plate in the case of AF-UF_4 (A = Na, K, Cs). A UO_2-BN pellet was used as reference for the UF_4 sample at room temperature. The references were located between the second and third ionization chambers and measured simultaneously with the sample. Data treat-

ment of the raw XAS data was done with the ATHENA software [38], version 9.25. The XANES data were analyzed to confirm that the actinide cations remained tetravalent (refer to Electronic Supporting Information, ESI†).
Fitting of the treated data with the standard EXAFS equation was done with Artemis software [38], version 0.8.012. No third-order cumulant parameter was used. The use of the standard EXAFS equation on liquids has limitations, since liquids are highly disordered and display strong anharmonicity. Moreover, the coordination number and distance to nearest neighbor distributions are lost, replaced by averages. To complement the information obtained with fitting, this work has also relied on MD simulations.

4.3. MOLECULAR DYNAMICS SIMULATIONS

MD simulations were performed using the PIMAIM code [28] for all compositions measured by EXAFS at the corresponding experimental temperature: 50 K above the liquidus line. The form of the potential used for the study of these molten salt systems is the Polarizable Ion Model (PIM) [43]. It has been chosen because it has already shown its usefulness in the study of several molten systems such as alkali fluoride mixtures [43], LiF-BeF_2 [20], [41], AF-ZrF_4 (A = Li, Na, K) [36], LiF-UF_4[14], and LiF-ThF_4 [15]. The potential has four contributions with functional forms given in Eq. 5.1 to 5.5: charge-charge (Eq. 5.1), dispersion (Eq. 5.2), overlap repulsion (Eq.5.4) and polarization (Eq.5.5).

- Charge-charge:

$$V_{qq}(r_{ij}) = \sum_{i<j} \frac{q_i q_j}{r_{ij}} \tag{4.1}$$

  where q denotes the ionic formal charges.

- Dispersion:

$$V_{disp}(r_{ij}) = -\sum_{i<j} \left[f_{ij}^6(r_{ij}) \frac{C_{ij}^6}{r_{ij}^6} + f_{ij}^8(r_{ij}) \frac{C_{ij}^8}{r_{ij}^8} \right] \tag{4.2}$$

  where $C_{ij}^6(r_{ij})$ is the dipole-dipole dispersion coefficient and $C_{ij}^8(r_{ij})$ is the dipole-quadrupole dispersion coefficient, while $f_{ij}^6(r_{ij})$ and $f_{ij}^8(r_{ij})$ are Tang-Toennies dispersion damping functions; they are short-range corrections to the asymptotic multipole expansion of dispersions [48]:

$$f_{ij}^n(r_{ij}) = 1 - e^{-b_{ij}^n r_{ij}} \sum_{k=0}^{n} \frac{(b_{ij}^n r_{ij})^k}{k!} \tag{4.3}$$

  This work only consider dipoles and quadrupoles.

- Overlap repulsion

$$V_{rep}(r_{ij}) = \sum_{i<j} A_{ij} e^{-a_{ij} r_{ij}} \tag{4.4}$$

Here A_{ij} and a_{ij} are fitting parameters.

- Polarization

$$\begin{aligned} V_{pol}(r_{ij}) = \sum_{i<j} \Big[q_i \mu_{j\alpha} g_{ij}(r_{ij}) - q_i \mu_{i\alpha} g_{ij}(r_{ij}) \Big] T_{\alpha}^{(1)}(r_{ij}) \\ - \sum_{i<j} \mu_{i\alpha} \mu_{j\beta} T_{\alpha\beta}^{(2)}(r i_{ij}) + \sum_{i} \frac{1}{2\alpha_i} |\mu_i|^2 \end{aligned} \tag{4.5}$$

In the equation above, $T_{\alpha}^{(1)}$ is the charge-dipole interaction tensor, $T_{\alpha\beta}^{(2)}$ is the dipole-dipole interaction tensor, α_i is the polarizability of ion i, and μ_i is the set of dipoles, while $g_{ij}(r_{ij})$ is a damping function given by Eq. 5.6:

$$g_{ij}(r_{ij}) = 1 - C_{ij} e^{-b_{ij} r_{ij}} \sum_{k=0}^{4} \frac{(b_{ij} r_{ij})^k}{k!} \tag{4.6}$$

The parameters were taken from different sources, and are listed in Tables 2 and 2. Aside from LiF-ThF_4, the parameters were not derived *ab initio* especially for the binary systems in this work, but rather for other fluoride-based ionic systems (e.g. pure alkali fluorides).

The systems were equilibrated for 500 ps in the NPT ensemble at 0 GPa and the corresponding temperature 50 K above the liquidus (Table 8), from which the equilibrium volume was taken. This was followed by a 100 ps equilibration and finally a 500 ps production run in the NVT ensemble at the same temperature. Time steps in all runs were set to 0.5 fs, while the relaxation time for both the Nosé-Hoover thermostat and barostat (for the NPT run) was set to 10 ps. The cubic simulation cell contained 600-800 ions in periodic boundary conditions. Cut-offs for the real space part of the Ewald sum and short-range potential were both set to less than half the length of the cell. After the production run, the extracted MD trajectories were used as input for the *ab initio* code FEFF8.40 [1] to compute a simulated EXAFS spectrum, to be compared with experimental data. The effect of anharmonic vibrations and Debye-Waller factor were accounted for by accumulating about 25000 ionic coordinates as input.

4.4. RESULTS AND DISCUSSION

4.4.1. LOCAL STRUCTURE OF URANIUM AND THORIUM TETRAFLUORIDE SOLID VS. LIQUID STATES.

The suitability of the experimental set-up was originally tested on ThF_4(cr) at room temperature as reported in [46]. In a later campaign the EXAFS spectrum of UF_4(cr) was collected and is shown in Fig. 4.1a, 4.1b. Fitting of the latter data (in green) was made

Table 1: Parameter values of the pair-wise ionic interactions in the PIM potential used in this work, with values in atomic units

Ion pair	A_{ij}	a_{ij}	C^6_{ij}	C^8_{ij}	b^6_{ij}	b^6_{ij}	Source
F^--F^-	282.3	2.44	15	150	1.9	1.9	[15]
F^--U^{4+}	70.623	1.666	38.7	387	1.9	1.9	[14]
F^--Th^{4+}	70.148	1.634	38.7	387	1.9	1.9	[15]
F^--Na^+	52.83	1.97	13.25	88.15	1.9	1.9	[42]
F^--K^+	138.8	2.043	3.9	38.7	1.9	1.9	[42]
F^--Cs^+	151.12	1.874	10.95	109.5	1.9	1.9	[43]
An^{4+}-An^{4+}	1	5	100	1000	1.9	1.9	[14]
Th^{4+}-Li^+	1	5	3.16	31.6	1.9	1.9	[14]
Th^{4+}-Na^+	1	5	0.001	0.001	1.9	1.9	[20, 43, 44]
U^{4+}-Na^+	1	5	10	100	1.9	1.9	[43, 42, 18]
An^{4+}-A^+ (An =U, Th; A = K, Cs)	1	5	10	100	1.9	1.9	[43, 18]
Na^+-Na^+	1	5	11.7	51.8	1.9	1.9	[42]
K^+-K^+	1	5	1	10	1.9	1.9	[42]
Cs^+-Cs^+	5000	3	8	80	1.9	1.9	[2]

[a] Modified from c^D_{UF} = -0.84905 in Ref. [14].

using the neutron diffraction refinement by Kern et al. [24] as a structural model. The spectra of molten UF_4 (T = 1357 K, also shown in Fig. 4.1a, 4.1b) and ThF_4 (T = 1433 K, Fig. 4.2) were also collected.

Uranium tetrafluoride is isostructural with thorium tetrafluoride, with space group *C2/c*. There are two uranium sites, both 8-coordinated, with U-F distances within ∼0.1 Å of each other (see Table 4). In EXAFS, the threshold above which it is possible to discriminate between neighboring shells depends on the k-range of the spectra, Δk, as $\Delta R = \pi/(2\Delta k)$. For the solid-state measurement in Fig. 4.1a, $\Delta R = 0.17$ Å. This means that the resolution in this case is not sufficient to distinguish between more than one U-F first coordination shell and more than one U-U second-nearest neighbor shell, so only one of each was included in the fit. The results are summarized in Table 4 and compared with the structural model used. The bond lengths are within error of each other.

In the molten state, the loss of long-range order gives rise to strong damping of the EXAFS signal, as can be seen in Fig. 4.1. The disorder is also manifest in the Fourier transform (FT) modulus of the signal, where the intensity of the first peak in the liquid state is much diminished with respect to that of the solid. Furthermore, the second shell of U neighbors, displayed by the crystal phase as a peak centered at ∼4.5 Å, can no longer be resolved in the liquid. The same is true in the case of ThF_4: the crystal has its second shell centered around ∼4.6 Å [46] and in the liquid it is not visible anymore.

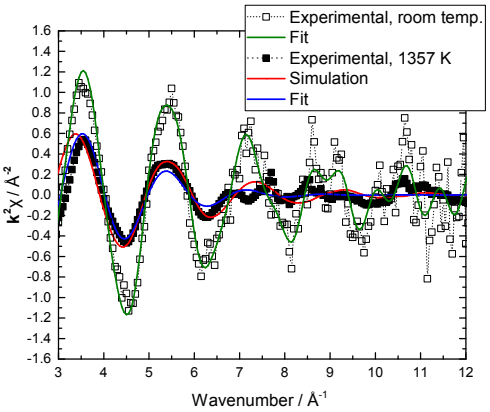

(a)

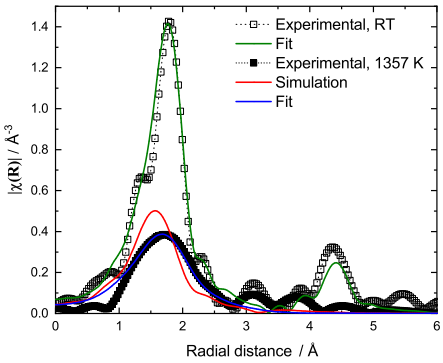

(b)

Figure 4.1: (a) Experimental (fluorescence, room temperature: □, transmission, T = 1357 K: ■), fitted (green, blue) and simulated (red) $k^2\chi(k)$ oscillations of UF_4. (b) Fourier transform moduli $|\chi(R)|$ of the EXAFS spectra.

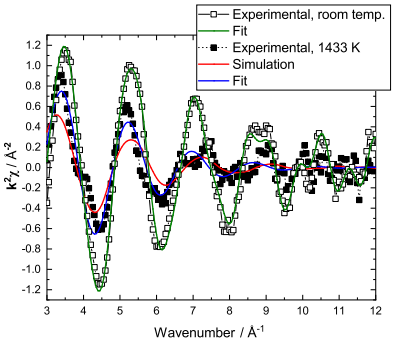

(a)

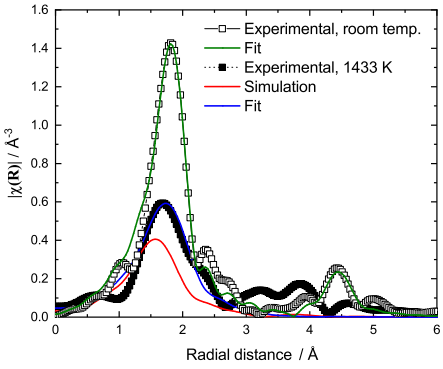

(b)

Figure 4.2: (a) Experimental (transmission, room temperature: □, transmission, T = 1433 K: ■), fitted (green, blue) and simulated (red) $k^2\chi(k)$ oscillations of ThF_4. (b) Fourier transform moduli $|\chi(R)|$ of the EXAFS spectra. Room temperature experimental data and fit taken from Smith et al. [46].

Table 2: Pair-wise damping terms in the PIM potential used in this work

Interaction	b_{ij}^D	c_{ij}^D		Source
F^--U^{4+}	$b_{EU}^D = b_{UF}^D = 1.7516$	$c_{EU}^D = 1.8148$	$c_{UF}^D = 0.84905$[a]	[14]
F^--Th^{4+}	$b_{EU}^D = b_{UF}^D = 1.938$	$c_{EU}^D = 2.791$	c_{UF}^D = -0.60906	[15]
F^--Na^+	$b_{FNa}^D = b_{NaF}^D = 1.84$	$c_{FNa}^D = 2.54$	c_{NaF}^D = -0.19	[42]
F^--K^+	$b_{FK}^D = b_{KF}^D = 1.75$	$c_{FK}^D = 2.5$	c_{KF}^D = -0.31	[42]
F^--Cs^+	$b_{FCs}^D = b_{CsF}^D = 1.93$	$c_{FCs}^D = 3.391$	$c_{CsF}^D = 0.485$	[2]
An^{4+}-A^+ [b]	$b_{AnA}^D = 10.0$	$c_{AAn}^D = 0.001$	-	-

[a] Modified from c_{UF}^D = -0.84905 in Ref. [14].

[b] Not defined elsewhere, set arbitrarily.

Table 3: Polarizabilities of the ions used in the MD simulations, atomic units

Ion	Polarizability	Ref.
F^-	7.8935	[15]
U^{4+}	5.8537	[14]
Th^{4+}	7.696	[15]
Na^+	0.991	[42]
K^+	5.0	[43]
Cs^+	14.8	[2]

STRUCTURAL MODELS FOR LIQUIDS.

Due to the caveats mentioned in the introduction regarding standard fits of the EXAFS equation for disordered states, MD simulations were used to generate atomic positions from which an EXAFS spectrum could be calculated, as described in Section 5.3. The large number of configurations allows to reproduce non-Gaussian features of the radial distribution function (RDF or $g(r)$), such as anharmonic vibrations. Despite the caveats, standard fits were included as well, and the MD results help illustrate why this was not an idle exercise. Fig. 4.3 shows the RDFs of molten UF_4 and ThF_4. It should be noticed that the first peak of the An-F RDFs, although certainly not Gaussian, can be modelled as having this behavior with reasonable accuracy. In contrast, modelling either the remaining peaks in the An-F RDFs or any peaks in the An-An and F-F distributions as Gaussian would be a poor approximation. In short, as long as the fitting of the standard EXAFS equation is limited to the first shell of a pair of species (in this case An-F with A = U, F) with a tail thin enough to resemble a Gaussian, then the fit may contribute useful quantitative information.

The EXAFS oscillations in the molten state become considerably noisy at high wavenumbers, but there is a fair agreement between the first three oscillations in the experi-

Table 4: Local environment around uranium as derived from the present study using EXAFS spectroscopy (room temperature), compared with neutron data from [24]. CN is the coordination number, σ^2 is the Debye-Waller factor, ΔE_0 = 4.8(4) eV is the energy shift from the L_3 edge, R_f = 0.014 is the goodness of fit. Standard deviations are given in parentheses.

Bond	CN	R/Å	σ^2/Å^2
Neutron data from [24]			
U1-F6	2	2.256(4)	
U1-F4	2	2.268(4)	
U1-F7	2	2.280(4)	
U1-F3	2	2.328(4)	
U2-F5	1	2.237(2)	
U2-F1	1	2.247(2)	
U2-F7	1	2.273(2)	
U2-F6	1	2.281(2)	
U2-F3	1	2.286(2)	
U2-F5	1	2.288(2)	
U2-F2	1	2.308(2)	
U2-F4	1	2.313(2)	
U1-U2	2	4.516(2)	
U2-U2	2	4.510(2)	
Averaged neutron data			
U-F	8	2.28(2)	
U-U	2	4.51(4)	
EXAFS data			
U-F	8	2.26(3)	0.008(6)
U-U	2	4.50(2)	0.0001(5)

mental $k^2\chi(k)$ EXAFS signal, the simulation, and the fit. The MD-generated signals are slightly out of phase with the EXAFS signal, which in many cases translates into an over or underestimation of the radial distance of the maximum of $|\chi(R)|$. The fits using the standard EXAFS equation match the phase and the intensity of the experimental signal more closely. However, the fits themselves were directed by the quantitative information which could be directly extracted from the MD trajectories, namely the coordination numbers (Table 8). These tended to be underestimated by the fitting algorithm, a common problem arising when fitting EXAFS signals of liquids [16]. Hence, if a fitting process is deemed appropriate for a given disordered system, it is good practice to combine it with another suitable structural model, e.g. MD, to gauge the results.

FEATURES OF THE RADIAL DISTRIBUTION FUNCTIONS.
A key advantage of using MD as a complementary tool is that a more comprehensive picture of the salt structure emerges than with fitting alone. First, the RDFs in Fig. 4.3,

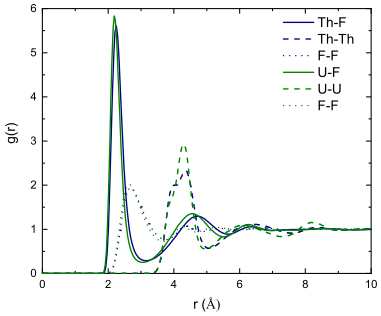

Figure 4.3: Pairwise radial distribution functions of molten UF_4 and ThF_4 calculated with MD at T = 1357 K and T = 1433 K, respectively.

nearly overlapping with each other, readily reveal that UF_4 and ThF_4 are isostructural melts, much like they are isostructural crystals. Second, it is seen that although there is long range order in the molten state, there is a structure of interlocking anionic and cationic coordination shells: three such An-F shells (centered at ∼2.2, ∼4.7, and ∼6.4 Å), are visible for each RDF before stabilizing around the mean value of $g(r) = 1$ (Fig. 4.3). There is a small but non-zero probability of having fluorides as first-nearest neighbors (FNN), yet the electric repulsion makes it is so unfavourable for actinides that such probability is zero. There is also a large probability of finding two actinides within a distance $r < 2 \cdot R_{An-F,cutoff}$, which is the basis for quantifying fluoride bridging between actinide centers, as detailed hereafter.

COORDINATION CHEMISTRY OF MOLTEN THORIUM AND URANIUM TETRAFLUORIDES.
The principal coordination shell is the An-F shell which, despite the thermal disorder, is made up of fluorides tightly bound to the actinide cation. Table 8 lists three different distances to characterize the distribution of distances within this shell: a most probable (R_{max}, corresponding to the maximum of the RDF), a bond cut-off (R_{cutoff}, corresponding to the first minimum of the RDF), and the expected distance E[R], obtained on the one hand by fitting with the standard EXAFS equation and on the other by computing the expectation value between 0 and R_{cutoff}:

$$E[R_{An-F}] = \frac{\int_0^{R_{cutoff}} r \cdot g(r) dr}{\int_0^{R_{cutoff}} g(r) dr} \tag{4.7}$$

The spread between $R_{max,Th-F}$ = 2.26 Å and $R_{cutoff,Th-F}$ = 3.17 Å is 0.91 Å, hence more than 6 times greater than in the solid state (0.141 Å), as derived from neutron diffraction data [46]. In the case of $UF_4(l)$, $R_{cutoff,Th-F}$ - $R_{max,U-F}$ = (3.06 - 2.21) Å= 0.85 Å, about 12 times greater than in $UF_4(cr)$ (0.072 Å, see Section 4.4.1 above). In that sense, there is an expansion of the coordination cage, as remarked by Bessada et al. [5]. Nevertheless, as Liu et al. suggested after finding R_{max} to be smaller than the sum of the

Shannon radii of Th^{4+} and F^-, there is a concordant strengthening of the local structure. Ocádiz-Flores et al. [33] reported the same phenomenon by comparing solid phases occurring in the LiF-UF_4 system with the melts at the corresponding mole fractions. On average, the strengthening can be observed because even though longer bond lengths close to R_{cutoff} become available, shorter bond lengths close to R_{max} are much more populated, with the result that the average U-F distance in the liquid mixtures is equal to or shorter than in the solids. For ThF_4: $E[R]$ = 2.26 < 2.324(19) Å in the solid[1]. For UF_4: $E[R]$ = 2.28 = 2.28(2) Å in the solid[2].
Bessada et al. [5] calculated average bond lengths in the LiF-ThF_4 melt as a function of coordination number, and the former are seen to consistently decrease as the latter increases. This can be explained mainly by an increased repulsion between the F^- ligands with increasing coordination. Decreased shielding from the 2^{nd} shell, evidenced by the absence of an An-An peak in the plots of $|\chi(R)|$ (Figs. 4.1b, 4.2b), is likely to contribute to the shortening of the An-F distance as well [52]. In the liquid phase, the coordination numbers are dominated by CN = 7, 8, 9, with an average close to 8, yet CN = 7 weighs more in the distribution than CN = 9 (see Table 6), allowing for tightening of the cage. It is 8 in the solid state. Finally, in the gas phase, where fluorides are not shared between actinide centers, it is found that E[$R_{Th-F,gas}$] = 2.08 Å [17], and E[$R_{U-F,gas}$] = 2.017(5) Å [25].

STRUCTURE BEYOND THE FIRST COORDINATION SPHERE.
Molten ThF_4 was described by Dai et al. [10] as a network of predominantly corner (∼69%), edge (∼27%), and face-sharing (<4%) $[ThF_n]^{4-}$ (n = 6, 7, 8, 9...) polyhedra. In order to characterize the network of UF_4 and ThF_4 in this work, a linkage analysis was performed by defining a bridging fluoride as one which is part of the first coordination shell of two given An^{4+}, while the distance between the two actinide centers is less than the minimum of their RDF (∼5.1 Å for both actinides, Fig. 4.3). The network structure found for molten UF_4 with a distribution of 70% corner-sharing, 27% edge-sharing, and 3% face-sharing is very similar to that of ThF_4, confirming the view of the melt provided by the RDFs. An MD snapshot of the networks, emphasizing An-An connectivity, is shown in Figure 4.4.

4.4.2. LOCAL STRUCTURE OF THE AF-UF_4 AND AF-ThF_4 MELTS

COORDINATION ENVIRONMENT OF THE ALKALI CATIONS.
As solids, all alkali fluorides crystallize in the rock salt structure (NaCl structure) [7], in which the coordination number is 6. In the molten state, alkali fluorides preserve their strong ionic character and local ordering, and on average have a coordination number close to 5 [52], as can be seen in Fig. 4.5a. In mixtures, as the fluoroacidity of the melt increases with AnF_4 (An = Th, U) content, fluoride donation by the alkalis is evidenced by a growing A-F distance (Fig. 4.5a). The gap between the A-F distance in molten alkali actinide fluorides and pure AF melts grows in the order Li< Na< K< Cs. This growing

[1] From neutron diffraction data, [46]
[2] Averaged from the crystallographic data in [24].

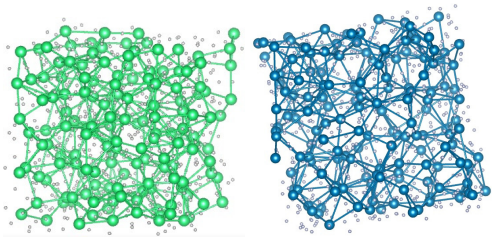

(a) (b)

Figure 4.4: (MD snapshot of (a) molten UF_4 and (b) ThF_4 at the EXAFS measurement temperatures, T = 1357 K and 1433 K, respectively, emphasizing An-An connectivity (U: green, Th: blue). Fluoride ions shown in gray.

distance is coupled with a substantial increase in the coordination number of the alkali cation (Fig. 4.5b). The general trends of the radial distance and coordination number of the alkali cations suggest that uranium molten fluorides are slightly more fluoroacidic than those of thorium, probably due to the actinide contraction.

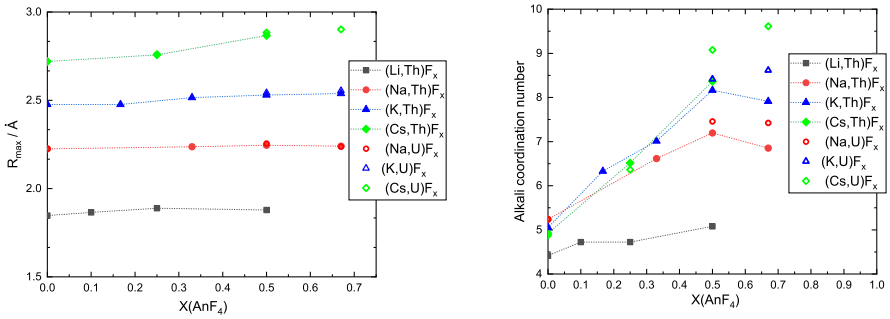

(a) (b)

Figure 4.5: (a) Most probable A-F (A = Li, Na, K, Cs) distance and (b) average coordination number around the alkali cations in the (A,An)F_x solutions as a function of composition, calculated with MD in this work. Temperatures are variable; they are indicated in Table 6. For the pure AF melts, T = 1200 K for all except NaF with T = 1270 K (above the melting point).

COORDINATION ENVIRONMENT OF THE ACTINIDE CATIONS.

This section presents EXAFS measurements carried out in the molten state for seven different alkali actinide fluoride systems at a few representative compositions. As above, accompanying the experimental data are the simulated EXAFS oscillations, generated as described in Section 5.3. The Fourier Transform moduli of the signals are shown alongside the EXAFS oscillations (Figs. 4.6-4.12). The features of the EXAFS spectra are similar to those of the end-members: damped sinusoidal oscillations, and $|\chi(R)|$ signals of which the only discernible peak is that of the An-F first solvation shell. The characteris-

tics of this shell as studied with MD and with standard fitting are summarized in Table 8. The composition LiF:ThF_4 = (0.75:0.25) (Fig. 4.6), which can be singled out because of its importance as Molten Salt Fast Reactor (MSFR) fuel , is compared with data by Bessada et al. [5]. Although recorded at different temperatures, the spectra are comparable to each other. The experimental data for all compositions can be found in the ESI†.

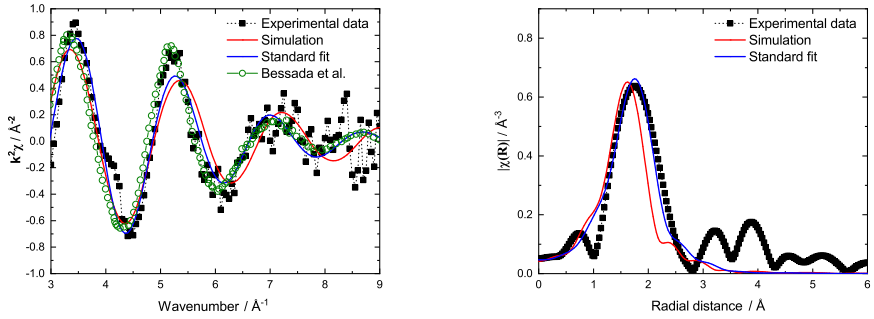

(a) (b)

Figure 4.6: (a) Experimental (■, [46]), simulated (red), and fitted (blue) $k^2\chi(k)$ oscillations of (LiF:ThF_4) = (0.75:0.25) (fluorescence, T = 898 K). Dotted green line: experimental data by Bessada et al. [5] at the same composition (absorption, T = 973 K). (b) Fourier transform modulus $|\chi(R)|$ of the EXAFS spectra.

Table 6 lists the distribution and expected values of coordination numbers as calculated in this work. They are also plotted in Fig. 4.13. In agreement with previous studies [10, 46, 5, 18, 4, 15], the distribution ranges between 6 and 10. From the works related to LiF-ThF_4 and LiF-UF_4 melts [46, 10, 15, 3, 14, 18, 33], it is clear that the dominant contributions are from CN = 7, 8, and 9 at all temperatures and compositions. Guo et al. [18], who performed MD calculations of dilute solutions of ThF_4 in AF (A = Li, Na, K) systems, observed a bimodal distribution with virtually only $[ThF_7]^{3-}$ and $[ThF_8]^{4-}$ complexes present, and very small concentrations of $[ThF_9]^{5-}$ (mean values at 1373 K indicated in cyan in Fig.4.13). Bessada et al. report the following mean CN in the NaF-ThF_4 system at 1223 K: 7.6 for X(ThF_4) = 0.10, ∼7.8 for X(ThF_4) = 0.45, and ∼8.0 for X(ThF_4) = 0.6 [5]. These results correlate well with those in Table 8, where it can be seen that NaF-UF_4 behaves similarly.

In the KF-ThF_4 system it was found previously [4], also with a combined EXAFS-MD approach, that the dominant complexes at X(ThF_4) = 0.25, 1073 K, were $[ThF_6]^{2-}$ (14.5%), $[ThF_7]^{3-}$ (68.7%), and $[ThF_7]^{3-}$ (16.8%), for an expected CN of 7.03 [4]. In a later work [5] the authors reported a mean coordination of 7.5 in the KF-ThF_4 system at X(ThF_4) = 0.45, T = 1173 K, and slightly higher at T = 1073 K. These values are in excellent agreement with the data collected in this work, i.e. E[CN] = 7.12 at X(ThF_4) = 0.167, T = 1060 K, E[CN] = 6.99 at X(ThF_4) = 0.33, T = 1123 K, and E[CN] = 7.53 at X(ThF_4) = 0.50, T = 1209 K (Tab. 6).

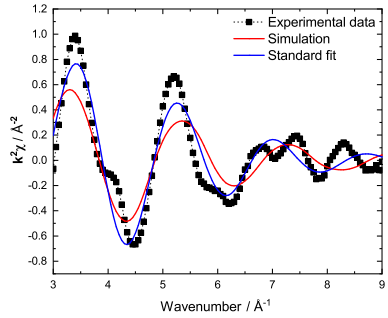

(a)

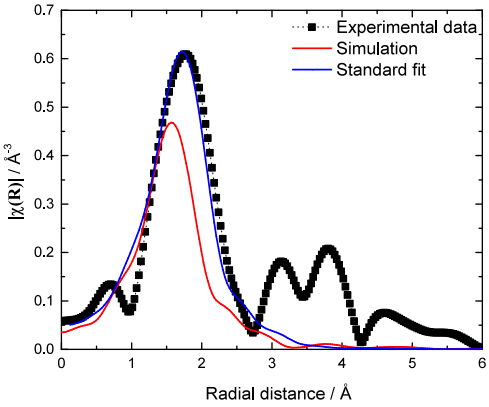

(b)

Figure 4.7: (a) Experimental (■) and calculated (red), and fitted (blue) $k^2\chi(k)$ oscillations of ($NaF:ThF_4$) = (0.33:0.67) (absorption, T = 1252 K). (b) Fourier transform modulus $|\chi(R)|$ of the EXAFS spectra.

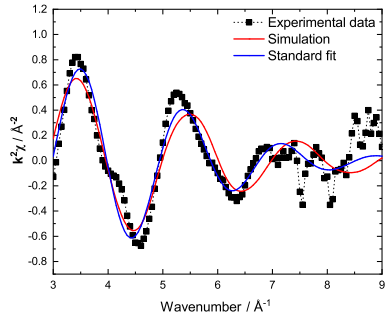

(a)

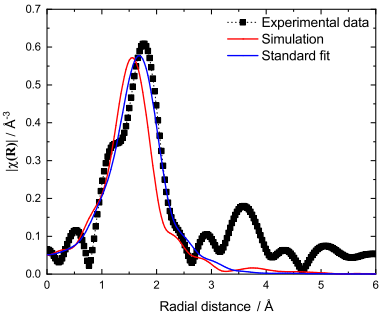

(b)

Figure 4.8: (a) Experimental (■) and calculated (red), and fitted (blue) $k^2\chi(k)$ oscillations of ($NaF:UF_4$) = (0.33:0.67) (absorption, T = 1153 K). (b) Fourier transform modulus $|\chi(R)|$ of the EXAFS spectra.

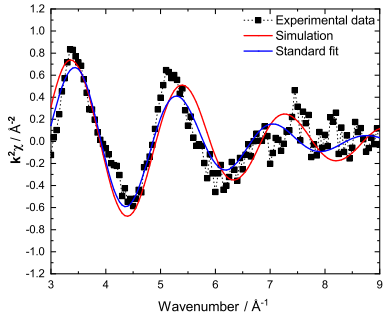

(a)

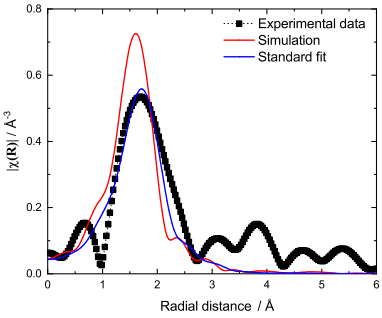

(b)

Figure 4.9: (a)Experimental (■), simulated (red), and fitted (blue) $k^2\chi(k)$ oscillations of (KF:ThF_4) = (0.67:0.33) (fluorescence, T= 1123 K). (b) Fourier transform modulus $|\chi(R)|$ of the EXAFS spectra.

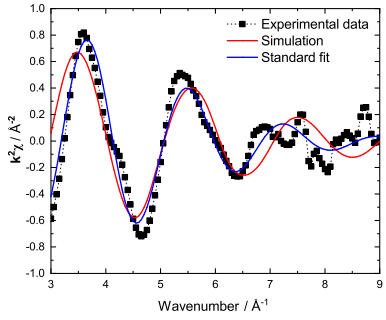

(a)

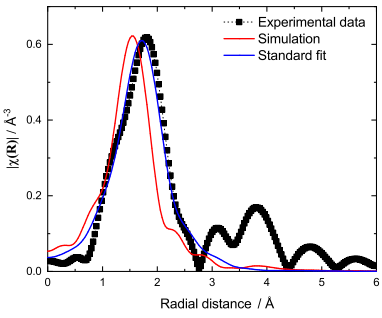

(b)

Figure 4.10: (a) Experimental (■), simulated (red), and fitted (blue) $k^2\chi(k)$ oscillations of (KF:UF_4) = (0.50:0.50) (absorption, T= 1098 K). (b) Fourier transform modulus $|\chi(R)|$ of the EXAFS spectra.

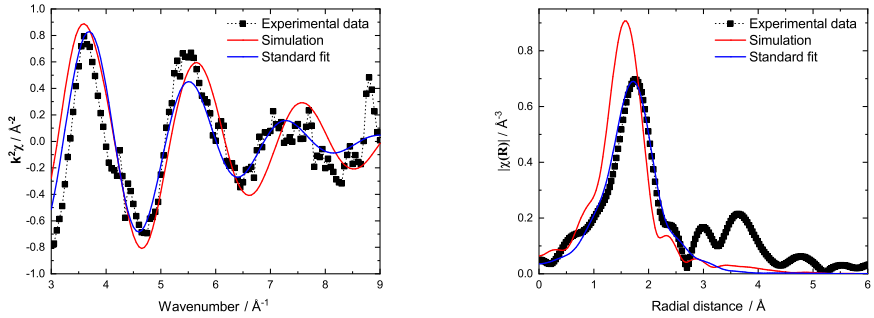

(a) (b)

Figure 4.11: (a) Experimental (■), simulated (red), and fitted (blue) $k^2\chi(k)$ oscillations of ($CsF:UF_4$) = (0.75:0.25) (absorption, T= 1293 K). (b) Fourier transform modulus $|\chi(R)|$ of the EXAFS spectra.

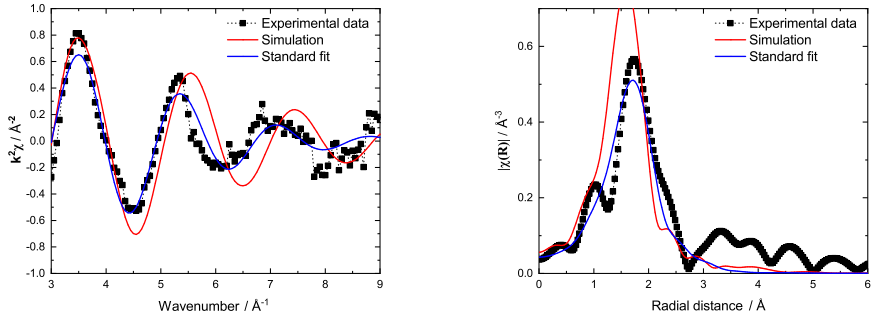

(a) (b)

Figure 4.12: (a) Experimental (■), simulated (red), and fitted (blue) $k^2\chi(k)$ oscillations of ($CsF:ThF_4$) = (0.75:0.25) (absorption, T= 1301 K). (b) Fourier transform modulus $|\chi(R)|$ of the EXAFS spectra.

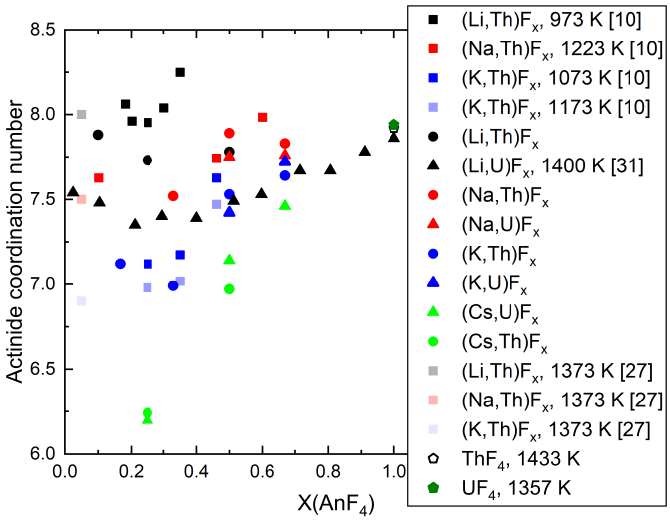

Figure 4.13: Average coordination number in the (A,An)F_x solutions as a function of temperature, and composition, calculated with MD. Unless otherwise indicated, the data is from this work. Where the temperature is not indicated, it is variable, indicated in Table 8.

Finally, there are, to the best of our knowledge, no EXAFS, MD, or otherwise stuctural studies available in the literature on the CsF-AnF_4 (A = U, Th) systems. Like for the other AF-AnF_4 systems, the CN distribution is calculated to be in the 6-10 range, with a small contribution from CN = 9 and a negligible one from CN = 10. The atomic environment for the An^{4+} cations in the crystal phases occurring in the CsF-AnF_4 binary systems is mostly a tricapped trigonal prism (CN = 9) [50] except for an octa-coordinated site in Cs_2UF_6 (space group *Cmcm*, [51]) and an exceptionally rare 1-coordinated site in one of the polymorphs of $CsThF_5$ (space group *P4/nmm* [49]). Hence, as discussed earlier for thorium and uranium tetrafluorides, thermal disorder reduces the coordination number in the first solvation shell, as CN =6 becomes more prevalent than in melts based on other alkali fluorides.
As for the An-F bond length, which was varied freely during the fitting process without constraints based on the MD simulations, the agreement between the fits and the simulations is quite good: in all cases, the average value of the fit falls between the most probable distance and the bond cutoff distance extracted from the MD trajectories, i.e., it is close to the expected value of the simulations.

4.4.3. MAIN STRUCTURAL FEATURES OF THE LIQUID MIXTURES

GENERAL FEATURES.

The An-F, An-An, and A-F RDFs have been plotted for the three most representative compositions: X(AnF_4) = 0.25 along with 0.33, 0.50, and 0.67 in Figs. 4.14-4.16. In a similar

Table 5: Structural information of the first fluoride coordination shell around the actinide ion in different melts as calculated in this work, 50 K above the liquidus line. CN is the coordination number, σ^2 is the Debye-Waller factor, ΔE is the energy shift from the L_3 edge, R_f is the goodness of fit. Standard deviations are given in parentheses. The amplitude reduction factor was fixed as $S_0^2 = 0.9$.

System	$X(AnF_4)^d$	CN_{An-F} MD	CN_{An-F} Fit	R^a_{An-F} MD / Å	R^c_{An-F} MD / Å	$E[R_{An-F}]^b$ MD / Å	$E[R_{An-F}]^b$ Fit / Å	ΔE Fit / eV	σ^2 Fit / Å^2	R_f Fit	T / K
LiF-ThF_4	0.10	7.88		2.21	3.14	2.32	2.34(1)	4(1)	0.020(6)	0.056	1133
	0.25	7.73		2.22	3.15	2.26	2.32(1)	4.59(72)	0.02(2)	0.015	973
	0.50	7.78		2.22	3.15	2.33	2.31(1)	1.31(79)	0.02(3)	0.027	1193
NaF-ThF_4	0.33	7.52	7.4(4)	2.21	3.17	2.31	2.30(1)	6.75(43)	0.020(1)	0.016	1073
	0.50	7.89	7.8(8)	2.20	3.18	2.33	2.34(1)	4.08(86)	0.021(2)	0.035	1108
	0.67	7.83	7.9(7)	2.21	3.18	2.33	2.31(1)	2.52(77)	0.019(1)	0.024	1252
NaF-UF_4	0.50	7.75	7.2(7)	2.15	3.07	2.27	2.26(1)	1.61(87)	0.020(2)	0.036	1033
	0.67	7.76	7.2(7)	2.16	3.05	2.27	2.23(1)	2.26(57)	0.019(2)	0.025	1153
KF-UF_4	0.50	7.42	6.9(4)	2.13	3.09	2.25	2.26(1)	7.07(50)	0.020(1)	0.012	1098
	0.67	7.72	7.8(7)	2.16	3.07	2.27	2.23(1)	2.56(94)	0.02(2)	0.049	1090
KF-ThF_4	0.167	7.12	7.0(7)	2.22	3.23	2.28	2.29(1)	3.71(94)	0.018(2)	0.033	1060
	0.33	6.99	6.5(8)	2.19	3.15	2.27	2.30(1)	2(1)	0.017(3)	0.048	1123
	0.50	7.53	7.6(8)	2.18	3.23	2.31	2.31(1)	3.17(92)	0.024(2)	0.040	1209
	0.67	7.70	8.0(4)	2.20	3.20	2.33	2.33(5)	-1(1)	0.020(3)	0.089	1266
CsF-ThF_4	0.25	6.24	6.6(7)	2.15	3.16	2.21	2.29(1)	3.65(92)	0.020(2)	0.043	1301
	0.50	6.97	6.9(5)	2.14	3.25	2.27	2.33(1)	4.48(64)	0.016(1)	0.028	1201
CsF-UF_4	0.25	6.2	7.0(6)	2.12	3.11	2.17	2.25(1)	7.48(78)	0.018(2)	0.027	1293
	0.50	7.14	7.8(6)	2.12	3.11	2.23	2.26(1)	2.75(71)	0.020(2)	0.019	1058
	0.67	7.46	8.2(8)	2.14	3.08	2.26	2.26(1)	-0.72(99)	0.021(2)	0.048	1191
ThF_4	1	7.92	8.0(8)	2.26	3.17	2.34	2.32(1)	2.38(87)	0.020(2)	0.035	1433
UF_4	1	7.94	8.0(7)	2.21	3.06	2.28	2.27(1)	3.52(71)	0.030(2)	0.031	1357

[a]Most probable distance,[b]expected value,[c]bond cut-off = maximum An-F distance.

[d]Standard uncertainty on the composition of starting reagents was u(X(AnF_4)) = 0.005.

[e]Standard uncertainty on the temperature is estimated to be u(T) =10 K.

Table 6: Coordination number distribution and expected CN of the EXAFS samples studied in this work

System	X(AnF_4)	Anionic Fraction $[AnF_x]^{4-x}$					Expected value
		6	7	8	9	10	CN
LiF-ThF_4	0.10	0.008	0.243	0.612	0.134	0.003	7.88
	0.25	0.037	0.322	0.518	0.121	0.004	7.73
	0.50	0.040	0.315	0.476	0.157	0.012	7.78
NaF-ThF_4	0.33	0.055	0.432	0.442	0.070	0.002	7.52
	0.50	0.0271	0.271	0.505	0.184	0.0134	7.89
	0.67	0.0367	0.294	0.484	0.171	0.0137	7.83
NaF-UF_4	0.5	0.036	0.323	0.503	0.133	0.006	7.75
	0.67	0.038	0.322	0.491	0.141	0.007	7.76
KF-ThF_4	0.167	0.836	0.163	0.001	0.0	0	7.12
	0.33	0.233	0.551	0.206	0.010	$5.85 \cdot 10^{-5}$	6.99
	0.5	0.089	0.396	0.412	0.098	0.005	7.53
	0.67	0.060	0.343	0.449	0.139	0.010	7.70
KF-UF_4	0.5	0.106	0.440	0.388	0.065	0.002	7.42
	0.67	0.041	0.333	0.491	0.129	0.006	7.72
CsF-UF_4	0.25	0.806	0.193	0.003	0.00	0.00	6.20
	0.5	0.209	0.475	0.283	0.033	$7.48 \cdot 10^{-4}$	7.14
	0.67	0.103	0.422	0.392	0.079	0.003	7.46
CsF-ThF_4	0.25	0.771	0.223	0.006	$3.31 \cdot 10^{-5}$	0	6.24
	0.5	0.294	0.469	0.212	0.025	$7.94 \cdot 10^{-4}$	6.97
ThF_4	1	0.034	0.262	0.473	0.210	0.021	7.92
UF_4	1	0.023	0.250	0.509	0.201	0.018	7.94

way to the pure actinide salts, a structural motif of interlocking shells can be observed: every distribution, with the exception of those for AnF_4 dissolved in CsF at concentration $X(AnF_4) = 0.25$, displays at least three local maxima before tending to bulk behavior. Hence there is strong ionic ordering, the characteristic range of which is around 3-4 hydrodynamic radii. In the special case of the An-F bond, there is also a degree of covalency, as indicated by the deep first minimum of the RDFs, whereas the broader peaks and shallower minima in the rest of the RDFs indicate more dynamic ion clusters in which a faster exchange of F^- ions occurs [27]. The ordering is strong enough so as to guarantee that no An-An or An-A FNN exist, yet weak enough such that A-A and F-F FNN are possible (see ESI for An-A, A-A, and F-F RDFs)†.

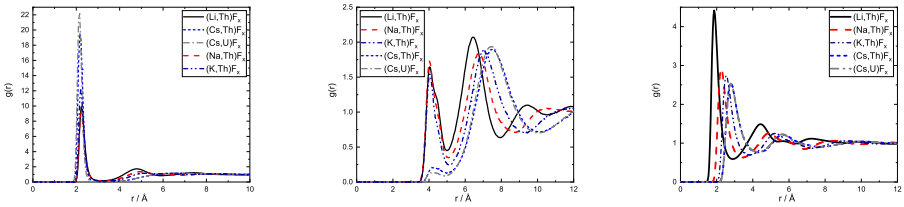

(a) (b) (c)

Figure 4.14: Radial distribution functions: (a) An-F, (b) An-An, and (c) A-F in the AF-AnF_4 melts at composition $X(AnF_4) = 0.25$ (Li and Cs-based melts) and $X(AnF_4) = 0.33$ (Na and K-based melts).

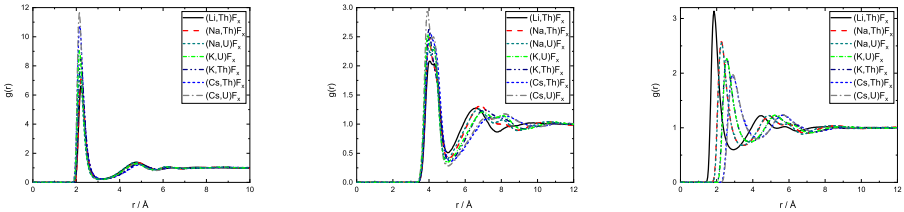

(a) (b) (c)

Figure 4.15: Radial distribution functions: (a) An-F, (b) An-An, and (c) A-F in the AF-AnF_4 melts at composition $X(AnF_4) = 0.50$.

The data available, with varying compositions across systems, allow for three main trends to be observed: i) trends across composition, ii) trends as a function of the actinide metal, and iii) trends as a function of the alkali metal.

TRENDS AS A FUNCTION OF COMPOSITION.
The RDFs in general vary little with increasing AnF_4 content, with the exception of An-An. At $X(AnF_4)$= 0.25 and 0.33 there is a first maximum centered close to 4 Å which is of

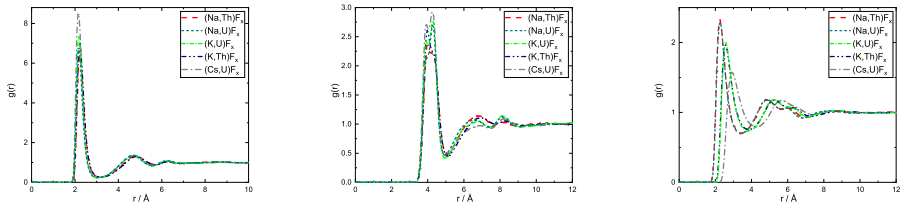

(a) (b) (c)

Figure 4.16: Radial distribution functions: (a) An-F, (b) An-An, and (c) A-F in the AF-AnF_4 melts at composition X(AnF_4) = 0.67.

lower intensity than the following one centered between 6 and 7 Å: it is more probable at that composition for An centers to be farther away from each other than second-nearest neighbors (SNN) because it is more favorable for alkali cations to occupy SNN sites. In melts richer in AnF_4 the An number density makes it more likely that actinide pairs will be SNN, so likely indeed that fluoride bridging is still possible, even in the presence of bulky Cs^+ cations. This change is apparent in the An-F RDFs when going from being dissolved in CsF (X(AnF_4) = 0.25) to AnF_4 being the solvent (X(AnF_4) = 0.67): in the former case only the first shell is distinguishable, while at the other two compositions there is a second shell centered at $\sim$4.8 Å where the majority of the fluorides meet the fluoride bridging criteria for r: r < 5.1 Å $\sim R_{An-An,max}$ and r < 6.2 Å $\sim 2R\cdot_{An-F,max}$.
The An-F bond cutoffs are not very sensitive to composition, a result which agrees with the analysis of Th-F [27], U-F [33], and Zr-F [36] bond lengths in mixtures with LiF. $R_{cutoff,An-F}$, however, becomes slightly more populated as the actinide cations start competing with each other for the fluoride counter ions, which results in an increase in the average bond length and the average coordination number. This increase is not monotonic, and actually both quantities were found to go through a minimum between 20 and 30 mol%, (where F:Th $\sim$7) in isothermal studies of AF-ThF_4 (A = Li, Na, K) mixtures [5]. This effect can be seen in Fig 4.13 as well.

TRENDS AS A FUNCTION OF THE TETRAVALENT CATION.
The F-F, A-A, An-A, (see ESI†) and An-An radial distribution functions (Figs. 4.14b, 4.15b, 4.16b) change very little with respect to each other upon replacement from Th^{4+} to U^{4+}. Once again the An-F distribution can be singled out. The subtle structural changes are dominated by the actinide contraction, which the potentials reproduce well: for a given alkali cation, the complete U-F bond distribution shortens with respect to that of Th-F as can be seen from the most probable, the expected, and the bond cutoff lengths (Table 8). If the distributions are further compared with AF-ZrF_4 (A = Li, Na, K) liquid solutions, with an even smaller tetravalent cation for a given coordination number [45], the trend is continued, as the bond cutoff distance in that case was identified as $R_{Zr-F,cutoff}$ = 2.8 Å [36]. Correspondingly, the coordination number distribution shifts from being dominated by 7, 8, and 9, in AF-AnF_4 (A = Li, Na, K, An = Th, U) mixtures, with CN = 6 being a negligible contribution, to being dominated by 6, 7, and 8 in ZrF_4-containing melts.

This agrees with the behavior in the solid fluoride compounds: structures with hexa-coordinated An^{4+} (An = Th, U) are unknown, but common in the case of Zr^{4+} [37].

TRENDS AS A FUNCTION OF THE ALKALI CATION.

The substitution of the alkali cation results in pronounced structural changes: all RDFs (Figs. 4.14a- 4.16c) show a marked evolution when the alkali cation is substituted. The change is dominated by the size of the cation: the RDFs have their maxima ordered from lowest to largest distance in the order Li, Na, K, Cs, except in the case of the An-F distance. The AnF_4 (A = Th, U) salts are Lewis acids, readily accepting fluoride ions from their alkali fluoride solvents or solutes - Lewis bases- to form anionic coordination complexes. As the alkali cation becomes larger, and hence more fluorobasic, the fluorides bind more tightly to their coordinating An^{4+} cation, as can be confirmed from the An-F RDFs (Figs. 4.14a, 4.15a, 4.16a): there is a shift to lower bond lengths and they become sharper, with a lower minimum. A measure of the stabilization of the conjugate base was provided by Pauvert et al. [36], who calculated the lifetimes of the A-Zr coordination complexes in AF-ZrF_4 (A = Li, Na, K) mixtures, and found them to increase in the order Li < Na < K. The authors suggested that bulkier alkali cations implied larger distances between the complexes, in turn increasing the energy barrier to be overcome for a fluoride ion to leave a cage and incorporate into another. In addition, the stability of the conjugate acid A^+ itself also increases because the charge can spread over a larger cationic volume. The large stabilization of the conjugate base $[AnF_x]^{4-x}$ can be most clearly appreciated in Fig. 4.14a. The RDFs corresponding to the (Cs,An)F_x solutions are characterized by only one very sharp peak, followed by a diffuse layer which slowly approximates bulk behavior.

A second measure of the stabilization of the $[AnF_x]^{4-x}$ complexes in alkali fluoride melts is given by the negative mixing enthalpies in these systems. The liquid-liquid mixing enthalpies in AF-ZrF_4 (A = Li, Na, K, Rb) mixtures, are convex curves which become more negative in the order Li, Na, K, Rb [19]. The AF-ThF_4 (A = Li, Na, K) systems [9], [44], [34] obey the same trend. Moreover, the depth of the curves is greater in ZrF_4-based systems, due to the strength of the shorter Zr-F bond. The progressive tightening of the $[AnF_x]^{4-x}$ cage down the alkali family corresponds well to the trend in liquid-liquid mixing enthalpies.

Another important conclusion from the study by Pauvert et al. [36] was that large alkali cations favor lower coordination numbers around zirconium. In NaF and KF-based systems, $[ZrF_8]^{4-}$ complexes were only formed when the concentration of ZrF_4 exceeded 40-45 mol%. More recently, Bessada et al [5] pointed out that shorter AF-AnF_4 (A = Li, Na, K) bond lengths and lower CN are favored as the radius of the alkali cation grows. In the case of CsF-based systems, the trend is accentuated, such that the average CN around the tetravalent actinides is heretofore unseen: as low as 6.2 at X(AnF_4) = 0.25 (Table 8).

4.4.4. IMPLICATIONS FOR THE TRANSPORT PROPERTIES: VISCOSITY AND ELECTRICAL CONDUCTIVITY

Bessada et al. [5] pointed out that the viscosity of LiF-AnF_4 (A= Th, U) mixtures should be greater than that of LiF-ZrF_4 at a the same molar composition, since in the latter

system the emergent ionic network is weaker, having instead more stable coordination anions. At a given temperature, a dissociated melt should be less viscous than a molecular one, which in turn should be less viscous than a polymerized one. Nevertheless, it is interesting to consider the role of the alkali cation: the heavier and larger cations stabilize the coordination shell around the tetravalent cation, yet make the network more fragile [54], [36]. These two trends should have opposite effects, resulting in a non-monotonic increase of viscosity with AnF_4 concentration. This is what is observed in Fig. 4.17, adapted from [13]. At a temperature of 1230 K, LiF-UF_4, with relatively weak complexes but little ability to disrupt the ionic network, displays a viscosity increasing monotonically with UF_4 concentration. The KF-UF_4 system on the other hand, displays a local maximum in the vicinity of $X(UF_4) = 0.33$. The MD trajectories of the analogous Th composition KF:ThF_4 = (0.67:0.33) reveal a large fraction ($\sim$0.5) of isolated $[ThF_x]^{4-x}$ complexes. Then, there is a local minimum of the viscosity near $X(UF_4) = 0.5$. The KF:UF_4 = (0.5:0.5) simulation of the EXAFS sample, shows a large extent of network formation, ($\sim$66.5%), but the network appears to be fragile enough that the composition with more long-lived isolated complexes ($X(UF_4 \sim 0.33$) has a greater viscosity. From $X(UF_4) = 0.5$ onwards, the network becomes more robust as K^+ is diluted, and the viscosity increases, now monotonically.

While the viscosities of CsF-AnF_4 systems have not been measured, the electrical conductivities of AF-AnF_4 (A = Li, Na, K, Rb, Cs; An = Th, U) are available in the literature [29], [11], [12], and a similar interpretation may be given. For isotherms across AnF_4 mole fraction, the increasing alkali radius is reflected in decreasing electrical conductivities. The conductivities of AF-AnF_4 (A = Li, Na; An = Th, U) do not go through local minima, while those of KF, Rb, and CsF-based melts have minima in the 30-50 mol% region. The reduced ionic mobilities in those areas suggest that the viscosity could go through a local maximum as seen in Fig. 4.17.

4.5. CONCLUSION

Structural studies of alkali fluoride/actinide fluoride salt mixtures in the molten state have been presented, using a combined EXAFS-MD approach which has proven to be a valuable tool to explore the rich chemistry of molten salt systems. Fitting the standard EXAFS equation was done in parallel, and was shown to be an adequate means to extract information about the first coordination shell of thorium and uranium, provided there is another structural model, e.g. obtained from MD, to constrain the fit to physically realistic values. Remarkably, the EXAFS spectra of pure molten ThF_4 and UF_4 were experimentally measured for the first time: the PIM potential parameters derived *ab initio* by Dewan et al. [15] can approximate them well.

PIM potentials derived for other AF-based systems (A = Na, K, Cs) have shown to have good applicability for the corresponding AF-AnF_4 (An = U, Th) binaries. Fluorides are more loosely bound to alkali cations in mixtures with actinide fluorides than in the pure alkali fluoride melts, while the opposite is true for actinide cations. The observed trends of decreasing average bond length and coordination around the actinide with increasing alkali radius are followed when Cs^+ is present in the melt; surprisingly, Cs^+ can even promote an expected coordination number close to 6, something which had not been

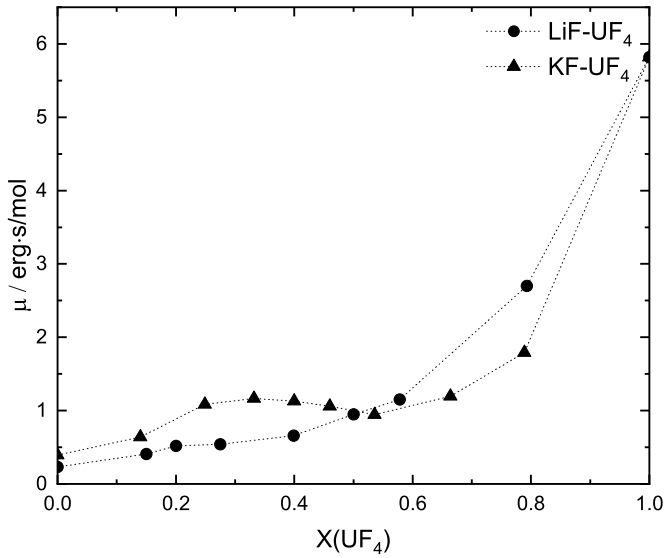

Figure 4.17: Molar viscosity (erg·s/mol) of AF-UF_4 (A = Li, K) melts at an isotherm of T = 1230 K. Adapted from [13].

observed for Li^+, Na^+, or K^+-based systems. The role alkali cations play in stabilizing coordination complexes while destabilizing networks in AF-AnF_4 mixtures, and the opposing effects that might have on the viscosity, was discussed. In future works the role of charge and electronegativity of other families of solvents in molten salt environments will be explored.

4.6. CREDIT AUTHOR STATEMENT

J.A. Ocádiz Flores: Conceptualization, Methodology, Investigation, Formal analysis, Visualization, Data Curation, Writing - Original Draft preparation **A.E. Gheribi**: Investigation **J. Vlieland**: Investigation **D. de Haas**: Investigation **K. Dardenne**: Investigation **J. Rothe**: Investigation **R.J.M. Konings**: Conceptualization, Supervision, Writing - Review & Editing **A.L. Smith**: Conceptualization, Methodology, Investigation, Supervision, Funding acquisition, Resources, Project Administration, Writing - Review & Editing

ACKNOWLEDGEMENTS

The authors would like to thank Pavel Souček and Ondrej Beneš for providing us with ThF_4 of high purity. We also thank Mathieu Salanne for the use of his Molecular Dynamics code, and fruitful discussions on these systems. We acknowledge the KIT light source for provision of instruments at the INE-Beamline of the Institute for Nuclear Waste Disposal and we would like to thank the Insitute for Beam Physics and Technology (IBPT) for the operation of the storage ring, the Karlsruhe Research Accelerator (KARA). A.L. Smith acknowledges financial support from the Netherlands Organisation for Scientific Research (NWO) (project 722.016.005). J.A. Ocádiz-Flores acknowledges CONACYT-SENER for financial support.

4.7. SUPPORTING INFORMATION FOR: EXAMINATION OF THE SHORT-RANGE STRUCTURE OF MOLTEN SALTS: ThF_4, UF_4, AND RELATED ALKALI ACTINIDE FLUORIDE SYSTEMS

4.7.1. COORDINATION ENVIRONMENT OF THE ACTINIDE CATIONS

Herein are the EXAFS measurements carried out in the molten state for seven different alkali actinide fluoride systems at a few representative compositions. Accompanying the experimental data are the simulated EXAFS oscillations, generated using molecular dynamics (MD) positions as input and those via fitting of the standard EXAFS equations. The Fourier Transform moduli of the signals are shown alongside the EXAFS oscillations (Figs. 4.18 to 4.29).

4.7.2. RADIAL DISTRIBUTION FUNCTIONS OF THE LIQUID MIXTURES

The An-F, An-An, and A-F RDFs have been plotted for the three most representative compositions: X(AnF_4) = 0.25 along with 0.33, 0.50, and 0.67 in Figs. 4.30-4.32.

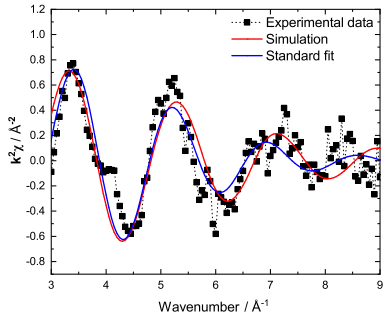

(a)

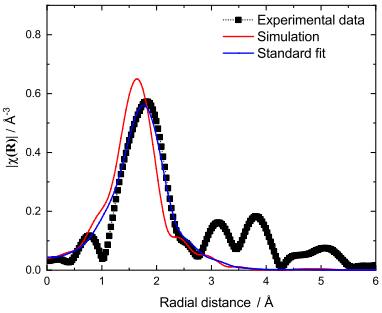

(b)

Figure 4.18: (a)Experimental (■), simulated (red), and fitted (blue) $k^2\chi(k)$ oscillations of (LiF:ThF_4) = (0.90:0.10) (fluorescence, T = 1133 K, data from [46]). (b) Fourier transform modulus $|\chi(R)|$ of the EXAFS spectra.

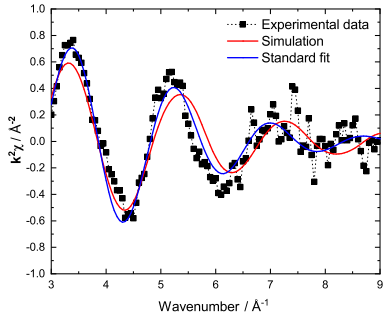

(a)

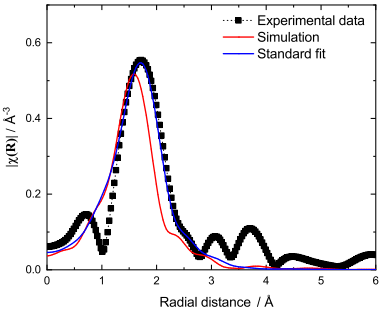

(b)

Figure 4.19: (a)Experimental (■), simulated (red), and fitted (blue) $k^2\chi(k)$ oscillations of (LiF:ThF_4) = (0.50:0.50) (fluorescence, T = 1193 K, data from [46]). (b) Fourier transform modulus $|\chi(R)|$ of the EXAFS spectra.

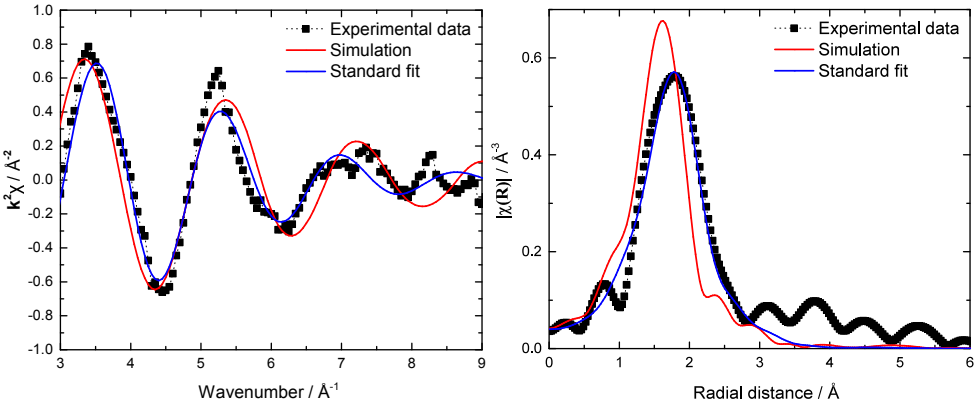

(a) (b)

Figure 4.20: (a)Experimental (■), simulated (red), and fitted (blue) $k^2\chi(k)$ oscillations of (NaF:ThF_4) = (0.67:0.33) (data taken from [46], T = 1073 K measured in absorption). (b) Fourier transform modulus $|\chi(R)|$ of the EXAFS spectra.

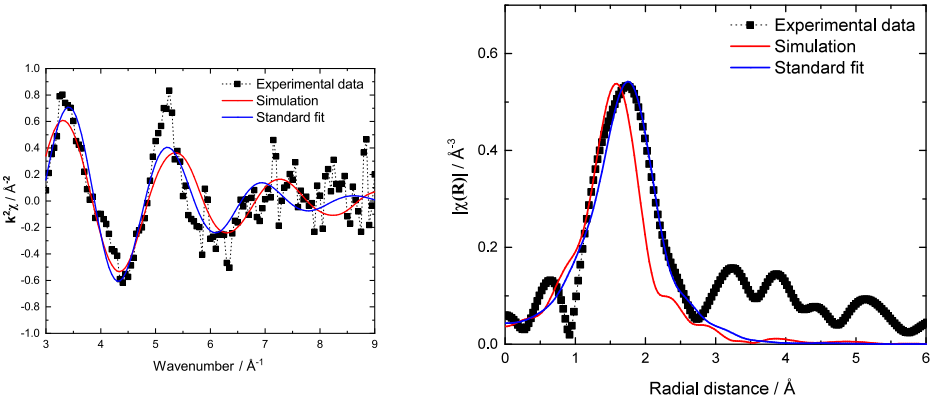

(a) (b)

Figure 4.21: (a)Experimental (■), simulated (red), and fitted (blue) $k^2\chi(k)$ oscillations of (NaF:ThF_4) = (0.50:0.50) (fluorescence, data taken from [46], T= 1108 K). (b) Fourier transform modulus $|\chi(R)|$ of the EXAFS spectra.

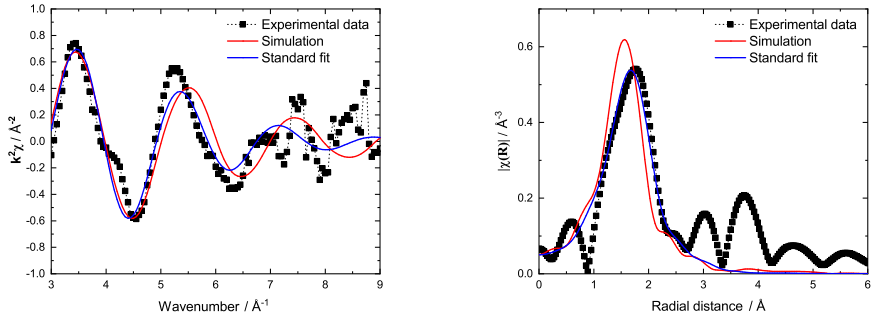

(a) (b)

Figure 4.22: (a)Experimental (■), simulated (red), and fitted (blue) $k^2\chi(k)$ oscillations of ($NaF:UF_4$) = (0.50:0.50) (absorption, T= 1033 K). (b) Fourier transform modulus $|\chi(R)|$ of the EXAFS spectra.

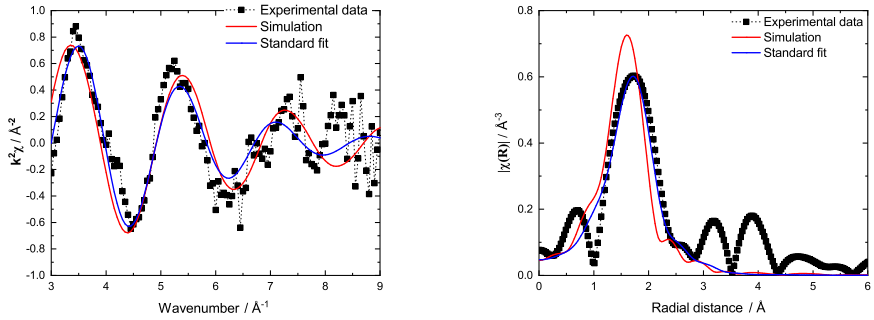

(a) (b)

Figure 4.23: (a)Experimental (■), simulated (red), and fitted (blue) $k^2\chi(k)$ oscillations of ($KF:ThF_4$) = (0.833:0.167) (fluorescence, T= 1060 K). (b) Fourier transform modulus $|\chi(R)|$ of the EXAFS spectra.

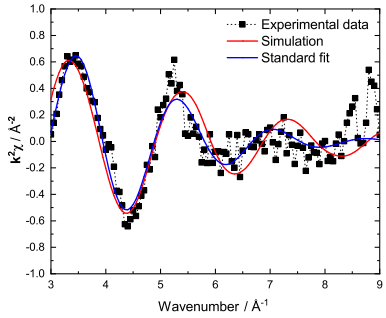

(a)

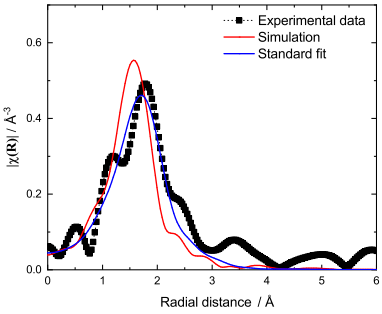

(b)

Figure 4.24: (a)Experimental (■), simulated (red), and fitted (blue) $k^2\chi(k)$ oscillations of (KF:ThF_4) = (0.50:0.50) (fluorescence, T= 1209 K). (b) Fourier transform modulus $|\chi(R)|$ of the EXAFS spectra.

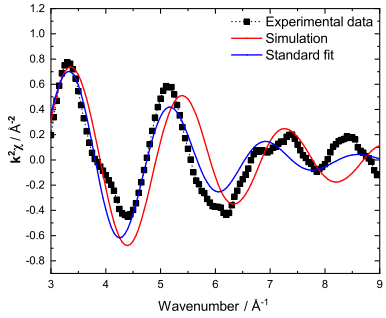

(a)

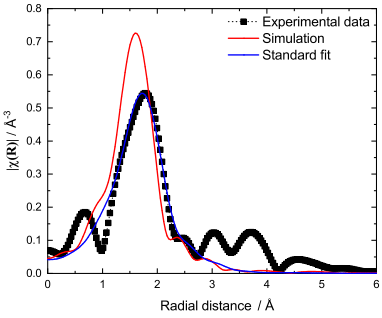

(b)

Figure 4.25: (a)Experimental (■), simulated (red), and fitted (blue) $k^2\chi(k)$ oscillations of (KF:ThF_4) = (0.33:0.67) (absorption, T= 1266 K). (b) Fourier transform modulus $|\chi(R)|$ of the EXAFS spectra.

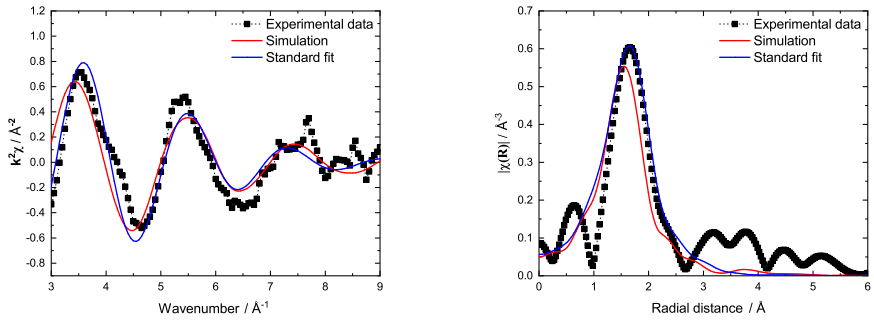

(a) (b)

Figure 4.26: (a)Experimental (■), simulated (red), and fitted (blue) $k^2\chi(k)$ oscillations of (KF:UF_4) = (0.33:0.67) (absorption, T= 1090 K). (b) Fourier transform modulus $|\chi(R)|$ of the EXAFS spectra.

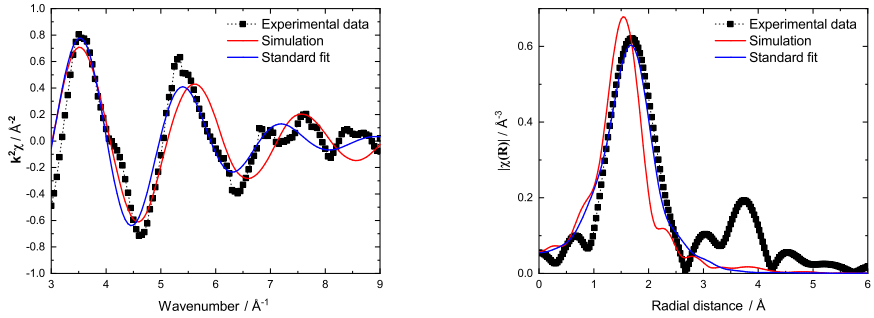

(a) (b)

Figure 4.27: (a)Experimental (■), simulated (red), and fitted (blue) $k^2\chi(k)$ oscillations of (CsF:UF_4) = (0.50:0.50) (absorption, T= 1058 K). (b) Fourier transform modulus $|\chi(R)|$ of the EXAFS spectra.

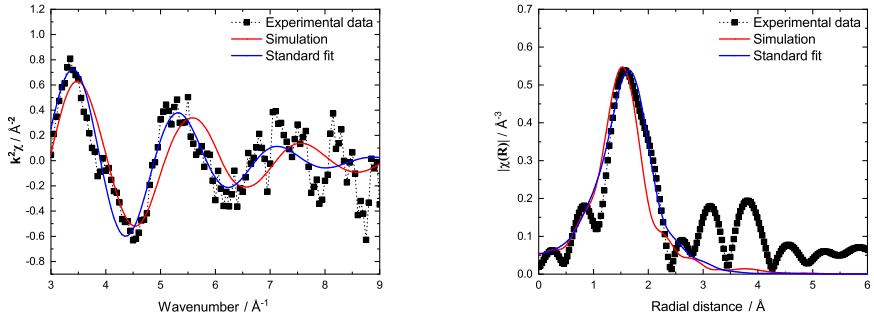

(a) (b)

Figure 4.28: (a)Experimental (■), simulated (red), and fitted (blue) $k^2\chi(k)$ oscillations of (CsF:UF_4) = (0.33:0.67) (fluorescence, T= 1191 K). (b) Fourier transform modulus $|\chi(R)|$ of the EXAFS spectra.

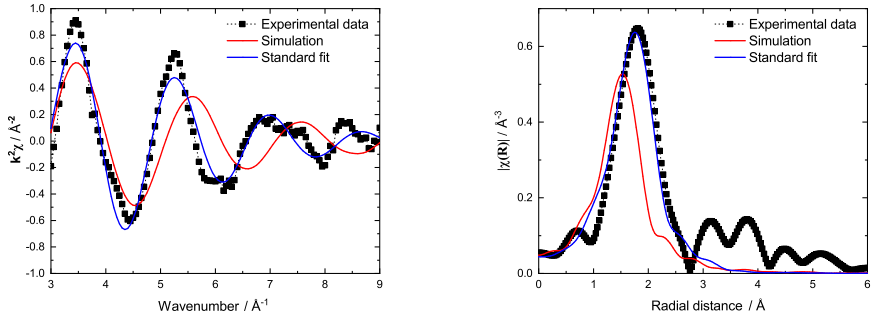

(a) (b)

Figure 4.29: (a)Experimental (■), simulated (red), and fitted (blue) $k^2\chi(k)$ oscillations of (CsF:ThF_4) = (0.50:0.50) (absorption, T= 1201 K). (b) Fourier transform modulus $|\chi(R)|$ of the EXAFS spectra.

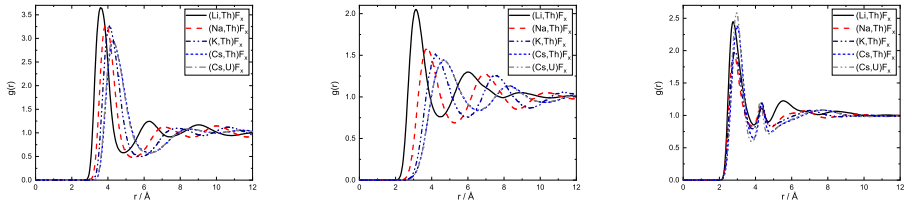

(a) (b) (c)

Figure 4.30: Radial distribution functions: (a) An-A, (b) A-A, and (c) F-F in the AF-AnF_4 melts at composition X(AnF_4) = 0.25 (Li and Cs-based melts) and X(AnF_4) = 0.33 (Na and K-based melts).

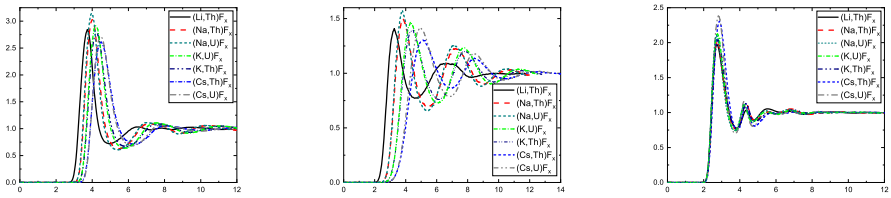

(a) (b) (c)

Figure 4.31: Radial distribution functions: (a) An-A, (b) A-A, and (c) F-F in the AF-AnF_4 melts at composition X(AnF_4) = 0.50.

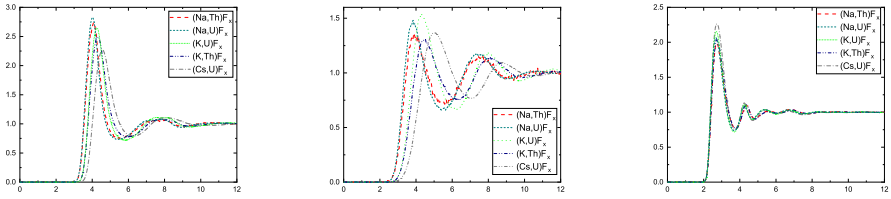

(a) (b) (c)

Figure 4.32: Radial distribution functions: (a) An-A, (b) A-A, and (c) F-F in the AF-AnF_4 melts at composition X(AnF_4) = 0.67.

4.7.3. XANES DATA

Both Th and U remained in the tetravalent oxidation state as revealed by the XANES data. Uranium in particular is problematic, as it has several valence states and may oxidize when exposed to the synchrotron beam, whereas Th may be expected to oxidize only as Th(IV). XANES data of uranium-bearing samples in this work are compared to data of uranium samples in three oxidation states: UO_2 (U(IV)), schoepite (hydrated UO_3, U(VI)), U_3O_8 (U(V)/U(VI)), measured at the same beamline with a metallic yttrium reference, taken from Kegler et al.[23] and Böhler et al. [8]. UO_2, used as a reference for UF_4 at room temperature in this work, is also included. The energy positions of the inflection points and of the white lines are tabulated in Table 7.

Table 7: Energies of the Inflection Points and White Lines of Th-L_3 and U-L_3 XANES Spectra

sample	inflection point (eV)	white line (eV)
ThF_4	16299.9(5)	16305.3(5)
ThO_2 RT	16300.0(5)	16305.2(5)
(LiF:ThF_4) = (0.90:0.10)	16300.0(5)	16304.9(5)
(LiF:ThF_4) = (0.75:0.25)	16298.9(5)	16304.9(5)
(LiF:ThF_4) = (0.50:0.50)	16300.8(5)	16305.1(5)
(NaF:ThF_4) = (0.67:0.33)	16300.1(5)	16304.9(5)
(NaF:ThF_4) = (0.50:0.50)	16299.1(5)	16304.9(5)
(NaF:ThF_4) = (0.33:0.67)	16300.7(5)	16305.1(5)
(KF:ThF_4) = (0.833:0.167)	16298.5(5)	16304.7(5)
(KF:ThF_4) = (0.50:0.50)	16301.0(5)	16305.6(5)
(KF:ThF_4) = (0.33:0.67)	16300.9(5)	16305.0(5)
(CsF:ThF_4) = (0.75:0.25)	16301.2(5)	16305.1(5)
(CsF:ThF_4) = (0.50:0.50)	16302.1(5)	16306.1(5)
UF_4 RT	17169.6(5)	17174.6(5)
UO_2 RT	17170(5)	17175.8(5)
UF_4	17170.4(5)	17176.3(5)
(NaF:UF_4) = (0.50:0.50)	17171.5(5)	17177.0(5)
(NaF:UF_4) = (0.33:0.67)	17170.5(5)	17176.1(5)
(KF:UF_4) = (0.50:0.50)	17170.7(5)	17176.5(5)
(KF:UF_4) = (0.33:0.67)	17171.2(5)	17176.2(5)
(CsF:UF_4) = (0.75:0.25)	17171.2(5)	17176.1(5)
(CsF:UF_4) = (0.50:0.50)	17171.2(5)	17176.1(5)
(CsF:UF_4) = (0.33:0.67)	17170.9(5)	17175.7(5)
Comparison with samples of Kegler et al. [23] (UO_2, schoepite) and Böhler et al. [8] (U_3O_8), RT.		
UO_2	17169.3(5)	17177.72(5)
schoepite	17175.5(5)	17179.73(5)
U_3O_8	17171.7(5)	17180.9(5)

Samples are at high temperature, unless otherwise labeled with room temperature (RT).

BIBLIOGRAPHY

[1] A. L. Ankudinov et al. “Real-space multiple-scattering calculation and interpretation of x-ray-absorption near-edge structure”. In: *Phys. Rev. B* 58 (12 Sept. 1998), pp. 7565–7576.

[2] O. Beneš et al. “Density functional theory, molecular dynamics, and differential scanning calorimetry study of the RbF–CsF phase diagram”. In: *The Journal of chemical physics* 130.13 (2009), p. 134716.

[3] C. Bessada et al. “High temperature EXAFS experiments in molten actinide fluorides: The challenge of a triple containment cell for radioactive and aggressive liquids”. In: *Journal of Nuclear Materials* 494 (2017), pp. 192–199.

[4] C. Bessada et al. “High temperature EXAFS experiments in molten actinide fluorides: The challenge of a triple containment cell for radioactive and aggressive liquids”. In: *Journal of Nuclear Materials* 494 (2017), pp. 192–199.

[5] C. Bessada et al. “Investigation of ionic local structure in molten salt fast reactor LiF-ThF4-UF4 fuel by EXAFS experiments and molecular dynamics simulations”. In: *Journal of Molecular Liquids* 307 (2020), p. 112927.

[6] E. S. Bettis et al. “The aircraft reactor experiment—design and construction”. In: *Nuclear Science and Engineering* 2.6 (1957), pp. 804–825.

[7] H. Bilz and W. Kress. “Alkali Halides (Rock Salt Structure)”. In: *Phonon Dispersion Relations in Insulators*. Springer, 1979, pp. 27–47.

[8] R. Böhler et al. “Recent advances in the study of the UO_2-PuO_2 phase diagram at high temperatures”. In: *Journal of Nuclear Materials* 448.1 (2014), pp. 330–339. ISSN: 0022-3115.

[9] E. Capelli et al. “"Thermodynamic investigation of the LiF–ThF_4 system "”. In: *The Journal of Chemical Thermodynamics* 58 (2013), pp. 110–116.

[10] J. Dai et al. “Molecular dynamics studies of the structure of pure molten ThF_4 and ThF4–LiF–BeF_2 melts”. In: *Journal of Molecular Liquids* 211 (2015), pp. 747–753.

[11] V.N. Desyatnik, A.N. Koverda, and N.N. Kurbatov. “Electrical conductivity of binary fused mixtures of potassium, rubidium, and cesium fluorides with uranium tetrafluoride”. In: *Soviet Atomic Energy* 55.2 (1983), pp. 544–546.

[12] V.N. Desyatnik, A.P. Koverda, and N.N. Kurbatov. “Electrical conductivity of binary melted mixtures of potassium, rubidium, and cesium fluorides with thorium tetrafluoride”. In: *Atomic Energy* 55.1 (1983), pp. 487–488.

[13] V.N. Desyatnik, A.I. Nechaev, and Y.F. Chervinskii. “Viscosities of molten mixtures of uranium tetrafluoride with alkali fluorides”. In: *Soviet Atomic Energy* 46.5 (1979), pp. 408–409.

[14] L. Dewan. “Molecular dynamics simulation and topological analysis of the network structure of actinide-bearing materials”. PhD thesis. Massachusetts Institute of Technology, 2013.

[15] L.C. Dewan et al. “Molecular dynamics simulation of the thermodynamic and transport properties of the molten salt fast reactor fuel LiF–ThF_4”. In: *Journal of Nuclear Materials* 434.1-3 (2013), pp. 322–327.

[16] A. Filipponi. “EXAFS for liquids”. In: *Journal of Physics: Condensed Matter* 13.7 (2001), R23.

[17] G.V. Girichev et al. “Molecular structure and vibrational characteristics of thorium tetrafluoride”. In: *Journal of Structural Chemistry* 40.2 (1999), p. 207.

[18] X. Guo et al. “Theoretical evaluation of microscopic structural and macroscopic thermo-physical properties of molten AF-ThF4 systems (A+= Li+, Na+ and K+)”. In: *Journal of Molecular Liquids* 277 (2019), pp. 409–417.

[19] G. Hatem, F. Tabaries, and M. Gaune-Escard. “Enthalpies de formation des melanges liquides ZrF4-MF (M= Li, Na, K, Rb)”. In: *Thermochimica Acta* 149 (1989), pp. 15–26.

[20] R.J. Heaton et al. “A first-principles description of liquid BeF_2 and its mixtures with LiF: 1. Potential development and pure BeF_2”. In: *The Journal of Physical Chemistry B* 110.23 (2006), pp. 11454–11460.

[21] P. Jemmer et al. “Dipole and quadrupole polarization in ionic systems: Ab initio studies”. In: *The Journal of chemical physics* 111.5 (1999), pp. 2038–2049.

[22] A.R. Kamali. “Clean production and utilisation of hydrogen in molten salts”. In: *RSC Advances* 10.59 (2020), pp. 36020–36030.

[23] P. Kegler et al. “Chemical and structural investigations on uranium oxide-based microparticles as reference materials for analytical measurements”. In: *MRS advances* (2021), pp. 1–6.

[24] S. Kern et al. “Temperature variation of the structural parameters in actinide tetrafluorides”. In: *The Journal of Chemical Physics* 101.11 (1994), pp. 9333–9337.

[25] R.J.M. Konings et al. “The infrared spectrum and molecular structure of gaseous UF4”. In: *Journal of Molecular Structure* 378.2 (1996), pp. 121–131.

[26] James J Laidler et al. “Development of pyroprocessing technology”. In: *Progress in Nuclear Energy* 31.1-2 (1997), pp. 131–140.

[27] J.-B. Liu et al. “Theoretical Studies of Structure and Dynamics of Molten Salts: The LiF–ThF4 System”. In: *The Journal of Physical Chemistry B* 118.48 (2014), pp. 13954–13962.

[28] P.A. Madden and M. Wilson. “‘Covalent’effects in ‘ionic’systems”. In: *Chemical Society Reviews* 25.5 (1996), pp. 339–350.

[29] R.E. Meaker, B. Porter, and D.G. Kesterke. *Electrical Conductivity and Density of Fluoride Systems*. Electrical Conductivity and Density of Fluoride Systems. U.S. Department of Interior, Bureau of Mines, 1971.

[30] T. Murakami et al. “Electrolytic synthesis of ammonia in molten salts under atmospheric pressure”. In: *Journal of the American Chemical Society* 125.2 (2003), pp. 334–335.

[31] M. Newville. “EXAFS analysis using *FEFF* and *FEFFIT*”. In: *Journal of Synchrotron Radiation* 8.2 (Mar. 2001), pp. 96–100.

[32] J.A. Ocádiz-Flores et al. “Examination of the short-range structure of molten salts: ThF_4, UF_4, and related alkali actinide fluoride systems”. In: *Phys. Chem. Chem. Phys.* 23 (18 2021), pp. 11091–11103.

[33] J.A. Ocádiz-Flores et al. “New insights and coupled modelling of the structural and thermodynamic properties of the LiF-UF_4 system”. In: *Journal of Molecular Liquids* 331 (2021), p. 115820.

[34] J.A. Ocádiz-Flores et al. “Thermodynamic assessment of the KF-ThF_4, LiF-KF-ThF_4 and NaF-KF-ThF_4 systems”. In: *The Journal of Chemical Thermodynamics* 145 (2020), p. 106069.

[35] Y. Okamoto. “XAFS simulation of highly disordered materials”. In: *Nuclear Instruments and Methods in Physics Research Section A: Accelerators, Spectrometers, Detectors and Associated Equipment* 526.3 (2004), pp. 572–583.

[36] O. Pauvert et al. “Ion specific effects on the structure of molten AF-ZrF4 systems (A+= Li+, Na+, and K+)”. In: *The Journal of Physical Chemistry B* 115.29 (2011), pp. 9160–9167.

[37] R.A. Penneman, R.R. Ryan, and A. Rosenzweig. “Structural systematics in actinide fluoride complexes”. In: *Rare Earths*. Springer, 1973, pp. 1–52.

[38] B. Ravel and M. Newville. “ATHENA, ARTEMIS, HEPHAESTUS: data analysis for X-ray absorption spectroscopy using IFEFFIT”. In: *Journal of synchrotron radiation* 12.4 (2005), pp. 537–541.

[39] C. Renault et al. “The Molten Salt Reactor (MSR) in Generation IV: Overview and Perspectives”. In: *GIF Symposium, Paris(France), 9-10 September 2009*. 2013, pp. 191–200.

[40] J. Rothe et al. “The INE-Beamline for actinide science at ANKA”. In: *Review of scientific instruments* 83.4 (2012), p. 043105.

[41] M. Salanne et al. “A First-Principles Description of Liquid BeF_2 and Its Mixtures with LiF: 2. Network Formation in LiF- BeF_2”. In: *The Journal of Physical Chemistry B* 110.23 (2006), pp. 11461–11467.

[42] M. Salanne et al. “Heat-transport properties of molten fluorides: Determination from first-principles”. In: *Journal of Fluorine Chemistry* 130.1 (2009), pp. 38–44.

[43] M. Salanne et al. “Including many-body effects in models for ionic liquids”. In: *Theoretical Chemistry Accounts* 131.3 (2012), p. 1143.

[44] M. Schreuder. “Experimental and computational investigations on the NaF-ThF4 system”. MA thesis. Delft University of Technology, 2019.

[45] R.D. Shannon. “Revised effective ionic radii and systematic studies of interatomic distances in halides and chalcogenides”. In: *Acta Crystallographica A* 32.5 (1976), pp. 751–767.

[46] A.L. Smith et al. “In situ high-temperature EXAFS measurements on radioactive and air-sensitive molten salt materials”. In: *Journal of synchrotron radiation* 26.1 (2019), pp. 124–136.

[47] P. Souček et al. “Synthesis of UF_4 and ThF_4 by HF gas fluorination and re-determination of the UF4 melting point”. In: *Journal of Fluorine Chemistry* 200 (2017), pp. 33–40.

[48] K.T. Tang and J.P. Toennies. “An improved simple model for the van der Waals potential based on universal damping functions for the dispersion coefficients”. In: *The Journal of Chemical Physics* 80.8 (1984), pp. 3726–3741.

[49] C.C. Underwood et al. “The polymorphism of CsThF5”. In: *Solid State Sciences* 14.5 (2012), pp. 574–579.

[50] P. Villars and K. Cenzual. “Pearson’s Crystal Data”. In: *Crystal Structure Database for Inorganic Compounds (Materials Park (OH): ASM International, 2012)* (2009).

[51] V.A. Volkov, I.G. Suglobova, and D.E. Chirkst. “Formation enthalpies of uranium tetrafluoride and some fluorouranates (4)”. In: *Koordinatsionnaya Khimiya* 6.3 (1980), pp. 417–422.

[52] M.M. Walz and D. Van der Spoel. “Molten alkali halides–temperature dependence of structure, dynamics and thermodynamics”. In: *Physical Chemistry Chemical Physics* 21.34 (2019), pp. 18516–18524.

[53] W. Weng, L. Tang, and W. Xiao. “Capture and electro-splitting of CO2 in molten salts”. In: *Journal of Energy Chemistry* 28 (2019), pp. 128–143.

[54] M. Wilson and P.A. Madden. ““Prepeaks”and “first sharp diffraction peaks”in computer simulations of strong and fragile ionic liquids”. In: *Physical review letters* 72.19 (1994), p. 3033.

5

NEW INSIGHTS AND COUPLED MODELLING OF THE STRUCTURAL AND THERMODYNAMIC PROPERTIES OF THE LiF-UF_4 SYSTEM

Jaén A. OCÁDIZ FLORES, Aimen E. GHERIBI, John VLIELAND, Kathy DARDENNE, Jörg ROTHE, Rudy J.M. KONINGS, Anna Louise SMITH

LiF-UF_4 is a key binary system for molten fluoride reactor technology, which has not been scrutinized as thoroughly as the closely related LiF-ThF_4 system. The phase diagram equilibria in the system LiF-UF_4 are explored in this work with X-ray diffraction (XRD) and differential scanning calorimetry (DSC). The short-range ordering in the molten salt solution is moreover surveyed with Extended X-ray Absorption Fine Structure spectroscopy (EXAFS) and interpreted using a combination of standard fitting of the EXAFS data and Molecular Dynamics (MD) simulations with a Polarizable Ion Model (PIM) potential. The density, excess molar volume, thermal expansion, heat capacity, and enthalpy of mixing are extracted from the MD simulations across a range of temperatures and compositions; the behavior is non-ideal, with reasonably good agreement with the experimental data. Also calculated is the distribution of heteropolyanions in the liquid solution, and modelled using the quasi-chemical formalism in the quadruplet approximation taking into account the existence of the single-shell complexes $[UF_7]^{3-}$, $[UF_8]^{4-}$, and the dimeric

This chapter has been published in its entirety in *Journal of Molecular Liquids* 331 (2021), 115820 [54].

species $[U_2F_{14}]^{6-}$. Subjecting the optimization of the excess Gibbs energy parameters of the liquid solution to the constraints of the phase diagram data and local structure of the melt as derived from the EXAFS and coupled MD simulations, a CALPHAD-type assessment is proposed, linking structural and thermodynamic properties, with a rigorous physical description of the melt.

5.1. INTRODUCTION

The Molten Salt Reactor (MSR) is a type of nuclear reactor whose main characteristic is a fuel in the liquid state that also serves as the primary coolant: a stream of molten fluorides or chlorides. The reactor was originally conceived as a candidate engine to power aircraft in the Aircraft Reactor Experiment (ARE) [8], designed, built and operated by Oak Ridge National Laboratory (ORNL) in the 1950's. Later, the potential of such reactors as a civilian power source was recognized and demonstrated during the Molten Salt Reactor Experiment (MSRE), also in ORNL in the 1960's [33]. More recently, the Generation IV International Forum, a group of fourteen member countries pursuing research and development for the next generation of nuclear reactors, has selected the MSR as one of six key nuclear energy systems to replace the current fleet of Generation II Light Water Reactors [29].

The LiF-UF_4 system was a key component of the MSRE fuel (^{7}LiF-BeF_2-ZrF_4-UF_4) [75], and its phase diagram was investigated as part of the original research effort at ORNL by Barton et al. in 1958 [4]. Many years later, in 2010, a CALPHAD (Calculation of PHase Diagram) [51] thermodynamic model of the binary system was optimized based on the experimental data from ORNL using a modified quasi-chemical model in the quadruplet approximation to describe the liquid solution [5]. This system is also critically important in the proposed fuel of future reactors, such as ^{7}LiF-ThF_4-$^{233}UF_4$ for the Molten Salt Fast Reactor (MSFR) [23], LiF-BeF_2-ThF_4-UF_4 for the liquid-fueled thorium molten salt reactor (TMSR-LF) [21], and the ThorCon reactor which aims to be a scale-up of the MSRE [42]. Despite this, there have been no more phase diagram data gathered since 1958 to compare with the original measurements, as it has been done extensively for other systems, e.g. LiF-ThF_4 [15].

This work gives new insights into the phase equilibria of this key system using Differential Scanning Calorimetry (DSC) combined with X-ray Diffraction (XRD) measurements. In a wider effort to understand the structure of molten (Li,U)F_x salt and its relationship with macroscopic thermodynamic (and transport) properties which are highly relevant for reactor design and operation, in-situ high temperature Extended X-ray Absorption Fine Structure (EXAFS) spectroscopy measurements of the system are performed for the first time at high UF_4 content. They are furthermore interpreted with the help of Molecular Dynamics (MD) simulations, which have proved throughout several years already to be an invaluable tool for characterizing the thermo-physical and thermo-chemical properties of molten salts [52], [40], [26], [35]. The structural information obtained from the EXAFS data, interpreted and extended to a wider range of temperatures and compositions using MD, is ultimately linked to the phase diagram equilibria and excess thermodynamic properties. Using both experimental and simulated data as input, a coupled structural-thermodynamic model is developed using an advanced modified quasi-chemical model in the quadruplet approximation, with a formalism similar to the recent assessment of the LiF-BeF_2 system [71].

5.2. EXPERIMENTAL METHODS

5.2.1. REAGENT PREPARATION AND HANDLING

The purity of LiF (ultra-dry from Alfa Aesar, 0.9999 $\pm$ 0.0001 mass fraction purity) and UF_4 (International Bio-Analytical Industries, 0.9999 $\pm$ 0.0001 mass fraction purity) reported by the suppliers correlated well with X-ray diffraction (XRD) and Differential Scanning Calorimetry (DSC) tests. LiF has a white color while UF_4 is green, and both were handled in either powder or pressed pellet form. The experimental compositions reported hereafter were prepared by mixing either powder or pellet fragments of the pure salts in the required stoichiometric ratios. As fluoride salts are highly sensitive to water and air, handling and preparation of samples took place inside the dry atmosphere of an argon-filled glove box, where H_2O and O_2 content were kept below 5 ppm.

The DSC heat flow signal for both LiF and UF_4 showed only one event assigned to the melting point, and no other thermal events that could be attributed to impurities. The measured onset temperatures, after correction for the effect of the heating rate, are in good agreement with the literature: (1118 $\pm$ 5 K) and (1306 $\pm$ 5 K), respectively, vs. 1121.3 K (LiF, [16]), and (1307.9 $\pm$ 3.0) K (UF_4, [73]).

5.2.2. SYNTHESIS

The samples whose X-ray diffraction patterns are shown in this work were prepared by grinding powder mixtures, and heating them above melting temperatures inside a closed stainless steel crucible with a nickel liner in a tubular furnace under argon flow, with slow cooling, typically 2 K·min^{-1}, to allow for a good re-crystallization. The specific conditions for each sample are given below in Table 1.

Table 1: Synthesis conditions

Starting reagents[a]	Ramp K·min^{-1}	Hold[b] K, min	Cooling K·min^{-1}	Composition[c]
(LiF:UF_4) = (0.877:0.123)	10	1350, 30	2	Li_3UF_7 + $LiUF_5$
(LiF:UF_4) = (0.75:0.25)	10	1350, 30	2	$LiUF_5$ + Li_4UF_8 + UF_3
(LiF:UF_4) = (0.5:0.5)	10	1350, 30	2	$LiUF_5$
(LiF:UF_4) = (0.2:0.8)	10	1350, 30	2	$LiUF_5$ + LiU_4F_{17} + UF_3

[a] Standard uncertainty on the composition of the starting reagents was u(X(UF_4)) = 0.005.

[b] Standard uncertainty u is u(T) = 15 K.

[c] As determined by XRD.

5.2.3. POWDER X-RAY DIFFRACTION

X-ray powder diffraction (XRD) data were collected at room temperature (T = 293 $\pm$ 5 K) using a PANalytical X'Pert PRO X-ray diffractometer and a Cu anode (0.4 mm x 12 mm line focus, 45 kV, 40 mA) by step scanning at a rate of 0.0104 $^o \cdot s^{-1}$ in the range 10^o<2θ<120^o in a Bragg-Brentano configuration. The X-ray scattered intensities were measured with a real time multi strip (RTMS) detector (X'Celerator). The samples were

measured inside a sealed sample holder, with kapton foil cover, maintaining the dry argon atmosphere of the glove box. Structural analysis was performed with the Rietveld and LeBail methods using the FullProf suite [66].

5.2.4. DIFFERENTIAL SCANNING CALORIMETRY

3D-heat flow DSC measurements were performed using a Setaram Multi-Detector HTC module of the 96 Line calorimeter under argon flow at a pressure of (0.10 ± 0.005 MPa). All samples were placed inside a nickel liner and encapsulated for the calorimetric measurements inside a stainless steel crucible closed with a screwed bolt as described in [6] to avoid vaporization at high temperatures. All measurement programs started with one heating cycle reaching ~1398 K and held at that temperature for 300 s (i.e. around 90 K above the fusion temperature of UF_4 as measured at 10 K·min^{-1} heating rate) to ensure complete mixing of the end-members and attainment of the equilibrium state. In general, this first cycle was followed by three successive heating cycles with a heating rate ranging between 4 to 10 K·min^{-1}, and 20-15-10-5 K·min^{-1} cooling rates.

A series of interconnected S-types thermocouples were used to record the sample temperature throughout the experiments. The temperature on the heating ramp was calibrated by measuring the melting points of standard high purity metals (In, Sn, Pb, Al, Ag, Au), following the procedure described in [36], [14], thereby ensuring the measured temperatures can be translated to the International Temperature Scale (ITS-90). The temperature on the cooling ramp was obtained by extrapolation to 0 K·min^{-1} cooling rate. The melting temperature of pure compounds and transition temperatures of mixtures were derived on the heating ramp as the onset temperature using tangential analysis of the recorded heat flow, while the liquidus temperature of mixtures was taken as the peak extremum of the last thermal event as recommended in [10]. The data measured on the cooling ramp were not retained for the phase diagram optimization due to the occurrence of supercooling effects, but were used to help data interpretation and identification of transition events. The uncertainty on the measured temperatures is estimated to be $\pm$ 5 K for the pure compounds and $\pm$ 10 K for mixtures.

5.2.5. HIGH-TEMPERATURE EXAFS MEASUREMENTS

EXAFS measurements were performed at the INE beamline [67] of the KARA synchrotron facility (Karlsruhe, Germany), with 2.5 GeV and 150-170 mA as operating conditions in the storage ring. The beamline uses a Ge(422) double-crystal monochromator (DCM). Rh-coated mirrors collimate and focus the beam with spot size 300 m $\times$ 500 m at the sample position. Samples were probed at the U L_3 edge (17.166 keV), scanning from ~17.14 to ~ 17.77 keV. Transmission and fluorescence yield detection mode (recording the U-L_α fluorescence line by two silicon drift detectors) were applied simultaneously.

A dedicated experimental set-up, described in detail in [72], designed and built to operate at the INE beamline was used for the measurements. The set-up consists of a purpose-designed furnace inside a custom-made glovebox filled with nitrogen atmosphere. The samples (8-20 mg) were prepared in the inert atmosphere of a purified-

argon glovebox by mixing and grinding stoichiometric amounts of LiF and UF_4 end-members, and then pressing pellets of thickness less than 100 m by applying a pressure of 10 tons·cm^{-2}. The prepared pellets were sealed in a pre-dried boron nitride containment cell and loaded into the furnace chamber which was evacuated down to $\sim 2 \cdot 10^{-5}$ mbar to avoid reaction of the salts with residual oxygen or water.
The EXAFS data were collected ∼50 K above liquidus temperature (as calculated from the CALPHAD model of Beneš et al. [5]). Short scans were made during the heating ramp to detect the melting of the material. The temperature was ramped up to the melting point of LiF and held for about 15 min to ensure complete melting and homogenization. The temperature was subsequently adjusted to a set value ∼50 K above liquidus. In addition, an equilibration time of ∼15-30 min was employed at the set temperature before collecting the data to ensure the signal had stabilized.
Each scan took close to 30 min, and three to four scans were accumulated to be averaged. A step size of 0.8 eV was used in the XANES region. The energy E_0 of the edge absorption threshold position was identified as the first node of the second derivative of the signal. Prior to averaging, the spectra were aligned with the XANES spectrum of a reference yttrium (K edge = 17.0384 keV) foil, located between the second and third ionization chambers and measured concurrently with the sample. EXAFS data were collected up to ∼12.5 Å, and were Fourier transformed using the Hanning window over the k-range 3-9 Å^{-1} (dk = 2). Data treatment (normalization and extraction) of the raw XAS data was done with ATHENA software [65], version 9.25.

5.3. MOLECULAR DYNAMICS SIMULATIONS

MD simulations were performed for all compositions measured by EXAFS at the corresponding experimental temperatures, i.e 50 K above the liquidus equilibrium. In addition, the entire composition range was studied in intervals of 0.10 X(UF_4), at temperatures in the 900-1400 K range (Tab. 3). The form of the potential used for the study of this molten salt system is the Polarizable Ion Model (PIM) with the general form suggested by Salanne et al. [69]. It has been chosen because it has already shown its usefulness in the study of several molten salt systems such as as alkali fluoride mixtures [69], LiF-BeF_2 [35], [68], AF-ZrF_4 (A = Li, Na, K) [60], and LiF-ThF_4 [25]. The potential has four contributions with functional forms given in Eq. 5.1 to 5.5: charge-charge (Eq. 5.1), dispersion (Eq. 5.2), overlap repulsion (Eq.5.4) and polarization (Eq.5.5).

- Charge-charge:

$$V_{qq}(r_{ij}) = \sum_{i<j} \frac{q_i q_j}{r_{ij}} \tag{5.1}$$

  where q denotes the ionic formal charges.

- Dispersion:

$$V_{disp}(r_{ij}) = -\sum_{i<j}\left[f_{ij}^{6}(r_{ij})\frac{C_{ij}^{6}}{r_{ij}^{6}} + f_{ij}^{8}(r_{ij})\frac{C_{ij}^{8}}{r_{ij}^{8}}\right] \tag{5.2}$$

where $C_{ij}^{6}(r_{ij})$ is the dipole-dipole dispersion coefficient and $C_{ij}^{8}(r_{ij})$ is the dipole-quadrupole dispersion coefficient, while $f_{ij}^{6}(r_{ij})$ and $f_{ij}^{8}(r_{ij})$ are Tang-Toennies dispersion damping functions; they are short-range corrections to the asymptotic multipole expansion of dispersions [74]:

$$f_{ij}^{n}(r_{ij}) = 1 - e^{-b_{ij}^{n} r_{ij}} \sum_{k=0}^{n} \frac{(b_{ij}^{n} r_{ij})^{k}}{k!} \tag{5.3}$$

This work only consider dipoles and quadrupoles.

- Overlap repulsion

$$V_{rep}(r_{ij}) = \sum_{i<j} A_{ij} e^{-a_{ij} r_{ij}} \tag{5.4}$$

Here A_{ij} and a_{ij} are fitting parameters.

- Polarization

$$\begin{aligned} V_{pol}(r_{ij}) = \sum_{i<j}\Big[q_i \mu_{j\alpha} g_{ij}(r_{ij}) - q_i \mu_{i\alpha} g_{ij}(r_{ij})\Big] T_{\alpha}^{(1)}(r_{ij}) \\ - \sum_{i<j} \mu_{i\alpha}\mu_{j\beta} T_{\alpha\beta}^{(2)}(r i_{ij}) + \sum_{i} \frac{1}{2\alpha_i}|\mu_i|^2 \end{aligned} \tag{5.5}$$

In the equation above, $T_{\alpha}^{(1)}$ is the charge-dipole interaction tensor, $T_{\alpha\beta}^{(2)}$ is the dipole-dipole interaction tensor, α_i is the polarizability of ion i, and μ_i is the set of dipoles, while $g_{ij}(r_{ij})$ is a damping function similar to Eq. (5.6):

$$g_{ij}(r_{ij}) = 1 - C_{ij} e^{-b_{ij} r_{ij}} \sum_{k=0}^{4} \frac{(b_{ij} r_{ij})^{k}}{k!} \tag{5.6}$$

The parameters were derived in a semi-classical approach from *ab initio* calculations by Dewan [25] and validated by comparing the data from simulations with experimental data on the phase diagram, density, viscosity, electrical conductivity, thermal conductivity, and heat capacity [25]. For completeness they are listed in Table 2:

The systems were equilibrated for 500 ps in the NPT ensemble at 0 GPa and the corresponding temperature 50 K above the liquidus (Table 8), from which the equilibrium volume was taken. This was followed by a 100 ps equilibration and finally a 500 ps production run in the NVT ensemble at the same temperature. Time steps in all runs were

Table 2: Parameter values for LiF-UF_4 PIM potential, with values in atomic units [25].

Ion pair	A_{ij}	a_{ij}	C^6_{ij}	C^8_{ij}	b^6_{ij}	b^8_{ij}	b^D_{ij}		c^D_{ij}
F^-- F^-	282.3	2.440	15.0	150.0	1.9	1.9			
F^--U^{4+}	70.623	1.666	38.7	387.0	1.9	1.9	$b^D_{FU} = b^D_{UF} = 1.7516$	$c^D_{FU} = 1.8148$	$c^D_{UF} = 0.84905^a$
F^--Li^+	18.8	1.97	1.22	12.2	1.9	1.9	$b^D_{FLi} = 1.834$	$c^D_{FLi} = 1.335$	-
U^{4+}-U^{4+}	1.0	5.0	100.0	1000.0	1.9	1.9			
U^{4+}-Li^+	1.0	5.0	3.16	31.6	1.9	1.9	$^b b^D_{ULi} = 10.0$	$^b c^D_{ULi} = 0.001$	-
Li^+-Li^+	1.0	5.0	0.10	1.0	1.9	1.9			

The polarizabilities of F^- and U^{4+} were set to 7.8935 au and 5.8537 au, respectively. Li^+ is considered to be non-polarizable.
[a] Modified from c^D_{UF} = -0.84905 in Ref. [25].
[b] Not defined in [25], set arbitrarily.

set to 0.5 fs, while the relaxation time for both the Nosé-Hoover thermostat and barostat (for the NPT run) was set to 10 ps. The cubic simulation cell contained 600-800 ions in periodic boundary conditions. Cut-offs for the real space part of the Ewald sum and short-range potential were both set to half the length of the cell. Simulations at higher temperatures and different compositions were also performed; they are summarized in Table 3. In this case, the NPT rus was 500 ps, and the NVT production run 500 ps to 2.5 ns.

5.4. THERMODYNAMIC MODELLING

Optimizations of the thermodynamic model for the LiF-UF_4 system was done according to the CALPHAD (CALculation of PHase Diagram) method [51] as implemented in the Factsage software [3]. To carry out such an optimization, the identity of the phases present in the system of interest must be known, as well as their respective Gibbs energy functions.

5.4.1. PURE COMPOUNDS

The Gibbs energy function of a pure compound is given by:

$$G(T) = \Delta_f H^{\circ}_{\mathrm{m}}(298) - S^{\circ}_{\mathrm{m}}(298)T + \int_{298}^{T} C_{\mathrm{p,m}}(T)dT - T\int_{298}^{T} \frac{C_{\mathrm{p,m}}(T)}{T}dT \tag{5.7}$$

where $\Delta_f H^{\circ}_{\mathrm{m}}(298)$ is the standard enthalpy of formation, $S^{\circ}_{\mathrm{m}}(298)$ is the standard absolute entropy, both evaluated at a reference temperature, in this case 298.15 K (throughout this work 298 will be understood to mean 298.15 K for simplicity), and $C_{\mathrm{p,m}}$ is the isobaric heat capacity expressed as a polynomial:

$$C_{\mathrm{p,m}}(T) = a + bT + cT^2 + dT^{-2} \tag{5.8}$$

with more terms added if necessary.

Table 3: Simulation conditions

Composition / X(UF_4)	$N_{U^{4+}}$	N_{Li^+}	N_{F^-}	N_{total}	T / K	NPT / ns	NVT[a] / ns
0.25	72	216	504	792	831	0.5	0.5
0.50	114	114	570	798	1040	0.5	0.5
0.67	132	66	594	792	1216	0.5	0.5
0	0	400	400	800	900-1400[b]	0.5	2.5
0.025	401	1	397	799	1121, 1400	0.5	0.5
0.104	36	310	454	800	900-1400[b]	0.5	2.5
0.211	64	240	496	800	900-1400[b]	0.5	2.5
0.296	82	195	523	800	900-1400[b]	0.5	2.5
0.400	100	150	550	800	900-1400[b]	0.5	2.5
0.513	116	110	574	800	900-1400[b]	0.5	2.5
0.597	126	85	589	800	900-1400[b]	0.5	2.5
0.715	138	55	607	800	900-1400[b]	0.5	2.5
0.807	146	35	619	800	900-1400[b]	0.5	2.5
0.911	154	15	631	800	900-1400[b]	0.5	2.5
1	160	0	640	800	900-1400[b]	0.5	2.5

[a] NVT equilibration time was 0.2 ns in all cases.

[b] The temperatures were: 900, 1000, 1121, 1300, and 1400 K wherever 900-1400 K is indicated.

In this work, the Neumann-Kopp rule [49] was used to approximate heat capacities of intermediate compounds in the absence of experimental data. The thermodynamic data for all compounds in this study are listed in Table 1. The data for both solid and liquid LiF and UF_4 were taken from [16] and [45], respectively. The standard enthalpy of formation and standard entropy at 298.15 K of the intermediate compounds were optimized to closely match phase equilibrium data.

5.4.2. LIQUID SOLUTION

All excess Gibbs energy terms of the liquid solution presented here have been modelled using an advanced modified quasi-chemical model akin to the one recently reported for the LiF-BeF_2 system [71]. The modified quasi-chemical model proposed by Pelton et al. [61] is particularly well adapted to describe ionic liquids such as in the present system, as it allows to select the composition of maximum short-range ordering (SRO) by varying the ratio between the cation-cation coordination numbers $Z^A_{AB/FF}$ and $Z^B_{AB/FF}$ (fluorine is in this case the only anion present). The quadruplet approximation assumes a quadruplet, composed of two anions and two cations, to be the basic unit in liquid solution, and the excess parameters to be optimized are those related to the following second-nearest neighbor (SNN) exchange reaction:

$$(A-F-A)+(B-F-B) \longrightarrow 2(A-F-B) \;\; \Delta g_{AB/F} \tag{5.9}$$

Table 4: Thermodynamic data for end-members and intermediate compounds used in this work for the phase diagram assessment: $\Delta_f H^o_m$(298 K)/(kJ·mol^{-1}), S^o_m(298 K)/(J·K^{-1}·mol^{-1}), and heat capacity coefficients $C_{p,m}$(T/K)/(J·K^{-1}·mol^{-1}), where $C_{p,m}(T/K) = a + b\cdot T + c\cdot T^2 + d\cdot T^{-2}$. Optimized data are shown in **bold**.

Compound	$\Delta_f H^o_m$(298 K)/ (kJ·mol^{-1})	S^o_m(298 K)/ (J·K^{-1}·mol^{-1})	$C_{p,m}$(T/K)/(J·K^{-1}·mol^{-1})= a + b·T + c·T^2 + d·T^{-2}				Reference
			a	b	c	d	
LiF(cr)	-616.931	35.66	43.309	$1.6312\cdot 10^{-2}$	$5.0470\cdot 10^{-7}$	-569124	[16]
LiF(l)	-598.654	42.962	64.183				[16]
UF_4(cr)	-1914.200	151.7	114.5194	$2.0555\cdot 10^{-2}$		-413159	[45]
UF_4(l)[a]	-1914.658	115.4	174.74				[45]
Li_4UF_8(cr)	**-4345.920**	357.55	287.75532	$8.5804\cdot 10^{-2}$	$2.0188\cdot 10^{-6}$	-2689653	This work, [5]
Li_3UF_7(cr)	**-3776.464**	258.68	244.44634	$6.9491\cdot 10^{-2}$	$1.5141\cdot 10^{-6}$	-2120530	This work
$LiUF_5$(cr)	**-2542.591**	187.4	157.8284	$3.6867\cdot 10^{-2}$	$5.0470\cdot 10^{-7}$	-982283	This work
LiU_4F_{17}(cr)	**-8292.061**	644.7	501.38658	$9.8532\cdot 10^{-2}$	$5.0470\cdot 10^{-7}$	-2221760	This work

[a] UF_4(l) is modelled as a [$U_{VII}F_4$(l)-$U_{VIII}F_4$(l)-$U_{2[XIV]}F_8$(l)] mixture with $g^0_{U_{[VII,VIII]}F_4}(l) = \frac{1}{2} g^0_{U_{2[XIV]}F_8(l)} + 150000\ J\cdot mol^{-1}$.

where the fluoride anions are represented by F, and A and B denote the cations. $\Delta g_{AB/F}$ is the Gibbs energy change associated with the SNN exchange reaction, and has the following form:

$$\Delta g_{AB/F} = \Delta g^{o}_{AB/F} + \sum_{i \geqslant 1} g^{i0}_{AB/F} \chi^{i}_{AB/F} + \sum_{j \geqslant 1} g^{0j}_{AB/F} \chi^{j}_{BA/F} \tag{5.10}$$

where $\Delta g^{o}_{AB/F}$ and $g^{ij}_{AB/F}$ are coefficients which may or may not be temperature-dependent, but which are independent of composition.

The dependence on composition is given by the $\chi_{AB/F}$ terms defined as:

$$\chi_{AB/F} = \frac{X_{AA}}{X_{AA} + X_{AB} + X_{BB}} \tag{5.11}$$

where X_{AA}, X_{BB} and X_{AB} represent cation-cation pair mole fractions.

The anion coordination number is finally fixed by conservation of charge in the quadruplet:

$$\frac{q_A}{Z^{A}_{AB/FF}} + \frac{q_B}{Z^{B}_{AB/FF}} = \frac{2q_F}{Z^{F}_{AB/FF}} \tag{5.12}$$

where q_i are the charges of the different ions, and $Z^{F}_{AB/FF}$ is the anion-anion coordination number, in this case fluorine-fluorine.

Despite its usefulness, the thermodynamic model just outlined does not account for the formation of molecular species or heteropolyanions in the melt. As will be discussed at length in the following sections, (Li,U)F_x is not a solution in which cations and anions are completely dissociated. UF_4 is a Lewis acid and accepts fluorine anions from LiF, a Lewis base. The solution, as UF_4 is added to LiF, is formed by discrete coordination complexes which link to each other as soon as their number density is high enough, forming dimers, trimers, and 'polymers' (see Figs. 5.10a, 5.10b). In order to capture this structural evolution and provide a more accurate description of the chemical speciation in the melt, a coupled structural-thermodynamic model comparable to the one recently reported for the LiF-BeF_2 system [71] was adopted. The key distinction made by Smith et al. [71], was to introduce quadruplets which not only include Be^{2+}, but also Be_2^{4+}, Be_3^{6+}, assigning them coordination environments 4, 7, and 10, respectively. That is, the authors effectively included monomers, dimers, and trimers, choosing suitable compositions of maximum short-range ordering for each one. In this work, two distinct cations were taken into account, with coordination numbers 7 and 8 (which dominate the distribution of $[UF_x]^{4-x}$ complexes as shown in Section 5.6.2), as well as a 14-coordinated cation (the most abundant according to MD simulations): $U^{4+}_{[VII]}$, $U^{4+}_{[VIII]}$, $U^{8+}_{2[XIV]}$. The cation-cation coordination numbers, shown in Table 3, were chosen to reflect the compositions of maximum SRO in the neighbordhood of X(UF_4) = 0.20 (Li_4UF_8), and X(UF_4) = 0.25 (Li_3UF_7, "$Li_6U_2F_{14}$").

The choice of assigning every species with two or more bridged U^{4+} centers to the dimer distribution was motivated by the need to keep fitting parameters from being too numerous to have a practical model, while still retaining a rigorous structural description. In this regard, the need to reflect more than one coordination number in the first shell

surrounding U^{4+}, which is such a salient feature of the (Li,U)F_x melt, motivated the inclusion of two distinct monomers. Ultimately, pure $UF_4(l)$ is modelled as a solution of dimers. To do so, the reactions $\frac{1}{2}U_{2[XIV]}F_8(l) = U_{[VII]}F_4(l)$ and $\frac{1}{2}U_{2[XIV]}F_8(l) = U_{[VIII]}F_4(l)$ were constrained by the following Gibbs energy expressions (respectively, Eq. 6.21, 6.22):

$$g^0_{U_{[VII]}F_4(l)} = \frac{1}{2}g^0_{U_{2[XIV]}F_8(l)} + 150000\ J\cdot mol^{-1} \tag{5.13}$$

$$g^0_{U_{[VIII]}F_4(l)} = \frac{1}{2}g^0_{U_{2[XIV]}F_8(l)} + 150000\ J\cdot mol^{-1} \tag{5.14}$$

The value of 150000 $J\cdot mol^{-1}$ is an arbitrary term to destabilize the monomers, insofar as it allows to reproduce the melting point (1307.8 K vs. (1307.9 $\pm$ 3.0) K [73]) and the enthalpy of fusion of UF_4 (45 kJ·mol^{-1} vs. 46.986 kJ·mol^{-1} [27]).

Table 5: Cation-cation coordination numbers of the liquid solution.

A	B	$Z^A_{AB/FF}$	$Z^B_{AB/FF}$
Li^+	Li^+	6	6
$U^{4+}_{[VII]}$	$U^{4+}_{[VII]}$	6	6
$U^{4+}_{[VIII]}$	$U^{4+}_{[VIII]}$	6	6
$U^{8+}_{2[XIV]}$	$U^{8+}_{2[XIV]}$	6	6
$U^{4+}_{[VII]}$	$U^{4+}_{[VIII]}$	6	6
$U^{4+}_{[VII]}$	$U^{8+}_{2[XIV]}$	6	6
$U^{4+}_{[VIII]}$	$U^{8+}_{2[XIV]}$	6	6
Li^+	$U^{4+}_{[VII]}$	2	6
Li^+	$U^{4+}_{[VIII]}$	1.5	6
Li^+	$U^{8+}_{2[XIV]}$	1	6

In the modified quasi-chemical model, interpolation to higher order systems is either symmetric or asymmetric, the choice depending on the similarity of the components between each other in a sublattice [62]. In the (Li,U)F_x solution, the uranium cations are taken to be symmetric with respect to each other, while the smaller, monovalent, non-polarizable Li_+ is taken to be the asymmetric component. Thus, the virtual ternary systems {LiF + $U_{[VII]}F_4$ + $U_{[VIII]}F_4$ }, {LiF + $U_{[VII]}F_4$ + U_2F_8 }, and {LiF + $U_{[VIII]}F_4$ + U_2F_8 } are asymmetric, while {$U_{[VII]}F_4$ + $U_{[VIII]}F_4$ + U_2F_8 } is symmetric. Then for each quadruplet, the composition dependence (Eq. 6.19) expressed as a function of cation-cation pair mole fraction is:

$$\chi_{LiU_{[VII]}/FF} = \chi_{LiU_{[VIII]}/FF} = \chi_{LiU_2/FF} = \frac{X_{LiLi}}{\sum_A \sum_B X_{AB/F_2}} \tag{5.15}$$

$$\chi_{U_{[VII]}Li/FF} = \chi_{U_{[VIII]}Li/FF} = \chi_{U_2Li/FF}$$
$$= \frac{X_{U_{[VII]}U_{[VII]}} + X_{U_{[VIII]}U_{[VIII]}} + X_{U_2U_2} + X_{U_{[VII]}U_{[VIII]}} + X_{U_{[VII]}U_2} + X_{U_{[VIII]}U_2}}{\sum_A \sum_B X_{AB/F_2}}$$

Note that the denominator $\sum_A \sum_B X_{AB/F_2}$ adds to 1 in the {LiF + "UF_4"} system.

Having established the composition dependence, the optimized excess Gibbs energy parameters of the binary liquid solution in the LiF-UF_4 system are shown in Eq. 6.24-6.26. The parameters were optimized based on the complex anion distribution as calculated with MD (see Figs. 5.15a, 5.15b) and phase diagram equilibria points of the liquidus (see Fig. 5.14).

$$\Delta g_{LiU_{[VII]}/FF} = -59500 + (-2600 + 0.4 \cdot T)\chi_{LiU_{[VII]}/FF}\, J \cdot mol^{-1} \tag{5.16}$$

$$\Delta g_{LiU_{[VIII]}/FF} = -59500 + (-2600 - 0.3 \cdot T)\chi_{LiU_{[VIII]}/FF}\, J \cdot mol^{-1} \tag{5.17}$$

$$\Delta g_{LiU_{2[XIV]}/FF} = -32000 + (-1000 - 0.8 \cdot T)\chi_{LiU_{2[XIV]}/FF} - 26 \cdot T\chi_{U_{2[XIV]}Li/FF}\, J \cdot mol^{-1} \tag{5.18}$$

5.5. BRIEF REVIEW OF LITERATURE DATA ON THE LiF-UF_4 SYSTEM

Barton et al. [4] was the first to produce a sketch of the LiF-UF_4 phase diagram in 1958, shown in Fig. 5.1. The authors used a combination of i) thermal analysis, namely examination of cooling curves, ii) quenching of samples after equilibration, iii) differential thermal analysis, and iv) visual observation methods coupled with XRD. The authors identified three incongruently melting compounds: Li_4UF_8 ($T_{peritectic}$ = 773 K), $Li_7U_6F_{31}$ ($T_{peritectic}$ = 883 K), LiU_4F_{17} ($T_{peritectic}$ = 1048 K) and a single eutectic at T = 763 K, X(UF_4) = 0.27. The features of the diagram are summarized in Table 6. Besides the stable phases, a meta-stable, so-called "X-phase" was detected by them and hypothesized to be Li_3UF_7.

A few years later Weaver et al. [78] studied the LiF-ThF_4-UF_4 system and reported no ternary compounds but four solid solutions, amongst which was Li_3(Th,U)F_7. In 2010, the binary system was optimized by Beneš et al. [5] based on the experimental data from Barton et al. [4] using a modified quasi-chemical model in the quadruplet approximation to describe the liquid solution. The optimization included $Li_7U_6F_{31}$ instead of $LiUF_5$ and did not consider Li_3UF_7 as a phase in the binary system, but did model the Li_3(Th,U)F_7 solid solution. Hereafter is a discussion of the findings in this work compared to the phase diagram as reported by Barton et al.

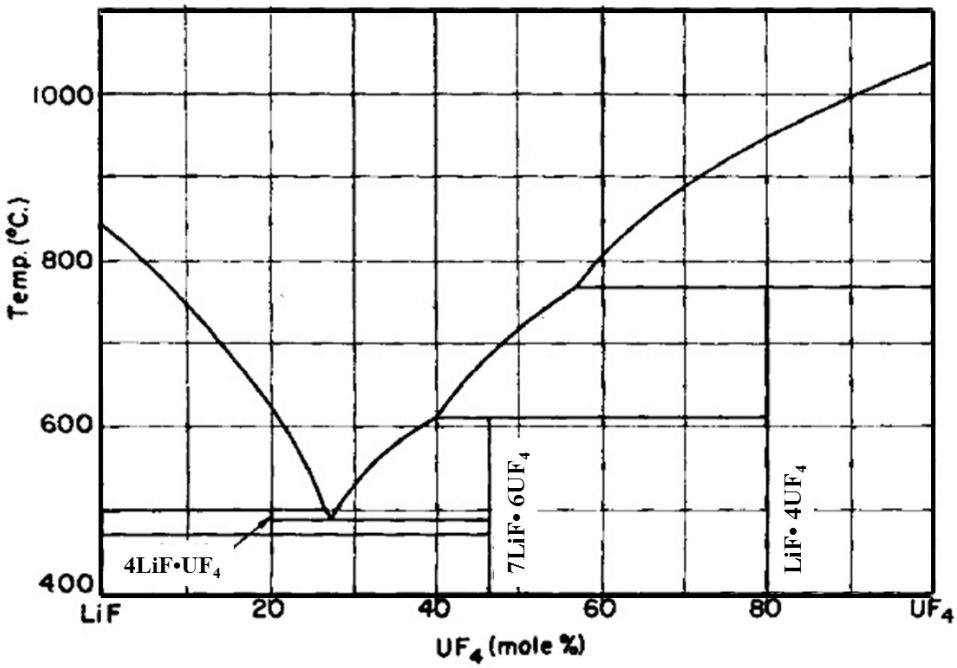

Figure 5.1: The system LiF-UF_4 as reported by Barton et al.[4]. Reproduced with permission from Wiley and Sons.

5.6. RESULTS AND DISCUSSION

5.6.1. PHASE DIAGRAM STUDIES IN THE LIF-UF_4 SYSTEM

Li_4UF_8

Barton et al. [4] reported quite a narrow range of stability for Li_4UF_8, i.e. from 743 K to 773 K (Fig. 5.1). Our attempts to quench a pure sample of composition Li_4UF_8 were unsuccessful. Nevertheless, it was found in combination with $LiUF_5$ and UF_3 impurity in an attempt to isolate Li_3UF_7; Li_4UF_8 has orthorhombic symmetry and belongs to space group *Pnma* as identified by Brunton [11]. The diffractogram of this three-phase mixture with its LeBail refinement is shown in Figure 5.2.

In another synthesis attempt, at composition $X(UF_4)$ = 0.123 (diffractogram shown in Fig 5.3), Li_4UF_8 was not observed anymore, in agreement with the phase equilibria reported by Barton et al. [4].

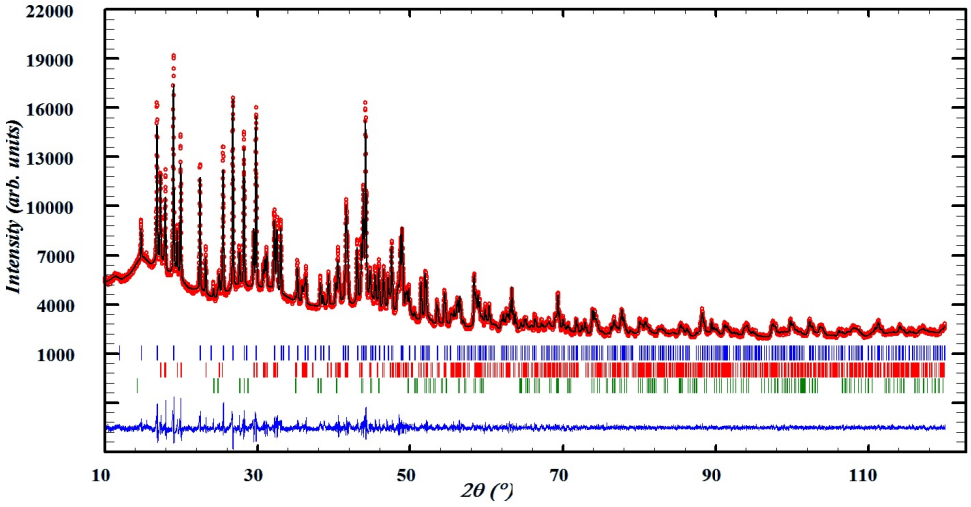

Figure 5.2: Diffractogram of the $LiUF_5$-Li_4UF_8 mixture, $X(UF_4)$ = 0.25. Comparison between the observed (Y_{obs}, in red) and calculated (Y_{calc}, in black) X-ray diffraction patterns. Y_{obs} - Y_{calc}, in blue, is the difference between the experimental and calculated intensities. The Bragg's reflection angular positions are marked in blue ($LiUF_5$), red (Li_4UF_8), and green (UF_3).

Li_3UF_7

Upon quenching samples with compositions ranging from $X(UF_4)$ = 0.2 to 0.32 from above the solidus temperature, Barton et al. [4] observed a crystalline phase with a diffraction pattern they could not match with the established phases in the system. The authors simply designated it as X-phase and concluded that it was metastable, since it formed only during certain cooling conditions. In particular, it formed when the mass of the samples was large, but not when optimal quenching conditions (small masses) were used. They suggested $3LiF{\cdot}UF_4$ to be the stoichiometry of the X-phase. As mentioned above, an attempt to synthesize the Li_3UF_7 phase in this work resulted in the quenching of the high temperature phase Li_4UF_8 along with $LiUF_5$, as well as a UF_3 impurity, probably due to reduction from the nickel liner. Yet in an attempt to ascertain whether or

not Li_4UF_8 is stable down to room temperature, $LiUF_5$ could be identified as expected, but interestingly, the other crystalline phase belonged to the same space group as one of the known phases of Li_3ThF_7 [18], *P4/ncc* (Fig. 5.3). Thus the hypothesis that Li_3UF_7 was the identity of the X-phase appears to be correct, as well as its metastability given the absence of the line compound at the composition where it should have formed, X(UF_4) = 0.25 (Fig.5.2).

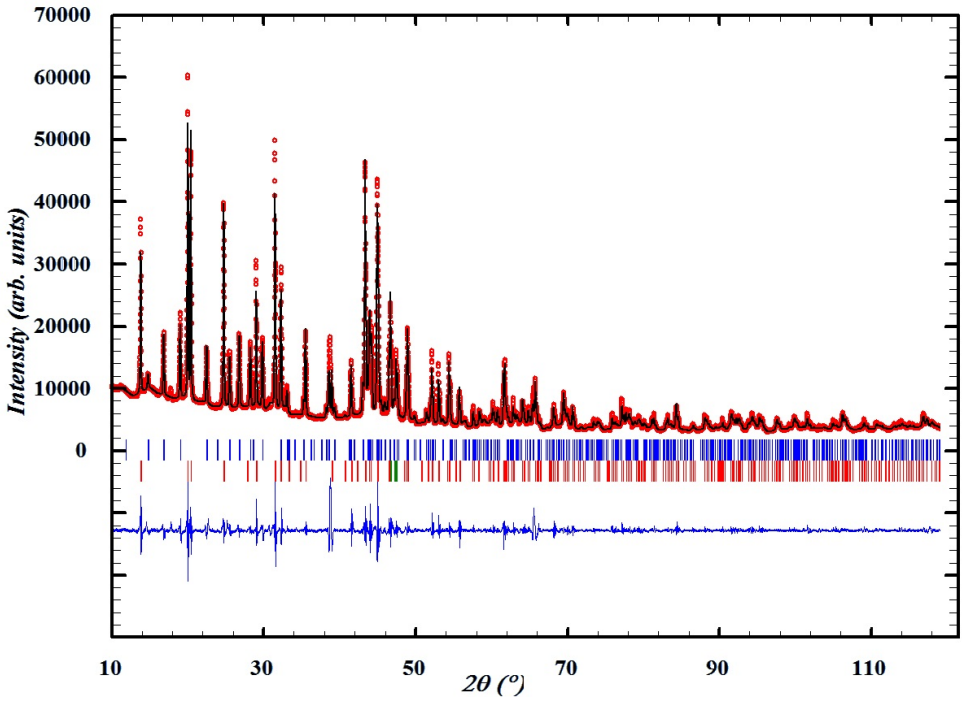

Figure 5.3: Diffractogram of the $LiUF_5$-Li_3UF_7 mixture, X(UF_4) = 0.123. Comparison between the observed (Y_{obs}, in red) and calculated (Y_{calc}, in black) X-ray diffraction patterns. Y_{obs} - Y_{calc}, in blue, is the difference between the experimental and calculated intensities. The Bragg's reflection angular positions are marked in blue ($LiUF_5$), and red (Li_3UF_7).

$LiUF_5$

Barton et al. [4] reported the line compound $Li_7U_6F_{31}$ to be stable, guessing the stoichiometry based on the existence of $Na_7U_6F_{31}$ and $K_7U_6F_{31}$. Discrepancies between the density obtained from the mass of two formula units and the proposed cell parameters [31], and that obtained from measurements raised doubts about the validity of the 7:6 stoichiometry, however. The mismatch between the crystal sytem and space group of the putative phase $Li_7U_6F_{31}$ (tetragonal, $I4_1/a$) and $A_7U_6F_{31}$ (A = Na, K) (trigonal, $R\bar{3}$) raised further concerns. Addressing these doubts, Brunton [12] later showed that the correct formula is $LiUF_5$. More recently Yeon et al. also grew $LiUF_5$ crystals in a hydrothermal environment [41]. In this work, a sample of high purity $LiUF_5$ (space group $I4_1/a$) could be crystallized from a melt with composition X(UF_4)=0.5 (Fig. 5.4). $LiUF_5$

was thus included in the thermodynamic model and it is recommended that molten salt databases use this compound rather than $Li_7U_6F_{31}$.

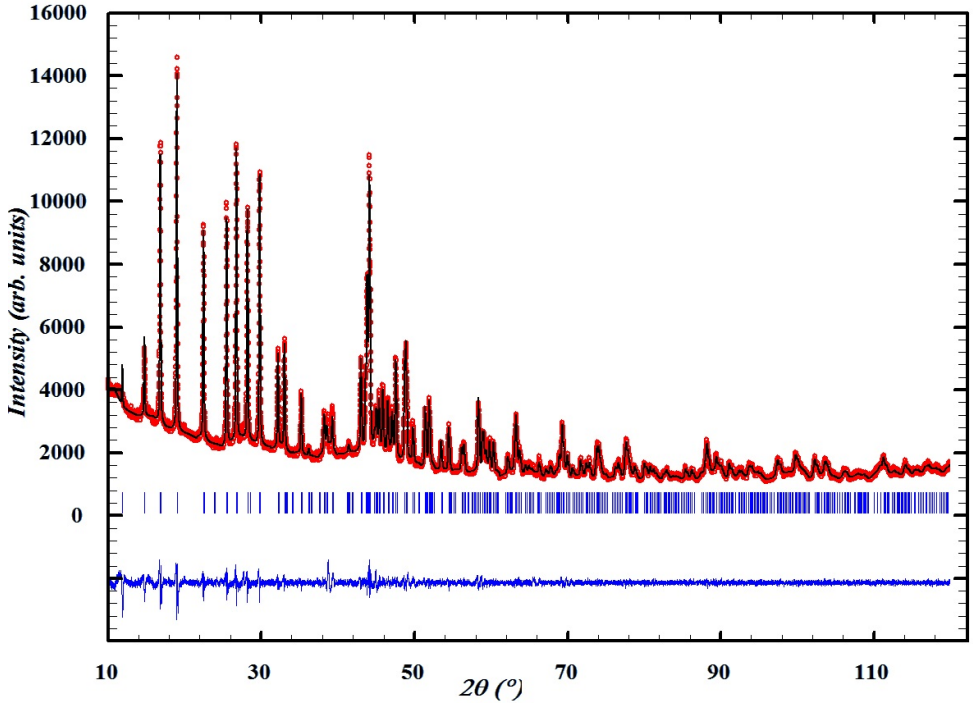

Figure 5.4: Diffractogram of $LiUF_5$, $X(UF_4)$ = 0.5. Comparison between the observed (Y_{obs}, in red) and calculated (Y_{calc}, in black) X-ray diffraction patterns. Y_{obs} - Y_{calc}, in blue, is the difference between the experimental and calculated intensities. The Bragg's reflection angular positions are marked in blue.

LiU_4F_{17}

No crystal structure determination could be found in the literature for either LiU_4F_{17} or $LiTh_4F_{17}$, and there were no thermal-analysis data collected by Barton et al. [4] in the vicinity of $X(UF_4)$=0.8. However, the calorimetric measurements reported in the LiF-ThF_4 system [15] support the existence of such a phase, as do the DSC data collected in this work, listed in Table 7. Furthermore, Cousson and Pages [19] were able to prepare crystals of $LiAn_4F_{17}$ (An = Th, U), of tetragonal symmetry, and narrowed down the possible space groups of the compounds to three: *I4/m*, *I4*, or $I\bar{4}$. Unfortunately LiU_4F_{17} could not be isolated as a pure phase material in the present work, but a sample with composition $X(UF_4)$ = 0.80 yielded a phase which could not be attributed to either $LiUF_5$ (which also precipitated in the sample), or UF_4, as would be the case if LiU_4F_{17} did not exist. With the aid of a LeBail refinement, it could be established that amongst the space groups suggested by Cousson and Pages, *I4* is the most likely one, as it resulted in the best fit to the data, shown in Figure 5.5. Note that there is a third phase in the refinement, again identified as UF_3.

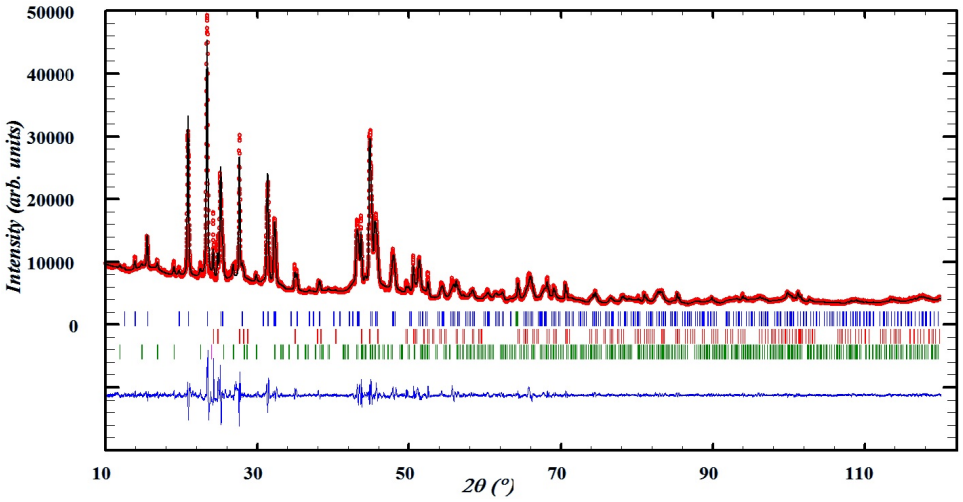

Figure 5.5: XRD pattern of a sample with composition X(UF_4) = 0.8. Three phases contribute to the pattern: $LiUF_5$ (Bragg's reflection angular position marked in blue), LiU_4F_{17} (red), and UF_3 (green). Comparison between the observed (Y_{obs}, in red) and calculated (Y_{calc}, in black) X-ray diffraction patterns. Y_{obs} - Y_{calc}, in blue, is the difference between the experimental and calculated intensities.

DSC MEASUREMENTS

The equilibria data in LiF-UF_4 were investigated in this work with DSC, with good agreement with the equilibria reported by Barton et al. [4]. The invariant equilibria as reported by the authors is compared to those calculated and measured in the present work, Table 6. The calorimetric measurements are presented in Table 7, and overlayed with the calculated phase diagram in Fig. 5.14 (▲, red).

Table 6: Invariant equilibria in the LiF-UF_4 system.

Equilibrium	Invariant reaction	This study (calc.)		DSC equilib.[b]		Barton et al. [4]	
		X(UF_4)	T/K	X(UF_4)[a]	T/K	X(UF_4)[c]	T/K[d]
Eutectoid	Li_4UF_8 = LiF + $LiUF_5$	0.20	750	0.20	755 ± 2	0.20	743
Peritectic	Li_4UF_8 = LiF + L	0.257	766	-	761 ± 1	0.26	773
Eutectic	L = Li_4UF_8 + $LiUF_5$	0.263	758	0.27	762 ± 4	0.27	763
Peritectic[e]	$LiUF_5$ = LiU_4F_{17} + L	0.396	879	-	877 ± 7	0.4	883
Peritectic	LiU_4F_{17} = UF_4 + L	0.568	1044	-	1044 ± 20	0.57	1048

[a] Standard uncertainties u are u(X(UF_4))) = 0.05.

[b] Global average of the experimental runs appearing in Table 7.

[c] Standard uncertainty u reported by the authors: u(X(UF_4))) = 0.01.

[d] Standard uncertainty u reported by the authors: u are u(T) = 1 K.

[e] Authors mention phase $Li_7U_6F_{31}$ instead of $LiUF_5$, see Section 5.6.1.

[b] Measurements done at (0.10 ± 0.005) MPa.

Table 7: Equilibrium data in the LiF-UF_4 system as measured in this work by DSC.

$X(UF_4)^a$	T/K^b	Equilibrium	Equilibrium reaction
0.000	1118	LiF congruent melting	LiF = L
0.094	753	Eutectoid	Li_4UF_8 = LiF + $LiUF_5$
0.094	761	Peritectic	Li_4UF_8 = LiF + L′
0.094	1074	Liquidus	LiF + L′ = L
0.2	756	Eutectoid	Li_4UF_8 = LiF + $LiUF_5$
0.2	762	Peritectic	Li_4UF_8 = LiF + L′
0.27	770	Eutectic	Li_4UF_8 + $LiUF_5$ = L
0.329	762	Eutectic	Li_4UF_8 = LiF + $LiUF_5$
0.329	830	Liquidus	$LiUF_5$ + L′ = L
0.399	760	Eutectic	Li_4UF_8 = LiF + $LiUF_5$
0.399	881	Peritectic	$LiUF_5$ = L + LiU_4F_{17}
0.445	761	Eutectoid	Li_4UF_8 = LiF + $LiUF_5$
0.445	878	Peritectic	$LiUF_5$ = L + LiU_4F_{17}
0.499	759	Eutectic	L = $LiUF_5$ + Li_4UF_8
0.499	882	Peritectic	$LiUF_5$ = L + LiU_4F_{17}
0.499	1060	Liquidus	L′ + LiU_4F_{17} = L
0.602	758	Unknown	-
0.602	875	Peritectic	$LiUF_5$ = L + LiU_4F_{17}
0.602	1026	Peritectic	LiU_4F_{17} = UF_4 + L
0.642	872	Peritectic	$LiUF_5$ = L + LiU_4F_{17}
0.642	1092	Liquidus	UF_4 + L′= L
0.717	867	Peritectic	$LiUF_5$ = L + LiU_4F_{17}
0.717	1095	Liquidus	UF_4 + L′= L
0.804	1057	Peritectic	LiU_4F_{17} = UF_4 + L
0.804	1222	Liquidus	UF_4 + L′= L
0.876	1031	Peritectic	LiU_4F_{17} = UF_4 + L
0.876	1263	Liquidus	UF_4 + L′= L
1.000	1306	Congruent melting	UF_4 = L

[a] Standard uncertainties u are $u(X(UF_4))$= 0.005.

[b] Standard uncertainties u are u(T)= 5 K for the pure end-members, u(T)= 10 K for mixtures. The pressure was (0.10 ± 0.005) MPa.

5.6.2. LOCAL STRUCTURE OF THE (LI,U)F_x MELT

EXAFS SPECTRA AND CHARACTERIZATION OF THE LOCAL STRUCTURES

The local structure characteristics of molten (Li,U)F_x salt were studied as a function of composition with three samples with increasing UF_4 content: X(UF_4) = 0.25, 0.50, 0.67. Their $k^2\chi(k)$ spectra are shown in Figs. 5.6a-5.8a, accompanied by the corresponding Fourier transform moduli in Figs. 5.6b-5.8b. In all figures the experimental data are compared with the results obtained from our MD simulations (red). These were computed by using the Cartesian coordinates of the ions in the NVT production runs as input for the FEFF8.40 code [2] and averaging over ∼ 25000 configurations. The resulting EXAFS

signal could then be directly compared to the experimental one. Additionally, fits were calculated using the standard EXAFS equation [48] without cumulants (blue). Four parameters were refined during the fitting process with the standard EXAFS equation: the energy shift from the L_3 edge (ΔE_0), Debye-Waller factor (σ^2), the expected U-F distance $E[R_{U-F}]$, and the coordination number (CN). They are listed in Table 8.
Even though fitting of the EXAFS equation is routinely applied to liquid systems, it assumes a Gaussian distribution of interionic distances between equivalent neighbors and the absorbing central atom which does not reflect distributions in actual liquids, especially at high temperatures, where thermal disorder and anharmonicity start to play a major role [28]. The actual radial distribution functions (denoted as $g(r)$ or RDF) can, for instance, be obtained from neutron diffraction data or tallied from a large number of observations so as to capture thermal disorder and anharmonicity, as in MD. An example, at the composition $X(UF_4) = 0.25$, is shown in Fig. 5.9, where two peaks corresponding to the first two U-F coordination shells are shown. A fluoride ion can be defined to belong to the first coordination shell of U^{4+} when the U-F distance is less than R_{cutoff}, i.e. the first minimum of the U-F RDF (marked by the red line). The peak is skewed to the right, such that the most probable distance (maximum of the first peak) and expected bond length within the first shell, given by:

$$E[R^{U-F}] = \frac{\int_0^{R_{cutoff}^{U-F}} r_{U-F} \cdot g_{U-F}(r) dr}{\int_0^{R_{cutoff}^{U-F}} g_{U-F}(r) dr} \tag{5.19}$$

although close, do not coincide, a feature which cannot possibly be captured by a Gaussian distribution. Notwithstanding, it can be seen that the tail on the right is thin and comes close to zero, such that the peak can be reasonably approximated by a bell curve. In contrast, the same is not true for the second peak visible in the RDF, which has a fat tail on the right, and a bell curve would surely make a poor fit of it. For that reason, the fits included here are only for the first coordination shell, and are intended as an approximation to gauge the MD results.

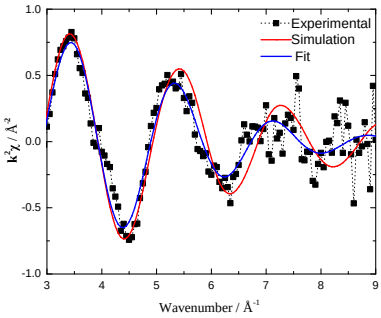

(a)

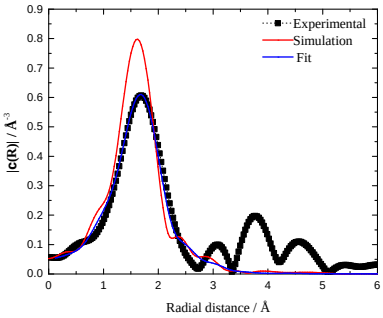

(b)

Figure 5.6: (a) Experimental (■), simulated (red), and fitted (blue) $k^2\chi(k)$ spectra (collected in fluorescence mode) of a sample with composition X(UF_4) = 0.25 at T = 831 K. (b) Fourier transform modulus $|\chi(R)|$ of the EXAFS spectra.

5

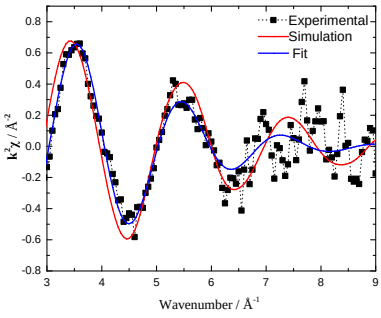

(a)

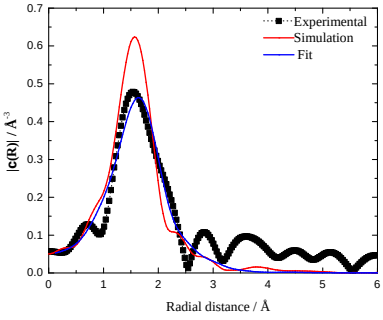

(b)

Figure 5.7: (a) Experimental (■), simulated (red), and fitted (blue) $k^2\chi(k)$ spectra (collected in fluorescence mode) of a sample with composition X(UF_4) = 0.50 at T = 1040 K. (b) Fourier transform modulus $|\chi(R)|$ of the EXAFS spectra.

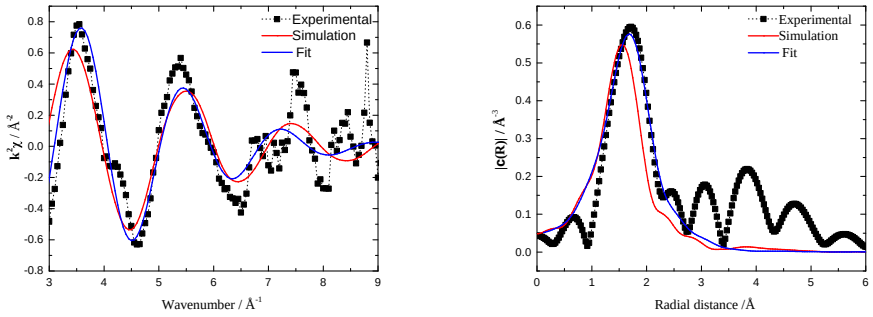

(a) (b)

Figure 5.8: (a) Experimental (■), simulated (red), and fitted (blue) $k^2\chi(k)$ spectra (collected in transmission mode) of a sample with composition X(UF_4) = 0.67 at T = 1216 K. (b) Fourier transform modulus $|\chi(R)|$ of the EXAFS spectra.

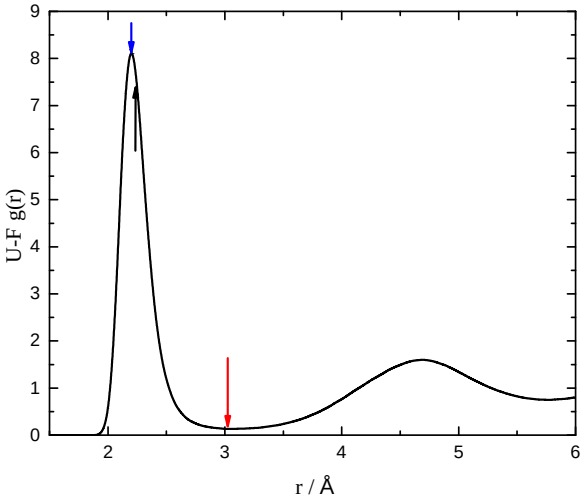

Figure 5.9: Example of a U-F radial distribution function, X(UF_4) = 0.25. From left to right, the arrows indicate the position of the most probable, expected, and bond cutoff lengths.

STRUCTURAL CHARACTERISTICS OF THE FIRST COORDINATION SHELL

The evolution of the average coordination around U^{4+} and the U-F interionic distance obtained by both methods is listed in Table 8. As already mentioned, an illustration of the tabulated most probable, expected, and bond cutoff lengths of the MD simulations is shown in Fig. 5.9. The agreement between both sets of data is good. The coordination

number distribution which can be derived from the MD simulations (listed in Table 10) is dominated by 7, 8, and 9-coordinated U^{4+}, resulting in an average coordination between 7 and 8. This is consistent with the coordination environment of U(IV) fluorocomplexes in the solid state [63] as well as the 7 and 8-coordinations which have been observed by absorption spectroscopy in U(IV)-containing FLiNaK and FLiBE melts by Toth [76]. Most recently, molten-state EXAFS studies on LiF-UF_4 mixtures in the 5 to 30 mol% UF_4 range confirmed the coexistence of $[UF_7]^{3-}$ with $[UF_8]^{4-}$ and $[UF_9]^{5-}$ [7], which also result in an average CN between 7 and 8 (Table 8).

As for bond lengths, Bessada et al. [7] studied the average U-F distances as a function of the coordination number using MD simulations and found averages of 2.17-2.18 Å, 2.23-2.24 Å, 2.29-2.30 Å, 2.35-2.38 Å, and 2.42-2.46 Å in the case of CN = 6, 7, 8, 9, and 10, respectively. The global averages found by the authors are listed in Table 8. They are rather insensitive to temperature and composition. The expected U-F distances according to the simulations in this work and in a related manuscript [53] (2.26-2.28 Å) are in good agreement with those of Bessada et al. (2.28-2.29 Å) and the standard fits (2.23-2.27 Å). From the Fourier transform moduli of the EXAFS data at compositions $X(UF_4)$ = 0.25 and 0.67, it seems that the most probable bond length is slightly underestimated in the MD calculations. In general, the polarizability of species, and thus the potential itself, can change as a function of composition [34], and this underestimation could perhaps be corrected by adjusting the polarizability for every composition. Nevertheless, given the thorough validation of the potential by Dewan [25], and the good results it has also produced with the EXAFS spectra collected by Bessada et al. [7], the results are satisfactory.

It is also instructive to compare with simulations of LiF-ThF_4 melts at several compositions [26], [72], [50], [20], [7]. The results of these different authors are summarized in Table 9. Even if the most probable actinide-fluoride distance is very similar in both binary systems, the actinide contraction effect is evident in the bond cutoff distances, as $max[R_{U-F}] < max[R_{Th-F}]$ at all compositions. Similarly one can observe that, $E[R_{U-F}] < E[R_{Th-F}]$.

Another interesting feature is that the average U-F distance either shortens or remains the same in molten (Li,U)F_x when compared to the distance in the known solid phases (see Section 5.6.1): 2.34(11)[1] Å in $LiUF_5$, 2.29(6)[2] Å in Li_4UF_8 and 2.28(2)[3] Å in UF_4. Dai et al.[20] observed a similar Th-F shortening in molten ThF_4 compared to $ThF_4(cr)$, although the authors incorrectly interpreted it as an expansion of the Th^{4+} coordination cage upon melting. This was because they incorrectly identified a shorter bond length of 2.087 Å as the average Th-F distance in $ThF_4(cr)$ when in fact this distance corresponds to $ThF_4(g)$ [30]. Liu et al. [50] identified a strenghtening of the local structure upon melting by comparing the bond length in their MD simulations with a sum of the Th^{4+} and F^- crystal radii as tabulated by Shannon [70]: r_{Th-F} = 2.36 Å. Again, a better approach would be to look at the average distances in $ThF_4(cr)$ as measured

[1] Averaged from the crystallographic data in [41].
[2] Averaged from the crystallographic data in [11].
[3] Averaged from the crystallographic data in [43].

experimentally: 2.30(1)[4] Å, 2.324(19)[5] Å, and 2.32(3)[6] Å. In the aforementioned bonding analysis per CN done by Bessada et al. [7], it is clear that this strengthening of the local structure is allowed by the reduced repulsion between fluorides in the first shell as the CN decreases, and so it does from solid to liquid. Experimental [39], [57] and computational [46], [13], [56], [77] results on alkali halides reveal the same behavior. A decreased shielding of the 2^{nd} shell, which expands and becomes less populated, could also contribute to these changes in interionic distances [77].

Table 9: Summarized Th-F first neighbor distances as extracted from MD simulations of the (Li,Th)F_x melt by different authors

X(ThF_4)	R^a_{Th-F} / Å	E[R^b_{Th-F}] / Å	R^c_{Th-F}	T / K	Reference
0.15		2.35		850	[7]
0.20		2.34		850	[7]
0.22	2.3		3.4	850	[26]
0.25		2.34		850	[7]
0.30		2.35		850	[7]
0.35		2.36		850	[7]
0.5	2.23		3.2	1193	[72]
0.67[d]	2.24		3.2	1200	[50]
1	2.215		3.1	1633	[20]

[a]Most probable distance,[b]expected value (Eq. 5.19), [c]bond cut-off = maximum Th-F distance. Fig. 5.9 illustrates how these distances differ.

[d]Other compositions were studied as well by the authors, but the maximum of the RDF was found to be insensitive to the ThF_4 concentration.

[4]From EXAFS data, [72].

[5]From neutron diffraction data, [72]

[6]Averaged from the crystallographic data in [43].

Table 8: Structural information of the first fluoride coordination shell around U^{4+} in the (Li,U)F_x solution as calculated in this work, 50 K above the liquidus line, compared to data by Bessada et al. [7] and Ocádiz-Flores et al. [53]. CN is the coordination number, σ^2 is the Debye-Waller factor, ΔE is the energy shift from the L_3 edge, R_f is the goodness of fit. Standard deviations are given in parentheses.

	Coordination number		Bond length				EXAFS fitting				
X(UF_4)	CN_{U-F} MD	CN_{U-F} Fit	R^a_{U-F} MD / Å	R^b_{U-F} MD / Å	$E[R_{U-F}]^c$ MD / Å	$E[R_{U-F}]^b$ Fit / Å	ΔE Fit / eV	σ^2 Fit / Å^2	R_f Fit	T / K	Source
0.05	7.75				2.29					1175	[7]
0.10	7.68				2.28					1125	[7]
0.15	7.82				2.29					1075	[7]
0.20	7.86				2.29					1000	[7]
0.25	7.92	8.0(6)	2.18	3.00	2.26	2.26(1)	2.70(52)	0.021(1)	0.012	831	This work
0.274	7.90				2.29					825	[7]
	7.91				2.29					875	[7]
	7.85				2.29					925	[7]
	7.86				2.29					975	[7]
0.30	7.89				2.29					875	[7]
0.5	7.80	7.6(7)	2.16	3.05	2.27	2.23(1)	1.24(8)	0.025(2)	0.004	1040	This work
0.67	7.72	7.7(8)	2.16	3.03	2.27	2.25(1)	4.14(92)	0.022(2)	0.039	1216	This work
1	7.94	8.0(7)	2.21	3.06	2.28	2.27(1)	3.52(71)	0.030(2)	0.031	1357	[53]

[a]Most probable distance, [b]bond cut-off = maximum U-F distance, [c]expected value (Eq. 5.19). Fig. 5.9 illustrates how these distances differ.

Table 10: Isothermal coordination number distribution and average or expected value of CN (E[CN]) of the (Li,U)F_x melts at T = 1400 K.

Composition X(UF_4)	6 CN %	7 CN %	8 CN %	9 CN %	10 CN %	E[CN]
0.025	4.4	42.4	48.2	4.9	0.1	7.54
0.104	5.5	46.0	43.5	4.9	0.1	7.48
0.211	10.0	49.3	36.3	4.3	0.1	7.35
0.296	10.0	46.1	37.6	6.0	0.2	7.40
0.400	11.5	45.3	36.3	6.6	0.3	7.39
0.513	9.5	41.9	39.4	8.7	0.5	7.49
0.597	8.6	40.4	40.8	9.6	0.6	7.53
0.715	5.9	35.5	44.9	12.9	0.9	7.67
0.807	5.9	35.7	44.8	12.7	0.8	7.67
0.911	4.1	31.4	47.7	15.6	1.2	7.78
1	3.0	28.1	49.7	17.8	1.4	7.86

MEDIUM-RANGE ORDERING

In addition to providing information on the coordination environment of the U species, the MD simulations have the benefit of giving detailed information on the medium-range structure. Two uranium ions are considered fluoride-bridged when the distance between them is less than $2 \cdot R_{U-F,cutoff}$ and less than the first minimum in the U-U RDF. As the UF_4 concentration increases, the number of fluoride bridges increases as well. The bridges identified consisted of 1 F^- (corner-sharing), 2 F^- (edge-sharing), or 3 F^- (face-sharing), with corner-sharing being the dominant bridging mechanism. Dimers and trimers start to appear until a 'polymerized network' is formed, in which all the U cations are connected by bridging fluorides. This evolution is shown in Table 11 and plotted at 1121 K and 1400 K in Figs. 5.10a, 5.10b. The concentration of both isolated coordination complexes and dimers decrease monotonically while the fraction of polymerized species rapidly increases; trimers reach a maximum at around X(UF_4) = 0.2, accounting for less than 20% of the species. The speciation is quite insensitive to temperature, with the polymer fraction increasing only slightly slower with UF_4 addition at T =1400 K.

Network-like behavior has also been observed in MD simulations of LiF-BeF_2 [35], LiF-ZrF_4 [60], LiF-ThF_4 [50], [20], LiF-BeF_2-ThF_4 [50], and LiF-ThF_4-UF_4 [7]. From the cage-out correlation function computed in some of those studies, it seems that the fragility of the coordination environments (as measured by their lifetimes) from lowest to highest is LiF-BeF_2 > LiF-ZrF_4 > LiF-ThF_4. This has implications on the properties at the macroscopic scale, e.g. the viscosity can change around 7 orders of magnitude from LiF to BeF_2 at a given temperature [1], while it only varies around one order of magnitude from LiF to ThF_4 [17], as it does from LiF to UF_4 [24]. Molten LiF-UF_4 is thus expected to have a similar fragility to LiF-ThF_4, as characterized by the cage-out correlation function.

Table 11: Isothermal speciation distribution and expected value of CN of the (Li,U)F_x melt at T = 1400 K.

Composition	Fraction					
X(UF_4)	[a] $[UF_7]^{3-}$	$[UF_8]^{4-}$	[b] $[UF_9]^{5-}$	[c] $[U_2F_x]^{8-x}$	[d] $[U_3F_y]^{12-y}$	"Polymer"
0.025	0.468	0.482	0.050	0.00	0.00	0.00
0.104	0.317	0.268	0.030	0.239	0.027	0.118
0.211	0.143	0.087	0.011	0.160	0.116	0.483
0296	0.037	0.025	0.004	0.039	0.027	0.867
0.40	0.007	0.005	0.001	0.004	0.002	0.981
0.513	0.0	0.0	0.0	0.0	0.0	1.0

[a] The tails of the monomer distribution with lower CN have been added to CN =7.

[b] The tails of the monomer distribution with higher CN have been added to CN =9.

[c] The dominant dimer is $[U_2F_{14}]^{6-}$.

[d] The dominant trimer is $[U_3F_{19}]^{7-}$.

The solution remains saturated with 'polymer' beyond X(UF_4) = 0.513, see Fig. 5.10b.

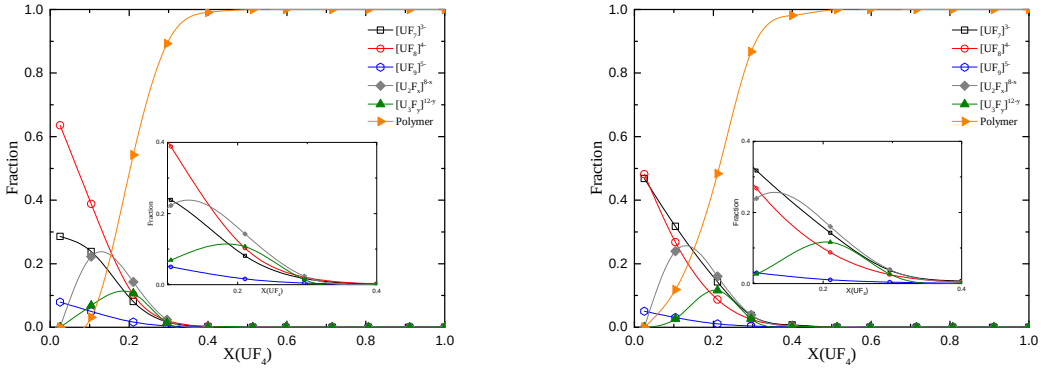

(a) T = 1121 K

(b) T = 1400 K

Figure 5.10: Fraction of species in the (Li,U)F_x solution as a function of UF_4 mole fraction. The monomer contribution is split into the complex anions $[UF_7]^{3-}$ (□, black), $[UF_8]^{4-}$ (○, red), $[UF_9]^{5-}$ (⬡, blue). Dimers indicated by: ⧫, gray, trimers: ▲, green; chains with more than three U^{4+} centers are counted as 'polymers' (▸, orange). (a) T = 1123 K, (b) T = 1400 K. The inset is a zoom of the X(UF_4) = [0,0.4] interval, showing only the evolution of monomer, dimer and trimer. The values at T = 1400 K are listed in Table 11.

5.6.3. EXCESS PROPERTIES OF THE (LI,U)F_x LIQUID SOLUTION

EXCESS DENSITY AND MOLAR VOLUME

Relating the excess properties of molten salts to their structural properties is one of the motivations of the present work. Fig. 5.11a shows the comparison between density isotherms interpolated from the fitting equations to experimental data, given by Klimenkov et al. [44], and those calculated via MD in this work, in the 1000-1400 K range (in some cases the densities are extrapolated beyond the experimentally measured range).

Superposed to these data are the experimental points by Blanke et al. [9] and Porter and Meaker [64], both at 1073 K. The agreement is quite good, with a slight overestimation of the density of pure $UF_4(l)$. The inset in Fig. 5.11a shows the relative excess molar volume, i.e. $(V_{m,real} - V_{m,ideal})/V_{m,ideal}$, calculated from the density data shown in Fig. 5.11a. The volumes of the end-members to compute the ideal volume of mixtures was calculated from the equations of Klimenkov et al. for the three studies in the literature.

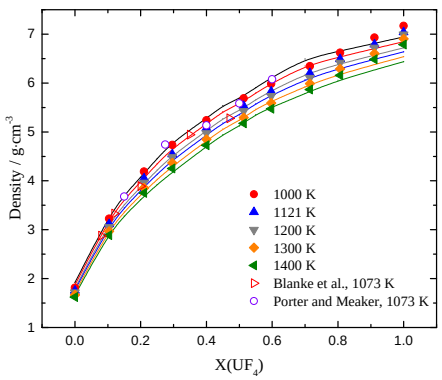

(a)

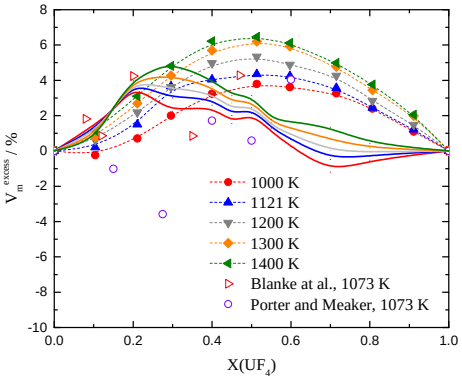

(b)

Figure 5.11: Evolution of density. (a) Solid lines: isotherms calculated from the empirical equations reported by Klimenkov et al. [44]; solid symbols: results derived from MD simulations; ▷, red, experimental data by Blanke et al. [9] and ○ (purple) by Porter and Meaker [64], T = 1073 K. (b) Relative excess molar volume (%), of the (Li,U)F_x solution.

The MD predicts a positive excess of the molar volume, growing with increasing temperature, except in a very limited region at very high LiF content for the supercooled liquid at 1000 K. The excess deduced from Porter and Meaker [64] is also negative at high LiF content, while that from Blanke et al. [9] is positive throughout the reported compositions. In both cases the linear dependences of real molar volumes with composition (not shown) indicate that the behavior is not far from ideality [45]. Finally, the excess from Klimenkov et al. [44] is mostly positive except at high UF_4 content in the case of undercooled solution at T = 1000, 1121 K. As pointed out by the authors, positive deviations from ideality indicate interaction of the components, and they attributed the maximum in the 20 to 30 mol% region (for an isotherm they examined at 1270 K) to the formation of stable $[UF_7]^{3-}$ complexes. As was discussed before (Section 5.6.2), the first coordination shell may even contract upon melting, so it does not contribute to free volume. Instead, the 2nd (and higher order) shells expand and have more voids, i.e., coordination complexes are farther apart from each other in the liquid than in the solid, and even more so in the mixtures than in the pure liquids, as the positive excess volume reveals. This is probably due to the solvation of Li^+, which is nevertheless small

enough to allow extended network formation. Indeed, in the 20 to 30 mol% region the degree of polymerization rapidly increases, reaching a fraction of about 0.9 by 30 mol% (see Figs. 5.10a, 5.10b).

The thermal expansion (shown in the Electronic Supporting Information, ESI), calculated from the density, showed a linear dependence in temperature, and the expansion decreases as a function of UF_4 content. Network formation is likely to account for this, since there is a greater bond strength between neighboring U^{4+} ions. The fits of the linear variations with temperature are listed in the ESI.

HEAT CAPACITY

Enthalpies were extracted directly from the ensemble averages of the potential energy of 0.5 ns NPT production runs at several temperatures: 900 K, 1000 K, 1121 K, 1200 K, 1300 K, and 1400 K. For every composition studied, a linear evolution of the molar enthalpy vs. temperature was obtained (see ESI). Taking linear fits of the molar enthalpies, the heat capacity could then be calculated from:

$$C_{p,m} = \left(\frac{\partial H_m}{\partial T} \right)_P \tag{5.20}$$

The heat capacities of the end-members are very well reproduced: 65.9 vs. 64.183 [16] $J{\cdot}mol^{-1}{\cdot}K^{-1}$ (LiF) and 173.3 vs. 174.4 [45] $J{\cdot}mol^{-1}{\cdot}K^{-1}$ (UF_4). The heat capacity as a function of composition as calculated via MD is compared to the ideal heat capacity. Figures 5.12a and 5.12b show that the heat capacity extracted from MD simulations has small deviations from additivity: much like the density, the heat capacity of the mixtures is close to ideal. For an industrial application setting this is convenient, since a reliable estimate can easily be made for both properties.

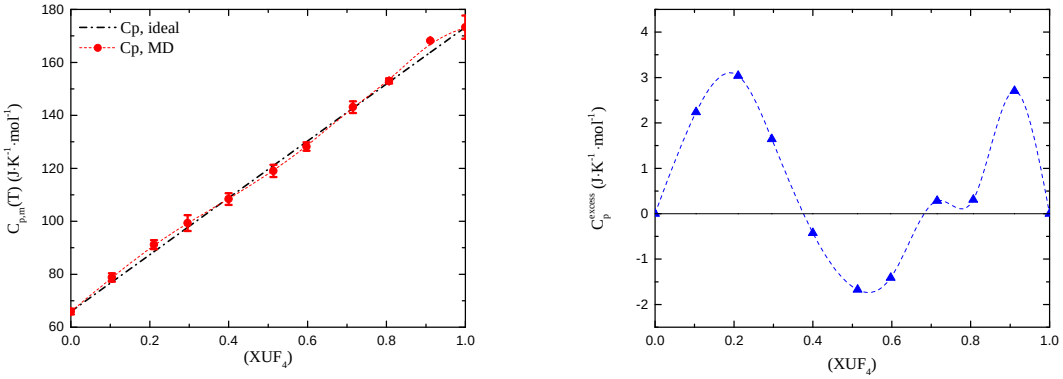

(a) (b)

5

Figure 5.12: (a) Heat capacity of the (Li,U)F_x solution as calculated via MD (●, red) in the 900-1400 K temperature range, compared to the ideal heat capacity (black dashed line) obtained from the experimental heat capacities of the end-members (see Table 1 also). (b) Excess heat capacity of the (Li,U)F_x solution derived from MD simulations.

MIXING ENTHALPY, ENTROPY AND GIBBS ENERGY

Plotted in Fig. 5.13 are the enthalpies of mixing at different temperatures (1000-1400 K) extracted from the MD simulations. Although the magnitude is likely overestimated, the negative excess at all compositions and position of the minima near X(UF_4) = 0.3 are reproduced at all temperatures. The Gibbs energies of mixing display similar trends to the mixing enthalpies, as the mixing entropies also contribute to favorable mixing (see ESI). The shape of the mixing entropy curve (ESI) in (Li,U)F_x as calculated with the structural-thermodynamic model is somewhat closer to ideal mixing entropy than that of (Li,Th)F_x, yet with significant asymmetry and an inflection point near X(UF_4) = 0.2 which corresponds to the strong SRO evidenced by the rapidly rising 'polymer' fraction (see Fig. 5.10b).

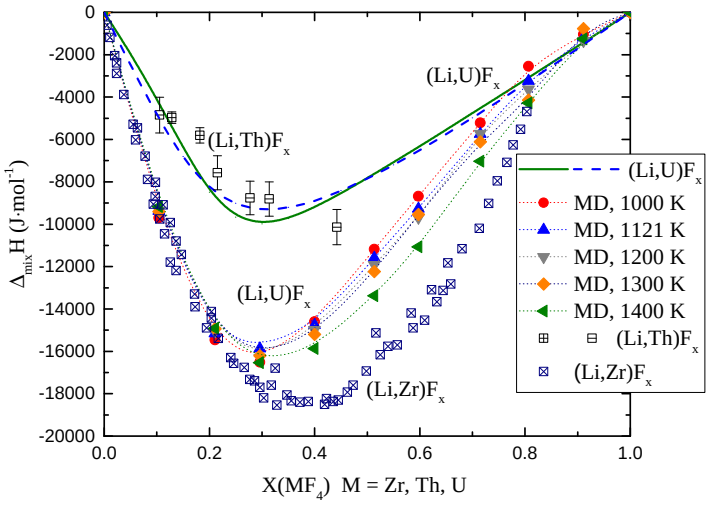

Figure 5.13: Enthalpy of mixing of the (Li,U)F_x solution as calculated at T = 1400 K with the present CALPHAD model (solid green line), and with the model by Beneš et al. [5], (blue dahsed line). Mixing enthalpies for the same system at different temperatures (900-1400 K) were also calculated with MD, shown with symbols as indicated in the legend. Also shown are experimental measurements of the (Li,Th)F_x solution at T = 1121 K, (⊟) and 1383 K (⊞) [15], and the (Li,Zr)F_x solution at 1150 K (⊠) [32].

Several calorimetric measurements reveal that the enthalpy of mixing in binary molten salt systems is usually negative (LiF-BeF_2 being a notable exception, with an S-shaped curve [38]) [59], [58], [32], [37], [15]. This is also the case for the LiF-UF_4 system according to our MD simulations, coupled structural-thermodynamic model, and the optimization previously reported by Beneš et al. [5] (Fig. 5.13). Danek [22], suggested four main reasons to account for this behavior: i) change in the Coulombic repulsion energy of cations, ii) small structural changes during mixing, iii) no change in the number of first-nearest neighbors, iv) change in the state of ion polarization. In the LiF-UF_4 system, effect i) is probably the dominant one given that the uranium cation is tetravalent, and effect iii) is also likely to play a major role, as U^{4+} remains 7, 8, and 9-coordinated when dissolved in LiF (Section 5.6.2), with Li^+ only loosely associated in the second shell. The speciation of the complexes, however, does vary (Table. 11). In contrast, considering the loss of the network-like structure going from pure $UF_4(l)$ to $LiF(l)$, the overall structural changes are not so small and effect ii) probably contributes little to the negative enthalpy in this sytem. Effect iv) would become more evident by changing the alkali second-nearest neighbor, as the polarization ability of the alkali metals reduces down the alkali metal family. This will be studied in more detail in coming works.

Although there is no data on the mixing enthalpy of LiF-UF_4, its magnitude, calculated from the thermodynamic models (the present structural-thermodynamic and that of Beneš), is very similar to that of LiF-ThF_4, for which experimental measurements and

thermodynamic calculations are available (Fig. 5.13). It is expected that the mixing enthalpy will be more negative across AF-UF_4 (A = alkali metal) with increasing radius of the alkali ion, as has been observed in many systems and in particular AF-ZrF_4 [32] and AF-ThF_4 [15], [55] (although more measurements are needed, e.g. in the RbF and CsF-based systems). More interesting is the influence of the tetravalent cation. Substituting $Zr^{4+}_{[VII]}$ (r_{ionic} ~0.78 Å [70]) with $Th^{4+}_{[VIII]}$ (r_{ionic} ~1.05 Å [70]) results in a less negative excess mixing enthalpy as can be seen in Fig. 5.13. The more negative excess in the (Li,Zr)F_x solution is related to the higher stability of $[ZrF_z]^{4-z}$ anions with respect to $[ThF_z]^{4-z}$ ones, and their reduced tendency to form Zr-F-Zr bridges [7]. The tendency towards a less negative deviation from ideal behavior with increasing size of the multivalent cation has been observed in other AX-MX_n systems [22]. Thus, the actinide contraction effect given by the substitution of Th^{4+} by U^{4+} likely results in a more negative deviation from ideality, which may be offset to some extent by the larger polarizability of Th^{4+}.

5

5.6.4. CALPHAD ASSESSMENT OF THE LiF-UF_4 SYSTEM

The LiF-UF_4 binary system shown in Fig. 5.14 was optimized using both structural (Section 5.6.2) and calorimetric data from the literature and measured in this work by DSC (Table 7). Regarding the structural data, the complex anion distribution of the main species $[UF_7]^{3-}$, $[UF_8]^{4-}$, and $[U_2F_{14}]^{6-}$ could be reproduced accurately, as shown in Figs. 5.15a, 5.15b. Recall that for modelling purposes, $[U_2F_{14}]^{6-}$ species encompass dimers, trimers, and polymers. The calculated phase diagram is also in agreement with the data gathered in the present work and with the data from Barton et al. [4]. The invariant equilibria are summarized in Table 6. The system is characterized by the formation of three ternary salts, all of which melt incongruently and at higher temperatures with increasing UF_4 content: Li_4UF_8 , $LiUF_5$, and LiU_4F_{17}, and the existence of a fourth metastable phase with formula Li_3UF_7 (not visible on the calculated phase diagram). The melt is characterized by a predominance of hepta, octa, and nona-coordinated $[UF_x]^{4-x}$ complexes which remain isolated or form dimers, trimers, and chains of higher nuclearity through fluoride bridging, 'polymers'. Near X(UF_4) =0.4, the solution is saturated with these polymeric chains, and remains so until the end-member UF_4. This evolution is rather insensitive to temperature, at least until 1400 K, which was the maximum temperature studied here.

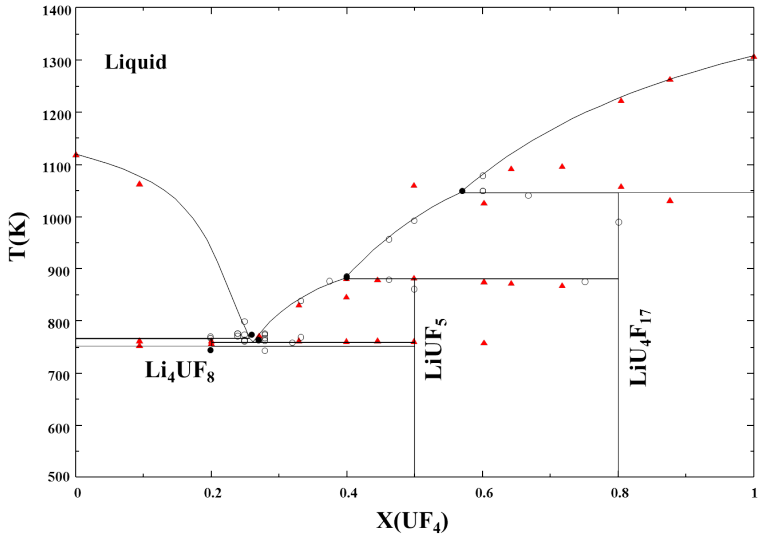

Figure 5.14: LiF-UF_4 phase diagram as calculated in this work, superimposed against experimental points by Barton et al. (○,●) [4] and this study (▲, red, see also Table 7).

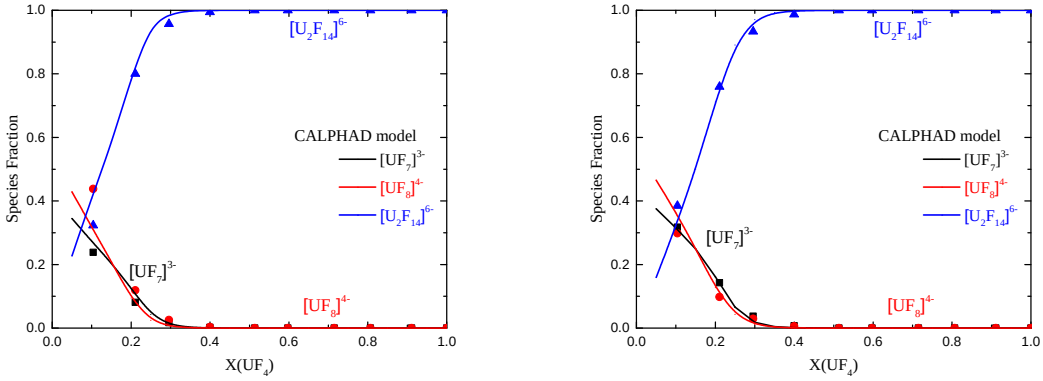

(a) T = 1121 K

(b) T = 1400 K

Figure 5.15: Complex anion distribution obtained with the CALPHAD model (solid lines) and compared with the MD data shown in Table 10 (symbols): $[UF_7]^{3-}$ (black), $[UF_8]^{4-}$ (red), and $[U_2F_{14}]^{6-}$ (blue). (a) T = 1121 K. (b) T = 1400 K.

5.7. CONCLUSIONS

A structural and thermodynamic study of the LiF-UF_4 binary system is reported herein, in light of its relevance for MSR technology. The study set out two main objectives: i) con-

firm decades-old phase equilibria reported by Barton et al. [4] on which state-of-the-art MSR thermochemistry relies, ii) understand the structure of the molten salt as a function of composition, so as to link it with thermo-chemical properties and use it as input to develop a coupled structural-thermodynamic model. With regard to the first objective, it was found that the phase diagram proposed by Barton et al. is essentially correct, except for the phase with LiF:UF_4 = 7:6 stoichiometry which was found by other authors to be $LiUF_5$. It was also confirmed that Li_3UF_7 is a meta-stable phase, and it is suggested to belong to the space group *P4/ncc* like the isostructural Li_3ThF_7 compound. Following Cousson and Pages [19], who narrowed down the possible space groups of LiU_4F_{17} to three (I4/m, I4, $I\overline{4}$), it was found from a LeBail refinement that the most probable one is I4. Further work could aim to obtain these intriguing phases with high purity and elucidate their crystal structures (the structure of $LiTh_4F_{17}$ also remains unknown).
The second objective relied on EXAFS spectroscopy as an experimental technique. Measurements were carried out at three compositions about 50 K above the liquidus temperature: X(UF_4) = 0.25, 0.50, and 0.67. Fitting of the standard EXAFS equation as well as MD simulations were used to interpret the EXAS measurements, while it was possible to extend the composition and temperature space of analysis with the latter technique. The calculations, in agreement with other sources in the literature, showed that (Li,U)F_x(l) is a melt dominated by three coordination complexes throughout the entire composition range: $[UF_7]^{3-}$, $[UF_8]^{4-}$, and $[UF_5]^{9-}$, able to form a network of face, edge, or corner-sharing polyhedra. An advanced thermodynamic assessment was able to reproduce the distribution of $[UF_7]^{3-}$, $[UF_8]^{4-}$, and species of higher nuclearity accounted for by the $[U_2F_{14}]^{6-}$ dimer as calculated with MD simulations, while maintaining sound phase equilibria. Actinide contraction is apparent when the melt is compared to its (Li,Th)F_x analogue, although there do not seem to be significant changes between the excess properties of both systems. It remains to be seen if in other alkali fluoride-based systems the variability is more evident.

5.8. CREDIT AUTHOR STATEMENT

J.A. Ocádiz-Flores: Conceptualization, Methodology, Investigation, Formal analysis, Visualization, Data Curation, Writing - Original Draft preparation **A.E. Gheribi**: Investigation, Software, Formal Analysis, Resources, Writing - Review & Editing **J. Vlieland**: Investigation **K. Dardenne**: Investigation **J. Rothe**: Investigation **R.J.M. Konings**: Conceptualization, Supervision, Writing - Review & Editing **A.L. Smith**: Conceptualization, Methodology, Investigation, Supervision, Funding acquisition, Resources, Project Administration, Writing - Review & Editing

5.9. ACKNOWLEDGEMENTS

A.L. Smith acknowledges financial support from the Netherlands Organisation for Scientific Research (NWO) (project 722.016.005). J.A. Ocádiz-Flores acknowledges CONACYT-SENER for financial support. The authors would like to thank Mathieu Salanne for helpful discussions and for pointing out the PhD dissertation by Leslie Dewan on which they relied for the MD part of this work. The authors acknowledge the KIT light source for provision of instruments at the beamline INE of the Karlsruhe Institute of Technology

(KIT) and would like to thank the Institute for Beam Physics and Technology (IBPT) for the operation of the storage ring, the Karlsruhe Research Accelerator.

5.10. SUPPLEMENTARY INFORMATION FOR: NEW INSIGHTS AND COUPLED MODELLING OF THE STRUCTURAL AND THERMODYNAMIC PROPERTIES OF THE LiF-UF_4 SYSTEM

5.10.1. LATTICE PARAMETERS OF RIETVELD AND LEBAIL REFINEMENTS

Table 12 contains the lattice parameters of the phases identified in this work at different compositions. The initial guesses for the parameters were taken from the literature references. The goodness of fit as measured by the χ^2 factor is also tabulated.

5.10.2. THERMAL EXPANSION

The thermal expansion was calculated from the density from the relation:

$$\beta = -\frac{1}{\rho}\left(\frac{\partial \rho}{\partial T}\right)_P = \frac{1}{V_m}\left(\frac{\partial V_m}{\partial T}\right)_P \tag{5.21}$$

The variation is linear in temperature, and the fits are shown in Table 13 and Fig. 5.16.

Table 13: Thermal expansion in the (Li,U)F_x liquid, in the 900-1400 K range.

X(UF_4)	β / (K^{-1})
0	$1.282{\cdot}10^{-7} \cdot T + 3.134{\cdot}10^{-4}$
0.104	$8.880{\cdot}10^{-8} \cdot T + 2.216{\cdot}10^{-4}$
0.211	$7.545{\cdot}10^{-8} \cdot T + 1.873{\cdot}10^{-4}$
0.296	$7.054{\cdot}10^{-8} \cdot T + 1.835{\cdot}10^{-4}$
0.4	$6.640{\cdot}10^{-8} \cdot T + 1.818{\cdot}10^{-4}$
0.513	$5.551{\cdot}10^{-8} \cdot T + 1.733{\cdot}10^{-4}$
0.597	$4.950{\cdot}10^{-8} \cdot T + 1.679{\cdot}10^{-4}$
0.715	$3.871{\cdot}10^{-8} \cdot T + 1.502{\cdot}10^{-4}$
0.807	$2.886{\cdot}10^{-8} \cdot T + 1.375{\cdot}10^{-4}$
0.911	$1.829{\cdot}10^{-8} \cdot T + 9.742{\cdot}10^{-5}$
1	$8.550{\cdot}10^{-9} \cdot T + 6.145{\cdot}10^{-5}$

Table 12: Experimental lattice parameters of pure phases and mixtures obtained with LeBail refinements at 0.10 $\pm$ 0.005 MPa

Phases	X(UF_4)[a]	a[b](Å)	b[b](Å)	c[b](Å)	α, β, γ [o]	Space Group	Reference	χ^2 factor
Li_3UF_7	0.123	6.1471	6.1471	12.7985	$\alpha = \beta = \gamma = 90$	*P4/ncc*	[18][d]	26.7
$LiUF_5$	0.123	14.8703	14.8703	6.5371	$\alpha = \beta = \gamma = 90$	$I4_1/a$	[12], [41]	26.7
UF_3	0.123	7.1773	7.1773	7.3357	$\alpha = \beta = 90, \gamma = 120$	$P6_3cm$	[47]	26.7
$LiUF_5$	0.25	14.8725	14.8725	6.5415	$\alpha = \beta = \gamma = 90$	$I4_1/a$	[12], [41]	3.79
Li_4UF_8	0.25	9.9593	9.8773	5.9824	$\alpha = \beta = \gamma = 90$	*Pnma*	[11]	3.79
$LiUF_5$	0.50	14.8709	14.8709	6.5410	$\alpha = \beta = \gamma = 90$	$I4_1/a$	[12], [41]	2.99
LiU_4F_{17}	0.80	9.0038	9.0038	11.3953	$\alpha = \beta = \gamma = 90$	*I4*	[19][e]	14.2
UF_3	0.80	7.1730	7.1730	7.3436	$\alpha = \beta = 90, \gamma = 120$	$P6_3cm$	[47]	14.2

[a] Standard uncertainties u are u(X(UF_4))=0.005.

[b] Standard uncertainties u are $u(a)$=0.005 Å.

[c] The reported uncertainties correspond to the standard uncertainty.

[d] The reference describes the structure of Li_3ThF_7 found to have the same space group as Li_3ThF_7 in this work.

[e] The reference suggests three possible space groups to which LiU_4F_{17} can belong, *I4* being one of them.

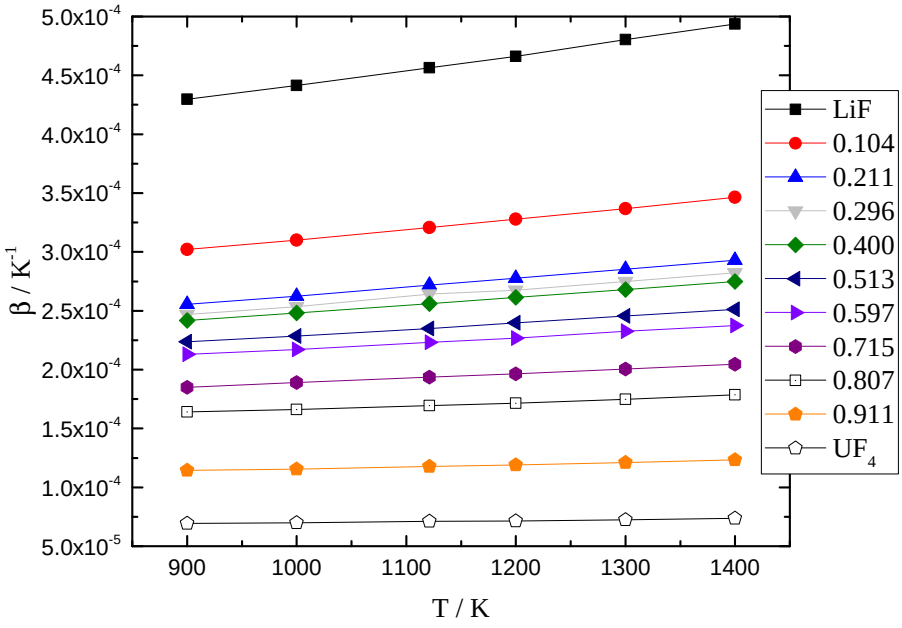

Figure 5.16: Thermal expansion of the (Li,U)F_x solution as a function of temperature.

5.10.3. MOLAR ENTHALPY

The molar enthalpies could be extracted directly from the simulations, and the heat capacities were calculted from them. They are shown below, Fig. 5.17.

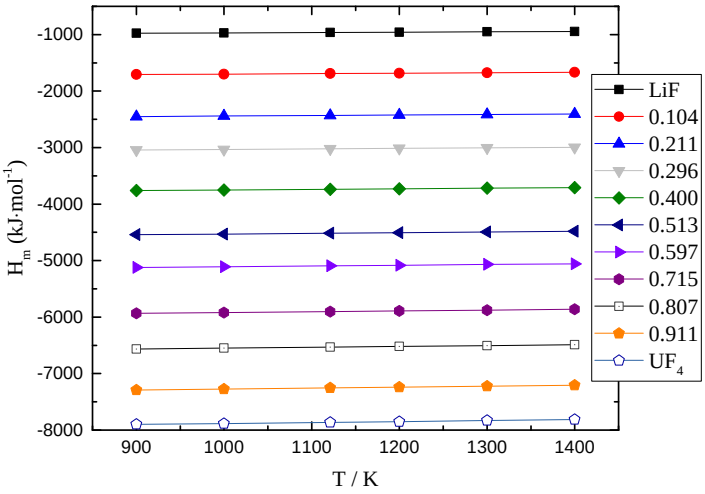

Figure 5.17: Evolution of the molar enthalpies of the (Li,U)F_x solution as a function of temperature.

5.10.4. MIXING GIBBS ENERGIES AND ENTROPIES OF MIXING

As can be seen in Fig. 5.18a, the shape of the mixing entropy curve in (Li,U)F_x as calculated with the structural-thermodynamic model (green curve) is somewhat closer to ideal mixing entropy (red curve) than that of (Li,Th)F_x, yet with significant asymmetry and an inflection point near X(UF_4) = 0.2 which corresponds to the strong SRO of a rapidly rising 'polymer' fraction.

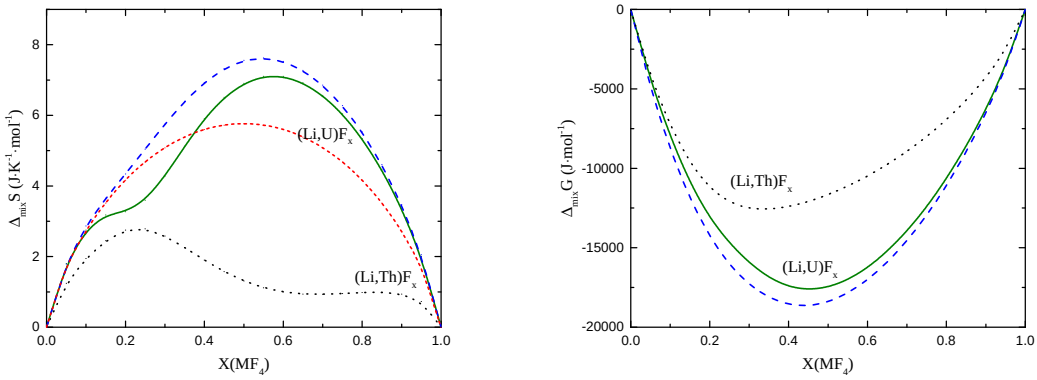

(a) Mixing entropy

(b) Gibbs energy of mixing

Figure 5.18: (a) Mixing entropies and (b) Gibbs energies of mixing of (Li,U)F_x solution in the present CALPHAD model (green, solid), in the model by Beneš et al. [5], and (Li,Th)F_x (black, dotted) [15] at T = 1400 K. The red line represents the ideal mixing entropy.

BIBLIOGRAPHY

[1] Y. Abe, O. Kosugiyama, and A. Nagashima. "Viscosity of LiF-BeF_2 eutectic mixture ($XBeF_2$= 0.328) and LiF single salt at elevated temperatures". In: *Journal of Nuclear Materials* 99.2-3 (1981), pp. 173–183.

[2] A.L. Ankudinov et al. "Real-space multiple-scattering calculation and interpretation of x-ray-absorption near-edge structure". In: *Physical Review B* 58.12 (1998), p. 7565.

[3] C.W. Bale et al. "FactSage thermochemical software and databases, 2010–2016". In: *Calphad* 54 (2016), pp. 35–53.

[4] C.J. Barton et al. "Phase Equilibria in the Alkali Fluoride-Uranium Tetrafluoride Fused Salt Systems: I, The Systems LiF-UF4 and NaF-UF4". In: *Journal of the American Ceramic Society* 41.2 (1958), pp. 63–69.

[5] O. Beneš, M. Beilmann, and R.J.M. Konings. "Thermodynamic assessment of the LiF–NaF–ThF_4–UF_4 system". In: *Journal of Nuclear materials* 405.2 (2010), pp. 186–198.

[6] O. Beneš et al. "A DSC study of the $NaNO_3$–KNO_3 system using an innovative encapsulation technique". In: *Thermochimica Acta* 509.1-2 (2010), pp. 62–66.

[7] C. Bessada et al. "Investigation of ionic local structure in molten salt fast reactor LiF-ThF4-UF4 fuel by EXAFS experiments and molecular dynamics simulations". In: *Journal of Molecular Liquids* 307 (2020), p. 112927.

[8] E. S. Bettis et al. "The aircraft reactor experiment—design and construction". In: *Nuclear Science and Engineering* 2.6 (1957), pp. 804–825.

[9] B.C. Blanke et al. "Density and molar volumes of binary fluoride mixtures". In: *Technical Report USAEC MLM-1086* (1956).

[10] W.J. Boettinger et al. "DTA and Heat-flux DSC measurements of alloy melting and freezing". In: *Methods for Phase Diagram Determination*. Ed. by J.-C. Zhao. Oxford: Elsevier Science Ltd, 2007, pp. 151–221.

[11] G. Brunton. "The crystal structure of Li4UF8". In: *Journal of Inorganic and Nuclear Chemistry* 29.7 (1967), pp. 1631–1636.

[12] G. Brunton. "The crystal structure of LiUF5". In: *Acta Crystallographica* 21.5 (1966), pp. 814–817.

[13] C. Caccamo and M. Dixon. "Molten alkali-halide mixtures: a molecular-dynamics study of Li/KCl mixtures". In: *Journal of Physics C: Solid State Physics* 13.10 (1980), p. 1887.

[14] H.K. Cammenga et al. "The temperature calibration of scanning calorimeters: Part 2. Calibration substances". In: *Thermochimica Acta* 219 (1993), pp. 333–342.

[15] E. Capelli et al. ""Thermodynamic investigation of the LiF–ThF_4 system "". In: *The Journal of Chemical Thermodynamics* 58 (2013), pp. 110–116.

[16] M.W. Chase. *NIST-JANAF Thermochemical Tables (Journal of Physical and Chemical Reference Data Monograph No. 9)*. 1998.

[17] Y.F. Chervinskij, V.N. Desyatnik, and A.I. Nechaev. "Molar viscosity of molten mixtures of lithium and thorium fluorides". In: *Zhurnal Fizicheskoj Khimii* 56.8 (1982), pp. 1946–1949.

[18] A. Cousson, M. Pagès, and R. Chevalier. "The crystal structure of Li_3ThF_7". In: *Acta Crystallographica Section B* 34.6 (June 1978), pp. 1776–1778.

[19] A. Cousson et al. "Flux growth of flourides of lithium and thorium or uranium". In: *Journal of Crystal Growth* 40.1 (1977), pp. 157–160.

[20] J. Dai et al. "Molecular dynamics studies of the structure of pure molten ThF_4 and ThF4–LiF–BeF_2 melts". In: *Journal of Molecular Liquids* 211 (2015), pp. 747–753.

[21] Z. Dai. "17 - Thorium molten salt reactor Nuclear energy system (TMSR)". In: *Molten Salt Reactors and Thorium Energy*. Ed. by T.J. Dolan. Woodhead Publishing, 2017, pp. 531–540. ISBN: 978-0-08-101126-3.

[22] V. Danek. *Physico-chemical analysis of molten electrolytes*. Elsevier, 2006.

[23] S. Delpech et al. "Reactor physic and reprocessing scheme for innovative molten salt reactor system". In: *Journal of Fluorine Chemistry* 130.1 (2009). Fluorine Nuclear Energy, pp. 11–17. ISSN: 0022-1139.

[24] V.N. Desyatnik, A.I. Nechaev, and Y.F. Chervinskii. "Investigation into viscosity of uranium tetrafluoride with lithium fluoride molten mixtures". In: *Zhurnal Fizicheskoj Khimii* 53:4 (1979).

[25] L. Dewan. "Molecular dynamics simulation and topological analysis of the network structure of actinide-bearing materials". PhD thesis. Massachusetts Institute of Technology, 2013.

[26] L.C. Dewan et al. "Molecular dynamics simulation of the thermodynamic and transport properties of the molten salt fast reactor fuel LiF–ThF4". In: *Journal of Nuclear Materials* 434.1 (2013). Special Section on Spent Nuclear Fuel, pp. 322–327. ISSN: 0022-3115.

[27] A.S. Dworkin. "Enthalpy of uranium tetrafluoride from 298–1400°K: enthalpy and entropy of fusion". In: *Journal of Inorganic and Nuclear Chemistry* 34.1 (1972), pp. 135–138.

[28] A. Filipponi. "EXAFS for liquids". In: *Journal of Physics: Condensed Matter* 13.7 (2001), R23.

[29] *GIF, Annual report 2013, Generation IV International Forum, Tech. Rep., www.gen-4.org/gif/upload/docs/application/pdf/2014-06/gif_2013_annual_report-final.pdf*. 2013.

[30] G.V. Girichev et al. "Molecular structure and vibrational characteristics of thorium tetrafluoride". In: *Journal of Structural Chemistry* 40.2 (1999), p. 207.

[31] L.A. Harris, G.D. White, and R.E. Thoma. “X-Ray analyses of the solid phases in the system LiF-ThF”. In: *The Journal of Physical Chemistry* 63.11 (1959), pp. 1974–1975.

[32] G. Hatem, F. Tabaries, and M. Gaune-Escard. “Enthalpies de formation des melanges liquides ZrF4-MF (M= Li, Na, K, Rb)”. In: *Thermochimica Acta* 149 (1989), pp. 15–26.

[33] P.N. Haubenreich and J.R. Engel. “Experience with the molten-salt reactor experiment”. In: *Nuclear Technology* 8.2 (1970), pp. 118–136.

[34] R.J. Heaton and P.A. Madden. “Fluctuating ionic polarizabilities in the condensed phase: first-principles calculations of the Raman spectra of ionic melts”. In: *Molecular Physics* 106.12-13 (2008), pp. 1703–1719.

[35] R.J. Heaton et al. “A first-principles description of liquid BeF_2 and its mixtures with LiF: 1. Potential development and pure BeF_2”. In: *The Journal of Physical Chemistry B* 110.23 (2006), pp. 11454–11460.

[36] G.W.H. Höhne et al. “The temperature calibration of scanning calorimeters”. In: *Thermochimica Acta* 160.1 (1990), pp. 1–12.

[37] J.L. Holm and O.J. Kleppa. “Enthalpies of mixing in binary liquid alkali fluoride mixtures”. In: *The Journal of Chemical Physics* 49.5 (1968), pp. 2425–2430.

[38] J.L. Holm and O.J. Kleppa. “Enthalpies of mixing in liquid beryllium fluoride-alkali fluoride mixtures”. In: *Inorganic Chemistry* 8.2 (1969), pp. 207–212.

[39] M.A. Howe, R.L. McGreevy, and W.S. Howells. “The analysis of liquid structure data from time-of-flight neutron diffractometry”. In: *Journal of Physics: Condensed Matter* 1.22 (1989), p. 3433.

[40] P. Jemmer et al. “Dipole and quadrupole polarization in ionic systems: Ab initio studies”. In: *The Journal of chemical physics* 111.5 (1999), pp. 2038–2049.

[41] Y. Jeongho et al. “Mild hydrothermal crystal growth, structure, and magnetic properties of ternary U (IV) containing fluorides: $LiUF_5$, KU_2F_9, $K_7U_6F_{31}$, $RbUF_5$, RbU_2F_9, and RbU_3F_{13}”. In: *Inorganic Chemistry* 53.12 (2014), pp. 6289–6298.

[42] L. Jorgensen. “ThorCon reactor”. In: *Molten Salt Reactors and Thorium Energy*. Elsevier, 2017, pp. 557–564.

[43] S. Kern et al. “Temperature variation of the structural parameters in actinide tetrafluorides”. In: *The Journal of Chemical Physics* 101.11 (1994), pp. 9333–9337.

[44] A.A. Klimenkov et al. “Density and surface tension of molten mixtures of uranium tetrafluoride with lithium and sodium fluorides”. In: *Atomic Energy* 56.5 (1984), pp. 339–341.

[45] R.J.M. Konings, J.P.M. Van der Meer, and E. Walle. “Chemical Aspects of Molten Salt Reactor Fuel”. In: *European Commission Joint Research Centre* (2005).

[46] F. Lantelme and P. Turq. “Ionic dynamics in the LiCl–KCl system at liquid state”. In: *The Journal of Chemical Physics* 77.6 (1982), pp. 3177–3187.

[47] J. Laveissière. “Application de la diffraction de neutrons à l’étude de la structure cristalline du trifluorure d’uranium UF_3”. In: *Bulletin de Minéralogie* 90.3 (1967), pp. 304–307.

[48] P.A. Lee and J.B. Pendry. “Theory of the extended x-ray absorption fine structure”. In: *Physical Review B* 11.8 (1975), p. 2795.

[49] J. Leitner et al. “Application of Neumann–Kopp rule for the estimation of heat capacity of mixed oxides”. In: *Thermochimica Acta* 497.1-2 (2010), pp. 7–13.

[50] J.-B. Liu et al. “Theoretical Studies of Structure and Dynamics of Molten Salts: The LiF–ThF4 System”. In: *The Journal of Physical Chemistry B* 118.48 (2014), pp. 13954–13962.

[51] H.L. Lukas, S.G. Fries, and B. Sundman. *Computational Thermodynamics. The Calphad Method*. Cambridge University Press, 2007.

[52] P.A. Madden and M. Wilson. “‘Covalent’effects in ‘ionic’systems”. In: *Chemical Society Reviews* 25.5 (1996), pp. 339–350.

[53] J.A. Ocádiz-Flores et al. “Examination of the short-range structure of molten salts: ThF_4, UF_4, and related alkali actinide fluoride systems”. In: *Phys. Chem. Chem. Phys.* 23 (18 2021), pp. 11091–11103.

[54] J.A. Ocádiz-Flores et al. “New insights and coupled modelling of the structural and thermodynamic properties of the LiF-UF_4 system”. In: *Journal of Molecular Liquids* 331 (2021), p. 115820.

[55] J.A. Ocádiz-Flores et al. “Thermodynamic assessment of the KF-ThF_4, LiF-KF-ThF_4 and NaF-KF-ThF_4 systems”. In: *The Journal of Chemical Thermodynamics* 145 (2020), p. 106069.

[56] I. Okada, R. Takagi, and K. Kawamura. “A molecular dynamics simulation of molten (Li-Rb) Cl implying the Chemla effect of mobilities”. In: *Zeitschrift für Naturforschung A* 35.5 (1980), pp. 493–499.

[57] I. Okada et al. “Structural determination of a molten (Li-K) Cl mixture of the eutectic composition by x-ray diffraction and molecular dynamics simulation”. In: *Chemical Physics Letters* 100.5 (1983), pp. 436–441.

[58] G.N. Papatheodorou and O.J. Kleppa. “Enthalpies of mixing in the liquid mixtures of the alkali chlorides with MnCl2, FeCl2 and CoCl2”. In: *Journal of Inorganic and Nuclear Chemistry* 33.5 (1971), pp. 1249–1278.

[59] G.N. Papatheodorou and O.J. Kleppa. “Enthalpies of mixing of liquid nickel (II) chloride-alkali chloride mixtures at 810 C”. In: *Journal of Inorganic and Nuclear Chemistry* 32.3 (1970), pp. 889–900.

[60] O. Pauvert et al. “Ion specific effects on the structure of molten AF-ZrF4 systems (A+= Li+, Na+, and K+)”. In: *The Journal of Physical Chemistry B* 115.29 (2011), pp. 9160–9167.

[61] A. D. Pelton et al. “"The modified quasichemical model I—Binary solutions"”. In: *Metallurgical and Materials Transactions B* 31.4 (2000), pp. 651–659.

[62] A.D. Pelton and P. Chartrand. “The modified quasi-chemical model: Part II. Multicomponent solutions”. In: *Metallurgical and Materials Transactions A* 32.6 (2001), pp. 1355–1360.

[63] R.A. Penneman, R.R. Ryan, and A. Rosenzweig. “Structural systematics in actinide fluoride complexes”. In: *Rare Earths*. Springer, 1973, pp. 1–52.

[64] B. Porter and R.E. Meaker. “Density and molar volumes of binary fluoride mixtures”. In: *Technical Report BMI RI-6836* (1966).

[65] B. Ravel and M. Newville. “ATHENA, ARTEMIS, HEPHAESTUS: data analysis for X-ray absorption spectroscopy using IFEFFIT”. In: *Journal of synchrotron radiation* 12.4 (2005), pp. 537–541.

[66] J. Rodriguez-Carvajal. “Recent advances in magnetic structure determination by neutron powder diffraction”. In: *Physica B* 192 (1993), pp. 55–69.

[67] J. Rothe et al. “The INE-Beamline for actinide science at ANKA”. In: *Review of scientific instruments* 83.4 (2012), p. 043105.

[68] M. Salanne et al. “A First-Principles Description of Liquid BeF_2 and Its Mixtures with LiF: 2. Network Formation in LiF- BeF_2”. In: *The Journal of Physical Chemistry B* 110.23 (2006), pp. 11461–11467.

[69] M. Salanne et al. “Including many-body effects in models for ionic liquids”. In: *Theoretical Chemistry Accounts* 131.3 (2012), p. 1143.

[70] R.D. Shannon. “Revised effective ionic radii and systematic studies of interatomic distances in halides and chalcogenides”. In: *Acta Crystallographica A* 32.5 (1976), pp. 751–767.

[71] A.L. Smith et al. “A new approach for coupled modelling of the structural and thermo-physical properties of molten salts. Case of a polymeric liquid LiF-BeF_2”. In: *Journal of Molecular Liquids* 299 (2020), p. 112165.

[72] A.L. Smith et al. “In situ high-temperature EXAFS measurements on radioactive and air-sensitive molten salt materials”. In: *Journal of synchrotron radiation* 26.1 (2019), pp. 124–136.

[73] P. Souček et al. “Synthesis of UF4 and ThF4 by HF gas fluorination and re-determination of the UF4 melting point”. In: *Journal of Fluorine Chemistry* 200 (2017), pp. 33–40.

[74] K.T. Tang and J.P. Toennies. “An improved simple model for the van der Waals potential based on universal damping functions for the dispersion coefficients”. In: *The Journal of Chemical Physics* 80.8 (1984), pp. 3726–3741.

[75] R.E. Thoma. *Chemical Aspects Of MSRE Operations*. Tech. rep. Oak Ridge National Lab., Tenn., 1971.

[76] L.M. Toth. “Coordination effects on the spectrum of uranium (IV) in molten fluorides”. In: *The Journal of Physical Chemistry* 75.5 (1971), pp. 631–636.

[77] M.M. Walz and D. Van der Spoel. “Molten alkali halides–temperature dependence of structure, dynamics and thermodynamics”. In: *Physical Chemistry Chemical Physics* 21.34 (2019), pp. 18516–18524.

[78] C.F. Weaver et al. *Phase Equilibria in the Systems UF_4-ThF_4 and LiF-UF_4-ThF_4*. Tech. rep. Oak Ridge National Lab., Tenn., 1959.

6

EXPERIMENTAL AND COMPUTATIONAL EXPLORATION OF THE NAF-ThF_4 FUEL SYSTEM: STRUCTURE AND THERMOCHEMISTRY

The structural, thermochemical and thermophysical properties of the NaF-ThF_4 fuel system were studied with experimental methods and Molecular Dynamics (MD) simulations. Equilibrium Molecular Dynamics (EMD) simulations using the Polarizable Ion Model (PIM) were performed to calculate the density, molar volume, thermal expansion, mixing enthalpy, heat capacity and distribution of $[ThF_n]^{m-}$ complexes in the (Na,Th)F_x melt over the full concentration range at various temperatures. The phase equilibria in the 10 - 50 mol% ThF_4 and 85 - 95 mol% ThF_4 regions of the NaF-ThF_4 phase diagram were measured using Differential Scanning Calorimetry (DSC), as were the mixing enthalpies at 1266 K of (NaF:ThF_4) = (0.8:0.2), (0.7:0.3) mixtures. Furthermore, the β-Na_2ThF_6 and $NaTh_2F_9$ compounds were synthesized and subsequently analyzed with the use of X-ray Diffraction (XRD). The heat capacities of both compounds were measured in the temperature ranges (2 - 271 K) and (2 - 294 K), respectively, by thermal relaxation calorimetry. Finally, a CALPHAD model coupling the structural and thermodynamic data was developed using both EMD and experimental data as input and a quasichemical formalism in the quadruplet approximation. Here, 7 and 8-coordinated Th^{4+} cations were introduced on the cationic sublattice alongside a 13-coordinated dimeric species to reproduce the chemical speciation as calculated by EMD simulations and to provide a physical description of

This chapter has been published in *The Journal of Physical Chemistry B*, 2021, **Article ASAP**, DOI: 10.1021/acs.jpcb.1c04830 [65].

the melt.

Maarten B.J.W. Schreuder, Jaén A. Ocádiz-Flores, Aimen E. Gheribi, Ondrej Beneš, Jean-Christophe Griveau, Eric Colineau, Rudy J.M. Konings, Anna Louise Smith

6.1. INTRODUCTION

From a structural viewpoint, inorganic melts can generally be classified as molecular, ionic, metallic, and network-forming, as well as having combined features from these categories[17]. In the case of molten salts, ionic, molecular, and network-forming regimes may be observed depending on the temperature and composition[64]. The LiF-BeF_2 system is a canonical example: LiF is an ionic melt, while BeF_2 is a fully connected network of bridged tetrahedral units[63]. In the process of adding BeF_2 to LiF melts, the corresponding changes in the short-range order manifest themselves in the excess thermodynamic properties, and also significantly alter the transport properties. For instance, the mechanism of electrical conductivity goes from independently diffusing ions to a mechanism where the Li^+ ions travel through channels in the network. At the same time, the viscosity increases by several orders of magnitude[63]. By and large, molten salts are thus a class of ionic liquids displaying a wide range of thermal and electrical conductivities, densities, viscosities, and melting points, amongst other thermophysical properties. This rich chemistry makes them ideally suited as solvents and reaction media for numerous industrial uses.

In recent times, the applications investigated include recovery of valuable metals from spent batteries[23], carburisation of steel[68], carbon capture and storage[81], and the production of hydrogen[36] and ammonia[52]. Yet in a 21st century faced with growing energy demand in combination with the need to cut greenhouse gas emissions, one of the most promising uses of molten salts would be as fuels and coolants for a class of advanced nuclear power systems called Molten Salt Reactors (MSRs)[8]. The current reference fuel mixtures for the European Molten Salt Fast Reactor (MSFR) concept, LiF-ThF_4-$^{233}UF_4$ (77.5-20-2.5 mol%) and LiF-ThF_4-$^{enr}UF_4$-(Pu,MA)F_3 (77.5-6.6-12.3-3.6 mol%, MA = minor actinides)[78], use ^{7}LiF as carrier salt. Interestingly, it was shown in a previous thermodynamic assessment that the addition of NaF to the LiF-ThF_4-UF_4 fuel matrix could lower the melting point of the mixture[7], thereby limiting solidification risks and allowing for possible improvement of the overall thermodynamic efficiency of the reactor. Next to this, NaF is a significantly cheaper alternative compared to ^{7}LiF, which could be particularly appealing in a MSR concept operated in the fast neutron spectrum.

Accordingly, the NaF-ThF_4 fuel system has been investigated herein with experimental and computational methods, to substantiate the knowledge on its materials' properties and the structural behaviour of the melt over wide ranges of temperature and composition. The density, molar volume, thermal expansion, mixing enthalpy, heat capacity, and chemical speciation of NaF-ThF_4 mixtures have been calculated with Molecular Dynamics (MD) simulations across the entire composition space in the 1270 K $<$ T $<$ 2000 K range. Furthermore, the standard entropy of β-Na_2ThF_6 and $NaTh_2F_9$ have been determined using low temperature heat capacity measurements. The mixing enthalpy of (NaF:ThF_4) = (0.8:0.2), (0.7:0.3) compositions, as well as several thermal events in the NaF-ThF_4 phase diagram were determined using Differential Scanning Calorimetry (DSC). Finally, an advanced structural-thermodynamic model has been developed, by using MD and experimental results as input. A test of the general applicability of the model oustide the parameters used to optimize it was made by calculating activities and comparing to experimental results, with satisfactory agreement.

6.2. METHODS

6.2.1. COMPUTATIONAL METHODS

MOLECULAR DYNAMICS SIMULATIONS

The PIM model [48, 64, 32] was used for the MD simulations. This model, based on a semi-classical approach, has proven to be very suitable for simulating fluoride salt systems [64, 72, 32, 20, 26]. The PIM potential energy function is described by the sum of four interaction terms, including charge-charge V_{qq}, repulsion V_{rep}, dispersion V_{disp} and polarization V_{pol} contributions. Each term is explained in the Supporting Information (SI), along with listing of the parameter values. The code used to run the simulations was PIMAIM[48].

In general, the simulation cell consisted of approximately 600 ions (see SI). The temperatures ranged from 1270 to 2000 K. All simulations were started with a NpT run of 500 ps at 0 GPa. Depending on the properties to be calculated, the NpT run was followed by a NVT equilibration run of 200 ps and a NVT production run of 500 ps. The time steps in all ensembles were set to 0.5 fs. The Nosé-Hoover thermostat and Martyna barostat relaxation times were both set to 10 ps. The Ewald sum cutoff radius, which sets a limit to the long-range electrostatic interactions between ions, and the short-range potential cutoff radius were both set to half of the length of the simulation cell.

DENSITY FUNCTIONAL THEORY

The energy curves ($E(V)$) of Na_2ThF_6 and $NaTh_2F_9$ were calculated via DFT. For that purpose, the Vienna ab initio Simulation Package (VASP) [41, 42, 40, 39] was used to perform plane wave computations with the projected augmented wave (PAW) approach [11, 43] and the generalized gradient approximation (GGA) of Perdew, Burke and Ernzerhof (PBE) [58, 59]. Convergence in the energy and cell volume was tested and the results indicated a cut-off energy of 520 eV and $5\times5\times8$ and $5\times5\times5$ Γ-centered k-points grid in the first Brillouin zone for Na_2ThF_6 and $NaTh_2F_9$, respectively, with a Gaussian smearing parameter of 0.02 eV to ensure that the accuracy in the energy of the system was more than 0.01 meV. The self-consistent field (SCF) convergence criterion was 1×10^{-5} eV per electronic iteration and 0.02 eV/Å for each ionic loop that was updated by the conjugate gradient approach. To calculate the energy of the equilibrium lattice, the atomic positions, cell volume and cell shape, were given freedom to relax. To calculate the energy curves, both cell volume and cell shape were fixed and only the atoms were free to move. More detailed information is found in the SI.

6.2.2. EXPERIMENTAL METHODS

SAMPLE PREPARATION

NaF was obtained from Alfa Aesar, with 99.99% purity and was dried for 4 h at 673 K in a furnace under argon flow. The post X-ray diffraction (XRD) and DSC measurements showed no secondary phases. ThF_4 was obtained from JRC Karlsruhe. It was synthesized by fluorination of ThO_2 [73]. No impurities were detected by XRD, and DSC also showed a high purity based on the melting point: (1381 ± 5) K vs. 1383.0 K [38]. Because of their hygroscopic nature, all samples investigated in this work were prepared under dry argon atmosphere in a glovebox, where the oxygen and water contents were kept below 5

ppm. The DSC and XRD measurements were also done under the same protected atmosphere. The samples were sealed under argon atmosphere in the glovebox in specifically designed tightly closed sample holders, such that reactions with water or oxygen from the environment were minimized and radioactive contamination was prevented. The thermal relaxation calorimetry measurements were done under vacuum.

β-Na_2ThF_6 AND $NaTh_2F_9$ SYNTHESIS

NaF and ThF_4 were mixed in the appropriate stoichiometric ratios and were placed inside a nickel liner closed by a nickel lid. A stainless steel crucible enclosed the nickel assembly, and was sealed with a stainless steel screw bolt. The crucible was subsequently annealed in a tubular furnace (Borel, Switzerland) up to 1423 K (above the melting point of pure ThF_4), with a 250 K / h heating ramp. A plateau of 1 h was maintained, after which the sample was slowly cooled down to room temperature with a 25 K / h cooling ramp. An argon flow was applied throughout the routine, to prevent reactions with oxygen or water.

X-RAY DIFFRACTION

A X'pert Pro (PANAlytical) diffractometer mounted in the Bragg-Bretano configuration, with a copper anode (45 kV, 40 mA) was used for the XRD measurements. The intensities of the scattered X-rays were measured with a X'Celerator real time multi strip detector. The angle range was set to $10^\circ \leqslant 2\theta \leqslant 120^\circ$, with an integration time of about 8 h and a step size of 0.008°. The purity of the synthesized compounds was checked by LeBail refinement [3] of the XRD pattern using the FullProf sofware suite [62].

THERMAL RELAXATION MEASUREMENTS USING A PHYSICAL PROPERTY MEASUREMENT SYSTEM (PPMS)

The heat capacity of the synthesized β-Na_2ThF_6 and $NaTh_2F_9$ materials was measured with a PPMS (Quantum Design) instrument. This technique is based on the thermal relaxation method, which is described and evaluated in great detail by Lashley et al. [44]. The samples were pelletized and were subsequently enclosed with Stycast encapsulant, to prevent radioactive contamination and degradation of the hygroscopic samples. The masses of the pellets with Stycast were 13.2 mg (10.3 mg without) for β-Na_2ThF_6 and 12.7 mg (10.9 mg without) for $NaTh_2F_9$, respectively. The contributions of the grease, platform, heater, wires and temperature sensor were measured in a separate run prior to the measurement of the heat capacity of the actual sample (the addenda curve). The addenda and Stycast heat capacity contributions were then subtracted from the measured values of the sample run. The heat capacity was measured between (2 - 271 K) for β-Na_2ThF_6 and between (2 - 294 K) for $NaTh_2F_9$. No magnetic field was applied during the experiments. Based on the experience with the PPMS instrument, and the encapsulation of similar materials in Stycast [70],[35], the uncertainty of the measurements was estimated to be 3% for temperatures lower than 100 K and 1% between (100 - 300 K). Treatment of the data was done as outlined in Section 6.2.5 and described at length in references [66, 67, 27].

PHASE EQUILIBRIA MEASUREMENTS BY DSC

The transition temperatures were measured using a Setaram multi-detector high temperature calorimeter (MHTC-96 type) operating in DSC mode, equipped with S-type thermocouples, capable of measuring up to 1673 K.

NaF-ThF$_4$ mixtures were placed in a nickel liner. A stainless steel crucible encapsulated the liner and a nickel lid was pressed into the liner by screwing a stainless steel bolt onto the crucible, such that the sample was hermetically sealed from the environment, as in [9] (see SI also). The transition temperatures were measured for the compositions (NaF:ThF$_4$) = (0.9:0.1), (0.8:0.2), (0.7:0.3), (0.6:0.4), (0.5:0.5), (0.15:0.85), (0.1:0.9) and (0.05:0.95). For every experiment, four heating cycles were applied, in which the sample was annealed approximately 90 K above the melting points of the end-members during the first cycle, and above the liquidus line for the subsequent cycles, as seen in the reported phase diagrams[7, 51]. Subsequently, the recorded temperatures assigned to a particular event were averaged over the successive cycles, excluding the first one. The measured temperatures were corrected with a temperature calibration equation, derived by measuring the melting points of different high purity metallic standards (In, Pb, Sn, Al, Ag, Au), following the procedure described in [33], [13]. The uncertainty on the measured temperatures is estimated to be ś5 K for pure compounds and ś10 K for mixtures. The onset temperature obtained by tangential analysis of the heat flow was selected for transitions and congruent melting temperatures. The extremum of the heat flow peak was selected for the liquidus events as recommended by Boettinger et al[12].

ENTHALPY OF MIXING MEASUREMENTS BY DSC

Mixing enthalpy experiments were performed with the same type of crucibles as used in the DSC measurements. The technique and determination of the detector sensitivity are described in great detail in [14] (see SI as well). A pellet of NaF was placed below a ThF$_4$ pellet. A small nickel liner separated the end-member compounds such that eutectic melting or solid phase reactions were prevented, up until melting of NaF, which initiated the mixing event. Au reference material ($>$ 99.99% purity) was measured at the same time as the sample, which allowed to determine the detector sensitivity and subsequently the total enthalpy involved in the mixing event $\Delta_{meas}H^o_m(T_{fus,NaF})$. The enthalpy of mixing is then calculated by subtracting the fusion enthalpies of the end-members from the measured heat:

$$\begin{aligned}\Delta_{mix}H^o(T_{fus,NaF}) = \Delta_{meas}H^o(T_{fus,NaF}) - x_{NaF}\Delta_{fus}H^o(KF, T_{fus,NaF}) \\ -x_{ThF_4}\Delta_{fus}H^o(ThF_4, T_{fus,NaF})\end{aligned} \tag{6.1}$$

The samples were heated beyond the melting point of ThF$_4$, to check if any material remained unreacted.

Note that it is assumed that the fusion enthalpy of ThF$_4$ is temperature-independent and is thus the same at the melting temperature of NaF. This is a reasonable approximation according to the work of Capelli et al[14]. The fusion enthalpies used were 36.4 kJ mol^{-1} for ThF$_4$[78] and 33.3 kJ mol^{-1} for NaF[2]. The uncertainties in the mixing enthalpy $\Delta_{mix}H^o_m(T_{fus,NaF})$ were determined from the standard uncertainty of the calibration process. The setup was the same as the one used to measure mixing enthalpies

in the KF-ThF_4 system, with which the fusion enthalpies of LiF, NaF, KF, and ThF_4 were measured within experimental error [54].

6.2.3. CALPHAD MODELLING

PURE COMPOUNDS

The optimization of the NaF-ThF_4 thermodynamic model was carried out using the Factsage software[4] (Version 7.2). To assess a phase diagram, the identity of the phases present in the system of interest must be known, as well as their respective Gibbs energy functions. In this work, the Neumann-Kopp rule [46] was used to approximate the heat capacities of intermediate compounds in the absence of experimental data, with the exception of β-Na_2ThF_6 and $NaTh_2F_9$. For each of these two phases, a polynomial fit bridging the measured low-temperature heat capacity data ($\sim$2 to $\sim$298 K, Section 6.2.5) and behavior at high temperatures (500 K to melting point) as predicted by the Quasi-Harmonic Approximation (QHA) was used. The thermodynamic data for all compounds in this study are listed in Table 1. The data for solid and liquid NaF and ThF_4 were taken from NIST-JANAF[15] and the work by Tosolin et al.[77] and Konings and van der Meer[38], respectively. The standard enthalpies of formation and standard entropies of all the intermediate compounds were optimized to closely match phase equilibria data and thermodynamic data reported herein (mixing enthalpies, standard entropies of α-Na_2ThF_6 and $NaTh_2F_9$).

LIQUID SOLUTION

The excess Gibbs energy terms of the (Na,Th)F_x liquid solution have been modelled in the present work using a modified quasi-chemical model similar to the one recently optimized for the LiF-BeF_2 system [71]. A detailed description is given in the SI. As will be examined in the following sections, (Na,Th)F_x is not a solution in which cations and anions are completely dissociated. Rather, the solution is formed by discrete coordination complexes of F^- ligands around Th^{4+}. At low ThF_4 concentrations, most Th^{4+} are present as monomers, primarily with coordination numbers 7 and 8: $[ThF_7]^{3-}$ and $[ThF_8]^{4-}$. Hence, in this work, two distinct Th^{4+} cations were taken into account: $Th^{4+}_{[VII]}$ and $Th^{4+}_{[VIII]}$. At higher ThF_4 concentrations, the number density of the monomers increases, leading to dimers $[Th_2F_x]^{8-x}$, trimers $[Th_3F_y]^{12-y}$, and longer chains or 'polymers' of thorium cations linked together by bridging fluorides (see Fig. 6.19). There are many chain lengths possible, not all of which can be taken into account if the number of fitting parameters is to be kept from becoming too large. Hence, dimers and all species of higher nuclearity were included in the model as dimers in which the overall coordination sphere around the two Th atoms is made of 13 fluorine atoms (the most abundant according to MD simulations), with the corresponding cation $Th_2[XIII]^{8+}$. Given that pure $ThF_4(l)$ is a network of mostly corner-sharing coordination polyhedra [16, 53], it was modelled as a solution of dimers. Such a choice is a simplification, yet one which already reflects a main structural characteristic of the network: fluoride bridging. A detailed description of the complete model as well as the optimized parameters are provided in the SI.

Table 1: Thermodynamic data for end-members and intermediate compounds used in this work for the phase diagram assessment: $\Delta_f H^o_m(298\,K)/(kJ\cdot mol^{-1})$, $S^o_m(298\,K)/(J\cdot K^{-1}\cdot mol^{-1})$, and heat capacity coefficients $C_{p,m}(T/K)/(J\cdot K^{-1}\cdot mol^{-1})$, where $C_{p,m}(T/K) = a + b\cdot T + c\cdot T^2 + d\cdot T^{-2}$. Optimized data are shown in **bold**.

Compound	$\Delta_f H^o_m(298\,K)/$ $(kJ\cdot mol^{-1})$	$S^o_m(298\,K)/$ $(J\cdot K^{-1}\cdot mol^{-1})$	$C_{p,m}(T/K)/(J\cdot K^{-1}\cdot mol^{-1})$= a + b·T + c·$T^{-2}$			Reference
			a	b	c	
NaF(cr)	-576.650	51.21	47.63	$1.479\cdot 10^{-2}$	-464300	[15]
NaF(l)	-557.730	52.755	72.989			[15]
ThF_4(cr)	-2097.900	142.05	111.46	$2.6900\cdot 10^{-2}$	-780000	[38],[77]
ThF_4(l)[a]	-2100.360	106.61	168.0			[38, 77]
Na_4ThF_8(cr)	**-4360.695**	**436.4**	301.98	$8.6060\cdot 10^{-2}$	-2637200	This work
$Na_7Th_2F_{15}$(cr)	**-8272.950**	**675.6**	556.33	$1.5733\cdot 10^{-1}$	-4810100	This work
Na_2ThF_6(cr)	**-3276.100**	257.3	**207.5043**	$\mathbf{4.5076\cdot 10^{-2}}$	**-1824833**	This work
$Na_3Th_2F_{11}$(cr)	**-5899.800**	**525.0**	365.81	$9.8170\cdot 10^{-2}$	-2952900	This work
$Na_7Th_6F_{31}$(cr)	**-16689.725**	**1300.0**	1002.17	$2.6493\cdot 10^{-1}$	-7930100	This work
$NaThF_5$(cr)	**-2696.500**	**194.2**	159.09	$4.1690\cdot 10^{-2}$	-1244300	This work
$NaTh_2F_9$(cr)	**-4808.106**	333.7	**287.165**	$\mathbf{2.7885\cdot 10^{-2}}$	**-2574616**	This work

[a] ThF_4(l) is modelled as a [$Th_{VII}F_4$(l)-$Th_{VIII}F_4$(l)-$Th_{2[XIII]}F_8$(l)] mixture with $g^0_{Th_{[VII,VIII]}F_4}(l) = \frac{1}{2}g^0_{Th_{2[XIII]}F_8(l)} + 150000\ J\cdot mol^{-1}$.

SOLID SOLUTION

A solid solution appears in the system in the ThF_4-rich side of the phase diagram according to Thoma et al[76], although earlier work by Emelyanov and Evstyukhin[22] did not find evidence of the solid solution. The DSC data in this work do not give conclusive evidence on the matter. The solid solution phase was thus not retained in this work.

6.2.4. STRUCTURAL INVESTIGATIONS OF THE (NA,TH)F_x MELT VIA MOLECULAR DYNAMICS

DENSITY AND MOLAR VOLUME

The densities ρ and molar volumes V_m (Fig. 6.1a) of the (Na,Th)F_x melt were calculated with MD from the mean volume of the cubic simulation cells after the NpT run at 1270, 1433, 1500, 1600 and 2000 K, over the full concentration range. The results at 1270 K are compared to the experimental data obtained by Desyatnik et al. [18] (for the mixtures) and Kirschenbaum et al. [37] (for pure ThF_4) by interpolating at the same temperature. A maximum relative deviation of less than 3 % is observed, hence good agreement was found between the calculated density data using MD and the experimental values, especially when considering the fact that experimental works on densities of salt mixtures can vary by several percent [8].

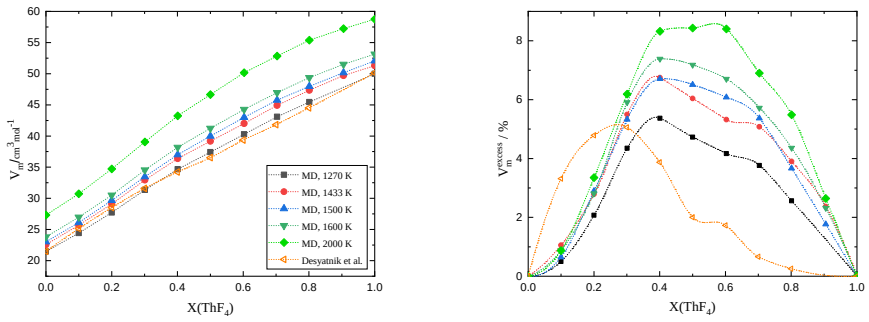

(a) (b)

Figure 6.1: (a) Molar volumes versus composition at T = 1270, 1433, 1500, 1600, and 2000 K. (b) Excess molar volumes versus composition at the same temperatures. Both are compared to data by Desyatnik et al.[18] at 1270 K.

The molar volume increases quasi linearly with increasing concentration of ThF_4 and increases with temperature as expected. The excess molar volume is shown in figure 6.1b. A positive excess molar volume is observed for the MD and experimental data. The local maximum at T = 1270 K is at 40 mol%, slightly shifted compared to the maximum of the experimental data (30 mol%). The magnitude of the excess is similar in that region, close to 5%. As temperature is increased, the excess molar volume grows. The maxima of the MD calculated curves are reached at approximately 40 mol% ThF_4 for all temperatures, which coincides with the complete polymerization of the melt (see Fig. 6.19).

ORDER AT SHORT RANGE

Fluoride melts display strong short-range order (SRO), with a coordination environment of fluorides around cations and vice-versa. The coordination numbers of the $[ThF_n]^{m-}$ complexes in the melt were calculated from the radial distribution functions $g(r)$ (RDF) of the Th-F pair. Here, the output of the NVT production runs over the full composition range at 1270, 1433, 1500 and 1600 K were used. The Th-F RDF at 70 mol% ThF_4 composition at 1500 K is shown in figure 6.2 (black line). The first minimum occurs around 3.17 Å. The Th-Th RDF is also shown in figure 6.2 (red line). The first minimum occurs around 5.10 Å, representing the radius of the second coordination shell. The first local minimum in the Th-F RDF was taken as the cut-off radius of the first coordination shell. Hence, the coordination numbers were determined by counting the number of F^- anions within the radius of the first coordination shell of a Th^{4+} cation.

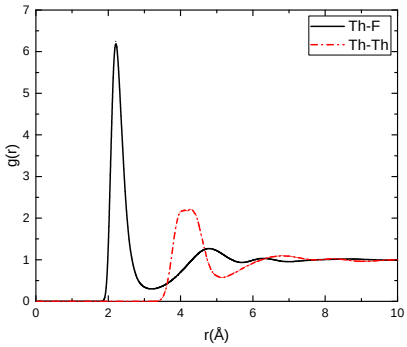

Figure 6.2: Radial distribution functions of Th-F and Th-Th bonds at 70 mol% ThF_4 at 1500 K, shown in black and red, respectively.

The calculations reveal coordinations of 6, 7, 8, 9 and 10, the 7, 8 and 9 being the predominant ones. Figure 6.3 shows the distribution of the 7, 8 and 9 coordinated $[ThF_n]^{m-}$ complexes in the melt. In general, $[ThF_8]^{4-}$ and $[ThF_9]^{5-}$ become more dominant as the concentration of ThF_4 increases. The increase in fractions of 8 and 9 coordinated $[ThF_n]^{m-}$ complexes was also observed in different studies in the high thorium concentration region for the LiF-ThF_4 system [20, 16, 47], and is related to the formation of a molecular network (see below). Furthermore, the predominance of 8-coordinated complexes and the substantial presence of 7-coordinated complexes as found in this work, was also observed experimentally with Raman spectroscopy in LiF-NaF-ThF_4 melts [79]. As temperature increases, the relative fractions of 7 and lower coordinated complexes increase. The same phenomenon was also observed during investigations on the LiF-ThF_4 system [20]. Bond rearrangement is facilitated at higher temperatures due to the increased kinetic energies of the ions, and thus the fraction of higher-coordinated complexes is smaller.

The average coordination number of $[ThF_n]^{m-}$ complexes versus composition in the NaF-ThF_4 melt is shown for various temperatures in figure 6.4. It decreases with temper-

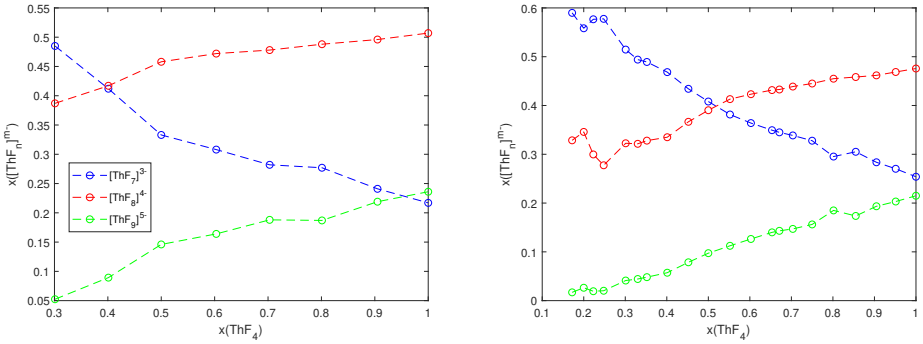

(a) T = 1270 K (b) T = 1433 K

Figure 6.3: Distribution of the 7, 8 and 9 coordinated $[ThF_n]^{m-}$ complexes versus composition in the NaF-ThF_4 system at 1270 (supercooled at X(ThF_4) >0.8) and 1433 K.

ature, due to a lower proportion of 8 and 9-coordinated complexes at higher temperatures. It increases gradually in the region 30 - 100 mol% ThF_4. The calculations at 1500 and 1600 K reveal a minimum in the average coordination numbers around 30 mol% ThF_4. The lower average coordination number indicates that smaller complexes form, which allow for more densely packed arrangements and hence results in a higher density and lower molar volume.

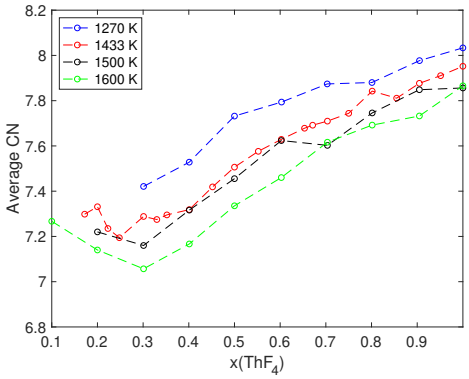

Figure 6.4: Evolution of the average coordination numbers of $[ThF_n]^{m-}$ complexes versus composition in the NaF-ThF_4 system at various temperatures.

MEDIUM-RANGE ORDER IN THE (NA,TH)F_x LIQUID SOLUTION

An advantage of MD simulations is that a detailed description of the structure of the salt is obtained at length scales accessible with total neutron/X-ray diffraction [1], that is, beyond those accessible with other experimental techniques, e.g. XAS and Raman spec-

troscopy. For example, links between thorium cations via fluoride bridging can be subject to analysis. Two thorium centers, separated by a distance *r*, are said to be fluoride-bridged if $r < R_{Th-Th,cutoff}$ and $r < 2 \cdot R_{Th-F,cutoff}$. $R_{Th-Th,cutoff}$ and $R_{Th-F,cutoff}$ denote the first local minima in the Th-Th and Th-F RDFs, respectively. Dimers, trimers, and species of higher nuclearity thus arise from fluoride bridging, up to the point where a network may emerge.
It has been observed that alkali cations, depending on their nature and concentration, can significantly impact the network-forming abilities of ionic systems due to steric effects[82, 55]. Na^+ is small enough to allow for the complexes to link via bridging fluorides and form a network, as can be seen in Fig. 6.19. The species are classified into three groups, namely monomers (ThF_x^{4-x}), dimers ($Th_2F_x^{8-x}$), and 'polymers', i.e., any chain where three or more Th^{4+} ions are linked together. The behavior is very similar across temperatures (see SI): with increasing ThF_4 content there is a monotonic decrease and increase of the monomer and polymer fractions, respectively, while the concentration of dimers reaches a maximum in the region $0.2 < X(ThF_4) < 0.25$. In the same region, Desyatnik et al.[18] found a local maximum of the viscosity, which the authors attributed to the specific stability of $[ThF_7]^{3-}$ complexes. The structural properties emerging from the MD simulations suggest that it is not only the single shells but their dimers which have a large contribution to the viscosity at that composition range.

6

6.2.5. THERMODYNAMIC STUDIES

PHASE DIAGRAM INVESTIGATIONS

To date, experimental data on the NaF-ThF_4 system are only available from a handful of studies. Zachariasen published a series of papers in 1948 – 1949 reporting the existence of the Na_4ThF_8, Na_2ThF_6 and $NaTh_2F_9$ intermediates [85]. In other studies, the author reported that four polymorphs existed for the Na_2ThF_6 compound [84, 83]. Later, Emelyanov and Evstyukhin[22] investigated the phase equilibria, and identified four phases: Na_4ThF_8, Na_2ThF_6 (with a phase transition), $NaThF_5$, and $NaTh_2F_9$. Making use of a wider set of experimental techniques, Thoma et al.[76] also assessed the system, and included six compounds in their description: two congruently melting phases, namely Na_2ThF_6 (without polymorphism) and $Na_3Th_2F_{11}$, as well as four other compounds: Na_4ThF_8, $Na_7Th_6F_{31}$, $NaThF_5$, and $NaTh_2F_9$. Making use of quenching techniques, the authors subsequently identified the $Na_7Th_2F_{15}$ compound[75].

More modern investigations by Grzechnik et al. provide a complete overview of structural properties of the β-Na_2ThF_6 [31] and $NaTh_2F_9$ [30] intermediates. Grzechnik et al. detected no phase transitions for β-Na_2ThF_6 in the temperature range 290-954 K, nor did Mukherjee et al.[51] in a recent experimental determination of the standard thermodynamic functions and melting point of this intermediate. A DSC scan of the synthesized β-Na_2ThF_6 in the present work was performed to see if transitions to other phases occur. However, only a congruent melting point was detected, in line with Thoma et al., Grzechnik et al., and Mukherjee et al. Moreover, there is no evidence of a phase transition in the low-temperature heat capacity data (see Section 6.2.5 below), so Na_2ThF_6 has only one phase from 0 K until its melting point. Data are more scarce on the phase equilibria at high ThF_4 content. In that region, the phase $NaTh_3F_{13}$ has also been reported,

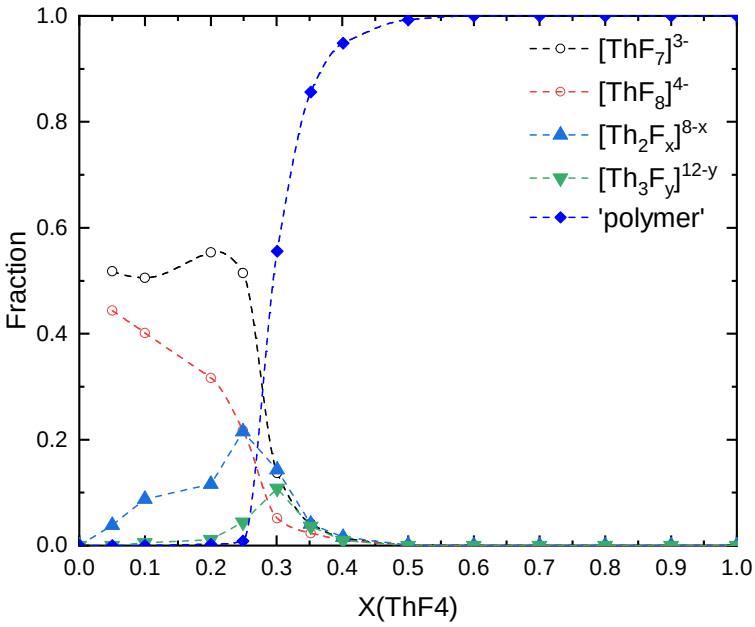

Figure 6.5: Fraction of monomers (○), dimers (⬥), and 'polymers' (▲), in the NaF-ThF_4 liquid solution at T = 1433 K.

synthesized via a hydrothermal route by Underwood et al.[80] and characterized with single crystal XRD. The melting point or other thermodynamic data were not measured. It is likely to be metastable, as previous investigations of the system did not find evidence for it, and indeed none the DSC measurements in this work (Table 2) seem to indicate that it is stable.

Figure 6.12 shows a great agreement between events measured in this work and the present description of the NaF-ThF_4 phase diagram in the region $x(ThF_4) \leqslant 0.33$. In the $0.33 < x(ThF_4) < 0.67$ region, there is a higher uncertainty. The eutectoid at 881 K, $x(ThF_4) = 0.401$ was not observed and only one event was measured at $x(ThF_4) = 0.497$, which could indicate congruent melting of $NaThF_5$. Furthermore, another sample was made from the $x(ThF_4) = 0.497$ composition, which was annealed up to 1423 K and analysed using XRD, following the same procedure as the syntheses of β-Na_2ThF_6 and $NaTh_2F_9$, described previously in the methods section. The Bragg reflections of the XRD pattern matched with the crystallographic data of [76] for $NaThF_5$, suggesting that $NaThF_5$ is stable from room temperature up to the point of congruent melting. However, more crystallographic investigations are needed to confirm this.

Table 2: Phase equilibria in the NaF-ThF_4 system measured using DSC in this work. [a]Standard uncertainty $u(x(ThF_4)) = 0.5$ mol%.

$x(ThF_4)$[a] / mol %	T / K	Equilibrium	Invariant Reaction
9.9	825.0	Eutectoid	$NaF + Na_2ThF_6 = Na_7Th_2F_{15}$
9.9	870.3	Eutectoid	$Na_7Th_2F_{15} + NaF = Na_4ThF_8$
9.9	905.2	Peritectic	$Na_4ThF_8 = L + NaF$
9.9	1178.7	Liquidus	NaF + L' = L
19.9	829.0	Eutectoid	$Na_7Th_2F_{15} + NaF = Na_4ThF_8$
19.9	872.3	Eutectoid	$Na_7Th_2F_{15} + NaF = Na_4ThF_8$
19.9	912.8	Peritectic	$Na_4ThF_8 = L + NaF$
29.8	834.8	Eutectoid	$NaF + Na_2ThF_6 = Na_7Th_2F_{15}$
29.8	886.2	Eutectic	$Na_7Th_2F_{15} + Na_2ThF_6 = L$
29.8	951.6	Liquidus	Na_2ThF_6 + L' = L
33.3	966.5	Liquidus	$Na_2ThF_6 = L$
40.1	949.4	Eutectic	$Na_2ThF_6 + Na_3Th_2F_{11} = L$
40.1	978.9	Peritectic	$Na_7Th_6F_{31} + L = Na_3Th_2F_{11}$
49.7	998.4	Peritectic	$Na_7Th_6F_{31} = L + NaTh_2F_9$
85.3	1086.4	Peritectic	$NaTh_2F_9 = L + ThF_4$
85.3	1343.3	Liquidus	ThF_4 + L' = L
89.7	1360.0	Liquidus	ThF_4 + L' = L
94.7	1379.2	Liquidus	ThF_4 + L' = L
1.0	1381.0	Congruent melting	$ThF_4 = L$

The region between 85 and 100 mol% is characterized by the presence of a solid solution according to Thoma et al[76]. However there is little experimental data confirming its existence. Therefore measurements were done at $x(ThF_4) = 0.853, 0.897, 0.947$. The peritectic at $x(ThF_4) = 0.853$, T = 1086.4 K, was observed as well as the liquidus equi-

librium at this composition. The presence of a solid solution was not detected in the measurements at x(ThF_4) = 0.897 and 0.947 using DSC. Hence, further investigations are needed to confirm its existence, using for instance high temperature XRD analysis or quenching techniques.

XRD ANALYSIS

The XRD patterns of β-Na_2ThF_6 and $NaTh_2F_9$ are shown in Figures 6.6 and 6.7, respectively. No secondary phases were detected and the purity was estimated $> 99\%$. The patterns were refined using the Le Bail method [45]. The refined values of the cell parameters of both compounds are given in Table 3. Good agreement was found with the cell parameters for β-Na_2ThF_6 and $NaTh_2F_9$ at ambient temperature and pressure reported by Grzechnik and co-workers, given by $a = 5.985(2)$ Å, $b = 5.985(2)$ Å, $c = 3.843(1)$ Å for β-Na_2ThF_6 with space group P321 (150) [31], and $a = 8.763(1)$ Å, $b = 8.763(1)$ Å, $c = 8.640(2)$ Å for $NaTh_2F_9$ [30] with space group $I\bar{4}2m$ (121).

Table 3: Cell parameters of refined XRD patterns.

Compound	Space Group	a / Å	b / Å	c / Å
β-Na_2ThF_6	P321 (150, trigonal)	5.983(3)	5.983(3)	3.833(5)
$NaTh_2F_9$	$I\bar{4}2m$ (121, tetragonal)	8.723(9)	8.723(9)	8.724(2)

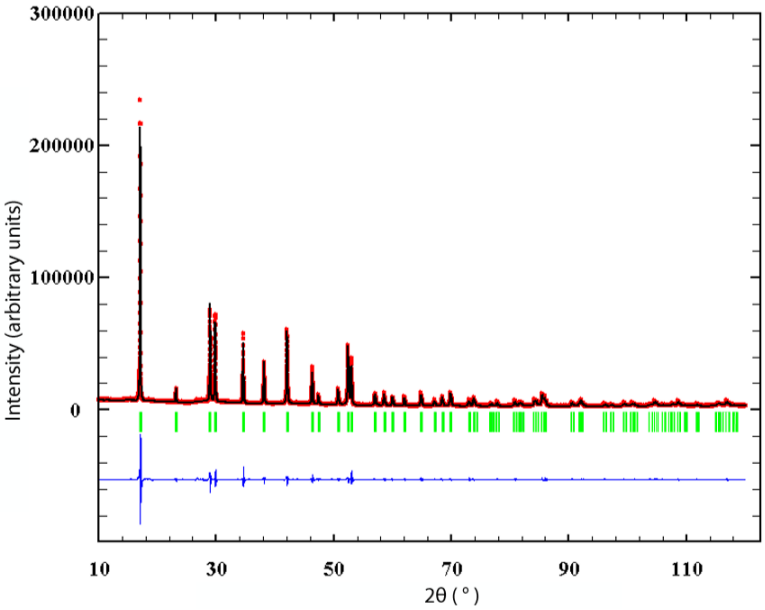

Figure 6.6: Comparison between the observed Y_{obs} (red) and calculated Y_{calc} (black) X-ray diffraction pattern of $NaTh_2F_9$. $Y_{obs} - Y_{calc}$ (blue) is the difference between the experimental and calculated intensities. The Bragg reflections' angular positions are marked in green. Measurement at λ = Cu - Kα.

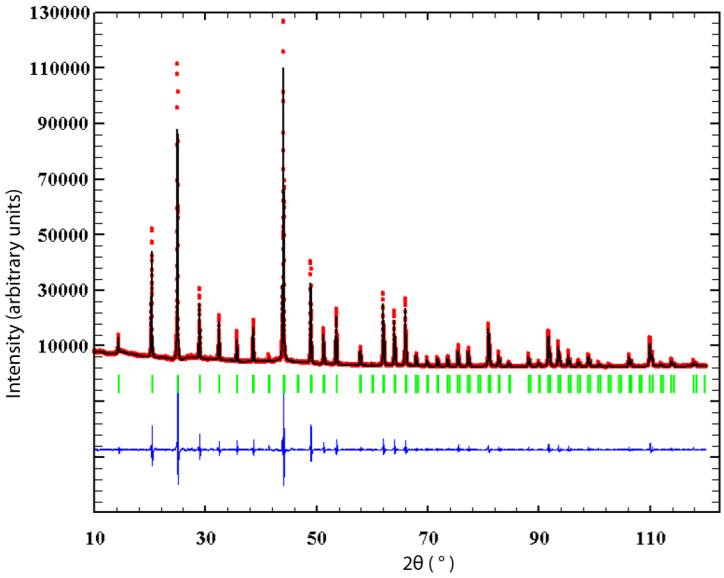

Figure 6.7: Comparison between the observed Y_{obs} (red) and calculated Y_{calc} (black) X-ray diffraction pattern of β-Na_2ThF_6. $Y_{obs} - Y_{calc}$ (blue) is the difference between the experimental and calculated intensities. The Bragg reflections' angular positions are marked in green. Measurement at λ = Cu - Kα.

LOW TEMPERATURE HEAT CAPACITY

Low temperature heat capacity data at constant pressure, $C_P = (\partial H/\partial T)_p$, were measured for β-Na_2ThF_6 and $NaTh_2F_9$ with thermal relaxation calorimetry between between 2 - 271 K and 2 - 294 K, respectively. Even though C_P is measured at low temperatures, it is in principle possible to extrapolate to higher temperatures via atomistic scale simulations. The thermodynamic properties of stoichiometric compounds can be calculated by combining DFT with the Quasi-Harmonic Approximation method (QHA, see SI also) [10]. It has been shown[28, 66], however, that the QHA method leads to an overestimation of the heat capacity at high temperature induced by an overestimation of the lattice expansion. To alleviate this inconsistency, Seifitokaldani and Gheribi [66, 67, 27] developed the so-called thermodynamically self-consistent (TSC) method, which is based on the QHA method but with an optimization of the volume-dependent Debye temperature through a rigorous minimization procedure in order to satisfy the Maxwell relations. Here, we propose to combine the experimental information on low temperature heat capacity with DFT simulations for an accurate parameterization of the quasi-harmonic Gibbs energy, treating both ternary salts as insulators.

The heat capacity of insulating materials is of vibrational origin and can be represented by the Debye-Grüneisen model[29], described by two parameters: the Debye temperature Θ_D, and the Grüneisen parameter, γ. Note that the Grüneisen parameter describes the volume dependence of the Debye temperature as $\gamma = (\partial ln\Theta_D/\partial lnV)$. At high temperature, for instance T $> 0.75 \cdot T_{fusion}$, defects (e.g. Schottky) may contribute significantly to the heat capacity. The defect contribution to the heat capacity

increases exponentially with temperature and its magnitude depends on the energy of formation of defects. However, experiments on high-temperature heat capacity of alkali fluoride-actinide fluoride compounds [50] show no significant contribution from the defects, therefore it can be reasonably assumed that the heat capacities of both Na_2ThF_6 and $NaTh_2F_9$ are uniquely of vibrational nature.

According to the Debye model, the vibrational heat capacity at constant volume can be described by:

$$C_V = 3NR \int_0^{\frac{\theta_D}{T}} \frac{e^x x^4}{(e^x - 1)^2} \cdot dx \tag{6.2}$$

With N the number of atoms in the formula unit and R the gas constant. Then, the heat capacity at constant pressure is expressed as:

$$C_P = C_V(1 + \alpha\gamma T) \tag{6.3}$$

α being the volumetric thermal expansion coefficient. Note that the QHA, with parameters derived either from DFT or from experimental elastic properties, cannot predict the intrisic anharmonic effect upon the lattice vibration, especially at low temperatures[29, 5] (extrinsic anharmonicity can be predicted by QHA through thermal expansion contribution). The combination of QHA and experimental measurement of C_P, even in a narrow range of temperature, can on the one hand provide valuable information on the anharmonic nature of the lattice vibration within the solid, and on the other hand significantly improve the accuracy in the representation of the temperature dependence of the heat capacity and the prediction of other equilibrium properties: thermal expansion, bulk modulus, among others.

First, the Debye temperature and the Grüneisen parameter were calculated at 0 K via DFT according to the methodology described in [66, 67, 27] (see SI also). Then the Debye temperature was calculated numerically at each measurement temperature to fit the heat capacity as measured in this work. The evolution of the Debye temperatures of both compounds as a function of temperature are shown in Figure 6.8. The behaviour of the Debye temperature is similar for both compounds. A similar behaviour is observed for several insulating materials and semiconductors[5, 29]: at low temperature the Debye temperature decreases to reach a minimum (here at about 20 K), then it increases to reach a plateau at about $\theta_D(\infty)/4$. Without any intrinsic anharmonic effect, the Debye temperature shows no temperature dependence. Even though several analytical expressions for the description of the temperature-dependence of the Debye temperature are proposed in the literature, the focus here is on the qualitative behavior: both Na_2ThF_6 and $NaTh_2F_9$ show an anharmonic behaviour at low temperature and become harmonic above about $\theta_D(\infty)/4$. A consequence of the harmonic behaviour at higher temperature can be observed from the quasi linear increase of C_p with temperature. At high temperature the harmonic heat capacity at constant volume, C_V, tends beyond the Dulong-Petit limit of 3nR, since the slope of the C_P induced by harmonic vibration within the crystal is about $\alpha\gamma$ (Eq.6.3). Above that threshold temperature the increase of C_p is linear, mainly due to the lattice expansion ($C_V\alpha\gamma T$). It is interesting to note the good interpolability between the Debye temperature at 0 K obtained by DFT and those derived from the

measured C_p. The high temperature limits of the Debye temperatures for both Na_2ThF_6 and $NaTh_2F_9$ are very close, i.e. 450-460 K. At low temperature the Debye temperature of Na_2ThF_6 is significantly lower than that of $NaTh_2F_9$, indicating a more pronounced anharmonicity for Na_2ThF_6 at low temperature.

The heat capacities calculated by the TSC method, considering the Debye temperature derived from the experimental measurements, are represented in Fig. 6.9 from 0 K up to the melting temperature and compared to the measured low temperature data. To extrapolate the heat capacity at higher temperatures we have assumed that: (i) the Debye temperature is constant above 200 K (ii) the Grüneisen parameter is assumed to be independent of temperature and equal to the DFT value (1.61 for Na_2ThF_6 and 1.56 for $NaTh_2F_9$). Values of $C_{p,m}$(298.15 K) = (200.4 ± 2.0) J K^{-1} mol^{-1} and (266.5 ± 2.7) J K^{-1} mol^{-1} were obtained from our model for β-Na_2ThF_6 and $NaTh_2F_9$, respectively. Upon integration of $C_{p,m}/T$, the corresponding standard entropies were S^o_m(298.15 K) = (257.3 ± 3.2) J K^{-1} mol^{-1} and S^o_m(298.15 K) = (333.7 ± 4.0) J K^{-1} mol^{-1}. The predicted thermal expansion coefficients of both Na_2ThF_6 and $NaTh_2F_9$ are reported in the Supporting Information of this paper.

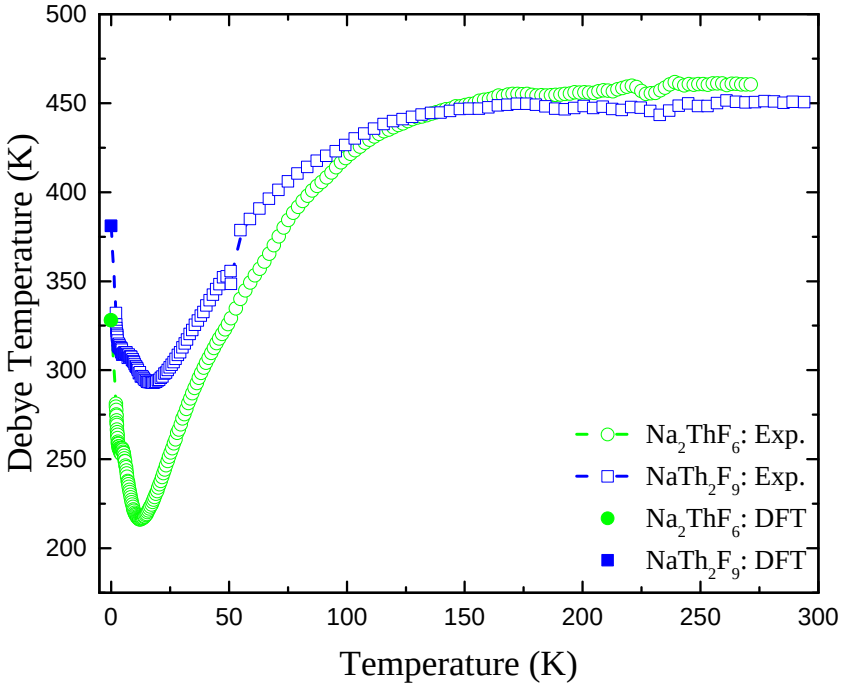

Figure 6.8: Temperature-dependent Debye temperature derived from experimental heat capacity (Exp., open symbol) for Na_2ThF_6 and $NaTh_2F_9$ compounds. The 0 K Debye temperatures determined by DFT for both compounds are represented by solid symbols).

The heat capacity of Na_2ThF_6 was measured from 313 to 773 K by Mukherjee and Dash [51] using a heat flux-type DSC. However, the heat capacity data reported by Mukher-

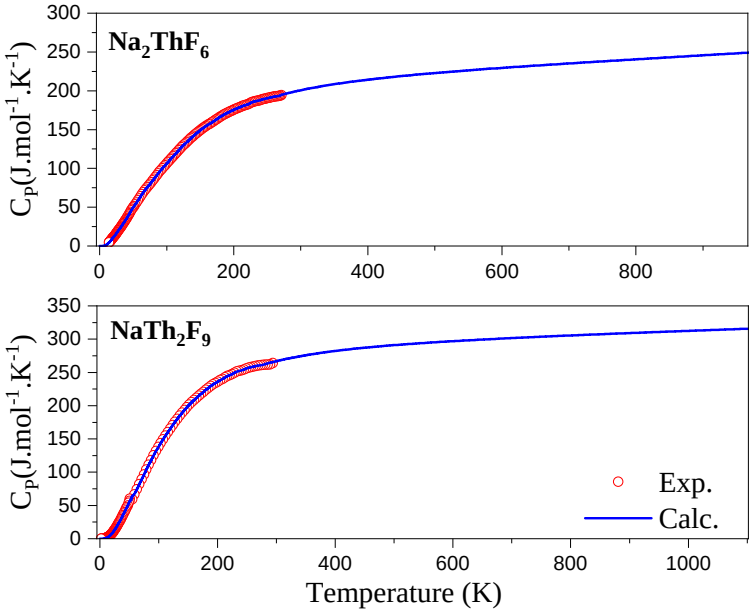

Figure 6.9: Experimental vs. calculated heat of Na_2ThF_6 and $NaTh_2F_9$ compounds from 0 K up to melting temperature.

jee and Dash [51] is likely too low as at high temperature (near the melting point) the heat capacity is much lower than the Dulong-Petit approximation (Figure 3 of their paper) which is a nonphysical behaviour. No comparison with their heat capacity data will be further discussed here.

MIXING ENTHALPY IN THE NAF-THF_4 SYSTEM

Experimental determination

The mixing enthalpies for the compositions ($NaF:ThF_4$) = (0.80:0.20), (0.70:0.30) were obtained at 1266 K (melting point of NaF) with DSC measurements. The measured mixing enthalpies (red circles), and the curve obtained from the CALPHAD model (red line), are shown in Figure 6.10. The mixing enthalpy values based on the quasichemical model of Beneš et al.[7] (dotted line, red), and the values of Mukherjee et al. [51] (polynomial formalism, red circles) are indicated as well. The results are summarized in Table 4. It must be noted that neither assessment was developed using experimental mixing enthalpy data. Still, relatively good agreement was achieved between the experimental data obtained in this work and both models.

MD calculations

The enthalpy was obtained directly from the mean of the internal energies calculated

Table 4: Mixing enthalpy in the NaF-ThF$_4$ system at 1266 ± 10 K and standard pressure (0.1 ± 0.01 MPa), as determined in this study.

x(ThF$_4$) / mol%[a]	$\Delta_{mix}H$[b] / kJ mol^{-1}	m(NaF)[c] / mg	m(ThF$_4$)[c] / mg
19.9	-13.0 ± 1.1	7.5	13.7
30.2	-17.9 ± 0.9	7.1	22.5

[a] Standard uncertainty u(x(ThF$_4$)) = 0.5 mol%.

[b] The error is based on the standard uncertainty determined during the calibration process.

[c] Standard uncertainty u(m) = 0.1 mg.

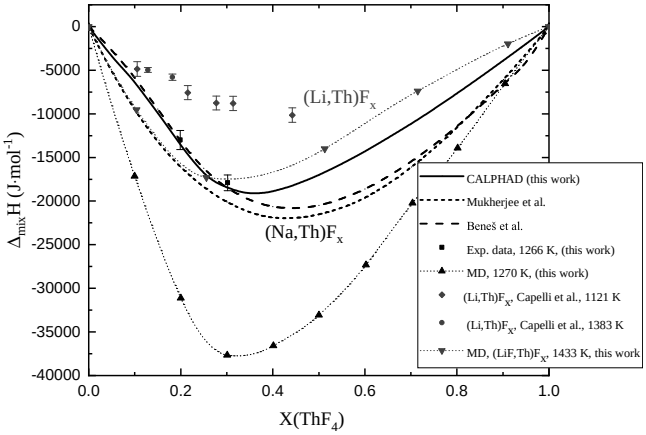

Figure 6.10: Mixing enthalpies in the NaF-ThF$_4$ system measured in this work at T = 1266 K (■) compared with the present model, those of Beneš et al.[7] and Mukherjee et al.[51] (black lines), and the MD simulations at 1270 K (this work, ▲). Also plotted are experimentally measured values in the LiF-ThF$_4$ system[14] (●, blue, T = 1383 K, ◆, T = 1121 K) and values obtained via MD simulations (▼, T = 1433 K).

after the NpT run. The molar enthalpy was calculated for each temperature (1270, 1433, 1500, 1600, 1800 and 2000 K) over the full composition range (see SI). In Figure 6.10, the results of the MD simulations at 1270 K are compared to the curve at 1266 K obtained from the CALPHAD optimization in our coupled model, and to experimental data. Similarly, the results of MD simulations at 1400 K (the potential parameters for the Li^+-Th^{4+}, Li^+-F^-, and Li^+-Li^+ interactions were taken from the study of Dewan et al. [20], more details can be found in the SI) and the experimental data and CALPHAD optimization at 1121 K reported by Capelli et al. [14] for the LiF-ThF$_4$ system are shown. In both systems, the results obtained with MD are much more negative than the experimental data. An optimization of the phase diagram data with the CALPHAD method based on the MD mixing enthalpy values for the NaF-ThF$_4$ system at 1270 K was attempted. However, this was not successful, even when the thermodynamic data of the NaF-ThF$_4$ intermediates were adjusted substantially. Consequently, it is likely that the MD overestimates the mixing enthalpy data: a small difference between two large numbers is difficult to capture accurately. Nevertheless, the compositions of the minima are similar, which are reached

at 30 and 40 mol% ThF_4 for the MD and CALPHAD curve, respectively. The minima of the mixing enthalpy curves calculated with MD in Figure 6.10 around 30 mol% ThF_4 moreover agree well with the maxima of the excess molar volume seen in Figure 6.1, and minima of average coordination number in Figure 6.4, which are situated around 30-40 mol% too: the region is characterized by complexes in which the fluorides are tightly bound to Th^{4+} and excess volume is found in the interstices between complexes. In the phase diagram, this high stability of the liquid related to maximum short-range ordering is reflected in the relatively low melting point of Na_2ThF_6 (Fig. 6.12).

HEAT CAPACITIES

The heat capacity was derived from the molar enthalpies calculated in steps of 10 mol% ThF_4 at 1433, 1500, 1600, 1800, 2000 K. The heat capacities calculated from MD are shown in Figure 6.11. The calculated heat capacity with MD for ThF_4 is 170.7 J K^{-1} mol^{-1}, which agrees very well with the literature value of (168.0 $\pm$ 10) J K^{-1} mol^{-1} [77]. The calculated heat capacity of NaF was 68.1 J K^{-1} mol^{-1}, which differs slightly from the reported value of 73.0 J K^{-1} mol^{-1} (uncertainty not reported)[15].

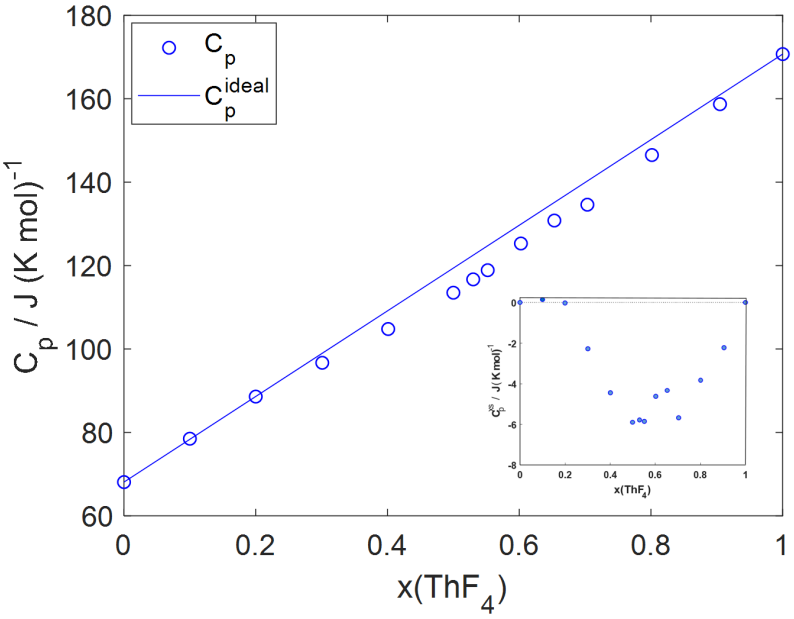

Figure 6.11: Evolution of heat capacity and ideal heat capacity in the NaF-ThF_4 system calculated from enthalpies obtained in MD simulations in the temperature region 1433 - 2000 K. Inset: excess heat capacity.

A slight negative deviation from ideal behaviour is predominant across all compositions, with a maximum deviation of 5% at X_{ThF_4} = 0.5. This stands in contrast with the positive excess heat capacity in binary mixtures of lithium fluoride with other alkali fluorides, found by Beilmann et al. via drop calorimetry. [6]. Beilmann et al. pointed out that an excess molar volume had been observed by Holm [34] in the same systems. Moreover,

they suggested that both phenomena could be explained by the long-lived structures observed by Dracopolous et al. [21] with Raman spectroscopy, of the type (LiF_x)A (A = K, Cs). On the one hand, the complexes could account for additional vibrational mechanisms for the storage of energy, explaining the increased heat capacity. On the other, if these complexes disturbed the close packing arrangement of the ions in the pure salts, then the excess volume would be accounted for. In the case of molten ThF_4, there are already chains present which contribute to the storing of energy: their partial disruption by the addition of Na^+ ions can explain a reduced capacity to retain heat with respect to the pure end-member. The partial disruption of the network may also explain the positive excess volume in the NaF-ThF_4 case (Fig. 6.1): similar to the disruption of loosely associated closely packed ions in the mixed alkali fluorides, a disruption of closely packed $[ThF_x]^{4-x}$ shells occurs, expanding the structure. The negative excess heat capacity is consistent with the negative excess thermal expansion (see SI), indicating a lower vibrational contribution to the total free energy than in an ideal mixture. Note that the ratio C_P^{xs}/C_P = -0.052 is close to β^{xs}/β = -0.096 as both thermal expansion and heat capacity originate from the vibrational state of the mixture.

6.2.6. COUPLED STRUCTURAL-THERMODYNAMIC MODEL OF THE NAF-THF$_4$ SYSTEM

The NaF-ThF_4 binary system shown in Fig. 6.12 was optimized taking into account coordination and speciation information derived from MD simulations (Section 6.2.4), heat capacity (Section 6.2.5), mixing enthalpy (Section 6.2.5) and calorimetric data from the literature and measured in this work by DSC (Table 2). Overall, the calculated phase diagram reproduces the data gathered in this work satisfactorily, as well as the data from Thoma et al. [76], and to a lesser extent, data by Emelyanov and Evstyukhin[22]. Additionally, the distribution of the main species $[ThF_7]^{3-}$, $[ThF_8]^{4-}$, and $[Th_2F_{13}]^{5-}$ could be reproduced accurately, as shown in Figs. 6.13a, 6.13b.

The model moreover seems to perform adequately for properties which were not taken into account for its optimization. Fig. 6.14 compares the activities calculated at T = 1241 K to determinations from mass-spectrometric measurements by Sidorov et al. [69]. The NaF activities are reproduced remarkably well. Although in the case of ThF_4 the agreement is not excellent, the model is capable of correctly predicting a significant negative deviation from ideality below X(ThF_4) = 0.3. The trend beyond that point, up until X(ThF_4) = 0.5, is a relatively large negative deviation, and it is also correctly predicted. A negative deviation from ideality is typical for electrolytes in concentrated regimes and is directly linked to a reduced availability of dissociated ions due to their incorporation into associated structures: this negative deviation is closely linked to the negative excess in the enthalpy of mixing (Fig. 6.10). The activities and the mixing enthalpies are thus related to the microscopic structure and are indicative of the stability of complexes in mixtures. Macroscopically, the implication is that the binary mixtures have a lower vapor pressure than the individual end-members, which is of course desirable since low vapor pressures are a design requirement of MSRs.

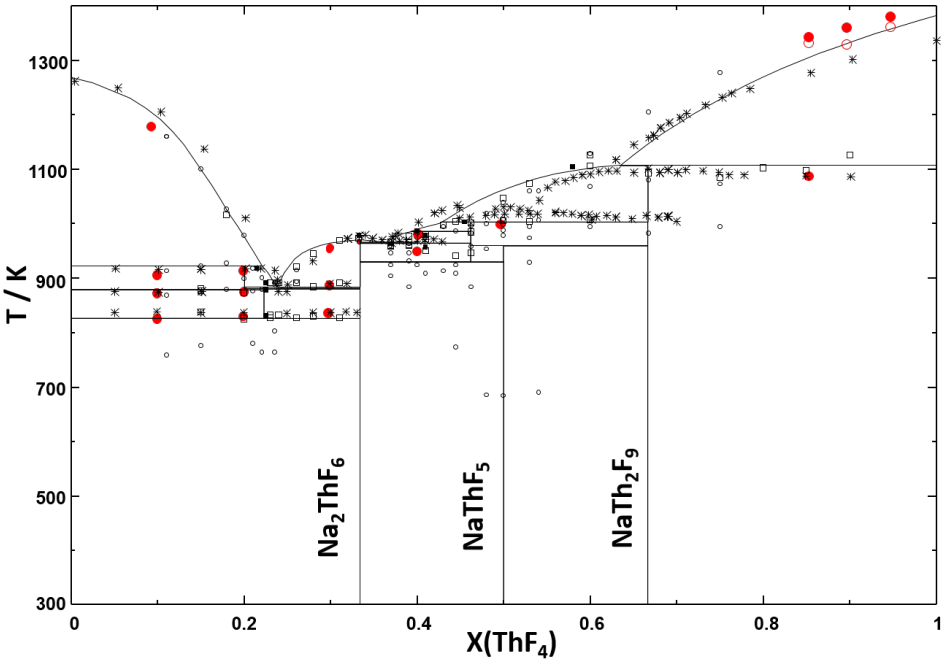

Figure 6.12: The NaF-ThF_4 phase diagram as calculated in this work with the coupled structural-thermodynamic model, compared to experimental data. The thermodynamic events measured in this work are indicated with ●. The filled red circles near the liquidus in the 85 - 95 mol% region indicate the extremum temperature and the hollow circles represent the onset temperature of the melting event. The phase diagram data reported by Emelyanov and Evstyukhin[22] are shown as ⁎. The thermodynamic events obtained by Thoma et al. [76] are indicated with the remaining black symbols. Thermal analysis data is indicated with ○, quenching data with ▫ and invariant equilibria with ●.

6.3. CONCLUSIONS

The thermodynamic, structural and physico-chemical properties of the NaF-ThF_4 system have been investigated with experimental and computational methods. The system is more complex than LiF-ThF_4, with more intermediate phases and larger deviations from ideality. Generally speaking, these deviations make NaF an adequate component in molten salt reactor fuels. Under neutron irradiation, an excess molar volume can be regarded as negative excess reactivity, i.e. an inherent safety feature. The negative mixing enthalpy, related to the strong negative deviations in the activity, imply a reduced vapor pressure with respect to end-members which themselves have a low vapor pressure, another beneficial feature. The negative excess heat capacity of the mixtures seems too small to be a concern; however, it deserves further study. Examining the transport properties, chiefly the viscosity and thermal conductivity, is also needed.

ACKNOWLEDGEMENTS

The authors are grateful to Pavel Souček for providing us with ThF_4 of high purity. We would also like to thank Mathieu Salanne for the use of his Molecular Dynamics code.

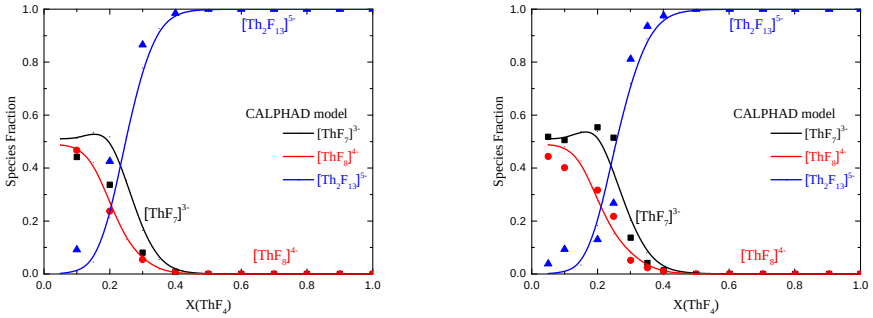

(a) T = 1270 K (b) T = 1433 K

Figure 6.13: Complex anion distribution obtained with the CALPHAD model (solid lines) and compared with the MD data shown in Fig. 6.19 (symbols): $[ThF_7]^{3-}$ (black), $[ThF_8]^{4-}$ (red), and $[Th_2F_{13}]^{5-}$ (blue). (a) T = 1270 K, (b) T = 1433 K.

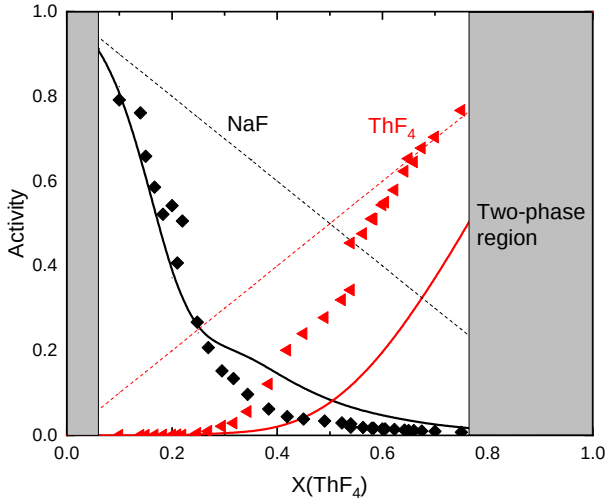

Figure 6.14: Activities in the $Na_xTh_{1-x}F_{4-3x}$ liquid solution at T = 1241 K. The solid lines correspond to the activities predicted by the present structural-thermodynamic model. The symbols are experimental data by Sidorov et al. [69] at T = 1241 K. The dashed lines represent ideal behavior.

A.L. Smith acknowledges gratefully financial support from the Netherlands Organisation for Scientific Research (NWO) (project 722.016.005). J.A. Ocádiz-Flores would like to thank CONACYT-SENER for financial support.

6.4. CREDIT AUTHOR STATEMENT

M.B.J.W. Schreuder: Conceptualization, Methodology, Investigation, Formal analysis, Visualization, Data Curation, Writing - Original Draft preparation **J.A. Ocádiz Flores**: Conceptualization, Methodology, Supervision, Investigation, Formal analysis, Visualization, Data Curation, Writing - Original Draft preparation **A.E. Gheribi**: Conceptualization, Investigation, Software, Formal Analysis, Visualization, Writing - Original Draft preparation **J.-C. Griveau**: Investigation **E. Colineau**: Investigation **O. Beneš**: Verification, Resources **R.J.M. Konings**: Supervision, Resources, Writing - Review & Editing **A.L. Smith**: Conceptualization, Methodology, Supervision, Funding acquisition, Resources, Project Administration, Writing - Review & Editing

6.5. SUPPLEMENTARY INFORMATION: EXPERIMENTAL AND COMPUTATIONAL EXPLORATION OF THE NAF-ThF_4 FUEL SYSTEM: STRUCTURE AND THERMOCHEMISTRY

6.5.1. MOLECULAR DYNAMICS CALCULATIONS

The PIM potential is based on four terms:

$$V(r_{ij}) = V_{qq}(r_{ij}) + V_{rep}(r_{ij}) + V_{disp}(r_{ij}) + V_{pol}(r_{ij}) \tag{6.4}$$

Here, V_{qq} accounts for the forces between ions resulting from their respective electric charges. The charge-charge term is given by:

$$V_{qq}(r_{ij}) = \sum_{i<j} \frac{q_i q_j}{r_{ij}} \tag{6.5}$$

with q_i and q_j the formal charges of ions i and j. The repulsion term $V_{rep}(r_{ij})$, resulting from the overlap of electron clouds between two neighbouring ions, is described by:

$$V_{rep}(r_{ij}) = \sum_{i<j} A_{ij} e^{-a_{ij} r_{ij}} \tag{6.6}$$

where A_{ij} and a_{ij} are fitting parameters. Dipole-dipole and dipole-quadrupole dispersion forces, that arise due to fluctuations in the electron densities are described according to equation 6.7.

$$V_{disp}(r_{ij}) = -\sum_{i<j} \left(f_{ij}^6(r_{ij}) \frac{C_{ij}^6}{r_{ij}^6} + f_{ij}^8(r_{ij}) \frac{C_{ij}^8}{r_{ij}^8} \right) \tag{6.7}$$

Here C_{ij}^6 and C_{ij}^8 are the dipole-dipole and dipole-quadrupole dispersion coefficients, respectively. The Tang-Toennis dispersion damping functions [74], which correct for the asymptotic multipole expansion of dispersions in the short range, are given by:

$$f_{ij}^n(r_{ij}) = 1 - e^{-(b_{ij}^n r_{ij})} \sum_{k=0}^{n} \frac{(b_{ij} r_{ij})^k}{k!} \tag{6.8}$$

where b_{ij} is the distance at which the correction is applied. The polarization term, that takes into account the interaction of a molecule's electron density with its direct environment is given in equation 6.9:

$$V_{pol}(r_{ij}) = \sum_{i<j} \left(q_i \mu_{j\alpha} g_{ij}(r_{ij}) - q_i \mu_{i\alpha} g_{ij}(r_{ij}) \right) T_{\alpha}^{(1)}(r_{ij}) - \sum_{i<j} \mu_{i\alpha} \mu_{j\beta} T_{\alpha\beta}^{(2)}(r_{ij}) + \sum_{i} (2\alpha_i)^{-1} |\mu_i|^2 \tag{6.9}$$

in which $T_{\alpha}^{(1)}$ is the charge-dipole interaction tensor, $T_{\alpha\beta}^{(2)}$ is the dipole-dipole interaction tensor, μ_i is the set of induced dipoles in the system and α_i is the polarizability of ion i. Furthermore, g_{ij} represents the following damping function:

$$g_{ij}(r_{ij}) = 1 - c_{ij} e^{-b_{ij} r_{ij}} \sum_{k=0}^{4} \frac{(b_{ij} r_{ij})^k}{k!} \tag{6.10}$$

The interaction parameters A_{ij}, a_{ij}, C_{ij}^6, C_{ij}^8, b_{ij}^6, b_{ij}^8, polarizability α_i and damping constants b_{ij} and c_{ij} are determined by fitting the forces and dipoles on all ions derived from *ab initio* calculations on condensed phases [49]. The values used in this work are summarized in tables 5 and 6. The F^--F^-, F^--Th^{4+} and Th^{4+}-Th^{4+} interaction parameters were taken from [19]. The F^--Na^+, Th^{4+}-Na^+ and Na^+-Na^+ potential parameters and damping coefficients, were obtained from *ab initio* calculations by us. The polarizability of fluorine was set to 7.8935 Bohr^3 and a value of 7.6960 Bohr^3 was used for the polarizability of thorium, which both equal the values used by Dewan et al. for calculations on the LiF-ThF$_4$ system [19]. The compositions and temperatures of the MD simulations performed in this work are summarized in Table 7.

Table 5: Overview of interaction potential parameters used in the MD simulations for the NaF-ThF$_4$ system. The values are given in atomic units: for length in Bohr radii (1 Bohr = 0.052918 nm) and for energy in Hartree (1 $E_H = 4.3597 \cdot 10^{-18}$ J).

Ion pair	a_{ij}	A_{ij}	$C_{ij}^{(6)}$	$C_{ij}^{(8)}$	$b_{ij}^{(6)}$	$b_{ij}^{(8)}$
F^--F^-	2.44	282.3	15	150.0	1.9	1.9
F^--Th^{4+}	1.634	70.148	38.7	387.0	1.9	1.9
F^--Na^+	1.97	52.83	13.25	88.15	1.9	1.9
Th^{4+}-Th^{4+}	5	1	100	1000	1.9	1.9
Th^{4+}-Na^+	5	1	0.001	0.001	1.9	1.9
Na^+-Na^+	5	1	11.7	51.8	1.9	1.9

Table 6: Overview of damping coefficients in the damping function of $V_{pol}(r_{ij})$ used in this work.

Ion pair	b_{ij}	c_{ij}
Th^{4+}-F^-	1.938	-0.60906
F^--Th^{4+}	1.938	2.791
F^--Na^+	1.837	2.543

Table 7: Molecular dynamics system conditions used in this work. Simulations that were terminated after the NpT run are indicated with a *.

x(ThF_4)	N_{F-}	$N_{Th^{4+}}$	N_{Na+}	N_{total}	T / K
1.000	480	120	0	600	1270 / 1433 / 1500 / 1600 / 1800* / 2000*
0.951	474	117	6	597	1433
0.905	468	114	12	594	1270 / 1433 / 1500 / 1600 / 1800* / 2000*
0.855	467	112	19	598	1433
0.801	463	109	27	599	1270 / 1433 / 1500 / 1600 / 1800* / 2000*
0.750	455	105	35	595	1433
0.703	451	102	43	596	1270 / 1433 / 1500 / 1600 / 1800* / 2000*
0.671	449	100	49	598	1433
0.653	444	98	52	594	1433 / 1500* / 1600* / 1800* / 2000*
0.603	438	94	62	594	1270 / 1433 / 1500 / 1600 / 1800* / 2000*
0.552	433	90	73	596	1433 / 1500* / 1600* / 1800 * / 2000*
0.530	430	88	78	596	1433* / 1500* / 1600* / 1800* / 2000*
0.500	425	85	85	595	1270 / 1433 / 1500 / 1600 / 1800* / 2000*
0.452	417	80	97	594	1433
0.401	412	75	112	599	1270 / 1433 / 1500 / 1600 / 1800* / 2000*
0.352	403	69	127	599	1433
0.330	398	66	134	598	1433
0.301	392	62	144	598	1270 / 1433 / 1500 / 1600 / 1800* / 2000*
0.249	379	54	163	596	1433
0.223	374	50	174	598	1433
0.200	368	46	184	598	1270 / 1433 / 1500 / 1600 / 1800* / 2000*
0.172	361	41	197	599	1433
0.148	352	36	208	596	1433
0.100	338	26	234	598	1270 / 1433 / 1500 / 1600 / 1800* / 2000*
0.050	320	14	264	598	1433
0.000	300	0	300	600	1270 / 1433 / 1500 / 1600 / 1800* / 2000*

6.5.2. DFT AND TSC

Low temperature heat capacity at constant pressure were measured for β-Na_2ThF_6 and $NaTh_2F_9$ between 2 - 271 K and 2 - 294 K, respectively. Even though C_P is measured at low temperature, it is in principle possible to extrapolate to higher temperature via atomistic scale simulations. The thermodynamic properties of stoichiometric compounds can be calculated by combining Density Functional Theory (DFT) with the Quasi-Harmonic Approximation method (QHA) [10]. In a nutshell, in QHA, the Gibbs energy is expressed as as a function of temperature, pressure and volume[10]:

$$G^*(V;P,T) = E(V) + PV + NRT\left[\frac{9}{8}\frac{\Theta_D(V)}{T} + 3\,ln\left(1 - e^{-\Theta_D(V)/T}\right) - D\left(\Theta_D(V)/T\right)\right] \tag{6.11}$$

Where n is the number of atoms per formula unit, Θ_D is the volume-dependent Debye temperature, and D is the Debye integral defined as: $3y^{-3}\cdot\int_0^y \frac{x^3}{e^x-1}dx$. Note that the first term in the bracket represents the zero point lattice energy. The equilibrium volume at (T,P) is then determined by the Gibbs energy minimization with respect to V, i.e by solving:

$$\left(\frac{\partial G^*(V;P,T)}{\partial V}\right)_{T,P} = 0 \tag{6.12}$$

6

Note that the Grüneisen parameter which is used to define the temperature dependence of C_P does not appear explicitly in the definition of the quasiharmonic Gibbs energy (Eq. 6.11). The Grüneisen parameter defines the volume dependence of the Debye temperature as well, ($\gamma = (\partial ln\Theta_D/\partial lnV)$) and is in fact implicitly defined by the expresion Θ_D vs. V. It has been shown[28, 66] that the QHA method leads to an overestimation of the heat capacity at high temperature, induced by an overestimation of the lattice expansion at high temperature. To alleviate this inconsistency, Seifitokaldani and Gheribi [66, 67, 27] developed the so-called thermodynamically self-consistent (TSC) which is based on the QHA method, but with an optimization of the volume-dependent Debye temperature through a rigorous minimization procedure in order to satisfy to the Maxwell relations. Here, we propose to combine the experimental information on low temperature heat capacity to DFT simulations for an accurate parameterization of the quasiharmonic Gibbs energy.

Note that the Gibbs energy of insulating materials is of vibrational origin even though at high temperature, e.g. $T > 0.75\cdot T_{fusion}$, defects may contribute significantly to the heat capacity. The defect contribution to the heat capacity increases exponentially with temperature and its magnitude depends on the energy of formation of defects. However, experiments on high temperature heat capacity of alkali fluoride-actinide fluoride compounds[50] show no significant contribution of the defects. Therefore it can be reasonably assumed that the heat capacities of both Na_2ThF_6 and $NaTh_2F_9$ are uniquely of vibrational nature.

First, we have calculated the energy curve ($E(V)$) via DFT. For that purpose, the Vienna ab initio Simulation Package (VASP) [41, 42, 40, 39] has been used to perform the plane wave computations with the projected augmented wave (PAW) approach,[11, 43] and the generalized gradient approximation (GGA) of Perdew, Burke and Ernzerhof (PBE)[58,

59]. Convergence in the energy and cell volume was tested and our results indicated that a cut-off energy of 520 eV and 5×5×8 and 5×5×5 Γ-centered k-points grid in the first Brillouin zone for Na_2ThF_6 and $NaTh_2F_9$ respectively with a Gaussian smearing parameter of 0.02 eV to ensure that the accuracy in the energy of the system is more than 0.01 meV. The self-consistent field (SCF) convergence criterion was 1×10^{-5}eV for electronic iterations and 0.02 eV/Å for each ionic loop that was updated by the conjugate gradient approach. To calculate the energy of the equilibrium lattice, the atomic positions, cell volume and cell shape, were all free to be relaxed. To calculate the energy curve, both cell volume and cell shape were fixed and only the atoms were free to move. The volume-dependent Debye temperature was then derived from the energy curve according to [25, 10]:

$$\Theta_D(V) = \frac{\hbar}{k_B}\left[6\pi^2 n V^{1/2}\right]^{1/3} k(\nu)\sqrt{\frac{1}{\rho}\frac{d^2E(V)}{dV^2}} \tag{6.13}$$

$\hbar$ and k_B are the reduced Planck and the Boltzmann and ρ is the density of the compound at the corresponding volume. $k(\nu)$ is a function of Poisson ratio at equilibrium volume [24]:

$$k(\nu) = \left\{3\left[2\left(\frac{2}{3}\cdot\frac{1+\nu}{1-2\nu}\right)^{3/2} + \left(\frac{1}{3}\cdot\frac{1+\nu}{1-\nu}\right)^{3/2}\right]\right\}^{1/3} \tag{6.14}$$

To estimate the equilibrium Poisson ratio and therefore k, we have calculated the elastic constants of both Na_2ThF_6 and $NaTh_2F_9$ according to the methodology given in [61]; they are shown in Fig. 6.17. At equilibrium volume the Debye temperature and Grüneisen constant determined by DFT are respectively 328 K and 1.61 for Na_2ThF_6, while for $NaTh_2F_9$ they are 381 K and 1.56, respectively. The experimental Debye temperature was calculated numerically at each measurement temperature to fit the heat capacity as measured in this work while considering the DFT value of the Grüneisen constant.

6.5.3. CALPHAD MODELLING

6.5.4. CALPHAD MODELLING

The optimization of the NaF-ThF_4 thermodynamic model was carried out using the Factsage software [4]. To assess a phase diagram, the identity of the phases present in the system of interest must be known, as well as their respective Gibbs energy functions.

PURE COMPOUNDS

The Gibbs energy function of a pure compound is given by:

$$G(T) = \Delta_f H^{\circ}_{\mathrm{m}}(298) - S^{\circ}_{\mathrm{m}}(298)T + \int_{298}^{T} C_{\mathrm{p,m}}(T)dT - T\int_{298}^{T}\frac{C_{\mathrm{p,m}}(T)}{T}dT \tag{6.15}$$

where $\Delta_f H^{\circ}_{\mathrm{m}}(298)$ is the standard enthalpy of formation, $S^{\circ}_{\mathrm{m}}(298)$ is the standard absolute entropy, both evaluated at a reference temperature, in this case 298.15 K (throughout this work 298.15 will be written simply as 298 K for simplicity), and $C_{\mathrm{p,m}}$ is the isobaric heat capacity, represented by a polynomial:

$$C_{\mathrm{p,m}}(T) = a + bT + cT^2 + dT^{-2} \tag{6.16}$$

with more terms added if necessary.

In this work, the Neumann-Kopp rule [46] was used to approximate the heat capacities of intermediate compounds in the absence of experimental data, with the exception of β-Na_2ThF_6 and $NaTh_2F_9$. The data of solid and liquid NaF and ThF_4 were taken from [15] and [38], respectively. The standard enthalpies of formation and standard entropies of all the intermediate compounds were optimized to closely match phase equilibria data. Again β-Na_2ThF_6 and $NaTh_2F_9$ were exceptions as the experimentally derived standard entropies were used.

LIQUID SOLUTION

The excess Gibbs energy terms of the (Na,Th)F_x liquid solution have been modelled in the present work using an advanced modified quasi-chemical model similar to the one recently optimized for the LiF-BeF_2 system [71]. The modified quasi-chemical model [56] is well suited to describe ionic liquids, since the composition of maximum short-range ordering (SRO) may be selected by varying the ratio between the cation-cation coordination numbers $Z^A_{AB/FF}$ and $Z^B_{AB/FF}$. The quadruplet approximation takes a quadruplet to be the elementary unit in liquid solution, and each quadruplet is a set of two anions and two cations. The excess Gibbs energy parameters to be optimized are related to the second-nearest neighbor (SNN) exchange reaction:

$$(A-F-A)+(B-F-B) \longrightarrow 2(A-F-B) \;\; \Delta g_{AB/F} \tag{6.17}$$

where the fluoride anions are denoted by F; A and B denote the cations. $\Delta g_{AB/F}$ is the Gibbs energy change associated with the SNN exchange reaction, and has the form:

$$\Delta g_{AB/F} = \Delta g^{\mathrm{o}}_{AB/F} + \sum_{i\geqslant 1} g^{i0}_{AB/F}\chi^i_{AB/F} + \sum_{j\geqslant 1} g^{0j}_{AB/F}\chi^j_{BA/F} \tag{6.18}$$

where $\Delta g^{\mathrm{o}}_{AB/F}$ and $g^{ij}_{AB/F}$ are coefficients which may or may not be temperature-dependent, but which are independent of composition.

The dependence on composition is given by the $\chi_{AB/F}$ terms defined as:

$$\chi_{AB/F} = \frac{X_{AA}}{X_{AA}+X_{AB}+X_{BB}} \tag{6.19}$$

where X_{AA}, X_{BB} and X_{AB} represent cation-cation pair mole fractions.

The anion coordination number is then prescribed by conservation of charge in the quadruplet:

$$\frac{q_A}{Z^A_{AB/FF}} + \frac{q_B}{Z^B_{AB/FF}} = \frac{2q_F}{Z^F_{AB/FF}} \tag{6.20}$$

where q_i are the charges of the different ions, and $Z^F_{AB/FF}$ is the anion-anion coordination number.

Although it is very convenient, the thermodynamic model just outlined does not account for molecular species or network formation. (Na,Th)F_x is not a solution in which cations and anions are completely dissociated. Rather, the solution is formed by discrete coordination complexes of F^- ligands around Th^{4+}, which link to each other when their number density allows for it, leading to dimers, trimers, and 'polymers'. LiF-BeF_2 is also a polymeric liquid, and a recent assessment of this system by Smith et al. [71] using a structural-thermodynamic model provided a blueprint for the case of NaF-ThF_4. The crux of the model as developed by the authors, was to introduce quadruplets which not only include Be^{2+}, but also Be_2^{4+}, Be_3^{6+}, assigning them coordination environments 4, 7, and 10, respectively. In effect, the authors included monomers, dimers, and trimers, and assigned suitable compositions of maximum short-range ordering for each one. In this work, two distinct monomers were taken into account, with coordination numbers 7 and 8 (which dominate the distribution of $[NaF_x]^{4-x}$ complexes), as well as 13-coordinated dimers (the most abundant according to MD simulations): $[ThF_7]^{3-}$, $[ThF_8]^{4-}$, $[Th_2F_{13}]^{5-}$. All cation-cation coordination numbers are listed in Table 3. They were chosen to reflect maximum short-range ordering around the compositions X(ThF_4) = 0.2 (Na_4ThF_8), X(ThF_4) = 0.25 (Na_3ThF_7), and X(ThF_4) = 0.286 ("$Na_5Th_2F_{13}$").
Every species with two or more bridged Th^{4+} centers was assigned to the dimer distribution because the number of fitting parameters would have otherwise been too large, yet a dimer already implies fluoride bridging, a property which is essential to reproduce. Similarly, it is important to replicate varying coordination numbers, which is why two distinct monomers were retained in the assessment. In FLiBe, by contrast, Be^{2+} is exclusively tetra-coordinated. Finally, pure $ThF_4(l)$ is modelled as a solution of dimers. To do so, the reactions $\frac{1}{2}Th_{2[XIII]}F_8(l) = Th_{[VII]}F_4(l)$ and $\frac{1}{2}Th_{2[XIII]}F_8(l) = Th_{[VIII]}F_4(l)$ were constrained by the Gibbs energies associated with them (respectively, Eq. 6.21, 6.22):

$$g^0_{Th_{[VII]}F_4(l)} = \frac{1}{2}g^0_{Th_{2[XIII]}F_8(l)} + 150000\ J\cdot mol^{-1} \tag{6.21}$$

$$g^0_{Th_{[VIII]}F_4(l)} = \frac{1}{2}g^0_{Th_{2[XIII]}F_8(l)} + 150000\ J\cdot mol^{-1} \tag{6.22}$$

The value of 150000 $J\cdot mol^{-1}$ is an arbitrary term to destabilize the monomers, such that the melting point (1383 K vs. 1383 $\pm$ 3 K [60]) and the enthalpy of fusion of ThF_4 (36 kJ·mol^{-1} vs. 36.4$\pm$ 10 kJ·mol^{-1} [77]) are reproduced.

Extrapolation to the higher order systems which arise from a set of binary ones is either symmetric or asymmetric, depending on the affinity of the components between each other in a sublattice [57]. In the (Na,Th)F_x solution, the thorium cations are taken to be symmetric with respect to each other, while Na^+, a smaller cation with a weaker electric field strength, is taken to be the asymmetric component. Hence, the formal ternary systems {NaF + $Th_{[VII]}F_4$ + $Th_{[VIII]}F_4$ }, {NaF + $Th_{[VII]}F_4$ + Th_2F_8 }, and {NaF + $Th_{[VIII]}F_4$ + Th_2F_8 } are asymmetric, while {$Th_{[VII]}F_4$ + $Th_{[VIII]}F_4$ + Th_2F_8 } is symmetric. The composition dependence (Eq. 6.19) expressed as a function of cation-cation pair mole fraction becomes:

$$\chi_{NaTh_{[VII]}/FF} = \chi_{NaTh_{[VIII]}/FF} = \chi_{NaTh_2/FF} = \frac{X_{NaNa}}{\sum_A \sum_B X_{AB/F_2}} \tag{6.23}$$

Table 8: Cation-cation coordination numbers of the liquid solution.

A	B	$Z^A_{AB/FF}$	$Z^B_{AB/FF}$
Na^+	Na^+	6	6
$Th^{4+}_{[VII]}$	$Th^{4+}_{[VII]}$	6	6
$Th^{4+}_{[VIII]}$	$Th^{4+}_{[VIII]}$	6	6
$Th^{8+}_{2[XIII]}$	$Th^{8+}_{2[XIII]}$	6	6
$Th^{4+}_{[VII]}$	$Th^{4+}_{[VIII]}$	6	6
$Th^{4+}_{[VII]}$	$Th^{8+}_{2[XIII]}$	6	6
$Th^{4+}_{[VIII]}$	$Th^{8+}_{2[XIII]}$	6	6
Na^+	$Th^{4+}_{[VII]}$	2	6
Na^+	$Th^{4+}_{[VIII]}$	1.5	6
Na^+	$Th^{8+}_{2[XIII]}$	1.2	6

$$\chi_{Th_{[VII]}Na/FF} = \chi_{Th_{[VIII]}Na/FF} = \chi_{Th_2Na/FF}$$
$$= \frac{X_{Th_{[VII]}Th_{[VII]}} + X_{Th_{[VIII]}Th_{[VIII]}} + X_{Th_2Th_2} + X_{Th_{[VII]}Th_{[VIII]}} + X_{Th_{[VII]}Th_2} + X_{Th_{[VIII]}Th_2}}{\sum_A \sum_B X_{AB/F_2}}$$

where A and B denote the Na+, $Th^{4+}_{[VII]}$, $Th^{4+}_{[VIII]}$, and $Th^{8+}_{2[XIII]}$ cations. For the overall {NaF + "ThF_4"} system, the denominator $\sum_A \sum_B X_{AB/F_2}$ adds to 1.

The optimized excess Gibbs energy parameters of the (Na,Th)F_x liquid solution are shown in Eq. 6.24-6.26. The parameters were optimized based on the complex anion distribution as calculated with MD and on the phase diagram equilibria points of the liquidus plus the mixing enthalpy data.

$$\Delta g_{NaTh_{[VII]}/FF} = -70000 - 2.2 \cdot T + (-3000 + 0.3 \cdot T)\chi_{NaTh_{[VII]}/FF}\, J \cdot mol^{-1} \quad (6.24)$$

$$\Delta g_{NaTh_{[VIII]}/FF} = -70000 - 3 \cdot T + (-3000 + 1.3 \cdot T)\chi_{NaTh_{[VIII]}/FF}\, J \cdot mol^{-1} \quad (6.25)$$

$$\Delta g_{NaTh_{2[XIII]}/FF} = -52000 + 9 \cdot T - 2000\chi_{NaTh_{2[XIII]}/FF} + (-15000 - 8 \cdot T)\chi_{Th_{2[XIII]}Na/FF}\, J \cdot mol^{-1} \quad (6.26)$$

6.5.5. PHASE EQUILIBRIA AND ENTHALPY OF MIXING MEASUREMENTS BY DSC

Figure 6.15 shows a picture and a schematic representation of the crucible and liner used for the DSC measurements.

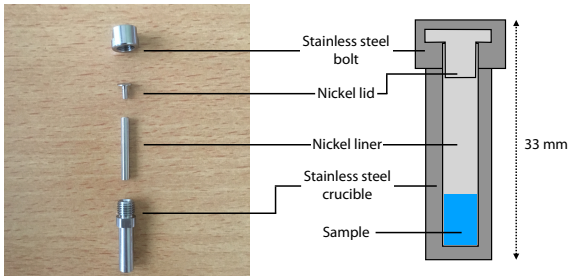

Figure 6.15: Schematic representation of the DSC sample crucible used in this work. Left, an overview of the parts of the crucible. Right, a schematic representation of an assembled DSC sample crucible.

The mixing enthalpy experiments were done with the same type of crucibles as used in the DSC measurements. The technique and determination of the detector sensitivity are described in great detail in [14]. A pellet of NaF was placed below a ThF_4 pellet. A small nickel liner separated the end-member compounds such that eutectic melting or solid phase reactions were prevented. Since NaF has a lower melting temperature than ThF_4, the nickel liner sinks to the bottom when the NaF pellet melts, such that both compounds come into contact and mix at the melting temperature of NaF. This results in a peak in heat flow. The peak area and the sensitivity of a reference material (Au in this work) measured at the same time as the sample are subsequently determined, such that the total enthalpy involved in the mixing event $\Delta_{meas}H^o_m(T_{fus,NaF})$ can be calculated. Au (> 99.99% purity) was used as reference material in this work. The enthalpy of mixing is then calculated by subtracting the fusion (melting) enthalpies of the end-members from the measured heat:

$$\Delta_{mix}H^o_m(T_{fus,NaF}) = \Delta_{meas}H^o_m(T_{fus,NaF}) - \left(x(ThF_4)\cdot\Delta_{fus}H^o_m(ThF_4,T_{fus,NaF}) + (1-x(ThF_4))\cdot\Delta_{fus}H^o_m(NaF,T_{fus,NaF})\right) \quad (6.27)$$

Note that it is assumed that the fusion enthalpy of ThF_4 is temperature independent and is thus the same at the melting temperature of NaF. The fusion enthalpies were taken from [77] for ThF_4 (36.4 kJ mol^{-1}) and from the SGTE database for NaF [2] (33.3 kJ mol^{-1}). The uncertainties in $\Delta_{mix}H^o_m(T_{fus,NaF})$ were determined from the standard uncertainty of the calibration process.

6.5.6. DENSITY AND THERMAL EXPANSION

6.5.7. DENSITY

The densities ρ and molar volumes V_m were calculated with MD from the mean volume of the cubic simulation cell after the NpT run at 1270, 1433, 1500, 1600 and 2000 K, over the full concentration range.

In addition, the density decreases with increasing temperature as expected. The calculated excess densities are shown in figure 6.16b.

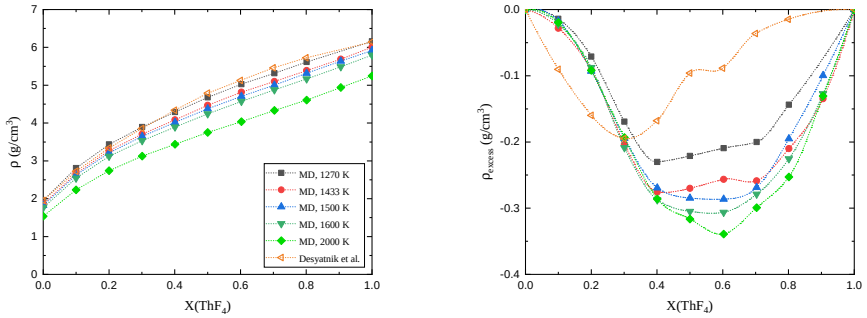

(a) (b)

Figure 6.16: In (a), the densities versus composition at different temperatures in the NaF-ThF$_4$ system. In (b) the excess density plotted for various temperatures calculated with MD compared to the excess values obtained from the experimental data.

6

6.5.8. THERMAL EXPANSION

SOLID PHASES

The thermal expansion coefficient β of the intermediate phases isolated in this work, Na_2ThF_6 and $NaTh_2F_9$, calculated with the QHA method, are plotted in Fig. 6.17.

LIQUID SOLUTION

The thermal expansion coefficient β was subsequently calculated by observing the behaviour of the density versus temperature. β is given by:

$$\beta = -\frac{1}{\rho}\left(\frac{\partial \rho}{\partial T}\right)_p \tag{6.28}$$

The thermal expansion coefficient increases quasi-linearly with temperature as shown in figure 6.18. The fitting equations as a function of temperature are given in table 9 for each composition. Overall, β increases with temperature and decreases with increasing x(ThF$_4$) concentration.

6.5.9. MEDIUM-RANGE ORDER IN THE (NA,TH)F$_x$ LIQUID SOLUTION

The speciation inf the (Na,Th)F$_x$ solution as a function of temperature and ThF$_4$ concentration is plotted in Fig. 6.19. A comparison between the simplified distribution and the CALPHAD distribution is shown in Fig.6.20.

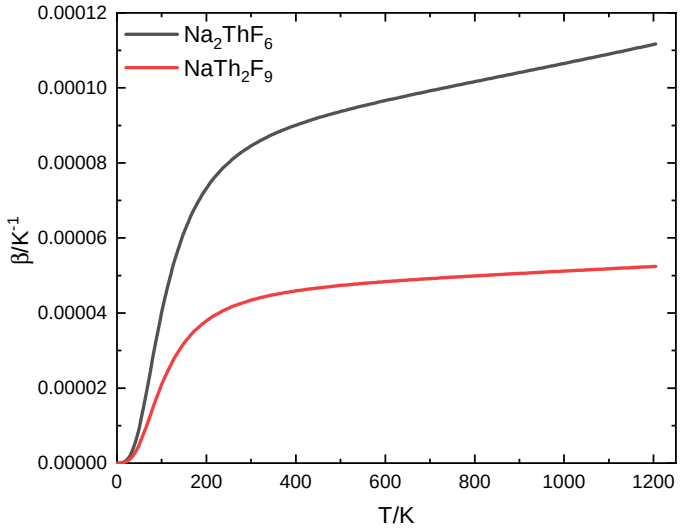

Figure 6.17: Thermal expansion coefficients versus temperature, derived via the TSC method.

Table 9: Thermal expansion versus temperature of the (Na,Th)F$_x$ melt obtained by fitting the simulation results in the temperature range (1270 - 2000 K).

x(ThF$_4$)	β / K^{-1}
1	$5.127{\cdot}10^{-8}$T + $1.408{\cdot}10^{-4}$
0.905	$5.817{\cdot}10^{-8}$T + $1.447{\cdot}10^{-4}$
0.801	$7.460{\cdot}10^{-8}$T + $1.494{\cdot}10^{-4}$
0.703	$7.908{\cdot}10^{-8}$T + $1.503{\cdot}10^{-4}$
0.603	$9.255{\cdot}10^{-8}$T + $1.512{\cdot}10^{-4}$
0.5	$9.301{\cdot}10^{-8}$T + $1.514{\cdot}10^{-4}$
0.401	$9.260{\cdot}10^{-8}$T + $1.514{\cdot}10^{-4}$
0.301	$9.111{\cdot}10^{-8}$T + $1.515{\cdot}10^{-4}$
0.2	$9.574{\cdot}10^{-8}$T + $1.511{\cdot}10^{-4}$
0.1	$9.916{\cdot}10^{-8}$T + $1.510{\cdot}10^{-4}$
0	$1.109{\cdot}10^{-7}$T + $1.498{\cdot}10^{-4}$

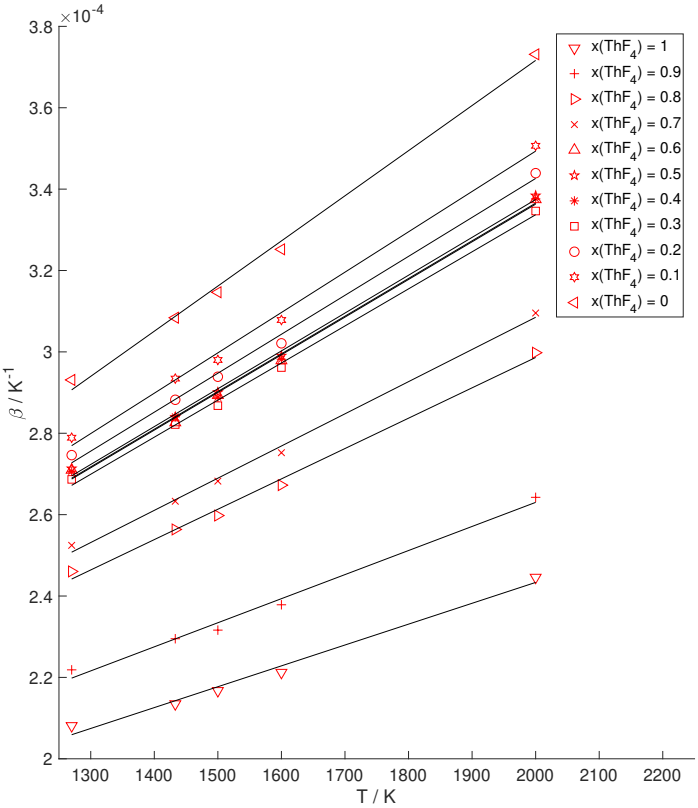

Figure 6.18: Evolution of the thermal expansion coefficients versus temperature.

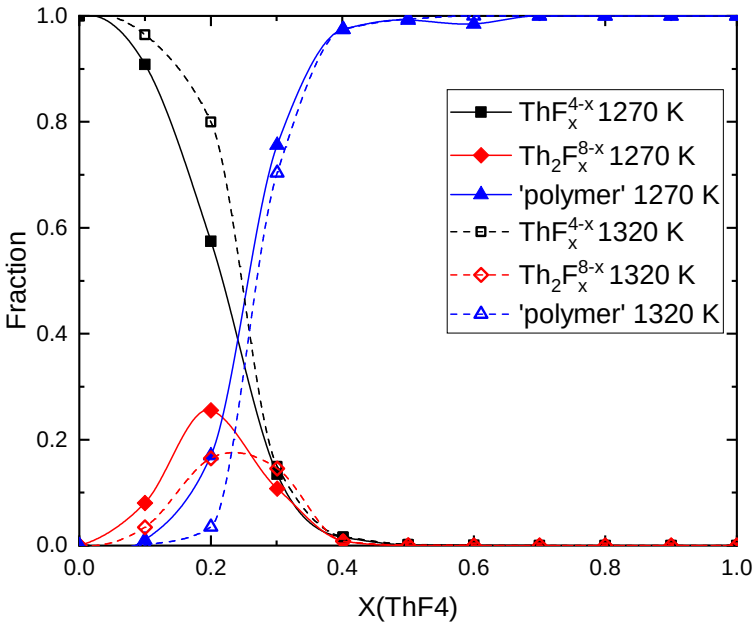

Figure 6.19: Fraction of monomers (■), dimers (♦), and 'polymers' (▲), in the NaF-ThF_4 liquid solution at T = 1270 K, 1320 K.

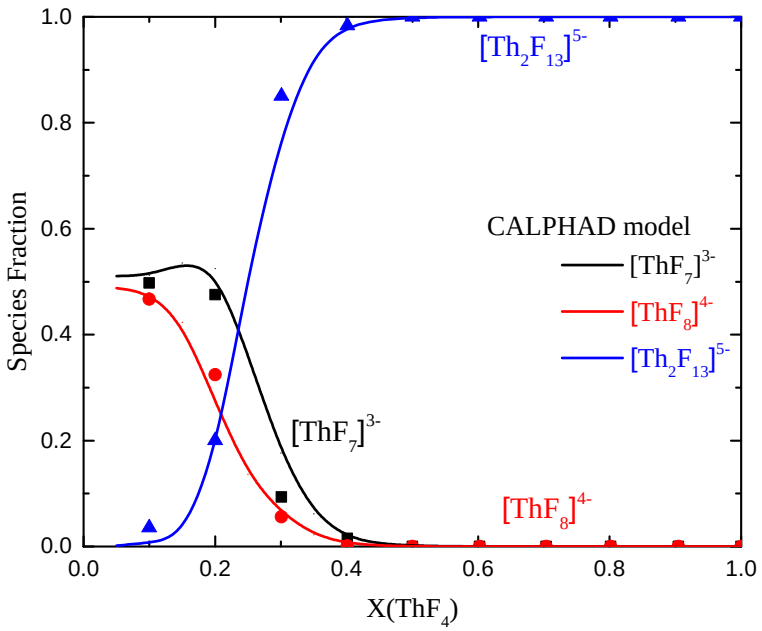

Figure 6.20: Distribution of the 7, 8 and 9 coordinated $[ThF_n]^{m-}$ complexes versus composition in the NaF-ThF$_4$ system at 1320 K.

BIBLIOGRAPHY

[1] A.K. Adya, R. Takagi, and M. Gaune-Escard. “Unravelling the internal complexities of molten salts”. In: *Zeitschrift für Naturforschung A* 53.12 (1998), pp. 1037–1048.

[2] I. Ansara and B. Sundman. *The Scientific Group Thermodata Europe in Computer Handling and Dissemination of Data*. Elsevier Science Publishers, Amsterdam, The Netherlands, 1986.

[3] A. Le Bail, H. Duroy, and J.L. Fourquet. “Ab-initio structure determination of $LiSbWO_6$ by X-ray powder diffraction”. In: *Materials Research Bulletin* 23.3 (1988), pp. 447–452. ISSN: 0025-5408.

[4] C.W. Bale et al. “FactSage thermochemical software and databases, 2010–2016”. In: *Calphad* 54 (2016), pp. 35–53.

[5] T.H.K. Barron and G.K. White. *Heat capacity and thermal expansion at low temperatures*. Springer Science & Business Media, 2012.

[6] M Beilmann et al. “Excess heat capacity in liquid binary alkali-fluoride mixtures”. In: *Inorganic Chemistry* 52.5 (2013), pp. 2404–2411.

[7] O. Beneš, M. Beilmann, and R.J.M. Konings. “Thermodynamic assessment of the LiF-NaF-ThF_4-UF_4 system”. In: *Journal of Nuclear Materials* 405.2 (2010), pp. 186–198.

[8] O. Beneš and R. J. M. Konings. “Molten Salt Reactor Fuel and Coolant”. In: 3 (Dec. 2012), pp. 359–389.

[9] O. Beneš et al. “A DSC study of the $NaNO_3$–KNO_3 system using an innovative encapsulation technique”. In: *Thermochimica Acta* 509.1-2 (2010), pp. 62–66.

[10] M.A. Blanco, E. Francisco, and V. Luana. “GIBBS: isothermal-isobaric thermodynamics of solids from energy curves using a quasi-harmonic Debye model”. In: *Computer Physics Communications* 158.1 (2004), pp. 57–72.

[11] P. E. Bloechl. “Projector augmented-wave method.” In: *Phys. Rev. B: Condens. Matter* 50.24 (1994), pp. 17953–79. ISSN: 0163-1829.

[12] W.J. Boettinger et al. “DTA and Heat-flux DSC measurements of alloy melting and freezing”. In: *Methods for Phase Diagram Determination*. Ed. by J.-C. Zhao. Oxford: Elsevier Science Ltd, 2007, pp. 151–221.

[13] H.K. Cammenga et al. “The temperature calibration of scanning calorimeters: Part 2. Calibration substances”. In: *Thermochimica Acta* 219 (1993), pp. 333–342.

[14] E. Capelli et al. “"Thermodynamic investigation of the LiF–ThF_4 system "”. In: *The Journal of Chemical Thermodynamics* 58 (2013), pp. 110–116.

[15] M. Chase Jr. “NIST-JANAF Thermochemical tables 4th edition”. In: *Journal of Physical and Chemical Reference Data* 85 (1998).

[16] J. Dai et al. “Molecular dynamics studies of the structure of pure molten ThF_4 and ThF_4-LiF-BeF_2 melts”. In: *Journal of Molecular Liquids* 211 (2015), pp. 747–753.

[17] V. Danek. *Physico-chemical analysis of molten electrolytes*. Elsevier, 2006.

[18] V.N. Desyatnik et al. “Density and kinematic viscosity of NaF-ThF_4 and KF-ThF_4 melts”. In: *Soviet Atomic Energy* 51.6 (1981), pp. 807–810.

[19] L. Dewan. “Molecular dynamics simulation and topological analysis of the network structure of actinide-bearing materials”. PhD thesis. Massachusetts Institute of Technology, 2013.

[20] L.C. Dewan et al. “Molecular dynamics simulation of the thermodynamic and transport properties of the molten salt fast reactor fuel LiF–ThF_4”. In: *Journal of Nuclear Materials* 434.1-3 (2013), pp. 322–327.

[21] V. Dracopoulos and G. N. Papatheodorou. “Isotropic and anisotropic Raman scattering from molten alkali-metal fluorides”. In: *Physical Chemistry Chemical Physics* 2.9 (2000), pp. 2021–2025.

[22] V.S. Emelyanov and A.I. Evstyukhin. “An investigation of fused-salt systems based on thorium fluoride-II”. In: *Journal of Nuclear Energy (1954)* 5.1 (1957), pp. 108–114.

[23] Ersha Fan et al. “Low-temperature molten-salt-assisted recovery of valuable metals from spent lithium-ion batteries”. In: *ACS Sustainable Chemistry & Engineering* 7.19 (2019), pp. 16144–16150.

[24] E. Francisco, M.A. Blanco, and G. Sanjurjo. “Atomistic simulation of SrF_2 polymorphs”. In: *Phys. Rev. B* 63 (9 Jan. 2001), p. 094107.

[25] E. Francisco et al. “Quantum-Mechanical Study of Thermodynamic and Bonding Properties of MgF_2”. In: *The Journal of Physical Chemistry A* 102.9 (Feb. 1998), pp. 1595–1601.

[26] A. E. Gheribi et al. “Prediction of the thermophysical properties of molten salt fast reactor fuel from first-principles”. In: *Molecular Physics* 112.9-10 (2014), pp. 1305–1312.

[27] A.E. Gheribi et al. “An ab initio method for the prediction of the lattice thermal transport properties of oxide systems: Case study of Li_2O and K_2O”. In: *Journal of Applied Physics* 118.14 (2015), p. 145101.

[28] A. Glensk et al. “Understanding Anharmonicity in fcc Materials: From its Origin to ab initio Strategies beyond the Quasiharmonic Approximation”. In: *Phys. Rev. Lett.* 114 (19 May 2015), p. 195901.

[29] Göran Grimvall. *Thermophysical Properties of Materials*. Elsevier, 1999.

[30] A. Grzechnik, W. Morgenroth, and K. Friese. “Twinned tetragonal structure and equation of state of $NaTh_2F_9$”. In: *Journal of Solid State Chemistry* 181.4 (2008), pp. 971–975.

[31] A. Grzechnik et al. “Crystal structure and stability of β-Na_2ThF_6 at non-ambient conditions”. In: *Journal of Physics: Condensed Matter* 19.26 (June 2007), p. 266219.

[32] R.J. Heaton et al. “A first-principles description of liquid BeF_2 and its mixtures with LiF: 1. Potential development and pure BeF_2”. In: *The Journal of Physical Chemistry B* 110.23 (2006), pp. 11454–11460.

[33] G.W.H. Höhne et al. “The temperature calibration of scanning calorimeters”. In: *Thermochimica Acta* 160.1 (1990), pp. 1–12.

[34] J.L. Holm. “Excess Volumes of Mixing in Liquid Binary Alkali-Halide Mixtures”. In: *Acta Chem. Scema* 25.10 (1971).

[35] P. Javorský et al. “Low-temperature heat capacity measurements on encapsulated transuranium samples”. In: *Journal of Nuclear Materials* 344.1 (2005), pp. 50–55.

[36] A.R. Kamali. “Clean production and utilisation of hydrogen in molten salts”. In: *RSC Advances* 10.59 (2020), pp. 36020–36030.

[37] A.D. Kirshenbaum and J.A. Cahill. “The density of molten thorium and uranium tetrafluorides”. In: *Journal of Inorganic and Nuclear Chemistry* 19.1 (1961), pp. 65–68.

[38] R.J.M. Konings, J.P.M. Van der Meer, and E. Walle. “Chemical Aspects of Molten Salt Reactor Fuel”. In: *European Commission Joint Research Centre* (2005).

[39] G. Kresse and J. Furthmueller. “Efficient iterative schemes for ab initio total-energy calculations using a plane-wave basis set.” In: *Phys. Rev. B: Condens. Matter* 54.16 (1996), pp. 11169–11186.

[40] G. Kresse and J. Furthmuller. “Efficiency of ab-initio total energy calculations for metals and semiconductors using a plane-wave basis set.” In: *Comput. Mater. Sci.* 6.1 (1996), pp. 15–50.

[41] G. Kresse and J. Hafner. “Ab initio molecular dynamics of liquid metals.” In: *Phys. Rev. B: Condens. Matter* 47.1 (1993), pp. 558–61.

[42] G. Kresse and J. Hafner. “Ab initio molecular-dynamics simulation of the liquid-metal-amorphous-semiconductor transition in germanium.” In: *Phys. Rev. B: Condens. Matter* 49.20 (1994), pp. 14251–69.

[43] G. Kresse and D. Joubert. “From ultrasoft pseudopotentials to the projector augmented-wave method.” In: *Phys. Rev. B: Condens. Matter Mater. Phys.* 59.3 (1999), pp. 1758–1775. ISSN: 0163-1829.

[44] J.C. Lashley et al. “Critical examination of heat capacity measurements made on a Quantum Design physical property measurement system”. In: *Cryogenics* 43.6 (2003), pp. 369–378.

[45] A. Le Bail. “Whole powder pattern decomposition methods and applications: A retrospection”. In: *Powder diffraction* 20.4 (2005), pp. 316–326.

[46] J. Leitner et al. “Application of Neumann–Kopp rule for the estimation of heat capacity of mixed oxides”. In: *Thermochimica Acta* 497.1-2 (2010), pp. 7–13.

[47] J. Liu et al. “Theoretical Studies of Structure and Dynamics of Molten Salts: The LiF–ThF_4 System”. In: *The Journal of Physical Chemistry B* 118.48 (2014), pp. 13954–13962.

[48] P.A. Madden and M. Wilson. “Covalent effects in ionic systems”. In: *Chemical Society Reviews* 25.5 (1996), pp. 339–350.

[49] P.A. Madden et al. “From first-principles to material properties”. In: *Journal of Molecular Structure: THEOCHEM* 771.1 (2006). Modelling Structure and Reactivity: the 7th triennial conference of the World Association of Theoritical and Computational Chemists (WATOC 2005), pp. 9–18.

[50] S. Mukherjee and S. Dash. “Determination of Gibbs energy of formation of $LiThF_5$, $LiTh_2F_9$, and $LiTh_4F_{17}$ in Li-Th-F system by using solid electrolyte galvanic cell”. In: *Journal of Solid State Electrochemistry* 23.11 (Nov. 2019), pp. 3043–3056.

[51] S. Mukherjee and S. Dash. “Thermodynamic investigation of NaF-ThF_4 system and fuel salts of Molten Salt Reactor”. In: *Journal of Fluorine Chemistry* 212 (2018), pp. 17–25.

[52] T. Murakami et al. “Electrolytic synthesis of ammonia in molten salts under atmospheric pressure”. In: *Journal of the American Chemical Society* 125.2 (2003), pp. 334–335.

[53] J.A. Ocádiz-Flores et al. “Examination of the short-range structure of molten salts: ThF_4, UF_4, and related alkali actinide fluoride systems”. In: *Phys. Chem. Chem. Phys.* 23 (18 2021), pp. 11091–11103.

[54] J.A. Ocádiz-Flores et al. “Thermodynamic assessment of the KF-ThF_4, LiF-KF-ThF_4 and NaF-KF-ThF_4 systems”. In: *The Journal of Chemical Thermodynamics* 145 (2020), p. 106069.

[55] O. Pauvert et al. “Ion specific effects on the structure of molten AF-ZrF4 systems (A+= Li+, Na+, and K+)”. In: *The Journal of Physical Chemistry B* 115.29 (2011), pp. 9160–9167.

[56] A. D. Pelton et al. “"The modified quasichemical model I—Binary solutions"”. In: *Metallurgical and Materials Transactions B* 31.4 (2000), pp. 651–659.

[57] A.D. Pelton and P. Chartrand. “The modified quasi-chemical model: Part II. Multicomponent solutions”. In: *Metallurgical and Materials Transactions A* 32.6 (2001), pp. 1355–1360.

[58] J.P. Perdew, K. Burke, and M. Ernzerhof. “Generalized gradient approximation made simple.” In: *Phys. Rev. Lett.* 77.18 (1996), pp. 3865–3868.

[59] John P. Perdew, Kieron Burke, and Matthias. Ernzerhof. “Generalized gradient approximation made simple. [Erratum to document cited in CA126:51093].” In: *Phys. Rev. Lett.* 78.7 (1997), p. 1396.

[60] M Rand et al. “Chemical Thermodynamics of Thorium (Chemical Thermodynamics”. In: *Paris: OCDE-NEA* (2008).

[61] P. Ravindran et al. “Density functional theory for calculation of elastic properties of orthorhombic crystals: Application to TiSi2”. In: *Journal of Applied Physics* 84.9 (1998), pp. 4891–4904.

[62] J. Rodriguez-Carvajal. “FULLPROF program: Rietveld pattern matching analysis of powder patterns”. In: *Institut Laue-Langevin, Grenoble* (1990).

[63] M. Salanne et al. “A First-Principles Description of Liquid BeF_2 and Its Mixtures with LiF: 2. Network Formation in LiF- BeF_2”. In: *The Journal of Physical Chemistry B* 110.23 (2006), pp. 11461–11467.

[64] M. Salanne et al. “Heat-transport properties of molten fluorides: Determination from first-principles”. In: *Journal of Fluorine Chemistry* 130.1 (2009), pp. 38–44.

[65] M.B. J. W. Schreuder et al. “Experimental and Computational Exploration of the NaF-ThF_4 Fuel System: Structure and Thermochemistry”. In: *The Journal of Physical Chemistry B* 0.0 (0). PMID: 34318676, null.

[66] A. Seifitokaldani and A.E. Gheribi. “Thermodynamically self-consistent method to predict thermophysical properties of ionic oxides”. In: *Computational Materials Science* 108 (2015), pp. 17–26.

[67] A. Seifitokaldani et al. “Thermophysical properties of titanium and vanadium nitrides: Thermodynamically self-consistent approach coupled with density functional theory”. In: *Journal of Alloys and Compounds* 662 (2016), pp. 240–251.

[68] N.J. Siambun et al. “Utilisation of carbon dioxide for electro-carburisation of mild steel in molten carbonate salts”. In: *Journal of the Electrochemical Society* 158.11 (2011), H1117.

[69] L. N. Sidorov et al. “Mass-spectrometric determination of enthalpies of dissociation of gaseous complex fluorides into neutral and charged particles. VII. MF-ThF_4 systems (M= Li, Na, K, Rb, Cs)”. In: *International Journal of Mass Spectrometry and Ion Physics* 51.2-3 (1983), pp. 291–311.

[70] A. L. Smith et al. “Thermodynamic study of $Cs_3Na(MoO_4)_2$: Determination of the standard enthalpy of formation and standard entropy at 298.15 K”. In: *The Journal of Chemical Thermodynamics* 120 (2018), pp. 205–216.

[71] A.L. Smith et al. “A new approach for coupled modelling of the structural and thermo-physical properties of molten salts. Case of a polymeric liquid LiF-BeF_2”. In: *Journal of Molecular Liquids* 299 (2020), p. 112165.

[72] A.L. Smith et al. “In situ high-temperature EXAFS measurements on radioactive and air-sensitive molten salt materials”. In: *Journal of synchrotron radiation* 26.1 (2019), pp. 124–136.

[73] P. Souček et al. “Synthesis of UF_4 and ThF_4 by HF gas fluorination and re-determination of the UF4 melting point”. In: *Journal of Fluorine Chemistry* 200 (2017), pp. 33–40.

[74] K.T. Tang and J.P. Toennies. “The damping function of the van der Waals attraction in the potential between rare gas atoms and metal surfaces”. In: *Surface Science Letters* 279.3 (1992), pp. L203–L206.

[75] R. E. Thoma et al. “Phase Equilibria in the System NaF-ThF_4-UF_4”. In: *Journal of the American Ceramic Society* 46.1 (1963), pp. 37–42.

[76] R.E. Thoma et al. “Phase Equilibria in the Fused Salt Systems LiF–$ThF_4$and NaF–TfF_4”. In: *The Journal of Physical Chemistry* 63.8 (1959), pp. 1266–1274.

[77] A. Tosolin et al. “Isobaric Heat Capacity of Solid and Liquid Thorium Tetrafluoride”. In: *Journal of Chemical & Engineering Data* 64.9 (2019), pp. 3945–3950.

[78] A. Tosolin et al. “Synthesis of plutonium trifluoride by hydro-fluorination and novel thermodynamic data for the PuF_3-LiF system”. In: *Journal of Nuclear Materials* 503 (2018), pp. 171–177.

[79] L.M. Toth and G.E. Boyd. “Raman spectra of thorium(IV) fluoride complex ions in fluoride melts”. In: *The Journal of Physical Chemistry* 77.22 (1973), pp. 2654–2657.

[80] C.C. Underwood, C.D. McMillen, and J.W. Kolis. “The crystal structures of $CsTh_6F_{25}$ and $NaTh_3F_{13}$”. In: *Journal of Chemical Crystallography* 42.6 (2012), pp. 606–610.

[81] W. Weng, L. Tang, and W. Xiao. “Capture and electro-splitting of CO2 in molten salts”. In: *Journal of Energy Chemistry* 28 (2019), pp. 128–143.

[82] M. Wilson and P.A. Madden. ““Prepeaks”and “first sharp diffraction peaks”in computer simulations of strong and fragile ionic liquids”. In: *Physical review letters* 72.19 (1994), p. 3033.

[83] W.H. Zachariasen. “Crystal chemical studies of the 5f-series of elements. I. New structure types”. In: *Acta Crystallographica* 1.5 (Nov. 1948), pp. 265–268.

[84] W.H. Zachariasen. “Crystal chemical studies of the 5f-series of elements. XII. New compounds representing known structure types”. In: *Acta Crystallographica* 2.6 (Dec. 1949), pp. 388–390.

[85] W.H. Zachariasen. “Double Fluorides of Potassium or Sodium with Uranium, Thorium or Lanthanum”. In: *Journal of the American Chemical Society* 70.6 (1948), pp. 2147–2151.

7

BEYOND THE PHASE DIAGRAM: DENSITY AND VISCOSITY MODELS FOR MOLTEN SALT FUEL SYSTEMS

Models to compute the density and viscosity of four keystone systems related to Molten Salt Reactor (MSR) technology have been optimized: NaCl-UCl_3, LiF-ThF_4, LiF-UF_4, and LiF-ThF_4-UF_4. Thermodynamic assessment of all four systems, using the modified quasichemical formalism in the quadruplet approximation for the description of the liquid solutions, are carried out. In the case of NaCl-UCl_3, phase diagram and mixing enthalpy data available in the literature are taken into account. For the fluoride systems, recently published data on some solid phases are taken into account, while retaining the most recently published descriptions of the liquid solutions. The densities of the liquid solutions are modelled using pressure-dependent terms of the excess Gibbs energy, while the viscosities are modelled using an Eyring equation. Both state functions are thus related to the thermodynamic assessments through the quadruplet distributions.

Jaén A. OCÁDIZ FLORES, Rudy J.M. KONINGS, Anna Louise SMITH

7.1. INTRODUCTION

The Molten Salt Reactor (MSR) is a class of fission reactor with the principal characteristic that the fuel is in the liquid state and also serves as the primary coolant [48]. The use of mixtures of uranium tetrafluoride and thorium tetrafluoride with alkali fluorides or beryllium or zirconium fluorides for the fuel system was originally proposed by Ray Briant at the Oak Ridge National Laboratory (ORNL) [10]. Eventually the concept was applied in the construction of the Aircraft Reactor Experiment (ARE) [8], designed, built, and operated by ORNL in the 1950's. Next to these developments, the first conceptual design of a reactor fueled with molten chlorides appears to have been made by Bulmer et al. [12] in 1956. Around the same time, the team at ORNL also considered the use of chloride salts in a fast reactor, as chlorine moderates significantly less than fluorine. However, they pointed out that the high (n,p) cross section of ^{35}Cl, resulting in the formation of corrosive sulphur, would impose the use of ^{37}Cl exclusively. Such an isotope separation is difficult, and so development of fast molten chloride reactors was thought unlikely at the time [10]. Following the ARE, Alvin Weinberg recognized the potential of molten salt reactors as a civilian power source and spearheaded a research program which culminated in the fluoride-fueled, thermal spectrum Molten Salt Reactor Experiment (MSRE), also in ORNL in the 1960's [53]. Despite the great success of the experiment, it was the last prototype MSR to be built. Later, the Generation IV International Forum, a group of fourteen member countries pursuing research and development for the next generation of nuclear reactors, selected the MSR as one of six key nuclear energy systems to replace the current fleet of Generation II Light Water Reactors [33].

Following the historical experience, modern research efforts in the nuclear community have been primarily focused on fluoride salts [29], resulting in a larger (albeit still not fully complete) body of knowledge than for chlorides. Nevertheless, research activities around chloride fuels have increased notably in recent years [51, 37, 78]. As pointed out by Merle [52], the design choice depends on the objective. Some advantages of chlorides over fluorides the author has identified are:

1. lower melting temperatures
2. a wider range of separation processes for salt clean-up, including existing processes
3. greater actinide solubility
4. higher breeding ratio when coupled with a U/Pu fuel cycle

While, vice-versa, some of the advantages of the fluorides are:

1. chemistry is well-characterized for nuclear applications
2. easier to dehydrate: reduced corrosion risk from initial impurities
3. softer spectrum: reduced radiation damage to structural materials
4. higher breeding ratio when coupled with a Th/U fuel cycle (epithermal/thermal spectrum)

As for radioisotopes formed during operation, both salt families have problematic products which require careful planning. In a nutshell, the heuristic proposed by Merle is that if the objective is a thorium breeder reactor, a LiF-based salt is more convenient, while for an actinide burner or breeder, NaCl is the main solvent of choice.

This work thus focuses on three keystone binary systems for MSR technology: LiF-UF_4, LiF-ThF_4, and NaCl-UCl_3, as well as the ternary system LiF-ThF_4-UF_4. Two state functions, the density and viscosity are computed. The models are linked to each other via the thermodynamic assessments of the corresponding systems by the CALPHAD method based on the modified quasi-chemical formalism in the quadruplet approximation [65]. The methodology of the density model as applied here was first developed by Robelin et al. [72] on a closely related system sharing NaCl as an end-member, namely NaCl-KCl-$MgCl_2$-$CaCl_2$, and with a well-established industrial application: the reduction of Mg. The same density modelling approach model was later successfully applied to the NaF-AlF_3-CaF_2-Al_2O_3 electrolyte [70]. In further work, Robelin and Chartrand extended the model to compute the viscosity of the same electrolyte [71]. The same methodology is applied herein to our systems of interest, as detailed hereafter.

7.2. THERMODYNAMIC MODELLING

7.2.1. PHASE DIAGRAMS

A thermodynamic assessment consists of optimizing unknown parameters (e.g. enthalpy of formation, standard entropy) and excess parameters associated with the Gibbs energy functions of all the phases occurring in a system, in order to reproduce known data such as phase diagram equilibria, thermodynamic data, vapor pressure, activities. In this work, FactSage 7.2 was used to perform the thermodynamic assessments.

PURE COMPOUNDS

The Gibbs energy function of a pure compound is given by:

$$G^o(T) = \Delta_f H^{\circ}_{\mathrm{m}}(298) - S^{\circ}_{\mathrm{m}}(298)\,T + \int_{298}^{T} C^o_{\mathrm{p,m}}(T)\,dT - T\int_{298}^{T} \frac{C^o_{\mathrm{p,m}}(T)}{T}\,dT \tag{7.1}$$

where $\Delta_f H^{\circ}_{\mathrm{m}}(298)$ is the standard enthalpy of formation, and $S^{\circ}_{\mathrm{m}}(298)$ is the standard absolute entropy, both evaluated at a reference temperature, usually taken to be 298.15 K (throughout this work 298 will be understood to mean 298.15 K for simplicity). $C_{\mathrm{p,m}}$ is the isobaric heat capacity expressed as a polynomial:

$$C^o_{\mathrm{p,m}}(T) = a + bT + cT^2 + dT^{-2} \tag{7.2}$$

In the absence of experimental data, the Neumann-Kopp rule [49] was applied to estimate the heat capacities of stoichiometric compounds.

In this work, the thermodynamic functions of the solid phases are very similar to those appearing in the most recent assessments of the systems studied (see Section 7.2.1

below), but slightly adjusted to reflect new experimental data published after the aforementioned assessments. First, the isobaric heat capacities of solid and liquid ThF_4 recently measured by Tosolin et al. [81] were used. The authors also re-calculated the enthalpy of fusion from their corresponding enthalpy increment measurements, and the newly assessed data were selected herein: (36.4 $\pm$ 10) kJ· mol^{-1}, while the previous reference value was (41.9 $\pm$ 2) kJ· mol^{-1} [16]. The chosen value affects the topology of the LiF-ThF_4 phase diagram (see Fig. 7.1) but does not affect the quadruplet distributions which serve as input for the viscosity model (see Section 7.2.3). Second, the heat capacities of $LiThF_5$(cr), $LiTh_2F_9$(cr), and LiU_4F_{17}(cr), measured with Differential Scanning Calorimetry (DSC) by Mukherjee and Dash [57] were taken into account. Third, the LiF-UF_4 system was slightly re-optimized to reflect new insights on the phase equilibria reported in [61]: Li_3UF_7 was included as a metastable phase, and $Li_7U_6F_{31}$ was replaced with $LiUF_5$. These changes required a slight re-optimization of the thermodynamic functions, indicated in bold in Table 1.
The thermodynamic functions of NaCl(cr,l) were taken from the IVTAN tables by Glushko et al. [35]. The heat capacity of NaCl(l) was recently recommended by van Oudenaren et al. [64], who critically reviewed the four studies available on the determination of the heat capacity of NaCl(l) [67, 69, 58, 23]. Although Glushko et al. had recommended to discard the data by Dawson et al. [23], van Oudenaren et al. [64] found that there was no discrepancy between their data and that reported by the other authors. Averaging over the four studies, van Oudenaren et al. recommend (68 $\pm$ 1) kJ·mol^{-1} in the 1074-2500 K range. The heat capacity of UCl_3(l) was also taken from van Oudenaren et al. [64], who derived the value from Molecular Dynamics (MD) simulations. The rest of the thermodynamic functions for UCl_3(cr,l) were taken from the recent review by Capelli and Konings [15].

7

SOLID SOLUTION
The total Gibbs energy function of the two-component solid solutions in this work is given by:

$$G(T) = X_1 G^{o}_{m,1}(T) + X_2 G^{o}_{m,2}(T) + X_1 RTlnX_1 + X_2 RTlnX_2 + G^{xs}_m \tag{7.3}$$

where X_i are the molar fractions and $G^{o}_{m,i}$(T) are the standard molar Gibbs energies of the pure end members. The excess Gibbs energy parameter is described using the polynomial formalism:

$$G^{xs}_m = \sum_{i,j} X_1^i \cdot X_2^j \cdot L_{i,j} \tag{7.4}$$

where $L_{i,j}$ is a coefficient which may depend on temperature in the form of the general equation:

$$L_{i,j} = A + BT + CTlnT + DT^2 \tag{7.5}$$

The values of the excess Gibbs energy parameters of the solid solutions in this study are summarized in Table 2. They belong to the UF_4-ThF_4 and LiF-ThF_4-UF_4 systems. All except the (Th,U)F_4 solution [5] were optimized in this work.

Table 1: Thermodynamic data for end-members and intermediate compounds used in this work for the phase diagram assessment: $\Delta_f H^o_m$(298 K)/(kJ ·mol^{-1}), S^o_m(298 K)/(J·K^{-1}·mol^{-1}), and heat capacity coefficients $C_{p,m}$(T/K)/(J·K^{-1}·mol^{-1}), where $C_{p,m}(T/K) = a + b{\cdot}T + c{\cdot}T^2 + d{\cdot}T^{-2}$. Optimized data are shown in **bold**.

Compound	$\Delta_f H^o_m$(298 K)/ (kJ·mol^{-1})	S^o_m(298 K)/ (J·K^{-1}·mol^{-1})	$C_{p,m}(T/K)/(J{\cdot}K^{-1}{\cdot}mol^{-1}) = a + b{\cdot}T + c{\cdot}T^2 + d{\cdot}T^{-2}$ a	b	c	d	Range	Reference
LiF(cr)	-616.931	35.66	43.309	0.016312	$5.0470{\cdot}10^{-7}$	$-5.691{\cdot}10^{5}$	298-2500	[18]
LiF(l)	-598.654	42.962	64.183				295-1500	[18]
ThF_4(cr)	-2097.900	142.05	111.46	$2.6900{\cdot}10^{-2}$		-780000	298-2500	[46],[81]
ThF_4(l)	-2100.360	106.61	168.0				298-1500	[46, 81]
UF_4(cr)	-1914.200	151.7	114.5194	$2.0555{\cdot}10^{-2}$		-413159	298-2500	[46]
UF_4(l)	-1914.658	115.4	174.74				298-1500	[46]
NaCl(cr)	-411.260	72.15	47.72158	0.0057	$1.21466{\cdot}10^{-5}$	-882.996	298-1074	[35]
			68.0				1074-2500	[64]
NaCl(l)	-383.060	98.407	47.72158	0.0057	$1.21466{\cdot}10^{-5}$	-882.996	298-1074	[35]
			68.0				1074-2500	[64]
UCl_3(cr)	-863.700	163.9	106.967	-0.02086	3.639E-5	-129900	298-2500	[15]
UCl_3(l)	-846.433	153.6	151.1				298-2500	[15], [64]
Li_3ThF_7(cr)	**-3960.000**	**248.9**	241.387	0.075836	$1.5141 \cdot 10^{-6}$	$-2.4873{\cdot}10^{6}$	298-2500	This work
$LiThF_5$(cr)	**-2720.300**	**179.1**	167.8	0.027		$-1.513510{\cdot}10^{6}$	298-2500	This work, [57]
$LiTh_2F_9$(cr)	**-4820.200**	324.29	291.3	0.0386		$-3.076934{\cdot}10^{6}$	298-2500	This work, [17], [57]
$LiTh_4F_{17}$(cr)	**-9016.100**	609.0	536.2	0.0622		$-5.051854{\cdot}10^{6}$	298-2500	This work, [17], [57]
Li_4UF_8(cr)	**-4347.620**	357.55	287.75532	$8.5804{\cdot}10^{-2}$	$2.0188{\cdot}10^{-6}$	-2689653	298-2500	This work, [17]
Li_3UF_7(cr)	**-3777.464**	258.68	244.44634	$6.9491{\cdot}10^{-2}$	$1.5141{\cdot}10^{-6}$	-2120530	298-2500	This work
$LiUF_5$(cr)	**-2543.591**	187.4	157.8284	$3.6867{\cdot}10^{-2}$	$5.0470{\cdot}10^{-7}$	-982259	298-2500	This work
LiU_4F_{17}(cr)	**-8293.861**	644.7	501.38658	$9.8532{\cdot}10^{-2}$	$5.0470{\cdot}10^{-7}$	-2221736	298-2500	This work, [17]

Table 2: Excess Gibbs energy of solid solutions appearing in this study.

Solid solution	ΔG_m^{xs} (J · mol^{-1})	Ref.
(Th,U)F_4	$\Delta G_m^{xs} = 400 \cdot X_{ThF_4} X_{UF_4}$	[43]
Li_3(Th,U)F_7	$\Delta G_m^{xs} = 5500 \cdot X_{Li_3ThF_7} X_{Li_3UF_7}$	this work
Li(Th,U)F_5	$\Delta G_m^{xs} = -2500 \cdot X_{LiThF_5} X_{LiUF_5}$	this work
Li(Th,U)$_2F_9$	$\Delta G_m^{xs} = -38000 \cdot X_{LiTh_2F_9} X_{LiU_2F_9}$	this work
Li(Th,U)$_4F_{17}$	$\Delta G_m^{xs} = -80500 \cdot X_{LiTh_4F_{17}} X_{LiU_4F_{17}}$	this work

LIQUID SOLUTION

The excess Gibbs energy terms of liquid solutions herein were modelled using the modified quasi-chemical model in the quadruplet approximation proposed by Pelton et al. [65]. In this formalism, a set of two anions and two cations makes up a quadruplet, taken to be the basic unit in liquid solution, and the excess parameters to be optimized are those related to the following second-nearest neighbor (SNN) exchange reaction:

$$(A-X-A)+(B-X-B) \longrightarrow 2(A-X-B) \;\; \Delta g_{AB/X} \tag{7.6}$$

where the halide anions are represented by X, and A and B denote the cations. $\Delta g_{AB/X}$ denotes the Gibbs energy change associated with the SNN exchange reaction:

$$\Delta g_{AB/X} = \Delta g^0_{AB/X} + \sum_{i \geqslant 1} g^{i0}_{AB/X} \chi^i_{AB/X} + \sum_{j \geqslant 1} g^{0j}_{AB/X} \chi^j_{BA/X} \tag{7.7}$$

$\Delta g^0_{AB/X}$ and $g^{ij}_{AB/X}$ are coefficients which may be taken to be temperature-dependent, but which are independent of composition. The composition dependence is given by the $\chi_{AB/X}$ terms defined as:

$$\chi_{AB/X} = \frac{X_{AA}}{X_{AA} + X_{AB} + X_{BB}} \tag{7.8}$$

where X_{AA}, X_{BB} and X_{AB} represent cation-cation pair mole fractions. Finally, charge conservation over the quadruplet imposes the anion coordination number:

$$\frac{q_A}{Z^A_{AB/X}} + \frac{q_B}{Z^B_{AB/X}} = \frac{2q_X}{Z^X_{AB/X}} \tag{7.9}$$

where q_i are the charges of the different ions, and $Z^X_{AB/X}$ is the anion-anion coordination number. For the fluoride systems, the cation-cation coordination numbers, as well as the optimized Gibbs energy terms were taken from previous assessments [17] and are shown below for completeness (Table 3, Eq. 7.10-7.11). For NaCl-UCl_3, the Gibbs energy terms were re-optimized in this work to take into account mixing enthalpy data by Matsuura et al. [54] (see Section 7.3.1).

Table 3: Cation-cation coordination numbers of the liquid solutions.

Fluoride solutions [17]			
A	B	$Z^A_{AB/X}$	$Z^B_{AB/X}$
Li^+	Li^+	6	6
Th^{4+}	Th^{4+}	6	6
U^{4+}	U^{4+}	6	6
Li^+	Th^{4+}	2	6
Li^+	U^{4+}	2	6
Th^+	U^{4+}	2	6
Chloride solutions, this work			
Na^+	Na^+	6	6
U^{3+}	U^{3+}	6	6
Na^+	U^{3+}	3	6

$$\Delta g_{LiTh/F} = -10883 + (-6697 + 2.93 \cdot T)\chi_{LiTh/F} + (-20930 + 19.25 \cdot T)\chi_{ThLi/F} \; J \cdot mol^{-1} \tag{7.10}$$

$$\Delta g_{LiU/F} = -16115 + (-711.6 + 1.256 \cdot T)\chi_{LiU/F} + (-1172 - 8.371 \cdot T)\chi_{ULi/F} \; J \cdot mol^{-1} \tag{7.11}$$

$$\Delta g_{NaU/Cl} = -9865 + 3.5 \cdot T - 1150\chi_{NaU/Cl} + (-4100 + 4 \cdot T)\chi_{UNa/Cl} \; J \cdot mol^{-1} \tag{7.12}$$

HIGHER ORDER SYSTEMS

The ternary diagram LiF-ThF_4-UF_4 has been extrapolated from the constituting binary sub-systems using the asymmetric Toop formalism [66]. The salts belong to two groups of symmetry based on their tendency to remain as dissociated ionic liquid (LiF) or associated species (molecular, network forming) in the melt (ThF_4, UF_4). No ternary excess parameters were used.

7.2.2. DENSITY MODEL

The density model based on the modified quasi-chemical model was introduced by Robelin et al. [72] and applied to the NaCl-KCl-$MgCl_2$-$CaCl_2$ system, and later to the NaF-AlF_3-CaF_2-Al_2O_3 electrolyte [70].

The volume of a solution is defined as the partial derivative of the Gibbs energy with respect to pressure [72]:

$$V = \left(\frac{\partial G}{\partial p}\right)_{T, n_{A/X}, n_{B/X}, n_{C/X}} \tag{7.13}$$

In Eq. 7.13 the temperature and the number of moles of the constituents are held constant. For a pure halide salt A/X the molar Gibbs energy can be written as:

$$g^{o}_{A/X}(T,p) = g^{o}_{A/X}(T,p^{o}) + \int_{p^{o}}^{p} V_m^{A/X}(T)\cdot dp = g^{o}_{A/X}(T,p^{o}) + V_m^{A/X}(T)\cdot(p-p^{o}) \quad (7.14)$$

where p^{o} is the standard pressure (1 bar) and $V_m^{A/X}(T)$ is the molar volume of the pure salt A/X at temperature T. It is a function of the volumetric thermal expansion $\alpha(T)$:

$$V_m^{A/X}(T) = V_m^{A/X}(T_{ref})\cdot exp\left(\int_{T_{ref}}^{T}\alpha(T)\cdot dT\right) \quad (7.15)$$

where T_{ref} is an arbitrarily chosen reference temperature and $\alpha(T)$ is given by:

$$\alpha(T) = a + bT + cT^{-1} + dT^{-2} \quad (7.16)$$

The volume of the solution is then given by:

$$V = \sum_i n_{i/X}\cdot V_m^{i/X}(T) + \sum_A\sum_{A>B}(n_{AB/X}/2)\cdot\left(\frac{\partial \Delta g_{AB/X}}{\partial p}\right)_{T,n_{i/X},n_{A/X},n_{B/X}\ldots} \quad (7.17)$$

The first term in Eq. 7.17 represents ideal (additive) volumetric behavior, while the second corresponds to deviations from ideality. $\Delta g_{AB/X}$ can be written as a polynomial in composition parameters (see Eq. 7.8) $\chi_{AB/X}$ and $\chi_{BA/X}$:

$$\begin{aligned}\Delta g_{AB/X} = [\Delta g^{o}_{AB/X} + \beta^{o}_{AB/X}\cdot(p-p^{o})] &+ \sum_{i\geqslant 1}\cdot[g^{i0}_{AB/X} + \beta^{i0}_{AB/X}\cdot(p-p^{o})]\cdot(\chi_{AB/X})^{i} \\ &+ \sum_{j\geqslant 1}\cdot[g^{0j}_{AB/X} + \beta^{0j}_{AB/X}\cdot(p-p^{o})]\cdot(\chi_{BA/X})^{j}\end{aligned} \quad (7.18)$$

where p is in bar, and $g^{o}_{AB/X}$, $g^{i0}_{BC/X}$, and $g^{0j}_{BC/X}$ are parameters from the thermodynamic assessment, while $\beta^{o}_{BC/X}$, $\beta^{i0}_{BC/X}$, and $\beta^{0j}_{BC/X}$ are the parameters (in general dependent on temperature) which belong to the density model and can be optimized to match deviations from ideality. Note that at 1 bar, the pressure-dependent terms in Eq. 7.18 cancel out, yet they can still have an effect on the volume through the partial derivative $\left(\frac{\partial \Delta g_{AB/X}}{\partial p}\right)_{T,n_{i/X},n_{A/X},n_{B/X}\ldots}$ (Eq. 7.17).

7.2.3. VISCOSITY MODEL

Robelin and Chartrand [71] proposed to use the following equation derived by Eyring [34], [32], [31] to model the viscosity of molten electrolytes:

$$\eta = \frac{hN_{Av}}{V_m} \cdot exp\left(\frac{G^*}{RT}\right) \tag{7.19}$$

where h is Planck's constant, N_{Av} is Avogadro's number, V_m is the molar volume, and G^* is the molar activation energy for viscous flow, expressed as a first order polynomial in the quadruplet mole fractions [71], which in turn can be calculated from a thermodynamic model:

$$G^* = \sum_{quad} X_{quad} G^*_{quad} = \sum_{quad} X_{quad}(A_{quad} + B_{quad} \cdot T) \tag{7.20}$$

such that

$$\eta = \frac{hN_{Av}}{V_m} \cdot exp\left(\frac{\sum_{quad} X_{quad}(A_{quad} + B_{quad} \cdot T)}{RT}\right) \tag{7.21}$$

Equation 7.19 can be re-written as:

$$ln(\eta \cdot V_m) = ln(hN_{Av}) + \sum_{quad} X_{quad}\left(\frac{A_{quad}}{RT}\right) + \sum_{quad} X_{quad} B_{quad}/R \tag{7.22}$$

leaving A_{quad} and B_{quad} as adjustable parameters for a linear fit of $ln(\eta \cdot V_m)$ vs. $1/T$. In melts with a common anion, G^* (Eq. 7.20) reduces to [71]:

$$G^* = \sum_{i,j} X_{ij} G^*_{ij} = \sum_{ij} X_{ij}(A_{ij} + B_{ij} \cdot T) \tag{7.23}$$

where each i and j are cations and X_{ij} is the mole fraction of $[i - X - j]$ SNN pairs. However, in melts with strong short-range ordering (SRO), a composition dependence may be introduced for the parameter G^*_{ij}, as proposed by Mizani [55], who modelled the viscosity of the NaCl-$MgCl_2$ melt over the entire composition range:

$$G^*_{ij} = (G^*_{ij})^{00} + (G^*_{ij})^{10} \cdot [x_{ii}/(x_{ii} + x_{jj} + x_{ij})] + (G^*_{ij})^{01} \cdot [x_{jj}/(x_{ii} + x_{jj} + x_{ij})] \tag{7.24}$$

In Eq. 7.24, each of $(G^*_{ij})^{00}$, $(G^*_{ij})^{10}$, and $(G^*_{ij})^{01}$ are of the form $A_{ij} + B_{ij} \cdot T$. For the halide mixtures in this work, which exhibit strong SRO, it was necessary to use the form proposed by Mizani to obtain adequate fits of the experimental data.

7.3. RESULTS AND DISCUSSION

7.3.1. THERMODYNAMIC ASSESSMENTS

LiF-ThF_4

The optimized phase diagram as calculated with the re-optimized functions for the ternary fluorides (see Section 7.2.1) is shown in Fig. 7.1 (red). The calculated phase diagram has a slightly better agreement with the liquidus data [16, 80] on the ThF_4-rich side than the previous optimization by Capelli et al. [17] from which the excess Gibbs energy parameters of the liquid solution were taken, while there is an overlap of both models on the LiF-rich portion of the phase diagram.

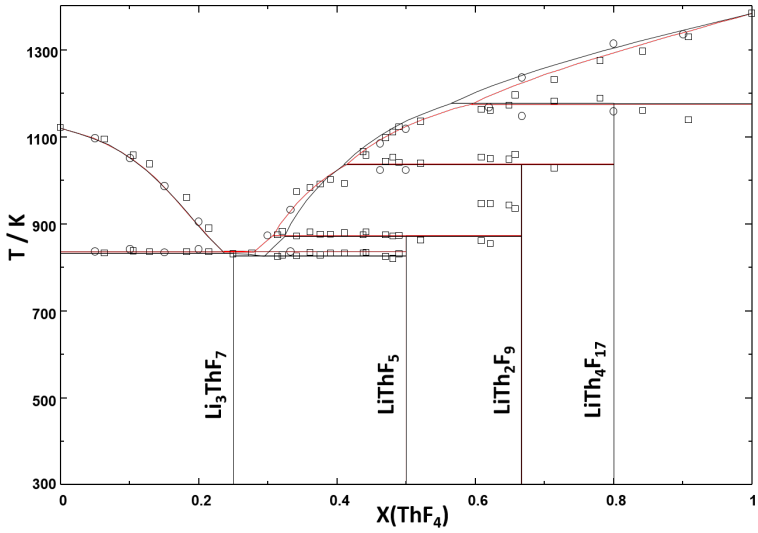

Figure 7.1: LiF-ThF_4 diagram as calculated in this work (red), overlaid with the optimization by Capelli et al. [17] (black), and the experimental data reported by Capelli et al. [16] (□) and Thoma et al. [80] (○).

LIF-UF_4

The newly optimized phase diagram is shown in Fig. 7.2 (red). Once again the parameters of the excess Gibbs energy were taken from Capelli et al. [17] (black lines) for the liquid solution. The agreement between both models is very good, the main difference being the shift from a line compound with formula $Li_7U_6F_{31}$, as was reported by Barton et al. [2] in the first study carried out on this system, to the line compound $LiUF_5$ as shown in more recent studies [42, 61].

NACL-UCL_3

The choice of $\Delta g_{AB/X}$ (Eq. 7.7) which can reproduce a phase diagram with great accuracy, together with the Gibbs energy functions of the rest of the phases in a system, is not unique. Hence, the mixing enthalpy is a very valuable property to assess experimentally as it provides a direct insight into the enthalpic part of the excess Gibbs energy of the liquid solution, and can result in a more physically realistic description. Hence, although a description of NaCl-UCl_3 using the quasi-chemical formalism already exists in the literature [6], it was updated in this study to take into account mixing enthalpy data measured by Matsuura et al. [54] (Fig. 7.3).

In addition to the mixing enthalpies, equilibrium data by Sooby et al. [77] and Kraus et al. [47] were considered during the optimization process. The calculated phase diagram is shown in Fig. 7.4. It is a simple eutectic system, with the eutectic point at X(UCl_3) = 0.33, T = (793 $\pm$ 5) K according to Kraus, and X(UCl_3) = (0.34 $\pm$ 0.02), T = (796 $\pm$ 2) K according to Sooby et al. [77]. At X(UCl_3) = 0.35, T = 796 K, the calculated eutectic point in this study closely matches the reported ones.

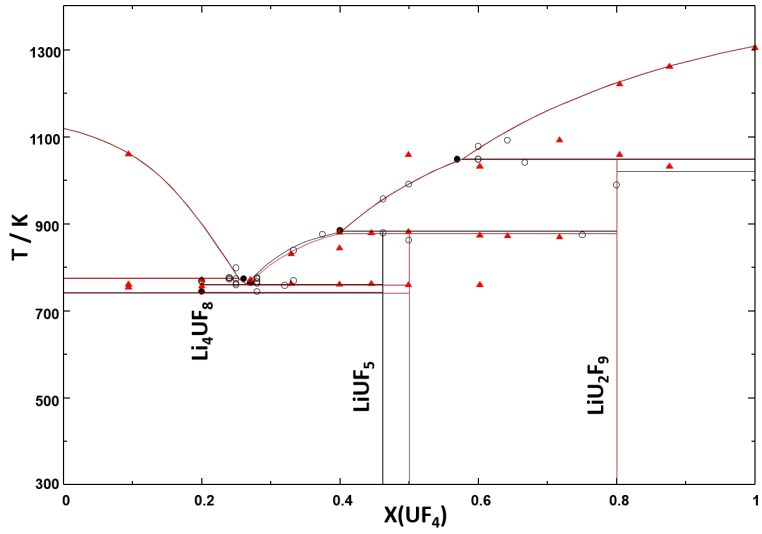

Figure 7.2: LiF-UF_4 diagram as calculated in this work (red), overlaid with the optimization by Capelli et al. [17] (black), and the experimental data reported by Ocádiz-Flores et al. [61] (▲) and Barton et al. [2] (○,●).

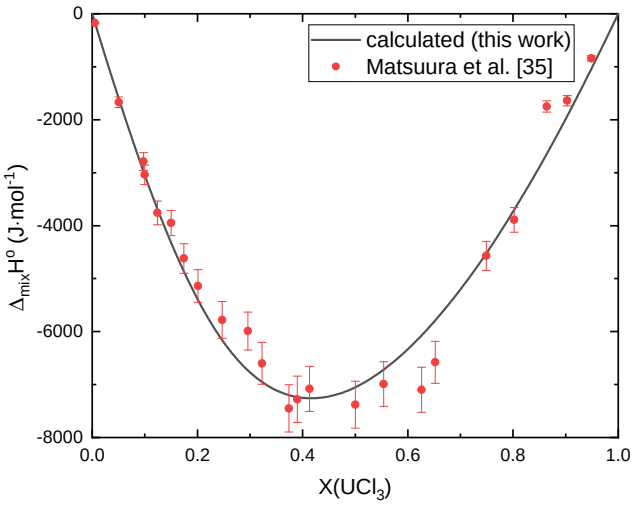

Figure 7.3: Calculated enthalpies of mixing in this study (T = 1100 K), for the NaCl-UCl_3 system, compared with the experimental data by Matsuura et al. [54].

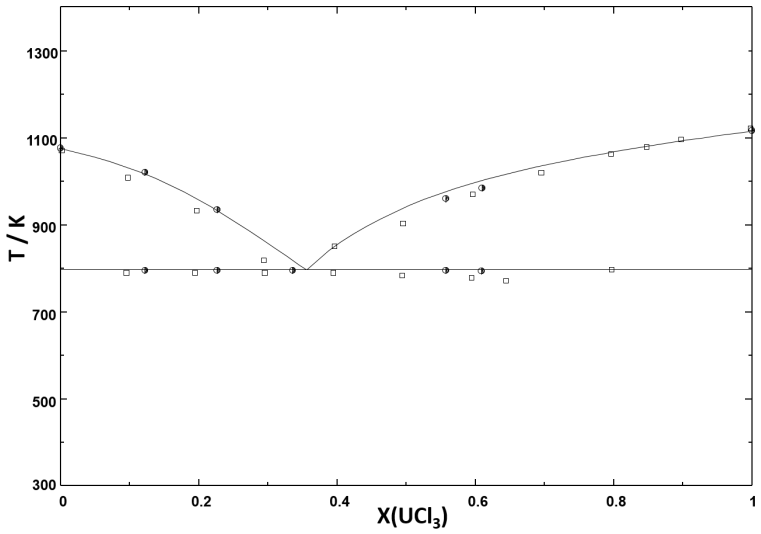

Figure 7.4: NaCl-UCl_3 phase diagram as calculated in this work, compared to experimental data by Sooby et al. [77] (◑) and Kraus [47] (□).

LiF-ThF_4-UF_4

The ternary LiF-ThF_4-UF_4 phase diagram was experimentally examined by Weaver et al. [86]. In their study, the authors found the UF_4-ThF_4 binary system to be characterized by a solid solution throughout the whole composition range, and four solid solutions were reported in the ternary domain: $Li_3(Th,U)F_7$, $Li_7(Th,U)F_{31}$, $Li(Th,U)_2F_9$, and $Li(Th,U)_4F_{17}$. No ternary stoichiometric compounds were observed, and three invariant equilibria were reported (Table 4). Based on these data, thermodynamic assessments were carried out by van der Meer et al. [83], who used a polynomial formalism for the solid and liquid solutions, and later by Beneš et al. [5], who retained a polynomial formalism for the solid solutions but introduced the modified quasi-chemical formalism for the liquid solutions.

From the LiF-ThF_4 (Fig. 7.1) and LiF-UF_4 (Fig. 7.2) binary descriptions, the solid solution $Li_7(Th,U)_6F_{31}$ reported by Weaver et al. must in fact correspond to $Li(Th,U)F_5$. As remarked by Beneš et al. [5], the choice of $LiThF_5$ over $Li_7Th_6F_{31}$ does not significantly alter the liquidus line, and the same can be seen in the LiF-UF_4 system (Fig. 7.2). However, the appearance of solid solutions does significantly alter the liquidus surface over the ternary domain [5], such that it is worthwhile to revise the ternary description with the correct solid solution. In doing so, a liquidus projection congruent with the description by Weaver et al. [86] could be retained, as can be seen in Table 4 and Fig. 7.5.

7.3.2. DENSITY AND VISCOSITY MODELS FOR THE PURE LIQUID COMPONENTS

The coefficients of the volumetric thermal expansion functions $\alpha(T)$ optimized for the pure liquid salts and their reference molar volume at 298.15 K are given in Table 5. All

Table 4: Invariant equilibria in the LiF-ThF_4-UF_4 system reported by Weaver et al. [86] and calculated in this study.

X(ThF_4)	X(LiF)	X(UF_4)	T_{calc} / K	Equilibrium	Solid phases present
			This study (calc.)		
0.213	0.641	0.146	899	Peritectic	$Li(Th,U)_2F_9$ + $Li(Th,U)_4F_{17}$ + $Li(Th,U)F_5$
0.087	0.740	0.173	777	Quasi-peritectic	$Li(Th,U)F_5$ + $Li_3(Th,U)F_7$ + LiF
0.019	0.738	0.243	759	Eutectic	$Li(Th,U)F_5$ + LiF + Li_4UF_8
			Weaver et al. [86]		
0.180	0.63	0.19	882	Peritectic	$Li(Th,U)_2F_9$ + $Li(Th,U)_4F_{17}$ + $Li(Th,U)F_5$
0.070	0.725	0.205	773	Peritectic	$Li(Th,U)F_5$ + $Li_3(Th,U)F_7$ + LiF
0.015	0.72	0.265	761	Eutectic	$Li(Th,U)F_5$ + LiF + Li_4UF_8

were derived in this work except those for NaCl, which were taken from [72]. The molar activation energies for viscous flow, G^*, as optimized in this study, are listed in Table 6.

Table 5: Molar Volume at 298.15 K and thermal expansion expressions of the pure molten halides.

Liquid salt	$V_m^{liquid}(298.15K)$ / $cm^3 \cdot mol^{-1}$	$\alpha(T)$ / K^{-1}			
LiF	12.92	$5.7407 \cdot 10^{-4}$	$-7.9134 \cdot 10^{-8} \cdot T$	$-2.4131 \cdot 10^{-1} \cdot T^{-1}$	$-1.0084 \cdot T^{-2}$
ThF_4	44.66	$9.1509 \cdot 10^{-5}$	$+1.9819 \cdot 10^{-8} \cdot T$	$+9.5286 \cdot 10^{-1} \cdot T^{-1}$	$-0.9999 \cdot T^{-2}$
UF_4	41.78	$1.0155 \cdot 10^{-4}$	$+3.0964 \cdot 10^{-8} \cdot T$	$+1.5016 \cdot 10^{-2} \cdot T^{-1}$	$-0.9997 \cdot T^{-2}$
NaCl[a]	29.56	$-0.910 \cdot 10^{-5}$	$+2.118 \cdot 10^{-7} \cdot T$	$+17.496 \cdot 10^{-2} \cdot T^{-1}$	$-37.278 \cdot T^{-2}$
UCl_3	57.41	$9.8724 \cdot 10^{-5}$	$+1.5423 \cdot 10^{-} \cdot T$	$+6.1909 \cdot 10^{-2} \cdot T^{-1}$	$-0.9998 \cdot T^{-2}$

[a] Taken from [72].

Table 6: Molar viscous activation energy for pure liquid salts.

Liquid salt	$G^* = A + B \cdot T$ / $J \cdot mol^{-1}$	
	A / $J \cdot mol^{-1}$	B / $J \cdot mol^{-1} K^{-1}$
LiF	18315.3	18.8078
ThF_4	69033.9	12.1230
UF_4	66145.1	6.7963
NaCl	28296.0	14.1019
UCl_3	21059.2	32.8274

DENSITY

The density of LiF has been measured by several authors (see Table 7), who report empirical fits of their data. The fit of the thermal expansion coefficient was made based on the empirical equation recommended by Janz in 1968 [40] in a critical literature review, as the equations reported by most of the other authors reviewed in this work cluster close to it. The calculated density is shown in Fig. 7.6a, and compared to the empirical equations available in the literature, drawn over the experimentally measured temperature

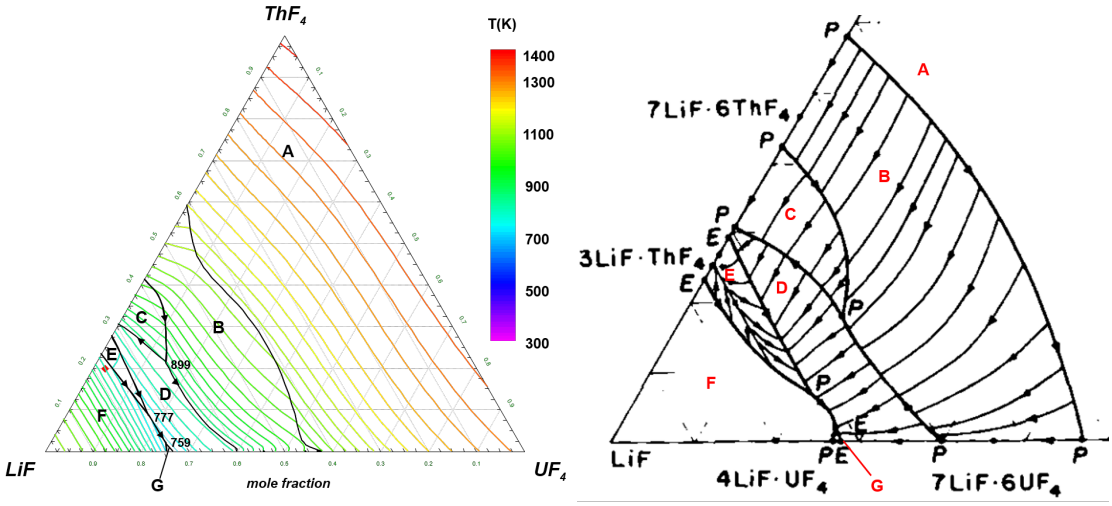

(a) (b)

Figure 7.5: (a) Calculated liquidus projection of the LiF-ThF_4-UF_4 system. Invariant equilibria are labelled with the temperatures at which they occur. Isotherms are shown every 25 K. Primary phase fields: (A) $(Th,U)F_4$; (B) $Li(Th,U)_4F_{17}$; (C) $Li(Th,U)_2F_9$; (D) $Li(Th,U)F_5$; (E) $Li_3(Th,U)F_7$; (F) LiF; (G) Li_4UF_8. $Li_{0.775}Th_{0.1995}U_{0.0255}F_{1.675}$ composition studied by Das et al. [22] and modelled in this work (see Section 7.3.4) is marked as ♦. (b) Detail of the LiF-rich corner of the phase diagram, adapted from [86], with permission from Wiley and Sons.

7

ranges. Apart from the equation by Porter and Meaker [68], which seems to underestimate the density, or that of Brown and Porter [11], which has a markedly different slope, the empirical equations of most authors agree quite well with the empirical equation recommended by Janz in 1968 [40] (derived by Yaffe and van Artsdalen [87]), and thus with the density calculated in this work (solid line, red, Fig. 7.6a).

The density of ThF_4 was first measured by Kirshenbaum and Cahill [44] in 1961, over a rather wide temperature range ranging from 1300 to ∼1650 K, using the suspender sinker mehod (Mo sinkers). A few years later Cantor et al. [13] and Hill et al. [39], both using Pt plummets, made new measurements over a narrower temperature range, which show a density ∼2% higher than that reported earlier. Kirshenbaum and Cahill [44] also examined the density of UF_4 over a similar temperature range as ThF_4, and the data were in good agreement with the empirical equation proposed by Klimenkov et al. [45]. Based on the recommendation of van der Meer and Konings [82], the density data selected for these two salts are those by Kirshenbaum and Cahill (Fig. 7.6b).

Desyatnik et al. (method of maximum bubble pressure) [26] and Cho et al. (pycnometric method) [56] measured the density of UCl_3, with widely differing results (Fig. 7.6b). Molecular dynamics simulations [62, 50, 63, 3] align more closely with the results of the former authors, so their data were taken as the basis for optimization in this work. As will be seen in section 7.3.3, this choice also works well when computing the molar volume of the NaCl-UCl_3 binary system.

Table 7: Studies of lithium fluoride density.

Reference	Method
Yaffe and van Artsdalen [87]	Archimedean, Submerged bob method
Brown and Porter [11]	Archimedean, quartz spring balance
Porter and Meaker [68]	Archimedean, quartz spring balance
Hill et al. [39]	Archimedean, Pt plummet immersion
Taniuchi and Toshiharo [79]	Archimedean, Pt plummet immersion
Matiasovsky et al. [41]	Archimedean
Smirnov and Stepanov [75]	Maximum bubble pressure, Pt capillary
Klimenkov et al. [45]	Maximum bubble pressure, Ni capillary
Hara and Ogino [36]	Archimedean, Pt plummet immersion
Chekhovskoi [19]	Archimedean, Mo plummet immersion

VISCOSITY

Several experimentally derived fits describing the viscosity of LiF as a function of temperature are found in the literature [24, 20, 25, 74, 84], although only Ejima et al. [30] and Abe et al. [1] explicitly report their experimental points. Both groups used an oscillating vessel viscometer, and their data are in excellent agreement with each other, as is the viscosity computed with the model (Fig. 7.7). The agreement with the empirical fit derived by Chervinskii et al. [20], who most likely[1] used the rotational oscillation of a liquid-filled cylindrical crucible, is also very good.

Following the recommendation of Janz et al. [40], the viscosity of NaCl was modelled after the empirical fit derived by Murgulescu and Zuca (oscillating sphere method) [59] based on their measurements. The fit derived by Desyatnik et al. (damped rotational oscillations) [26], correlates very well with the reference values. For each of the three actinide halide end-members there is only one study available. Desyatnik et al. [26] studied the viscosity of UCl_3 in the range 1128-1278 K. Desyatnik et al. [24] measured the viscosity of UF_4 in the range 1324-1428 K. Both studies used the method of damped rotational oscillations. Finally, Chervinskii et al. [20] measured the viscosity of ThF_4, probably using the same method[2]). The empirical fits to the data in each of the studies could all be modelled successfully (Fig. 7.7).

7.3.3. DENSITY AND VISCOSITY MODELS FOR THE BINARY SYSTEMS

Pressure-dependent contributions to the excess Gibbs energy of mixing (Eq. 7.6) needed to be optimized for the NaCl-UCl_3 system only:

$$\Delta g^{P}_{NaU/Cl} = (0.4945 - 0.505\chi_{NaU/Cl} - 0.5046\chi_{UNa/Cl}) \cdot (P - p^{o}) \ J \cdot mol^{-1} \qquad (7.25)$$

[1] Original work not available to us, but results summarized in [27].

[2] Original work was not available to us, but the results were summarized in [27].

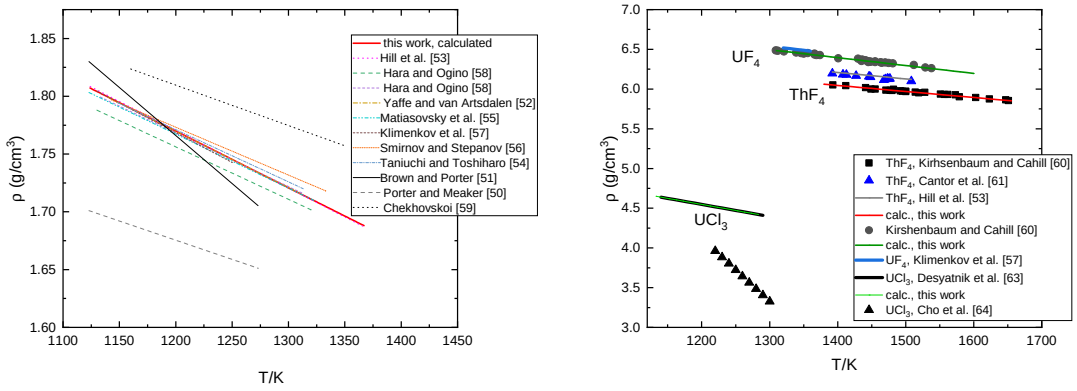

(a) (b)

Figure 7.6: Calculated densities of the end-members ((a) LiF, (b) actinide halide end-members) compared to empirical fits (lines) and experimental data (symbols) reported in the literature.

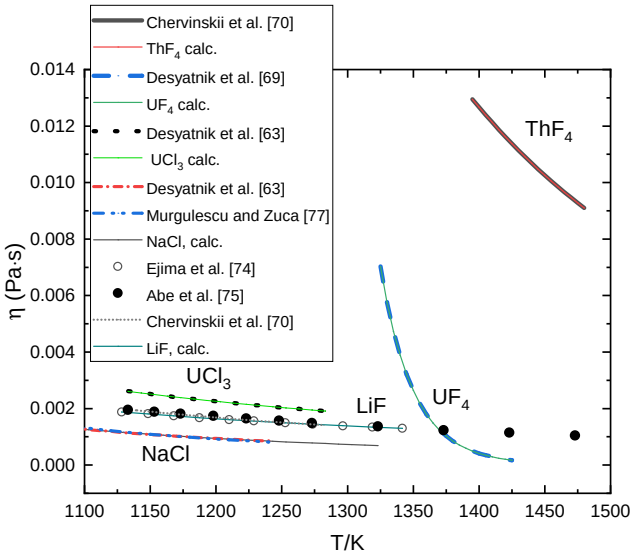

Figure 7.7: Calculated viscosities of the pure liquid end-members, compared to empirical fits (solid and dashed lines) and experimental data (●, ○) reported in the literature.

The optimized molar activation energies for viscous flow, G^*_{ij} (Eq. 7.24), are listed in Table 8.

Table 8: Molar viscous activation energy for liquid binary mixtures.

System		G^{00}_{ij}	G^{10}_{ij}	G^{01}_{ij}
LiF-ThF_4	A_{ij}	29011.0	9269.1	-13275.4
	B_{ij}	23.5862	7.5359	-10.8
LiF-UF_4	A_{ij}	24738.7	6254.0	-14161.7
	B_{ij}	20.1127	5.0845	-11.5136
NaCl-UCl_3	A_{ij}	27157.8	-3734.7	
	B_{ij}	22.0795	-3.0363	

A_{ij} in $J \cdot mol^{-1}$, B_{ij} in $J \cdot mol^{-1}K^{-1}$.

DENSITY

The densities of LiF-ThF_4 mixtures were measured by Brown and Porter [11] and Porter and Meaker [68] using a quartz spring balance. Hill et al. [39] also performed measurements using a similar method, with a Pt plummet; there is a good correlation between the datasets (Fig. 7.8a). All authors observed additivity. The ideal behavior of the density can be seen clearly when the molar volumes are plotted: there is a linear dependence with respect to the composition (Fig. 7.8b). The same holds true in LiF-UF_4 mixtures, which were also measured by Brown and Porter [11], as well as Blanke et al (Pt plummet) [9]. Klimenkov et al. [45], who used the method of maximum pressure in a gas bubble, found only very slight positive deviations from ideality in this system. Ideal behavior was retained in this work.

Fig. 7.9 shows the excess molar volumes, calculating the ideal behavior (dotted line) from the volumes of the end-members in the corresponding study (estimated from linear fits when not available). The molar volume of NaCl-UCl_3 mixtures, measured by Mochinaga et al. (pycnometric method) [21] as well as Desyatnik et al. (method of maximum bubble pressure) [26], show a greater deviation from ideality than the tetrafluoride-based melts. This had to be accounted for by introducing pressure-dependent parameters in the excess Gibbs free energy (Eq. 7.25). This larger deviation from ideality is probably related to a partial loss of ionic character and increased covalency in the melt [26]. In other words, the formation of molecular ions probably contributes to the free volume. There is spectroscopic evidence of such oligomerisation taking place in LiCl-UCl_3 melts [85], and NaCl-UCl_3 behaves similarly according to MD simulations [62, 50, 63, 3]. Incidentally, so do LiF-AnF_4 (An = Th, U) melts [27, 7, 76, 61], yet the smaller volume of Li^+, better suited to occupy interstitial spaces, may explain the difference.

VISCOSITY

Fig. 7.10a shows the isothermal viscosities of the three salt fuel systems at a representative temperature of 1230 K, computed with the model described herein and with the

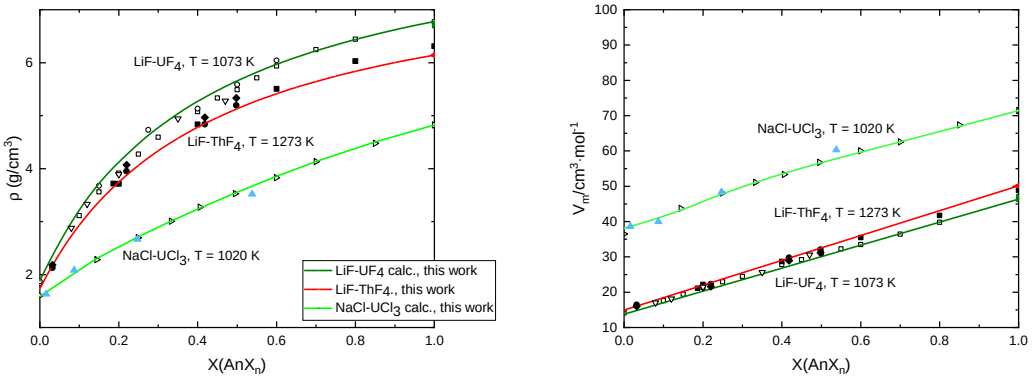

(a) (b)

Figure 7.8: (a) Calculated densities and (b) molar volumes of the binary mixtures compared to empirical equations and experimental data reported in the literature. LiF-UF_4: Klimenkov et al. [45] ▫, Brown and Porter [11] ○, Blanke et al. [9] ▽; LiF-ThF_4: Hill et al. [39] ■, Brown and Porter [11] ♦, Porter and Meaker [68] ●; NaCl-UCl_3: Desyatnik et al. [26] ▷, Mochinaga et al. [56] ▲.

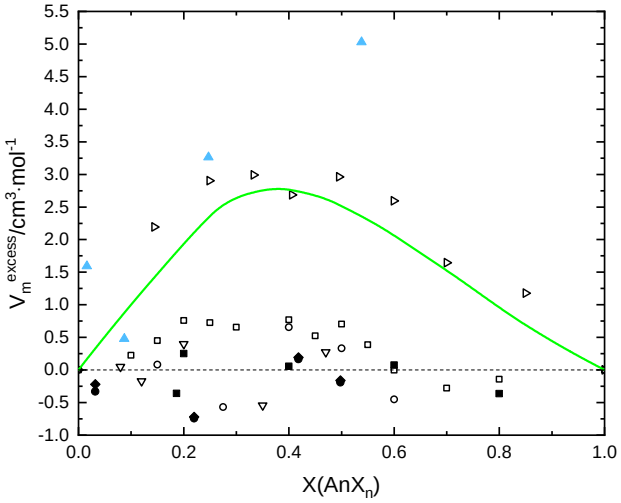

Figure 7.9: Excess molar volumes of the binary mixtures: LiF-UF_4 at T =1073 K, LiF-ThF_4 at T = 1273 K, NaCl-UCl_3 at T = 1020 K. Ideal behavior (dotted line), is calculated using the molar volumes of the end-members from the corresponding study, estimated from linear fits when not available. Green solid line: NaCl-UCl_3, this work. LiF-UF_4: Klimenkov et al. [45] ▫, Brown and Porter [11] ○, Blanke et al. [9] ▽; LiF-ThF_4: Hill et al. [39] ■, Brown and Porter [11] ♦, Porter and Meaker [68] ●; NaCl-UCl_3: Desyatnik et al. [26] ▷, Mochinaga et al. [56] ▲.

experimentally derived fits found in the literature, with quite a good agreement. All three melts become "polymeric" (there is network formation and short-range ordering) when the actinide halide concentration is high enough [27, 7, 76, 61, 62, 50, 63, 3], and the increase in viscosity with increasing actinide content is related to a greater extent of formation of associated structures [27]. The tetrafluoride-based melts are more viscous than the trichloride one, as the actinide halide end-members themselves (Fig. 7.7). This can be attributed to the greater ionic character of the tetrafluoride melts. In molten salts, cations carry anions with them as they diffuse [28, 38, 73]. In the tetrafluoride melts, the average An-F distance is ∼2.32-2.34 Åfor An = Th, and ∼2.26-2.28 for An= U according to X-ray Absorption spectroscopy (XAS) and MD simulations [60]. In NaCl-UCl_3, MD simulations show and average U-Cl distance of around 2.8 Å [50], in good agreement with X-ray diffraction (XRD) measurements [62]. This suggests fluorides are bound more tightly than the chlorides around the actinide center to which they are coordinated, contributing to a greater viscosity.

Fig. 7.10a shows the isomolar viscosities as a function of temperature, at compositions close to the equilibria in the different systems: X(ThF_4) = 0.30, X(UF_4) = 0.275, and X(UCl_3) = 0.30. The agreement is better at higher temperatures. NaCl-UCl_3 has the best agreement throughout both the isomolar and isothermal sections, since the viscosities of the end-members are closer to each other.

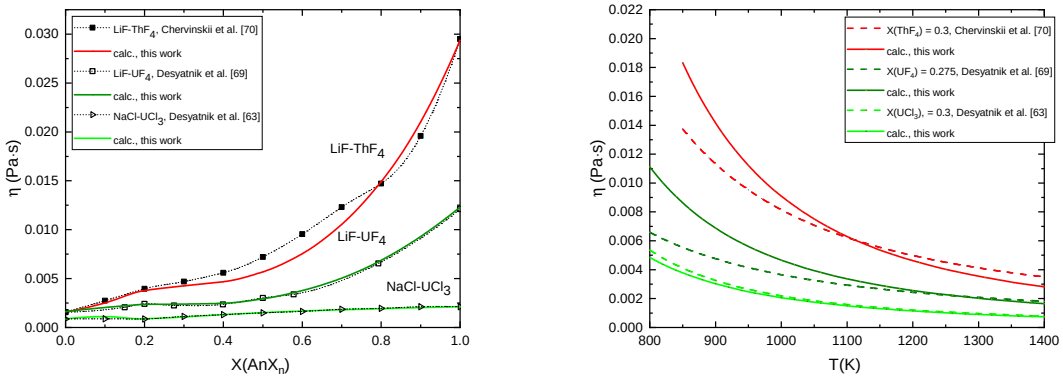

(a) (b)

Figure 7.10: (a) Isothermal (T = 1230) viscosities and (b) isomolar viscosities of the binary mixtures computed with the present thermodynamic models and with empirical fits reported in the literature.

7.3.4. DENSITY AND VISCOSITY MODELS OF THE LIF-ThF_4-UF_4 TERNARY SYSTEM

Only one composition has been studied for both density and viscosity, corresponding to fresh MSR fuel: $Li_{0.775}Th_{0.1995}U_{0.0255}F_{1.675}$, by Das et al. [22] (Fig. 7.5a, ♦). The authors studied the density over the 843-943 K temperature range using the Archimedean

method with a Pt sinker and wire, while the viscosity was studied over the range 873-931 K using the parallel plate method. The optimized molar activation energies for viscous flow, G^*_{ij} (Eq. 7.24), are listed in Table 9.

Table 9: Molar viscous activation energy for the liquid ternary solution LiF-ThF_4-UF_4.

System		G^{00}_{ThU}	G^{10}_{ThU}	G^{01}_{ThU}
LiF-ThF_4-UF_4	A_{ThU}	-11334638	15800299	
	B_{ThU}	723.267		

A in $J \cdot mol^{-1}$, B in $J \cdot mol^{-1}K^{-1}$.

The empirical equation for the molar volume of $Li_{0.775}Th_{0.1995}U_{0.0255}F_{1.675}$ derived by Das et al. is plotted in Fig. 7.11 (red dotted line). The molar volume falls between that of the pure end-members, although there is a large excess compared to ideal behavior (light green), itself practically identical to the molar volume of the $Li_{0.775}Th_{0.255}F_{1.675}$ solution, and slightly higher than that of the $Li_{0.775}U_{0.255}F_{1.675}$ solution. Like the LiF-based binaries, ThF_4-UF_4 is expected to form an ideal liquid solution –the phase diagram can be modelled successfully by treating the melt as such [5]. The ternary phase diagram can also be modelled successfully without any excess ternary terms, see Section 7.2.1, and it is difficult to explain why the molar volumes of the ternary mixture should deviate so much, if at all, from ideality. Thus, for the subsequent calculation of the viscosity, an ideal molar volume has been retained. For the viscosity computation, only the G^{00}_{ThU} and G^{10}_{ThU} terms, associated with the Th-U quadruplets, needed to be optimized, with good results (Fig. 7.12). More compositions, preferably richer in UF_4, would need to be measured to evaluate the robustness of this model.

7.4. CONCLUSIONS

Building up from the descriptions of the pure end-members, the density and viscosity of three key binary systems for MSR technology have been modelled: LiF-ThF_4, LiF-UF_4, and NaCl-UCl_3. The density and viscosity of a composition belonging to the LiF-ThF_4-UF_4 ternary system, $Li_{0.775}Th_{0.1995}U_{0.0255}F_{1.675}$, have been modelled as well. All are linked to the corresponding thermodynamic assessments via the distribution of the quadruplet fractions, and the viscosities further depend on the densities. The agreement between the computed values and empirical fits (based on experimental data) is generally very good, although there is a clear need for more data, particularly in the ternary composition space, to further validate and re-parametrize the models as needed. The quasi-chemical model has become a widely used formalism in the description of molten salts, and the number of systems assessed is already substantial [4, 14]. Thus, expanding databases of molten salt fuels beyond the thermodynamic properties, e.g. with density and viscosity parameters as herein, promises to be a powerful addition to the toolbox for MSR development.

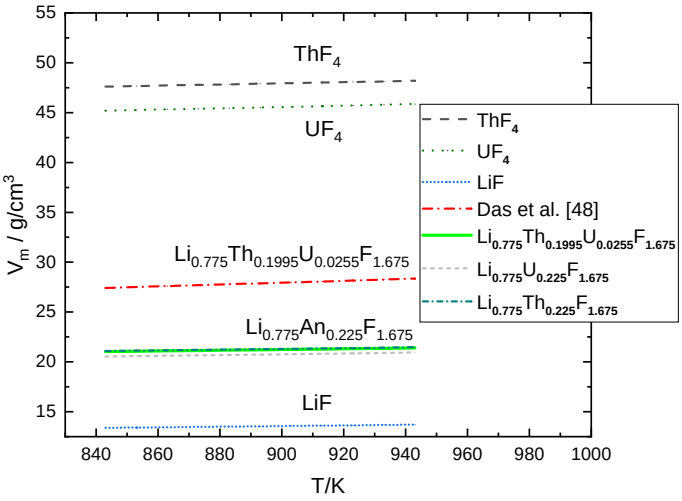

Figure 7.11: Molar volume of the $Li_{0.775}Th_{0.1995}U_{0.0255}F_{1.675}$ melt as detrmined experimentally [22] (red line), compared to the calculated (ideal) behavior, the end-members, and the ideal behavior predicted for the $Li_{0.775}An_{0.225}F_{1.675}$ (An = ThF_4, UF_4) binary mixtures with the present thermodynamic models.

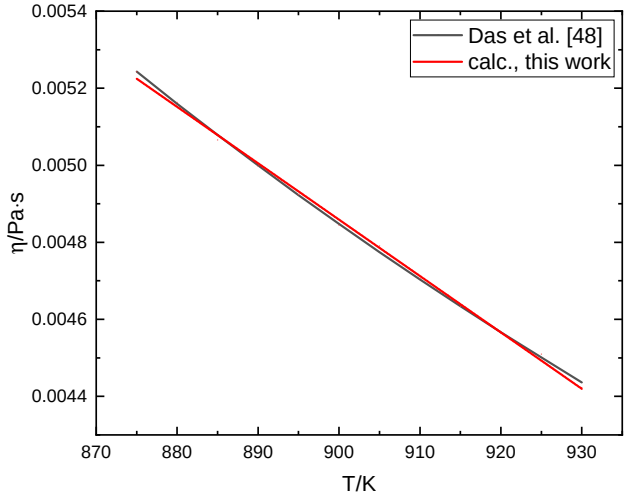

Figure 7.12: Evolution of the viscosity with temperature, at composition $Li_{0.775}Th_{0.1995}U_{0.0255}F_{1.675}$, as reported by Das et al. [22], compared to the values computed in this work.

7.5. ACKNOWLEDGEMENTS

A.L. Smith acknowledges financial support from the Netherlands Organisation for Scientific Research (NWO) (project 722.016.005). J.A. Ocádiz-Flores acknowledges the European Nuclear Education Network for supporting this work in the framework of the ENEN+ Project (mobility grant A-041841711), as well as CONACYT-SENER for financial support.

BIBLIOGRAPHY

[1] Y. Abe, O. Kosugiyama, and A. Nagashima. "Viscosity of LiF-BeF_2 eutectic mixture ($XBeF_2$= 0.328) and LiF single salt at elevated temperatures". In: *Journal of Nuclear Materials* 99.2-3 (1981), pp. 173–183.

[2] C.J. Barton et al. "Phase Equilibria in the Alkali Fluoride-Uranium Tetrafluoride Fused Salt Systems: I, The Systems LiF-UF4 and NaF-UF4". In: *Journal of the American Ceramic Society* 41.2 (1958), pp. 63–69.

[3] A.A. Baty. "Molecular Dynamics Simulation of the Transport Properties of Molten Transuranic Chloride Salts". PhD thesis. Texas A & M, 2013.

[4] O. Beneš. "Thermodynamics of molten salts for nuclear applications". PhD thesis. Institute of Chemical Technology, Prague, 2008.

[5] O. Beneš, M. Beilmann, and R.J.M. Konings. "Thermodynamic assessment of the LiF–NaF–ThF_4–UF_4 system". In: *Journal of Nuclear materials* 405.2 (2010), pp. 186–198.

[6] O. Beneš and R.J.M. Konings. "Thermodynamic evaluation of the NaCl–MgCl2–UCl3–PuCl3 system". In: *Journal of nuclear materials* 375.2 (2008), pp. 202–208.

[7] C. Bessada et al. "Investigation of ionic local structure in molten salt fast reactor LiF-ThF4-UF4 fuel by EXAFS experiments and molecular dynamics simulations". In: *Journal of Molecular Liquids* 307 (2020), p. 112927.

[8] E. S. Bettis et al. "The aircraft reactor experiment—design and construction". In: *Nuclear Science and Engineering* 2.6 (1957), pp. 804–825.

[9] B.C. Blanke et al. "Density and molar volumes of binary fluoride mixtures". In: *Technical Report USAEC MLM-1086* (1956).

[10] R.C. Briant and A.M. Weinberg. "Molten fluorides as power reactor fuels". In: *Nuclear science and engineering* 2.6 (1957), pp. 797–803.

[11] E.A. Brown and B. Porter. *Electrical Conductivity and Density of Molten Systems of Uranium Tetrafluoride and Thorium Fluoride and Alkali Fluorides*. Vol. 6500. US Department of the Interior, Bureau of Mines, 1964.

[12] J.J. Bulmer and U.S. Atomic Energy Commission. *Fused Salt Fast Breeder: Reactor Design and Feasibility Study*. CF (Series). United States Atomic Energy Commission, Technical Information Service Extension, 1957.

[13] S. Cantor, D.G. Hill, and W.T. Ward. "Density of molten ThF4: Increase of density on melting". In: *Inorganic and Nuclear Chemistry Letters* 2.1 (1966), pp. 15–18.

[14] E Capelli. "Thermodynamic characterization of salt components for Molten Salt Reactor fuel". PhD thesis. Delft University of Technology, 2016.

[15] E. Capelli and R.J.M. Konings. “Halides of the Actinides and Fission Products Relevant for Molten Salt Reactors”. In: *Comprehensive Nuclear Materials*. Elsevier, 2020.

[16] E. Capelli et al. “"Thermodynamic investigation of the LiF–ThF_4 system "”. In: *The Journal of Chemical Thermodynamics* 58 (2013), pp. 110–116.

[17] E. Capelli et al. “Thermodynamic assessment of the LiF–NaF–BeF_2–ThF_4–UF_4 system”. In: *Journal of Nuclear Materials* 449.1-3 (2014), pp. 111–121.

[18] M.W. Chase. *NIST-JANAF Thermochemical Tables (Journal of Physical and Chemical Reference Data Monograph No. 9)*. 1998.

[19] V.Y. Chekhovskoi. “A device for measuring the density and surface tension of melts”. In: *Instruments and Experimental Techniques* 43.3 (2000), pp. 415–418.

[20] Y.F. Chervinskii, V.N. Desyatnik, and A.I. Nechaev. “Molar Viscosity of Lithium and Thorium Fluoride Melted Mixtures”. In: *Zhurnal Fizicheskoi Khimii* 56.8 (1982), pp. 1946–1949.

[21] K. Cho et al. “Densities and equivalent conductivities of molten uranium trichloride-sodium chloride and uranium trichloride-(potassium chloride-sodium chloride eutectic) systems”. In: *J. Electrochem. Soc. Japan* 37.9 (1969), pp. 658–661.

[22] P. Das et al. “Thermodynamic and Physical Properties of Molten LiF-ThF4-UF4 Salts Mixture”. In: *Journal of Fluorine Chemistry* 226 (2019), p. 109349.

[23] R. Dawson, E.B. Brackett, and T.E. Brackett. “A high temperature calorimeter; the enthalpies of α-aluminum oxide and sodium chloride”. In: *The Journal of Physical Chemistry* 67.8 (1963), pp. 1669–1671.

[24] V.N. Desyatnik, A.I. Nechaev, and Y.F. Chervinskii. “Viscosities of molten mixtures of uranium tetrafluoride with alkali fluorides”. In: *Soviet Atomic Energy* 46.5 (1979), pp. 408–409.

[25] V.N. Desyatnik, A.I. Nechaev, and Y.F. Chervinskii. “Viscosity of fused mixtures of beryllium fluoride with lithium and sodium fluorides”. In: *Journal of Applied Chemistry of the USSR* 54.10 (1981), pp. 2035–2037.

[26] VN Desyatnik et al. “Density, surface tension, and viscosity of uranium trichloride-sodium chloride melts”. In: *Soviet Atomic Energy* 39.1 (1975), pp. 649–651.

[27] L. Dewan. “Molecular dynamics simulation and topological analysis of the network structure of actinide-bearing materials”. PhD thesis. Massachusetts Institute of Technology, 2013.

[28] L.C. Dewan et al. “Molecular dynamics simulation of the thermodynamic and transport properties of the molten salt fast reactor fuel LiF–ThF4”. In: *Journal of Nuclear Materials* 434.1 (2013). Special Section on Spent Nuclear Fuel, pp. 322–327. ISSN: 0022-3115.

[29] T.J. Dolan. *Molten salt reactors and thorium energy*. Woodhead Publishing, 2017.

[30] T. Ejima et al. “Viscosity of Molten Alkali Fluorides”. In: *Nippon Kinzoku Gakkai-si* 51.4 (1987), pp. 328–337.

[31] H. Eyring. *Statistical mechanics and dynamics*. Wiley, 1964.

[32] H. Eyring, D. Henderson, and T. Ree. "Thermodynamic and transport properties of liquids". In: *Progress in International Research on Thermodynamic and Transport Properties*. Elsevier, 1962, pp. 340–351.

[33] *GIF, Annual report 2013, Generation IV International Forum, Tech. Rep., www.gen-4.org/gif/upload/docs/application/pdf/2014-06/gif_2013_annual_report-final.pdf*. 2013.

[34] S. Glasstone, K. J Laidler, and H. Eyring. *The theory of rate processes*. McGraw-hill, 1941, pp. 480–484.

[35] V.P. Glushko et al. "The IVTAN Data Bank on the Thermodynamic Properties of Individual Substances". In: (1978).

[36] S. Hara and K. Ogino. "The densities and the surface tensions of fluoride melts". In: *ISIJ International* 29.6 (1989), pp. 477–485.

[37] L.-Y. He et al. "Effect of ^{37}Cl enrichment on neutrons in a molten chloride salt fast reactor". In: *Nuclear Science and Techniques* 31.3 (2020), pp. 1–12.

[38] R.J. Heaton et al. "A first-principles description of liquid BeF_2 and its mixtures with LiF: 1. Potential development and pure BeF_2". In: *The Journal of Physical Chemistry B* 110.23 (2006), pp. 11454–11460.

[39] D.G. Hill, S. Cantor, and W.T. Ward. "Molar volumes in the LiF ThF4 system". In: *Journal of Inorganic and Nuclear Chemistry* 29.1 (1967), pp. 241–243.

[40] G.J. Janz et al. *Molten salts: Volume 1. Electrical conductance, density, and viscosity data*. 1968.

[41] G.J. Janz et al. "Molten salts: volume 4, Part 1, fluorides and mixtures electrical conductance, density, viscosity, and surface tension data". In: *Journal of Physical and Chemical Reference Data* 3.1 (1974), pp. 1–115.

[42] Y. Jeongho et al. "Mild hydrothermal crystal growth, structure, and magnetic properties of ternary U (IV) containing fluorides: $LiUF_5$, KU_2F_9, $K_7U_6F_{31}$, $RbUF_5$, RbU_2F_9, and RbU_3F_{13}". In: *Inorganic Chemistry* 53.12 (2014), pp. 6289–6298.

[43] JRC-Karlsruhe. *JRCSMSD thermodynamic database on halide salts*. 2020.

[44] A.D. Kirshenbaum and J.A. Cahill. "The density of molten thorium and uranium tetrafluorides". In: *Journal of inorganic and nuclear chemistry* 19.1-2 (1961), pp. 65–68.

[45] A.A. Klimenkov et al. "Density and surface tension of molten mixtures of uranium tetrafluoride with lithium and sodium fluorides". In: *Atomic Energy* 56.5 (1984), pp. 339–341.

[46] R.J.M. Konings, J.P.M. Van der Meer, and E. Walle. "Chemical Aspects of Molten Salt Reactor Fuel". In: *European Commission Joint Research Centre* (2005).

[47] C. Kraus. *Phase Diagram of Some Complex Salts of Uranium with Halides of the Alkali and Alkaline Earth Metals*. Tech. rep. Naval Research Laboratory, 1943.

[48] J.A. Lane, H.G. MacPherson, and F. Maslan. *Fluid Fuel Reactors: Molten Salt Reactors, Aqueous Homogeneous Reactors, Fluoride Reactors, Chloride Reactors, Liquid Metal Reactors and Why Liquid Fission*. Addison-Wesley Pub. Co., 1958.

[49] J. Leitner et al. “Application of Neumann–Kopp rule for the estimation of heat capacity of mixed oxides”. In: *Thermochimica Acta* 497.1-2 (2010), pp. 7–13.

[50] B. Li, S. Dai, and D. Jiang. “Molecular dynamics simulations of structural and transport properties of molten NaCl-UCl3 using the polarizable-ion model”. In: *Journal of Molecular Liquids* 299 (2020), p. 112184.

[51] M. Lin, M.-S. Cheng, and Z.-M. Dai. “Feasibility of an innovative long-life molten chloride-cooled reactor”. In: *Nuclear Science and Techniques* 31.4 (2020), pp. 1–15.

[52] E.M. Lucotte. *Flexibility, features and advantages of Molten Salt Reactors*. 2020. URL: https://www.iaea.org/nptd-webinars/4-molten-salt-reactors-a-game-changer-in-the-Nuclear-industry.

[53] H. G. MacPherson. “The Molten Salt Reactor Adventure”. In: *Nuclear Science and Engineering* 90.4 (1985), pp. 374–380.

[54] H. Matsuura et al. “Enthalpies of mixing in molten UCl_3-NaCl system”. In: *Journal of Nuclear Science and Technology* 39.sup3 (2002), pp. 632–634.

[55] S. Mizani. *Modeling the viscosity of liquid solutions used in aluminum alloys production*. ProQuest, 2008.

[56] J. Mochinaga et al. “Densities and equivalent conductivities of molten uranium trichloride and uranium trichloride-potassium chloride systems”. In: *J. Electrochem. Soc. Japan* 37.9 (1969), pp. 654–658.

[57] S. Mukherjee and S. Dash. “Determination of Gibbs energy of formation of $LiThF_5$, $LiTh_2F_9$, and $LiTh_4F_{17}$ in Li-Th-F system by using solid electrolyte galvanic cell”. In: *Journal of Solid State Electrochemistry* 23.11 (2019), pp. 3043–3056.

[58] I.G. Murgulescu et al. “Heat Capacities in Molten Alkaline Halides”. In: *Rev. Roumaine Chim.* 22.5 (1977), pp. 683–689.

[59] I.G. Murgulescu and S. Zuca. In: *Zeitschrift für Physikalische Chemie* 222.300 (1963).

[60] J.A. Ocádiz-Flores et al. “Examination of the short-range structure of molten salts: ThF_4, UF_4, and related alkali actinide fluoride systems”. In: *Phys. Chem. Chem. Phys.* 23 (18 2021), pp. 11091–11103.

[61] J.A. Ocádiz-Flores et al. “New insights and coupled modelling of the structural and thermodynamic properties of the LiF-UF_4 system”. In: *Journal of Molecular Liquids* 331 (2021), p. 115820.

[62] Y. Okamoto, P.A. Madden, and K. Minato. “X-ray diffraction and molecular dynamics simulation studies of molten uranium chloride”. In: *Journal of nuclear materials* 344.1-3 (2005), pp. 109–114.

[63] G.I.L van Oudenaren. “Advanced modelling of chloride salt systems for use in molten salt reactor fuels”. PhD thesis. Delft University of Technology, 2020.

[64] G.I.L. van Oudenaren, J.A. Ocádiz-Flores, and Smith A.L. “Coupled structural modelling of the molten salt system NaCl-UCl_3”. Submitted. 2021.

[65] A. D. Pelton et al. “"The modified quasichemical model I—Binary solutions"”. In: *Metallurgical and Materials Transactions B* 31.4 (2000), pp. 651–659.

[66] A.D. Pelton. “A general “geometric” thermodynamic model for multicomponent solutions”. In: *Calphad* 25.2 (2001), pp. 319–328.

[67] W. Plato. “Erstarrungserscheinungen an anorganischen Salzen und Salzgemischen. I.” In: *Zeitschrift für Physikalische Chemie* 55.1 (1906), pp. 721–737.

[68] B. Porter and R.E. Meaker. “Density and molar volumes of binary fluoride mixtures”. In: *Technical Report BMI RI-6836* (1966).

[69] B.C. Pyashyenko. In: *Metallurgiya* 10.11 (1935), p. 85.

[70] C. Robelin and P. Chartrand. “A Density Model Based on the Modified Quasichemical Model and Applied to the NaF-AlF_3-CaF_2-Al_2O_3 Electrolyte”. In: *Metallurgical and Materials Transactions B* 38.6 (2007), pp. 881–892.

[71] C. Robelin and P. Chartrand. “A viscosity model for the (NaF+ AlF_3+ CaF_2+ Al_2O_3) electrolyte”. In: *The Journal of Chemical Thermodynamics* 43.5 (2011), pp. 764–774.

[72] C. Robelin, P. Chartrand, and G. Eriksson. “A Density Model for Multicomponent Liquids Based on the Modified Quasichemical Model: Application to the NaCl-KCl-$MgCl_2$-$CaCl_2$ System”. In: *Metallurgical and Materials Transactions B* 38.6 (2007), pp. 869–879.

[73] M. Salanne et al. “Conductivity- Viscosity- Structure: Unpicking the Relationship in an Ionic Liquid”. In: *The Journal of Physical Chemistry B* 111.18 (2007), pp. 4678–4684.

[74] M.V. Smirnov et al. “unknown”. In: *Zh. Fiz. Khim.* 48.11 (1974), p. 467.

[75] MV Smirnov and VP Stepanov. “Density and surface tension of molten alkali halides and their binary mixtures”. In: *Electrochimica Acta* 27.11 (1982), pp. 1551–1563.

[76] A.L. Smith et al. “In situ high-temperature EXAFS measurements on radioactive and air-sensitive molten salt materials”. In: *Journal of synchrotron radiation* 26.1 (2019), pp. 124–136.

[77] E.S. Sooby et al. “Measurements of the liquidus surface and solidus transitions of the NaCl–UCl3 and NaCl–UCl3–CeCl3 phase diagrams”. In: *Journal of Nuclear Materials* 466 (2015), pp. 280–285.

[78] M. Stika. “Actinide Concentration Monitoring and Extraction from Molten Fluoride and Chloride Salts”. PhD thesis. The University of Utah, 2017.

[79] Kentaro Taniuchi and Toshiharu Kanai. “Densities of Molten Salts of Some Binary Fluoride Systems Containing Lithium Fluoride”. In: *Science Reports of the Research Institutes Tohoku University Series A-Physics, Chemistry and Metallurgy* 26.6 (1977), pp. 333–343.

[80] R.E. Thoma. *Phase diagrams of nuclear reactor materials*. Vol. 2548. Oak Ridge National Laboratory, 1959.

[81] A. Tosolin et al. “Isobaric Heat Capacity of Solid and Liquid Thorium Tetrafluoride”. In: *Journal of Chemical & Engineering Data* 64.9 (2019), pp. 3945–3950.

[82] J.P.M. Van der Meer and R.J.M. Konings. “Thermal and physical properties of molten fluorides for Nuclear applications”. In: *Journal of Nuclear Materials* 360.1 (2007), pp. 16–24.

[83] J.P.M. Van der Meer, R.J.M. Konings, and H.A.J. Oonk. “Thermodynamic assessment of the LiF–BeF_2–ThF_4–UF_4 system”. In: *Journal of Nuclear Materials* 357.1-3 (2006), pp. 48–57.

[84] M.M. Vetyukov and G.I. Sipriya. “unknown”. In: *J. Appl. Chem (USSR)* 36 (1962), p. 1905.

[85] V.A. Volkovich et al. “Uranium Speciation in Molten Salts from X-Ray Absorption and Electronic Absorption Spectroscopy Measurements”. In: *Special Publication-Royal Society of Chemistry* 305.1 (2006), pp. 485–490.

[86] C.F. Weaver et al. “Phase Equilibria in the Systems UF_4-ThF_4 and LiF-UF_4-ThF_4”. In: *Journal of the American Ceramic Society* 43.4 (1960), pp. 213–218.

[87] I.S. Yaffe and E.R. van Artsdalen. “Fused Salts. Electrical conductance and density of fused halides.-Chemistry Division Semiannual Progress Report, Oak Ridge National Laboratory, ORNL-2159”. In: (1956).

8

CONCLUSIONS AND RECOMMENDATIONS

Phase diagrams are the beginning of wisdom
–not the end of it [17].

Sir William Hume-Rothery

8.1. GENERAL TRENDS IN STRUCTURAL AND THERMOCHEMICAL PROPERTIES OF MOLTEN SALTS

This dissertation is an investigation of elementary features of actinide-bearing molten salt systems: structure, phase equilibria, thermophysical properties, and the relationship between them. Let us begin then with a general account. As crystals, actinide fluorides form a 3-D network [13] with long-range ordering. UF_4 and ThF_4 in particular form a network of 8-coordinated An cages [9]. The picture that emerges from this work is that upon melting, these coordination environments remain, except that the thermal disorder results in decreased repulsion between the fluorides, accompanied by bond contraction and a lowering of the coordination number from 8 to 7 and 6. At the same time, the high temperature makes the coordination numbers 9 and, to a much lesser extent 10, accessible as well. To maintain the high coordination numbers, fluorides are shared between actinide centers, and so the melt remains a 3-dimensional network at short range. This network can be described as a polymer, certainly not in the organic chemistry sense, but from a statistical viewpoint: at any given time there are chains of several fluoride-bridged actinide centers. The ease with which these inter-actinide bonds are broken is evidenced by the relatively low viscosity of the actinide fluoride salts.

Addition of alkali fluorides disrupts the network, a process which is enthalpically favourable as shown by the negative mixing enthalpies at all compositions. At a given point, which for melts containing LiF and NaF is close to 40 mol% AnF_4, the degree of polymerization rapidly decreases, as the concentration of AnF_x^{4-x} complexes is not high enough

to maintain connectivity: the concentration of monomers, dimers, and trimers starts to rise. The concentration of dimers and trimers goes through a maximum somewhere in the interval $0 < AnF_4 < 0.3$, while that of monomers tends to an equilibrium between the most stable AnF_x^{4-x} coordinations at infinite dilution. With increasing temperature, polymerization and the maxima of dimers and trimers are shifted to a higher actinide fluoride concentration, and there is a higher content of monomers in AF-rich region compositions.

Alkali actinide halide salts with Li as the alkali cation display a rather symmetric enthalpy of mixing. Binary mixtures containing the rest of the alkali cations tend to have a minimum in the region $0.25 < X(AnX_n) < 0.33$. This is a region in which there is strong short-range order: the number of alkali-actinide second-nearest neighbors is maximized, which is favorable from an electrostatic point of view. Moreover, the mixing enthalpy becomes more negative going down the alkali family: as the alkali cation increases in size, its polarization ability is lowered, reducing its ability to attract halide ions. As a result, the complex anion of first nearest neighbors around the actinide cation, $[AnX_n]^{4-n}$, is stabilized. The increased stability of $[AnF_n]^{4-n}$ shells is also manifested in the intermediate solid phases appearing in the binary phase diagrams. Not only do more intermediate compounds arise down the alkali family, but their melting point increases, and generally changes from incongruent to congruent when the alkali cation is less polarizing. As an example, compare LiF-UF_4 (Fig. 5.14) with NaF-ThF_4 (Figs. 6.12), and KF-ThF_4 (Fig. 2.11). This is an effect that is seen in other systems containing "soft" cations [3]: the number of intermediate phases increases in the order Li < Na < K < Cs. Finally, the stability of the free alkali cations themselves increases as they grow in radius, since their charge can be distributed over a larger volume, contributing to the stabilization of the overall melt.

This increasing stability of the liquid solution leads to a deviation from ideal behavior; activity is another clear indicator of this non-ideal behavior, as for the NaF-ThF_4 system in Chapter 6. Despite this, other properties are not as sensitive to non-ideal behavior: LiF-ThF_4 and LiF-UF_4 both display ideal molar volume behavior. The heat capacity of the latter systems as calculated with Molecular Dynamics (MD) simulations also approximates ideal behavior, with small fluctuations. Following the trend in mixing enthalpies, NaF-ThF_4 showed greater deviations from ideality than LiF-UF_4. By looking at trends in viscosities and electrical conductivities, it is argued that most thermophysical properties would show increasing deviation from ideality with increasing radius of the alkali cation (see Chapter 4), due to a stabilization of heterpolyanions and a steric hindrance of the polymerization.

This account, although largely qualitative, provides us with a framework to make more informed estimates about systems that have never been measured. Remember for instance that Th will turn into Pa in the reactor, yet there are scarcely any studies on protactinium fluorides. We can be quite confident, however, that LiF-PaF_4 will display ideal molar volumes. We can expect the viscosities of a given composition to fall between that of the equivalent composition of ThF_4 and UF_4, and we could model them using an Eyring equation coupled with a thermodynamic assessment, with better than order-of-magnitude initial guesses of the activation energy terms in the Eyring equation. NpF_4-containing systems could be treated similarly.

Having presented a general view of what was learned about actinide-bearing molten salts, allow me to zoom in and discuss outcomes in more detail.

8.2. DETAILED OUTCOMES OF THIS DISSERTATION

8.2.1. STRUCTURE

Four crystal phases have been isolated and Rietveld or LeBail refinements of the powder X-ray diffraction (XRD) patterns have been performed: $LiUF_5$, Na_2ThF_6, $NaTh_2F_9$, K_2ThF_6. Although none of these have been reported for the first time, they have now been unequivocally assigned to their respective binary phase diagrams. Many other phases were observed as part of a mixture of phases, from which definitive conclusions could be drawn on the phase equilibria in the binary systems as well. Most notably, Li_4UF_8 and Li_3UF_7 were confirmed to be a high-temperature phase and a metastable phase, respectively. The latter, although not appearing in the phase diagram, was found to form rather easily, so its Gibbs energy function was optimized such that it was on the verge of forming as a line compound.

Structural measurements of the melts, namely high temperature *in situ* X-ray Absorption Fine Structure (EXAFS) spectroscopy, were also performed. The specific furnace used for that challenging purpose was designed and demonstrated [20] before this thesis work had begun. However, throughout the experimental campaigns required to gather the data reported here, we have developed a robust process spanning from sample preparation to furnace operation and data collection. It can be singled out that EXAFS spectra were collected for pure end-members with a high melting point, namely UF_4 and ThF_4. Data interpretation was carried out relying primarily on Molecular Dynamics (MD), yet the agreement with fits made with the standard EXAFS equation shows the latter can also be useful to qualitatively analyze the structure of highly ordered liquids such as molten salts. Analysis in that case must be restricted only to the first shell, and the fitting of the coordination number must be carried out carefully and with some physical constraints.

8.2.2. PHASE EQUILIBRIA

Four chloride binary systems were assessed: ACl-$ThCl_4$ (A = Li, Na, K) and $NaCl$-UCl_3. Although there is a lack of thermodynamic data for the $ThCl_4$-based systems, the optimizations are consistent with the general features of molten salts described above. Further work needed on these systems has clearly been outlined. The $NaCl$-UCl_3 description has been improved by incorporating mixing enthalpy of the liquid solution and revised heat capacity data of NaCl(l) in the assessment.

Three binary fluoride systems were thoroughly assessed: LiF-UF_4, NaF-ThF_4, and KF-ThF_4. Their topology is better known thanks to this work because of new differential scanning calorimetry (DSC) measurements (phase equilibria and mixing enthalpy measurements), powder XRD measurements, and experimental determinations of the standard entropy of some phases: Na_2ThF_6, $NaTh_2F_9$, and K_2ThF_6. The ternary systems LiF-KF-ThF_4 and NaF-KF-ThF_4 were described as well, also incorporating novel experimental observations. New thermodynamic data was incorporated in the LiF-ThF_4 system, which was re-optimized without modifying the excess Gibbs energy terms of the liquid

solution in the JRC database [7]. The LiF-ThF_4-UF_4 ternary phase diagram was updated to reflect these changes, also keeping the description of constitutive binaries and using no excess ternary terms.

8.2.3. THERMOPHYSICAL PROPERTIES

The low-temperature heat capacities of Na_2ThF_6, $NaTh_2F_9$, and K_2ThF_6 were measured, from which their standard entropies could be derived. A thermodynamic self-consistent (TSC) method [18, 19] using Density Functional Theory (DFT) and the Quasi-Harmonic approximation (QHA) could successfully bridge the low-temperature heat capacity with high-temperature behavior tending to Neumann-Kopp. MD simulations were used to calculate the molar volumes/densities, thermal expansions, and heat capacities of the (Li,U)F_x and (Na,Th)F_x solutions. Non-ideal behavior was observed, with smaller deviations for (Li,U)F_x than for (Na,Th)F_x, and ideal behavior was proposed to be a good approximation to describe the density and heat capacity of (Li,U)F_x.
With that insight, ideal molar volumes were retained for LiF-ThF_4 and LiF-UF_4 in an assessment of their density and viscosity. This CALPHAD-based assessment relates the density and viscosity to the quadruplet distributions calculated from the thermodynamic descriptions [16, 14, 15] of the systems under investigation. The density and viscosity of NaCl-UCl_3 were assessed in the same way, although for this system non-ideal density had to be accounted for. These three assessments pave the way to compute, beyond the phase diagram but related to it, molten salt fuel state functions.

8.2.4. STRUCTURE-PROPERTY RELATIONSHIP

The complexation and polymerization phenomena captured by MD simulations in the LiF-UF_4 and NaF-ThF_4 systems were explicitly linked to their thermodynamic descriptions by including liquid solution quadruplets with 8- and 7-coordinated actinide cations, as well as a dimeric species representing formation of polymers. This simplification of the melt speciation is necessary to keep the number of fitting parameters from growing too large. The phase diagrams could be correctly reproduced, and the calculated speciation in the melt followed the trends predicted by the MD. Although this dissertation did not reach that level of description, it is foreseeable that the density and viscosity assessments could also be related to the structure by expressing them in terms of these "structural" quadruplets.

8.3. RECOMMENDATIONS FOR FUTURE WORK

There has been an interest in Fluid Fuel Reactors since the dawn of the atomic age. Two early reactors, LAPRE-1 and LAPRE-2, were fueled with uranium oxide dissolved in concentrated phosphoric acid [10, 2]. The fuel was so corrosive that the cores and piping had to be plated with pure gold! A consideration that this anecdote brings to mind is of course corrosion. While there is significant knowledge on corrosion issues from the MSRE experience (see Chapter 1.3), the fuel salt-alloy thermodynamic database must

be expanded. There has already been some work done on the interaction of the corrosion product NiF_2 with alkali fluoride coolants (LiF, NaF, KF) [11], and at the time of this writing there is ongoing work regarding fluorides of chromium and molybdenum. The corrosion products of iron, an element which is nearly ubiquitous in structural alloys, are very important to consider as well. Likewise, the recent surge of interest on chloride fuels needs to be matched with work on alloy-salt interactions, and the effect of dissolved structural metal chlorides on the fuel matrix properties.

Long gone are the budgets allowing for gold-plated prototypes[1]. Still, back then reactors were being designed with the aid of slide rules. It does not cease to amaze me what can be achieved *in silico* with modern computers. Leslie Dewan, who performed extensive MD calculations on, among other systems, LiF-ThF_4 and LiF-UF_4, argued that MD was reliable enough to fill the gaps in experimental data [4]. I think she is right, provided the MD potentials have been benchmarked against known data, although MD calculations are still relatively expensive and cumbersome. In light of the present work, I think MD can have a very useful role as a source of high quality data which can then be used as input for CALPHAD techniques and eventually coupled with fluid dynamics and systems codes. A systematic, coordinated effort to derive MD potentials of (molten) salts, a companion, if you will, of thermodynamic databases, would be of great use. We have seen that CALPHAD itself goes beyond "just" the calculation of phase diagrams and can incorporate local structure information and handle functions like density and viscosity. The electrical conductivity, which may be useful to monitor during operation with online instrumentation, as well as to design reprocessing schemes, should also be linked to the thermodynamic assessments. Considering that they are heat-bearing liquids, data on the thermal conductivities of molten salts is surprisingly scarce, although to my knowledge there are current efforts to measure these at JRC-Karlsruhe. This crucial property, too, should be modelled.

Now, even with the computational techniques at hand, the combinatorial space of systems requiring a thermodynamic description in MSR fuel is to be reckoned with. Assuming a fresh fuel of three salts, and taking into account the 18 most important [1] salt-soluble fission products, and assuming only one oxidation state for each, yields 210 binary, 1330 ternary, and 5985 quaternary subsystems. High-throughput computational techniques similar to the tool recently created by Otis and Liu [12], but implementing the quasi-chemical formalism instead of the Compound Energy Formalism (CEF) [6], need to be developed. In any event, ternary descriptions usually require small excess terms to be optimized, and quaternary ones rarely do [8], so it may be the case that an accurate description of only a small subset of these is enough to get a good approximation of real salt behavior, especially since some fission products are there only in very small quantities. The size of this set, which we might call the Minimum Significant Set (MSS), and the identity of its elements, needs to be established. New irradiation experiments such as SALIENT-01 [5], in which fresh MSR fuel was irradiated in the High Flux Reactor (HFR) in Petten, will be invaluable to evaluate any high throughput techniques as well as hypotheses regarding the MSS.

[1] This is not to say that anyone today would think that is a good idea.

BIBLIOGRAPHY

[1] E. Capelli and R.J.M. Konings. “Halides of the Actinides and Fission Products Relevant for Molten Salt Reactors”. In: *Comprehensive Nuclear Materials*. Elsevier, 2020.

[2] R.A. Clark. *Los Alamos power reactor experiment no. II, LAPRE II*. Tech. rep. Los Alamos Scientific Lab., N. Mex., 1960.

[3] V. Danek. *Physico-chemical analysis of molten electrolytes*. Elsevier, 2006.

[4] L. Dewan. “Molecular dynamics simulation and topological analysis of the network structure of actinide-bearing materials”. PhD thesis. Massachusetts Institute of Technology, 2013.

[5] P.R. Hania et al. “Irradiation of thorium-bearing molten fluoride salt in graphite crucibles”. In: *Nuclear Engineering and Design* 375 (2021), p. 111094.

[6] M. Hillert. “The compound energy formalism”. In: *Journal of Alloys and Compounds* 320.2 (2001), pp. 161–176.

[7] JRC-Karlsruhe. *JRCSMSD thermodynamic database on halide salts*. 2020.

[8] U.R. Kattner. “The Calphad method and its role in material and process development”. In: *Tecnologia em metalurgia, materiais e mineracao* 13.1 (2016), p. 3.

[9] S. Kern et al. “Temperature variation of the structural parameters in actinide tetrafluorides”. In: *The Journal of Chemical Physics* 101.11 (1994), pp. 9333–9337.

[10] J.A. Lane, H.G. MacPherson, and F. Maslan. *Fluid Fuel Reactors: Molten Salt Reactors, Aqueous Homogeneous Reactors, Fluoride Reactors, Chloride Reactors, Liquid Metal Reactors and Why Liquid Fission*. Addison-Wesley Pub. Co., 1958.

[11] J.A. Ocádiz Flores et al. “Thermodynamic assessment of the LiF-NiF2, NaF-NiF2 and KF-NiF2 systems”. In: *The Journal of Chemical Thermodynamics* 121 (2018), pp. 17–26.

[12] R. A Otis and Z.-K. Liu. “High-throughput thermodynamic modeling and uncertainty quantification for ICME”. In: *JOM* 69.5 (2017), pp. 886–892.

[13] R.A. Penneman, R.R. Ryan, and A. Rosenzweig. “Structural systematics in actinide fluoride complexes”. In: *Rare Earths*. Springer, 1973, pp. 1–52.

[14] C. Robelin and P. Chartrand. “A Density Model Based on the Modified Quasichemical Model and Applied to the NaF-AlF_3-CaF_2-Al_2O_3 Electrolyte”. In: *Metallurgical and Materials Transactions B* 38.6 (2007), pp. 881–892.

[15] C. Robelin and P. Chartrand. “A viscosity model for the (NaF+ AlF_3+ CaF_2+ Al_2O_3) electrolyte”. In: *The Journal of Chemical Thermodynamics* 43.5 (2011), pp. 764–774.

[16] C. Robelin, P. Chartrand, and G. Eriksson. “A Density Model for Multicomponent Liquids Based on the Modified Quasichemical Model: Application to the NaCl-KCl-$MgCl_2$-$CaCl_2$ System”. In: *Metallurgical and Materials Transactions B* 38.6 (2007), pp. 869–879.

[17] R. Schmid-Fetzer. “Phase diagrams: the beginning of wisdom”. In: *Journal of Phase Equilibria and Diffusion* 35.6 (2014), pp. 735–760.

[18] A. Seifitokaldani and A.E. Gheribi. “Thermodynamically self-consistent method to predict thermophysical properties of ionic oxides”. In: *Computational Materials Science* 108 (2015), pp. 17–26.

[19] A. Seifitokaldani et al. “Thermophysical properties of titanium and vanadium nitrides: Thermodynamically self-consistent approach coupled with density functional theory”. In: *Journal of Alloys and Compounds* 662 (2016), pp. 240–251.

[20] A.L. Smith et al. “In situ high-temperature EXAFS measurements on radioactive and air-sensitive molten salt materials”. In: *Journal of synchrotron radiation* 26.1 (2019), pp. 124–136.

ACKNOWLEDGEMENTS

I originally came to Delft to step into the world of nuclear science and technology, with a view to focus on molten salt chemistry, as a Master's student. I want to wholeheartedly thank my promotors Prof. Rudy Konings and Dr. Anna Smith for opening that door and inviting me in way back then. Both have been very generous with their time and expertise. As my daily supervisor, Anna has taught me a lot of skills, asked piercing questions to guide my research, lent a sharp editorial eye to my manuscripts, and suggested interesting projects related to this dissertation and beyond.

I would further like to thank Prof. Mathieu Salanne for his invaluable help on Molecular Dynamics simulations and for putting me in contact with Prof. Aimen Gheribi, with whom we have a fruitful collaboration and who has also been a friend to talk to, especially during the long COVID days. Many thanks also to Dr. Ondrej Beneŝ for being a critical co-author, being my supervisor in JRC-Karlsruhe during my brief spell there, performing some measurements on my behalf, and providing me, along with Dr. Pavel Souĉek, with actinide fluorides of high purity. For their input and effort, without which this work would not have been possible, I also thank Kathy Dardenne, Jörg Rothe, Jean-Christophe Griveau, and Eric Colineau. To the talented MSc students Anna recommended I work with: thank you Maarten, Gilliam, and of course Dennis; let us keep doing worthwhile research.

Great colleagues contributed to a fantastic experience. At the Reactor Institute, thanks to Denis, Matteo, Aldo, Fulvio, Marco, Fahad, Guilhem, Sara, Enrica, Elisa, Óscar, Thomas, for some good times, from office chats, to beach volleyball, restaurant dinners, squash, padel, grabbing a beer, and a long etcetera. Elisa: thank you so much for all the 'how-to' knowledge you shared with me, whether in the lab or regarding data crunching and interpretation; the MSR community is very lucky to have you back from fusion. To John and Dick, thanks for the good lunch conversations, for your help in the lab, and making those long hours at the synchrotron seem much shorter. Thank you to the radiation protection department, and to Henk and Koos, thank you for founding and staffing that wonderful institution within the RID: 't Koepeltje.

I also have fond memories of Karlsruhe; for that I especially have to thank Emanuele, Pauline, Tommy, Luana, Luca, Jone, and Mathieu. I owe it to the administrative help of Petra Strube, Vladka Mestanova, Trudy Beentjes, and Karin van der Graaf, that I could go there in the first place, thanks a lot.

For funding I gratefully acknowledge the consortium between the Mexican Council of Science and Technology, and the Ministry of Energy, CONACYT-SENER, as well as the European Nuclear Education Network (mobility grant A-041841711). I hope these institutions continue investing in human capital in the nuclear sector.

Finally, I wish to express my gratitude towards my family. To my parents, Olimpia and Enrique, for a house full of books and lifelong encouragement to do what makes me happy. To Janny and Hans, Rein and Eline, for their warmth and support. Most of all to my beloved wife, Stefanie, who is my bedrock. Thank you for your endless patience and kindness.

LIST OF PUBLICATIONS

10. **J.A. Ocádiz Flores**, R.J.M. Konings, A.L. Smith, *Using the Quasi-chemical Formalism Beyond the Phase Diagram: Density and Viscosity Models for Molten Salt Fuel Systems*, submitted, (2021).

9. **J.A. Ocádiz Flores**, B.A.S. Rooijakkers, R.J.M. Konings, A.L. Smith, *Thermodynamic description of the ACl-$ThCl_4$ (A= Li, Na, K) systems*, Thermo **1(2)**, 122-133, (2021).

8. M.B.J.W. Schreuder **J.A. Ocádiz Flores**, A.E. Gheribi, O. Beneš, J.-C. Griveau, E. Colineau, R.J.M. Konings, A.L. Smith, *Experimental and Computational Exploration of the NaF-ThF_4 Fuel System: Structure and Thermochemistry*, Journal of Physical Chemistry B, **125**, 30, 8558–8571 (2021).

7. G.I.L. van Oudenaren, **J.A. Ocádiz Flores**, A.L. Smith, *Coupled structural-thermodynamic modelling of the molten salt system NaCl-UCl_3*, Journal of Molecular Liquids **342**, 117470, (2021).

6. **J.A. Ocádiz Flores**, A.E. Gheribi, J. Vlieland, K. Dardenne, J. Rothe, R.J.M. Konings, A.L. Smith, *New insights and coupled modelling of the structural and thermodynamic properties of the LiF-UF_4 system*, Journal of Molecular Liquids **331**, 115820 (2021).

5. **J.A. Ocádiz Flores**, A.E. Gheribi, J. Vlieland, D. de Haas, K. Dardenne, J. Rothe, R.J.M. Konings, A.L. Smith, *Examination of the short-range structure of molten salts: ThF_4, UF_4, and related alkali actinide fluoride systems*, Physical Chemistry Chemical Physics **23**, 18, 11091–11103 (2021).

4. **J.A. Ocádiz Flores**, E. Carré, J.-C. Griveau, E. Colineau, E. Capelli, P. Souček, O. Beneš, R.J.M. Konings, A.L. Smith, *Thermodynamic assessment of the KF-ThF_4, LiF-KF-ThF_4 and NaF-KF-ThF_4 systems*, The Journal of Chemical Thermodynamics **145**, 106069 (2020).

3. A.L. Smith, M.N. Verleg, J. Vlieland, D. de Haas, **J.A. Ocádiz Flores**, P. Martin, J. Rothe, K. Dardenne, M. Salanne, A.E. Gheribi, E. Capelli, L. van Eijck, R.J.M. Konings, *In situ high-temperature EXAFS measurements on radioactive and air-sensitive molten salt materials*, Journal of Synchrotron Radiation, **26**, 124-136 (2019).

2. **J.A. Ocádiz Flores**, E. Capelli, P.E. Raison, R.J.M. Konings, A.L. Smith, *Thermodynamic assessment of the LiF-NiF_2, NaF-NiF_2 and KF-NiF_2 systems*, The Journal of Chemical Thermodynamics **121**, 17–26 (2018).

1. F. Benyettou, **J.A. Ocádiz Flores**, F. Ravaux, R. Rezgui, M. Jouiad, S. Nehme, R.K. Parsapur, J.C. Olsen, P. Selvam, A. Trabolsi, *Mesoporous γ-Iron Oxide Nanoparticles for Magnetically Triggered Release of Doxorubicin and Hyperthermia Treatment*, Chemistry A European Journal **22**, 47, 17020–17028 (2016).

About the Author

Jaén A. Ocádiz Flores

Jaén Ocádiz Flores was born in Mexico City, in 1992. From a very early age he moved to Querétaro, where, aside from spending a year abroad in Moncton, Canada, he lived uninterruptedly until finishing high school. Upon graduating, he went on to study Chemistry and Mathematics at NYU Abu Dhabi, which was undoubtedly a very fortunate undergraduate experience. Having caught the travel bug, and eager to try his hand at molten salt chemistry, he went on to TU Delft to acquire a Master's degree in Chemical Engineering, specializing in Nuclear Science and Engineering. At the same research group in which he conducted his Master's thesis, Reactor Physics and Nuclear Materials (RPNM), he obtained a PhD position, which culminated in the present dissertation. Still very much fascinated by his field of study, and happy with his colleagues and workplace, he will remain for some more time at RPNM as a postdoctoral researcher.